Gyrofluid Theory and Simulation of Electromagnetic Turbulence and Transport in Tokamak Plasmas

Philip Benjamin Snyder

A Dissertation
Presented to the Faculty
of Princeton University
in Candidacy for the Degree
of Doctor of Philosophy

Recommended for Acceptance by the
Department of Astrophysical Sciences

November 1999

Dedicated to my parents,
Gene and Christine Snyder

Abstract

TURBULENCE AND TRANSPORT in toroidal plasmas is studied via the development of an electromagnetic gyrofluid model, and its implementation in realistic nonlinear simulations. This work extends earlier electrostatic gyrofluid models to include magnetic fluctuations and non-adiabatic passing electron dynamics. A new set of electron fluid equations is derived from the drift kinetic equation, via an expansion in the electron-ion mass ratio. These electron equations include descriptions of linear and nonlinear drift motion, Landau damping, and electron-ion collisions. Ion moment equations are derived from the electromagnetic gyrokinetic equation, and the gyrokinetic Poisson's Equation and Ampere's Law close the system. The model is benchmarked with linear gyrokinetic calculations, and good agreement is found for both the finite-β ion temperature gradient (ITG) and kinetic Alfvén ballooning (KBM) instabilities. Nonlinear simulations of ITG and KBM-driven turbulence are performed in toroidal flux tube geometry at a range of values of plasma β, and electromagnetic effects are found to significantly impact turbulent heat and particle transport. At low values of β, transport is reduced, as expected due to the finite-β stabilization of the ITG mode. However, as β approaches the ideal-MHD stability threshold, transport can increase. In the presence of dissipation provided by a model of electron Landau damping and electron-ion collisions, this transport increase can be quite dramatic. Finally, the results of the simulations are compared to tokamak experiments, and encouraging agreement is found with measured density and temperature fluctuation spectra. Direct comparisons of transport fluxes reveal that electromagnetic effects are important at characteristic edge parameters, bringing predicted fluxes more closely in line with observations.

Table of Contents

Abstract **v**

1 Introduction **1**

1.1 Background and Motivation 2

1.1.1 Physics Models for Turbulence Simulations 4

1.1.2 Current Understanding of Tokamak Transport 8

1.1.3 The Need for an Electromagnetic Model with Non-adiabatic Passing Electrons 11

1.1.4 A Brief History of Electromagnetic Microturbulence Simulations 15

1.2 Guiding Principles in Model Development 17

1.3 Outline 18

2 Simple Physics of Relevant Microinstabilities **21**

2.1 Shear Alfvén Waves and Instabilities 22

2.2 The ITG Mode 27

2.3 Local Fluid Analysis of the Finite-β ITG and KBM 29

2.3.1 The Electrostatic Limit 32

2.3.2 The Kinetic Ballooning Mode 33

2.3.3 The Finite-β ITG 34

2.3.4 Growth Rates in the Local Fluid Limit 35

2.3.5 Kinetic Effects 39

3 Derivation of the Electromagnetic Gyrofluid Equations 41

3.1 The Gyrokinetic Equation 42

3.2 The Ion Gyrofluid Equations 46

3.2.1 The Ion Moment Equations 52

3.2.2 Finite Larmor Radius Terms 54

3.2.3 Closures 60

3.2.4 Ion Collisions 64

3.2.5 Final Ion Gyrofluid Equations 65

3.2.6 The Multi-species Ion Equations 66

3.3 The Electron Landau Fluid Equations 68

3.3.1 Analytic Expansion in the Electron Mass Ratio 68

3.3.2 Derivation of the Electron Equations 72

3.3.3 Electron Collisions and Landau Damping 76

3.4 Poisson's Equation and Ampere's Law 79

4 Linear Benchmarks with Kinetic Theory 81

4.1 The Finite-β ITG Instability 82

4.1.1 Benchmarks in Slab Geometry 82

4.1.2 ITG Benchmarks in Toroidal Geometry 85

4.2 The Kinetic Alfvén Instability 88

4.2.1 Benchmarks with Zero Ion Temperature Gradient 89

4.2.2 Benchmarks with Finite Ion Temperature Gradient 89

4.3 Summary 93

5 Nonlinear Simulations 95

5.1 The Flux Tube Geometry 96

5.2 Computational Details 98

5.2.1 Numerical Convergence 100

5.3 Simulation Results . . . 102
5.3.1 Simulations without Electron Dissipation . . . 104
5.3.2 Simulations with Electron Dissipation . . . 113

6 Comparison with Experiment 123

6.1 Summary . . . 130

7 Conclusions and Future Directions 133

7.1 Summary and Conclusions . . . 134
7.2 Future Directions . . . 137

A Gyrofluid vs. δF Gyrokinetic Comparisons and the RH Mode 141

A.0.1 Conclusions . . . 146

B Flux Conservation 147

C Landau Fluid Models of Collisionless Magnetohydrodynamics 149

C.1 Abstract . . . 149
C.2 Introduction . . . 150
C.3 Collisionless MHD . . . 153
C.4 The Moment Hierarchy . . . 155
C.4.1 Conservation Properties . . . 158
C.5 The 4+2 Model . . . 159
C.5.1 Linear Response from Kinetic Theory . . . 160
C.5.2 The 4+2 Landau Closure . . . 161
C.6 The 3+1 Model . . . 166
C.7 Collisional Effects . . . 168
C.7.1 The High Collisionality Limit . . . 169
C.7.2 Collisionally Modified 3+1 Closure . . . 170
C.8 Nonlinear Implementation of the Closure . . . 171

C.9 An Example: The Mirror Instability 174
C.10 Discussion 179

Bibliography **183**

List of Figures

1.1 Comparison of measured stored energy to GLF23 model predictions 9

1.2 Finite-β effects on tokamak instabilities 14

2.1 Simple picture of the toroidal ITG instability mechanism 28

2.2 β dependence of growth rates in the local fluid limit 36

2.3 Growth rate of the dominant mode in the local fluid limit, compared with predictions of simplified electron fluid models 38

4.1 Growth rate spectra of the slab ITG mode 83

4.2 Growth rate and frequency spectra of the slab ITG mode 84

4.3 Scan of toroidal ITG growth rates vs. safety factor 86

4.4 Benchmark of toroidal ITG growth rates with the `GS2` code 87

4.5 Toroidal shear Alfvén growth rate and frequency spectra 88

4.6 β scan of toroidal shear Alfvén growth rate and frequency 90

4.7 Toroidal shear Alfvén growth rate and frequency spectra with $\eta_i = 2$ 91

4.8 β scan of the toroidal shear Alfvén growth rate with $\eta_i = 2$ 92

4.9 Toroidal shear Alfvén growth rate vs. magnetic shear 93

5.1 The toroidal flux tube simulation domain 96

5.2 Scaling of `Gryffin` performance with number of processors 99

5.3 Convergence in time step 101

5.4 Convergence in perpendicular and parallel resolution 101

5.5 Convergence in simulation box size 103

5.6 Linear growth rate and frequency spectra at six values of β 105
5.7 Time evolution of χ_i at four values of β 106
5.8 Time evolution of the ion density fluctuation spectrum 107
5.9 Ion heat conductivity χ_i vs. β 109
5.10 Ion density fluctuation spectra at four values of β 111
5.11 Ion perpendicular temperature fluctuation spectra at four values of β 111
5.12 Time evolution of the electrostatic potential 114
5.13 Impact of electron dissipation on linear growth rates 115
5.14 Time evolution of χ_i at four values of β, with electron dissipation . 116
5.15 Ion heat conductivity χ_i vs. β with electron dissipation 117
5.16 Time evolution of the electrostatic potential with electron dissipation 119
5.17 Particle diffusivity and electron heat conductivity vs. β 120

6.1 Density and temperature profiles for TFTR shot #65018 125
6.2 Density and temperature scale lengths for TFTR shot #65018 . . . 125
6.3 Profiles of q, $\hat{s}$, η_i and η_e for TFTR shot #65018 126
6.4 Plasma β and α_{MHD} profiles for TFTR shot #65018 127
6.5 Observed and predicted χ_i near the edge of an L-mode TFTR shot 128
6.6 Observed and predicted χ_e near the edge of an L-mode TFTR shot 131

A.1 Comparison of transport predictions from gyrofluid and δF gyrokinetic particle simulations 142
A.2 Comparison of the temperature gradient predicted by the IFS-PPPL model and δF gyrokinetic particle simulations 144

C.1 Comparison of linear density response for various models 164
C.2 Comparison of linear perpendicular pressure response for various models 165
C.3 Comparison of predicted growth rates for the mirror instability . . . 178

Acknowledgments

First and foremost I would like to thank my thesis advisor, Greg Hammett. His physical insight and clear explanations have been an invaluable guide throughout this work, and his determination and integrity have been an inspiration.

I owe a great deal of my understanding of gyrofluid simulations to Mike Beer. His toroidal gyrofluid model and simulation code are the foundation on which much of the work in this thesis has been built, and the many hours he spent explaining the nuances of his work have been greatly appreciated.

I thank Bill Dorland for his many contributions to this work, both indirectly, through his earlier development of the slab gyrofluid model and simulation code, and directly, through his advice and assistance on many numerical and physical issues.

I would like to thank my readers, Steve Jardin and Taik Soo Hahm, for their insightful comments and suggestions. I would also like to thank many other teachers at Princeton who have enlightened me and guided my development as a scientist, notably Nat Fisch, Bill Tang, Russell Kulsrud, Allan Reiman, Charles Karney, John Krommes, Masa Ono, Tom Stix, Roscoe White and Rob Goldston.

I am grateful to Mike Kotschenreuther for enlightening physics discussions, and for the use of his `GS2` code. I also thank John Reynders for the use of his slab eigenvalue code. In the course of my dissertation research, I have had the benefit of useful conversations with a great many physicists, including Jim Drake, Barrett Rogers, Ron Waltz, Scott Parker, Steve Cowley, Bruce Scott, Zhihong Lin, Jim Callen, Chris Hegna, Pat Diamond, Amita Das, Liu Chen, Fulvio Zonca, Jon Kinsey, Aaron Redd, Andris Dimits, Ron Cohen, Bruce Cohen, Rick Sydora and many others.

I have also had useful physics discussions with several fellow graduate students at Princeton, notably Steve Smith, Hong Qin, Yang Chen, Igor Manuilskiy, and

Steve Cauffman. Computer-related assistance from John Wright, Mark Herrmann, Peter Stoltz, Troy Carter, Charles Karney, Ernie Valeo, Greg Rewoldt, and the support staffs at NERSC and LANL-ACL has been much appreciated. Thanks also to the TFTR group for providing the data discussed in Ch. 6.

On a more personal note, my years at PPPL have been made far more rewarding and pleasant by friends like Scott Hsu, Troy Carter, Max Karasik, Ed Chao, Bryan Fong, Bob Heeter, Mike Beer, Mark Herrmann, John Wright, Steve Smith, Peter Stoltz and Hilary Oliver. I couldn't ask for better roommates than Max, Bryan and Bob, and the many hours spent with Scott and Helen Hsu and Troy and Becky Carter will not soon be forgotten. My years at Princeton have also been made much easier and more pleasant by the kind-hearted efforts of Barbara Sarfaty, as well as Lisa Carlucci and Heidi Hughes.

I would also like to thank professors Werner Wolf, Philippe Similon and Robert Wheeler for their guidance during my undergraduate years at Yale, and Greg Boebinger and Al Passner for their advice and guidance during an enjoyable summer of research at Bell Labs. And thanks to talented and inspirational high school teacher Howard Fowler, who first introduced me to physics.

This dissertation is dedicated to my parents, Gene and Christine Snyder, as the culmination of a long education that they have supported at every step. Many thanks to all of my family for their guidance and unfailing support.

And finally, thanks to my fiancée, Mary Moore. Her warmth, love, and compassion have enriched my life, and carried me through difficult times.

This work was supported in part by the DOE High Performance Computing and Communications Initiative (HPCCI) Grand Challenge Numerical Tokamak Turbulence Project, by US DOE contract No. DE-AC02-76-CHO-3073, and by a National Science Foundation Graduate Fellowship. Use of computer resources at the National Energy Research Supercomputer Center and at the Los Alamos National Laboratory Advanced Computing Lab is gratefully acknowledged.

August 17, 1999

Chapter 1

Introduction

UNDERSTANDING TURBULENT TRANSPORT has been a critical, but elusive, goal of the magnetic fusion program for decades. In the past few years, with the advent of powerful supercomputers and efficient physics models, much progress has been made toward the development of quantitatively accurate predictions of tokamak transport. However, there are still many transport phenomena which are poorly understood, and a complete model, which can reliably predict transport in future experiments, is lacking.

The primary goal of this thesis is to take a step towards a more complete understanding of turbulent transport. To this end, a new physics model is developed and implemented in nonlinear numerical simulations. The new model relaxes the electrostatic approximation made in many previous models, by adding the physics of magnetic fluctuations and non-adiabatic passing electrons.

The introduction of electromagnetic physics both quantitatively modifies previous electrostatic results, and introduces qualitatively new physics, making the model both more accurate and more complete. The model is used to assess the importance of electromagnetic effects on turbulence and transport, both in the plasma core and in the edge.[1] Comparisons are made both with electrostatic simulations and with experiment. The model should help bring theoretical predictions in line with experimental results, and shed light on previously poorly understood trans-

---

[1] The term edge here refers to the outer $\sim 20\%$ of the closed magnetic surfaces. The core refers to the inner $\sim 80\%$. Transport in the extreme edge, or the scrape off layer where magnetic surfaces are not closed, is not considered here.

port phenomena. We hope that, in addition to providing new physical insight, our model will ultimately aid in the design of low transport, cost effective magnetic fusion reactors.

1.1 Background and Motivation

Understanding and controlling the rate at which particles and heat escape from the reactor chamber is critical to the successful design and operation of a magnetic fusion device. In the early days of the fusion program, estimates of particle and heat transport based on simple collisional diffusion were made. However, these estimates were found to drastically under-predict the transport observed in experiments, and the large measured transport was labeled "anomalous." Understanding this "anomalous" transport has been a primary goal of the fusion program ever since.

While the magnetically confined plasmas in most present-day fusion experiments are believed to usually be stable to large-scale magnetohydrodynamic modes, there also exist smaller scale instabilities (often called "microinstabilities") which can drive turbulence, leading to the large observed transport. Recent improvements in tokamak diagnostics have allowed for the direct observation of fluctuations believed to be driven by these microinstabilities. These fluctuations typically have length scales perpendicular to the magnetic field on the order of the ion gyroradius, $k_\perp \rho_i \sim .1 - .5$, where $k_\perp$ is a typical perpendicular wave number, and ρ_i is the ion gyroradius, defined to be v_{ti}/Ω_{ci}, where v_{ti} is the ion thermal speed ($\sqrt{T_i/m_i}$), and Ω_{ci} is the ion cyclotron frequency, ($ZeB/m_i c$). The fluctuation frequencies are small compared to Ω_{ci}, often scaling like the diamagnetic drift frequency, $\omega_* = k_\theta \rho_i v_{ti}/L_n$, where k_θ is a typical poloidal mode number, and L_n is the density scale length, $-[d(\ln n_0)/dr]^{-1}$.

With these typical fluctuation length and time scales in mind, it is possible to make a simple mixing length estimate of the particle diffusivity (D), and heat conductivity (χ):

$$D, \chi \sim \frac{\Delta x^2}{\Delta t} \sim \rho_i^2 \omega_* \sim \rho_i^2 k_\theta \rho_i \frac{v_{ti}}{L_n} \sim \rho_i^2 v_{ti}/L_n$$

where we've taken $k_\theta \rho_i \sim 1$. The above result is known as the gyro-Bohm diffusivity, and it yields estimates of global confinement that agree with many broad trends observed in several tokamak experiments. This agreement is encouraging, insofar as it suggests that microturbulence is responsible for the "anomalous" transport. However, such simple mixing length estimates prove inadequate as transport models both because they predict global transport only within an order of magnitude, and because they are unable to properly account for local transport behavior. In particular, the mixing length estimate predicts that heat flux and diffusivity should decrease with minor radius (due to the $T^{3/2}$ dependence), while in experiments the heat diffusivity and fluctuation levels are generally observed to increase with radius, with a particularly dramatic increase near the plasma edge. Hence the mixing length model often predicts too large a flux in the core and too small a flux near the edge. In addition, mixing length models cannot fully account for the improved confinement modes and transport barriers seen in many experiments. More detailed gyro-Bohm based models are able to explain some of these effects despite their basic gyro-Bohm scaling by including effects such as critical gradients and stabilizing $\mathbf{E} \times \mathbf{B}$ shear.

Several more involved analytic theories of turbulent transport have been developed, such as those described in [Lee and Diamond 1986], [Terry et al. 1988], and [Biglari et al. 1989]. Each of these models contains a great deal of physical insight, but they all rely on assumptions which must be checked with more detailed analyses. Quantitative predictions based on these models suffer from many of the same limitations as simple mixing length estimates. A number of excellent review articles are available on analytic theories of turbulent transport, including [Krommes 1997; Connor and Wilson 1994].

In order to provide a more complete and accurate model of turbulent transport, direct numerical simulation (DNS) techniques have been employed. Nonlinear numerical simulation of plasma turbulence is very challenging, because of the large number of dimensions (six in a fully kinetic simulation), and the wide range of plasma length and time scales. However, dramatic increases in available computing power, combined with the development of efficient physics models have led to a great deal of progress.

1.1.1 Physics Models for Turbulence Simulations

Several different types of physics models have been employed for the study of turbulence and transport in fusion plasmas. These models can all be derived starting with a general six-dimensional plasma kinetic equation, and making a series of approximations. In all cases, tradeoffs between physical completeness of the model and its practicality for use in numerical simulations are made. The models can be broadly categorized into pure fluid models, kinetic models, and fluid/kinetic hybrid models.

Pure Fluid Models

The simplest models are pure fluid models. These models take velocity space moments of a kinetic equation, and then close the moment hierarchy by assuming the plasma is highly collisional. Note that the simplest fluid models, such as ideal MHD, omit the small scale dynamics necessary for an accurate description of microturbulence (note however that kinetic effects can be added to MHD-type models, as in Appendix C). More detailed models such as Braginskii's equations [Braginskii 1965] must be employed.

Fluid models are generally amenable to numerical simulation, since only a small number of equations need be solved in a three-dimensional space. A set of analytic approximations is generally made to focus the model on the length and time scales relevant for microturbulence and transport.

Earlier fluid simulations of plasma turbulence were carried out using simplified equations, often in local coordinates, two dimensions, or sheared slab geometry, for example [Horton et al. 1980]. Simulations in toroidal geometry were first made feasible by the development of the ballooning representation [Connor et al. 1979], and its extension to nonlinear problems [Cowley et al. 1991; Beer et al. 1995]. This representation utilizes the separation between equilibrium and perpendicular fluctuation scale lengths to set up an efficient computational domain, as described in Sec. 5.1.

Pure fluid simulations have revealed a great deal about the qualitative nature of plasma microturbulence. However, such simulations cannot provide a quantitatively accurate model of turbulence in the core of a fusion plasma, because they lack important kinetic effects. Only near the plasma edge, where high collisionality negates kinetic effects, can such models be reliably used.

Recent developments have centered around the use of Braginskii-based fluid equations to study turbulent transport near the plasma edge, *eg.* [Zeiler et al. 1998; Xu et al. 1998; Rogers and Drake 1997; Scott 1997; Carreras et al. 1991; Hasegawa and Wakatani 1987][2].

Kinetic Models and Gyrokinetics

The recognition of the importance of plasma kinetic effects in the growth and saturation of microinstabilities led to interest in more direct approaches to the solution of the kinetic equation.

The most general plasma kinetic equations are six-dimensional (three dimensions in real space and three in velocity space), and contain a wide range of spatial and temporal scales, making direct numerical simulation in realistic geometry difficult, beyond the early pioneering work of [Cheng and Okuda 1977]. However, several recent advances have led to great progress toward fully kinetic simulations.

The first is the development of the nonlinear gyrokinetic equation [Frieman and Chen 1982; Lee 1983; Dubin et al. 1983]. Gyrokinetics averages over the particles' fast gyromotion around a strong magnetic field, resulting in a five-dimensional equation describing the drift motion of charged rings. All time scales slower than the ion gyro-frequency ($\Omega_i = ZeB/m_i c$, where Ze is the ion charge, B is the equilibrium magnetic field, and m_i is the ion mass) are retained, as are

---

[2] The fluid equations of B. Scott employ a model of Landau damping, and thus can also be considered a gyrofluid model.

spatial scales of the order of the ion gyroradius ($\rho_i = v_{ti}/\Omega_i$ where v_{ti} is the ion thermal speed, defined to be $\sqrt{T_i/m_i}$).

The resulting gyrokinetic equation is still difficult to solve directly, and particle-in-cell methods [Birdsall and Langdon 1991], which follow the trajectories of many superparticles in order to resolve the phase space, were applied [Lee 1983; Lee 1987]. These techniques were made significantly more efficient for the study of realistic core turbulence systems with small fluctuation levels by the development of the δF method [Kotschenreuther 1988; Dimits 1988; Dimits and Lee 1993; Parker and Lee 1993], which removes the equilibrium distribution and its associated noise from the simulation.

δF gyrokinetic particle (GKP) simulations are now a primary tool for investigating plasma microturbulence, and they have been implemented both in flux tube [Dimits et al. 1994] and full torus geometries [Parker et al. 1993]. A massively parallel, full torus GKP code including ion-ion collisions has been developed by [Lin et al. 1998], and used to study zonal flow dynamics. While most past GKP simulations have been electrostatic with purely adiabatic electrons, extensions to include magnetic fluctuations and non-adiabatic electrons are a subject of current research, as is discussed in Sec. 1.1.4.

The direct approach of solving the gyrokinetic equation on a five-dimensional grid has also been attempted, and found to be computationally challenging. However, with recent improvements in computational power and algorithms, there has been an increasing amount of work employing this approach [Jenko and Scott 1998; Dorland et al. 1999].

Fluid/Kinetic Hybrids and the Gyrofluid Model

The computational advantages of fluid models, combined with the recognition of the importance of kinetic effects in microturbulence, encouraged the development of models which sought to incorporate kinetic effects into an enhanced fluid model. One approach involves treating one component of the plasma, often the bulk, with fluid equations, while treating another component, perhaps a fast beam distribution, with a kinetic particle simulation. While this method is effective for some problems, its usefulness in microturbulence is limited, because of the importance of kinetic effects within the bulk plasma itself.

Another approach is to include kinetic effects within the fluid equations themselves. Early efforts used artificial viscosities [Lee and Diamond 1986] and heat conductivities [Waltz 1988; Hamaguchi and Horton 1992] to produce rough models of kinetic effects. It was later recognized that a systematic approach to closing the highest fluid moment could provide an excellent model of linear Landau damping, while maintaining important conservation properties [Hammett and Perkins 1990; Chang and Callen 1992a].[3]

The "gyrofluid" or "gyro-Landau fluid"[4] approach, which takes velocity space moments of the gyrokinetic equation in gyrocenter space, and then closes the moment hierarchy with closures carefully chosen to model kinetic effects, has been widely employed in studies of plasma turbulence and transport. Gyrofluid models were developed first in slab geometry [Dorland 1993], and have since been implemented in toroidal geometry [Waltz et al. 1992; Beer et al. 1992; Hammett et al. 1993], with expanded closure terms which include models of linear and nonlinear finite-Larmor radius effects [Hammett et al. 1992; Dorland 1993] as well as toroidal drift resonances [Beer and Hammett 1996]. Trapped ion effects and a full model of bounce-averaged electron dynamics have also been implemented in gyrofluid models [Beer 1995].

An important benchmark of the accuracy of gyrofluid approximations is provided by benchmarks with δF gyrokinetic particle (GKP) simulations. A brief

---

[3] Nonlinear Landau damping effects are more difficult to include in a fluid model. Some types of nonlinear Landau damping are included in some models [Dorland 1993], while it has been shown that there can be errors near marginal stability in strongly kinetic regimes [Mattor 1992]. However, we believe that the regime where these errors occur is fairly narrow and may only lead to a small shift in the effective critical gradient predicted by the simulation [Dorland 1993; Hammett et al. 1993].

[4] A number of different terms has been used to describe such equations, including "gyrofluid", which emphasizes that the equations are moments of a gyrokinetic equation in gyrocenter space, "Landau fluid", which emphasizes that the fluid equations contain models of Landau damping, and "gyro-Landau-fluid" which emphasizes both. The term gyrofluid is used here for brevity to describe any model which takes moments of the gyrokinetic equation and includes models of kinetic effects.

discussion of comparisons between gyrofluid and GKP simulations is given in Appendix A.

1.1.2 Current Understanding of Tokamak Transport

The use of large-scale direct numerical turbulence simulations, in conjunction with linear stability calculations and analytic theory, has led to rapid progress in the understanding of tokamak transport over the past decade. The primary tools fueling this progress have been gyrofluid and δF gyrokinetic particle simulations, with Braginskii-based fluid simulations playing an important role near the more collisional edge of the plasma.

A great deal of physical insight has been generated by these simulations. It is now generally thought that the ion temperature gradient mode (ITG, see Sec. 2.2) plays a dominant role in driving the microturbulence and associated "anomalous" ion thermal transport observed in the core of many tokamak experiments. Additional instability drive due to impurities and trapped particles is often important, and an additional instability, the trapped electron mode (TEM), sometimes plays a role, as shown, for instance, in the gyrofluid simulations of [Beer 1995]. It has also been consistently observed in simulations [Parker et al. 1993; Dimits et al. 1994; Beer 1995] that the turbulent spectrum peaks at wavelengths longer than the linearly most unstable modes, yielding fluctuation spectra similar to those observed in experiments [Fonck et al. 1993].

The present state of transport modeling is illustrated by Fig. 1.1. The measured total plasma stored energy for a number of shots at three different tokamak experiments (DIII-D, JET, and TFTR) is plotted against the prediction of the GLF23 transport model [Waltz et al. 1997], using data provided by [Kinsey 1998]. This analysis is similar to that in [Kinsey et al. 1997]. The GLF23 model is constructed using a gyrofluid calculation of the linear mode growth rates and quasilinear transport fluxes, with a variant of a mixing length estimate of the nonlinear saturation level fit to 3-D nonlinear gyrofluid simulations [Beer 1995]. The model is based on theory and simulation results, and contains no fit coefficients from experiments. The plot shows broad-based agreement between theory and experi-

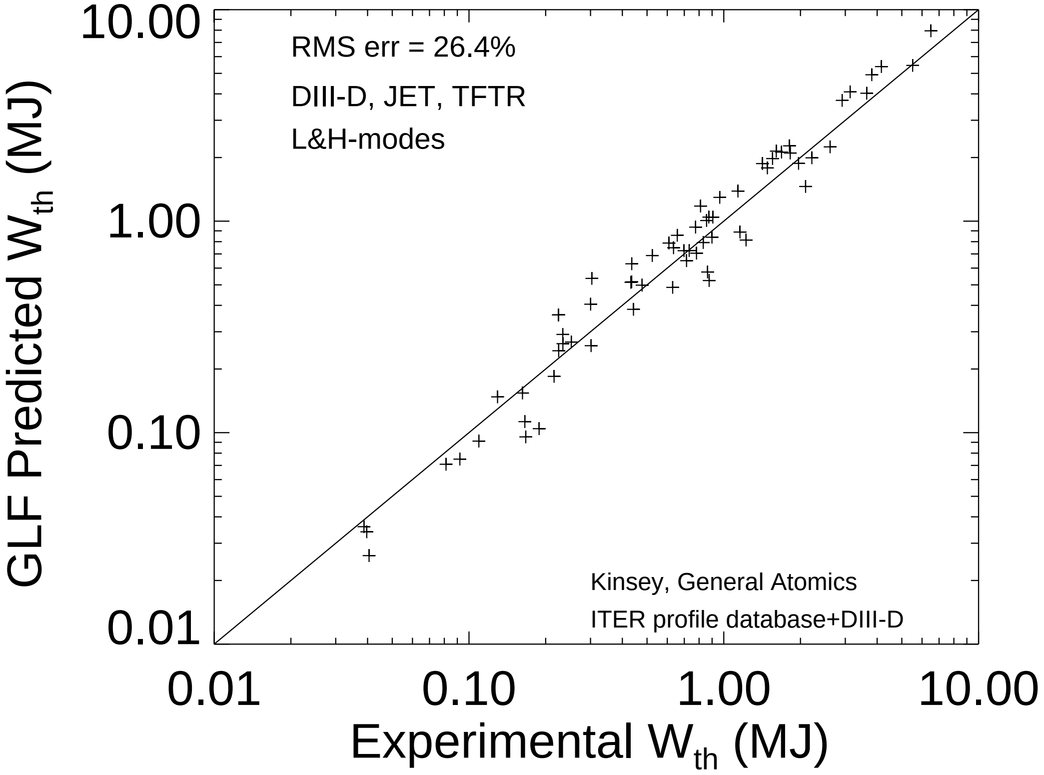

Figure 1.1: Plasma stored energy from several shots on three tokamaks is compared to predictions from the GLF23 transport model. Encouraging agreement is found in the underlying trends, but the scatter is significant, and a number of caveats are invoked. [data courtesy of J. Kinsey]

ment over more than two decades in stored energy. Reasonable agreement is found for data from all three tokamaks, in both H and L mode shots. This agreement is very encouraging. It strongly suggests that the "anomalous" transport measured in experiments can be explained by microinstability-driven turbulence, and it also suggests that many aspects of the turbulent transport are being correctly described by the model. However, there is a great deal of scatter in the plot (RMS error of 26%).[5] While some of this scatter can be attributed to uncertainties in experimental measurements, the discrepancies in the outliers and the overall scatter are large enough to indicate that important physics is absent from the transport model and the nonlinear simulations on which it is based.[6]

Furthermore, there are a number of caveats involved in producing the plot in Fig. 1.1. Measured density and rotation profiles are used. Hence, the model is using a fixed density profile and predicting only heat transport, not particle transport. Also, a measured temperature is used as a boundary condition at a radius of 90% of the total plasma minor radius, and heat transport is predicted only inside this fixed point. Hence the model is not predicting transport near the edge of the plasma. Despite the many caveats and uncertainties, the results produced by GLF23 and similar theory-based transport models, in conjunction with reasonable agreement between experiment and nonlinear simulations in turbulent spectra and fluctuation measurements [Fonck et al. 1993; Evensen et al. 1998], support ITG/TEM as an important instability mechanism in the core, and demonstrate clear progress toward a quantitative understanding of turbulent transport.

Another important insight relates to the role of $\mathbf{E} \times \mathbf{B}$ flows. Theoretical work has suggested that shear in large-scale $\mathbf{E} \times \mathbf{B}$ flows can break apart turbulent eddies and lead to a reduction in transport [Biglari et al. 1990; Hahm and Burrell 1995]. The component of the $\mathbf{E} \times \mathbf{B}$ flow with $k_\phi = k_\theta = 0$, where ϕ and θ are the toroidal and poloidal directions, has come to be called zonal flow, because

---

[5] The IFS-PPPL model [Kotschenreuther et al. 1995] has many similarities to GLF23 and achieves a comparable RMS error.

[6] It should be noted that there are a number of other theory-based and semi-empirical models which achieve similar levels of fit to the experiments despite fairly significant differences in the models. Efforts to extend the database to include transient and perturbative experiments and rotation scans are ongoing to help distinguish between the performance of the many models [Mikkelsen 1998; Kinsey et al. 1999].

it is radially localized. Both gyrofluid [Hammett et al. 1993; Beer 1995] and δF gyrokinetic [Dimits et al. 1994; Lin et al. 1998] simulations have observed the turbulent generation of small radial scale zonal flows. These simulation results, combined with recent theoretical developments [Hahm et al. 1999; Diamond et al. 1998] have demonstrated that turbulence-driven flows play a critical role in the saturation of turbulence. Sheared $\mathbf{E} \times \mathbf{B}$ flows are now widely believed to play an important role in the enhanced confinement modes observed in both the core and the edge of tokamak experiments. Improved understanding of these flows suggests the possibility that they may be used to control turbulent transport, and lead to at least a partial solution to the "anomalous transport problem."

1.1.3 The Need for an Electromagnetic Model with Non-adiabatic Passing Electrons

Significant progress toward a quantitative understanding of turbulent transport has been made at a rapid pace over the course of the last decade. This progress brings with it the promise that, with continuing refinement and improvement of physics models and simulation codes, a reliable and predictive understanding of transport may be within reach.

While progress has been great, there are still many uncertainties, and previous models have invoked a number of caveats and approximations that must be relaxed in a more complete model. Many of these caveats are mentioned above, and here we emphasize two of the most important: the electrostatic approximation and the use of adiabatic passing electrons.

Most previous gyrokinetic particle and gyrofluid simulations have invoked the electrostatic approximation, assuming that turbulence can be described purely in terms of a fluctuating electrostatic potential, with magnetic fluctuations neglected. Formally, this is equivalent to assuming zero plasma β, where β is the ratio of the plasma pressure to the magnetic field pressure. However, it is very important to note that, as explained in Sec. 2.3.1, the electrostatic approximation requires not only $\beta \ll 1$, but also requires that β be far below the ideal-MHD critical β_c, a condition rarely met in plasmas of fusion interest. This is especially important in the outer regions of the plasma, where β is generally small, yet large values of the safety factor q and sharp gradients often push the plasma close to the ideal ballooning limit. Furthermore, the validity of the electrostatic approximation will be more questionable in future high β experiments,[7] and in any attractive fusion reactor,[8] than it has been in past lower β experiments.

The electrostatic approximation removes the predominantly electromagnetic modes such as the shear Alfvén wave, and its associated instabilities (see Secs. 2.1 and 2.3), from the system. Hence electrostatic simulations cannot evaluate the importance of such modes, which are predicted by linear theory to be unstable in both the core and edge of some tokamak plasmas. In addition, well known finite-β modifications to predominantly electrostatic modes such as ITG (see Sec. 2.3) are neglected. The modifications to linear instability growth rates are substantial at experimentally observed β values, and there is reason to expect that the nonlinear evolution of the system is affected.

Electromagnetic effects are expected to be particularly important in the edge, where steep gradients often push the plasma close to the ideal-MHD stability threshold. In this region, disagreement between experimentally observed heat conductivity (which tends to dramatically increase near the edge), and the heat conductivity predicted by electrostatic simulations (which tends to decrease near the edge) has been so drastic that the edge region has often been entirely omitted from theory-based transport models. It is hoped that adding magnetic fluctuations to the simulations will dramatically improve agreement in the edge.

There are also expected to be important electromagnetic effects on the $\mathbf{E} \times \mathbf{B}$ flows. Recent work by [Das et al. 1999] has suggested that magnetic stresses may result in a reduction of zonal flows. This work further suggests that turbulent zonal flow generation may be quenched for purely Alfvénic turbulence. This could have a dramatic impact on nonlinear saturation and steady state transport levels, particularly as the ideal β limit is approached.

---

[7] The START tokamak has recently achieved a volume averaged $\beta \sim 25\%$, with local values exceeding 50% in the inner core, and similar values are expected in future low-aspect-ratio tokamaks.

[8] Fusion power scales with β^2, and most reactor studies indicate that achieving high β is crucial for an economical fusion reactor.

Particle transport is another critical issue. The use of the electrostatic approximation in conjunction with adiabatic electrons[9] leads to a non-physical prediction of zero particle transport.[10] Inclusion of a model of non-adiabatic trapped electrons leads to finite particle transport, but it is not clear that this transport should always be large compared to the passing particle transport. Relaxing the electrostatic approximation and the adiabatic passing electron approximation should allow for more accurate calculation of particle transport, and may eventually lead to a transport model which accurately accounts for both heat and particle transport.

A Simple Illustration

The importance of electromagnetic effects on typical tokamak core instabilities is illustrated in Fig. 1.2.[11] This schematic plot shows the instability growth rate as a function of the plasma β. The ITG mode is unstable at zero β (for sufficiently sharp temperature gradients), and it is stabilized as β increases. The mode labeled KBM is a shear Alfvén ballooning instability. It becomes unstable at a finite β and its growth rate increases with β in the range shown. The mode labeled MHD is not a different mode, but rather the growth rate that one would calculate for the KBM using the ideal-MHD model, which omits important kinetic effects. The point at which the MHD line intersects zero is thus the ideal-MHD β limit (β_c).

A traditional approach has been to calculate this β_c, and conclude that the tokamak must operate at $\beta < \beta_c$. Of course even at $\beta < \beta_c$ the plasma is often observed to be turbulent, and this microturbulence has been studied with electrostatic ($\beta = 0$) models of the ITG.

---

[9] In the electrostatic ($\beta = 0$) limit, the Alfvén wave becomes a very high frequency mode relative to drift waves. The assumption of adiabatic electrons is often made to remove this very fast mode from the system and make numerical simulations more feasible. Finite β slows the Alfvén wave, allowing its inclusion in practical simulations. Hence the inclusion of finite-β and relaxation of the adiabatic electron assumption go hand in hand. See Ch. 2 for a more detailed explanation.

[10] This is because, for adiabatic electrons, density is proportional to the electrostatic potential ($n_e \sim \phi$), while the $\mathbf{E} \times \mathbf{B}$ motion across the magnetic field is proportional to $\frac{\partial \phi}{\partial y}$ where y is the poloidal direction. The total cross field flux is then proportional to $\int \phi \frac{\partial \phi}{\partial y} dy$ which is exactly zero. The ion particle flux is then also zero, as should be evident from Poisson's Equation (see Ch. 3).

[11] Trapped particle effects and trapped electron modes are neglected here for simplicity.

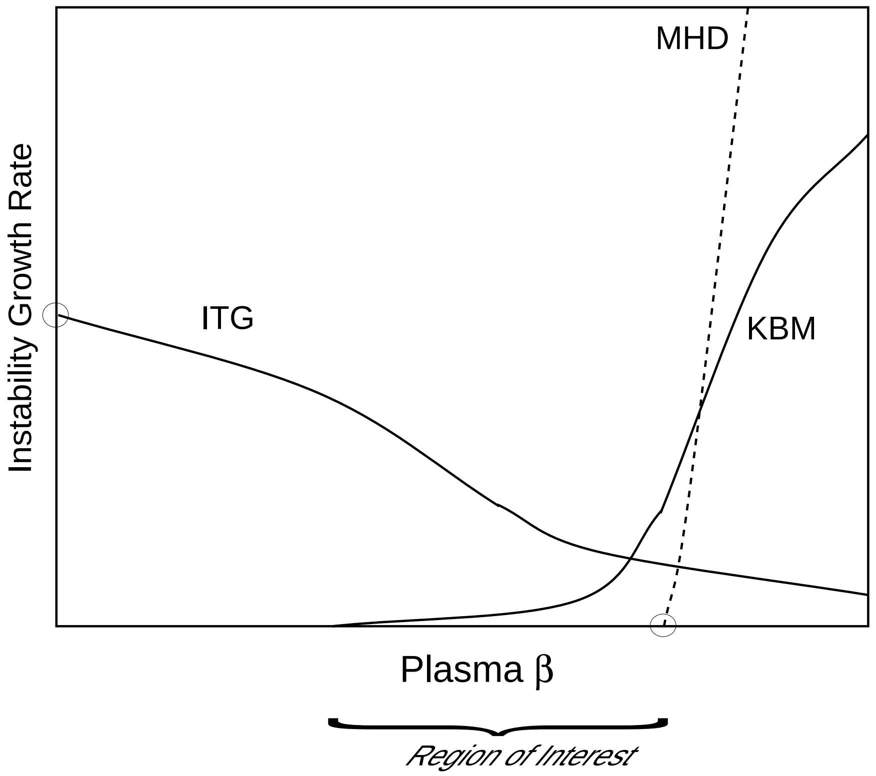

Figure 1.2: This schematic drawing sketches the typical effects of finite β on instabilities commonly seen in tokamaks. Mode growth rate is plotted vs. β with other equilibrium parameters held fixed. The mode labeled ITG is the ion temperature gradient mode. The mode labeled KBM is the kinetic Alfvén ballooning mode. The dotted line labeled MHD is not a different mode, but rather the growth rate one would calculate for the KBM using an ideal-MHD model without kinetic effects. The ideal MHD critical β and the electrostatic limit of the ITG mode are indicated with circles.

The reality is more complex. In the region of interest, where β approaches β_c, the ITG growth rate is significantly smaller than in the electrostatic limit. Furthermore, in the presence of finite ion temperature gradients, the kinetic Alfvén ballooning mode is driven unstable well below β_c. This second instability is fundamentally different in character than the ITG and its nonlinear behavior could be qualitatively different. A complete transport simulation must include both of these modes and the interaction between them.

1.1.4 A Brief History of Electromagnetic Microturbulence Simulations

While most prior microturbulence simulations have been electrostatic, there have been a number of efforts to include electromagnetic effects.

Pure fluid simulations based on Braginskii's equations have recently included magnetic fluctuations [Zeiler et al. 1996; Rogers and Drake 1997; Xu et al. 1998], and these simulations have proved very useful for understanding transport near the edge, where Braginskii's equations are valid. One principal result of this work is that electromagnetic effects are crucial for understanding edge transport. In particular, the simulations of [Zeiler et al. 1996; Rogers and Drake 1997] have identified the MHD α parameter, which is proportional to β, as a critical parameter in the L-H confinement bifurcation often observed in experiments.

[Scott 1997] has also developed an electromagnetic model which focuses on studying edge turbulence. This model emphasizes electron dynamics, including a rough model of electron Landau damping, and published results use a simplified cold ion model. Three dimensional simulations of electron drift wave turbulence have yielded a number of interesting results. Recent model improvements [Scott 1999] include a more extensive gyrofluid ion model, and general geometry. The focus of Scott's work is on the plasma edge where $\omega_* \sim k_\parallel v_{te}$, and nonlinearly sustained turbulence is thought to occur.

Another approach is to begin with a basic MHD-like model, which is electromagnetic but lacks small scale dynamics and kinetic effects, and add enhancements which make the model more appropriate for microturbulence studies. A method for adding a model of Landau damping to MHD-like equations is given in Appendix C. [Chang and Callen 1992a] have developed a model which adds kinetic effects and lowest order small scale dynamics to a fluid model using a Chapman-Enskog approach. These models have tended to focus on particular problems such as magnetic island formation and microtearing modes, rather than turbulent transport.

Work has also been done on developing electromagnetic gyrofluid models. [Brizard 1992] derived a general geometry electromagnetic gyrokinetic equation, and calculated the first few moment equations, but did not close the moment hierarchy. [Waltz et al. 1995] included magnetic fluctuations in a set of gyrofluid equations, but these contain time and space scales which make nonlinear simulation difficult.

Effort has also been made to generalize δF gyrokinetic particle simulations to include electron dynamics and/or magnetic fluctuations. The thesis work of [Cummings 1995] presents an electromagnetic δF model based on a gyrokinetic formulation utilizing a parallel momentum (p_z) rather than a parallel velocity ($v_\parallel$) [Hahm et al. 1988], along with simulation results in one and two dimensions. The computational intensity of particle simulations makes three-dimensional fully-explicit simulation difficult, and a number of methods have been developed to improve computational efficiency. [Cohen and Dimits 1997] have developed an implicit method in sheared slab geometry. [Lee et al. 1999] are developing a split weight scheme, which splits the standard δf response into adiabatic and non-adiabatic parts, and treats only the small non-adiabatic part dynamically. [Chen and Parker 1999] are developing a hybrid scheme using δF ions and a zero mass fluid model for the electrons.

The direct route of gridding and solving the five-dimensional electromagnetic gyrokinetic equation has been recently undertaken by [Jenko and Scott 1998; Dorland et al. 1999], with first applications focusing on edge simulations or electron temperature gradient mode (ETG) simulations where the range of time scales is not as extreme as for the core ITG and KBM simulations considered here.

1.2 Guiding Principles in Model Development

Our primary goal is to produce a realistic model of microturbulence-driven transport which includes both magnetic fluctuations and non-adiabatic passing electrons.

We choose an essentially gyrofluid approach, with the expectation that this will yield a model which includes the most important kinetic effects, while remaining practical for realistic nonlinear simulations in toroidal geometry. While δF particle simulations are more fundamental, gyrofluid simulations are less computationally demanding, and the use of multiple simulation methods can help develop physical insight into nonlinear dynamics. Gyrofluid codes run quickly enough on modern massively parallel supercomputers that, even with the expected slowdown due to the addition of electron dynamics and Alfvén waves, large numbers of realistic three-dimensional nonlinear simulations should be possible.[12]

A principal difference between this work and most previous electromagnetic tokamak microturbulence simulations [Scott 1997; Zeiler et al. 1996; Rogers and Drake 1997; Xu et al. 1998] is that the previous simulations have focused on the highly collisional edge region of the plasma where traditional Braginskii fluid treatments are expected to be valid. In some cases, these models have then added additional physics in an attempt to extend their validity inward. By contrast, the antecedents of our model focused on the relatively collisionless core region, where kinetic effects and finite-Larmor-radius effects play a critical role. We have added electromagnetic effects, non-adiabatic passing electron dynamics, and models of electron-ion collisions and electron Landau damping in an attempt to both improve the accuracy of core simulations and to extend the validity of the simulations further into the edge region.

A basic model of non-adiabatic passing electron dynamics would introduce fast time scales associated with the electron transit time into the simulations. Due to the Courant condition, these scales would require a dramatic reduction (roughly a factor of 60 for a deuterium plasma) in the time step of an explicit numerical

---

[12] Electromagnetic δF gyrokinetic simulations and/or direct gyrokinetic Vlasov simulations should eventually provide an excellent nonlinear benchmark. We also note that the combination of a δF model of the ions with a Landau fluid model of the electrons (such as the one developed in Ch. 3) may prove very useful.

simulation. These very fast time scales are not generally associated with microturbulence, and we employ a careful, consistent analytic expansion to remove them. This expansion maintains typical ion time scales, such as those associated with drift and sound waves, and Alfvén times scales (which are faster by $1/\sqrt{\beta}$), while eliminating thermal electron time scales (which are faster by $\sqrt{m_i/m_e}$). This expansion requires $\beta \gg m_e/m_i$, a condition generally met by fusion relevant plasmas everywhere except very near the edge. The resulting electron model is fairly elegant and simple, yet represents a very substantial improvement over the adiabatic electron models ($n_e \propto \phi - \langle\phi\rangle_{surface}$) that have been used to describe the passing electrons in most previous gyrofluid and gyrokinetic particle simulations. In addition to finite-β effects and Alfvén wave dynamics, the model incorporates electron $\mathbf{E} \times \mathbf{B}$, curvature, and ∇B drift motion, as well as the $\mathbf{E} \times \mathbf{B}$ nonlinearity and magnetic flutter nonlinearities.

Ion dynamics are described by a set of toroidal gyrofluid equations derived by taking velocity space moments of the electromagnetic gyrokinetic equation. The moment hierarchy is truncated using closures analogous to those developed by [Hammett and Perkins 1990; Dorland 1993; Beer 1995], which model the effects of Landau damping, linear and nonlinear finite-Larmor-radius (FLR) effects, toroidal drifts and drift resonances, and trapped ion effects.

This model, which is described in detail in Ch. 3, allows the nonlinear simulation of electromagnetic ITG and shear Alfvén wave turbulence, including the impact of non-adiabatic passing electrons.

1.3 Outline

Chapter 2 provides a simple description of the physics of microinstabilities, focusing on the ion temperature gradient and kinetic ballooning modes. The effects of finite β are studied in detail in the local fluid limit, and the limitations of some previous models are considered. This chapter is not intended to break new ground, but rather to provide the physical insight needed to understand finite-β microturbulence, and to motivate the derivation of the electromagnetic gyrofluid equations.

Chapter 3 presents a detailed derivation of the physics model used to study electromagnetic microturbulence. Ion equations are derived by taking moments of the electromagnetic gyrokinetic equation and implementing closures analogous to those derived by [Hammett and Perkins 1990; Dorland 1993; Beer 1995]. Electron equations, including models of collisions and Landau damping, are derived by taking moments of the electromagnetic drift kinetic equation, using a formal expansion in the smallness of the mass ratio m_e/m_i. The gyrokinetic versions of Poisson's equation and Ampere's law close the system.

In Chapter 4 the model is extensively benchmarked against linear kinetic theory. Benchmarks are performed both in sheared slab and toroidal geometry. The comparisons emphasize effects not included in previous electrostatic models. In particular, the effect of finite-β on the growth rates and frequencies of the ITG mode are studied, as are the growth rates and frequencies of the kinetic Alfvén ballooning mode.

Chapter 5 provides computational details of the nonlinear turbulence simulations, and discusses the results of those simulations. A set of runs at several values of plasma β is presented, and the impact of finite β and electron dissipation on plasma microturbulence is discussed. Turbulent transport is found to decrease with β at low $\beta < \beta_c/2$, but to increase with β as the MHD ballooning critical β_c is approached. This increase is found to be dramatic when the effects of electron Landau damping and electron-ion collisions are taken into account. Ion density and temperature fluctuation spectra from the simulations are found to agree with several measured trends.

Chapter 6 presents a direct comparison of simulation results with experimental data. The focus is on the edge region where electrostatic simulations have had little success in accounting for observed transport trends. It is demonstrated that electromagnetic physics plays an important role at typical L-mode edge parameters. Unlike electrostatic simulations, the electromagnetic simulations predict ion heat fluxes which can increase with radius, and are often in reasonable quantitative agreement with the values inferred from power balance.

The final chapter draws conclusions, emphasizing the importance of electromagnetic physics, and the need for a more complete understanding of the nonlinear evolution of electromagnetic turbulence, including zonal flow dynamics. The quantitative adjustment in core transport and the qualitative change in edge transport expected from finite-β effects, and its implications are briefly discussed. Future directions are also considered, including possible extensions of the physics model and interesting avenues for future investigations.

A brief summary of some of the key results from this thesis has been published in [SNYDER et al. 1999b; SNYDER et al. 1999a]. While most of the research presented in this thesis focuses on an electromagnetic gyrofluid turbulence model, work has also been done on Landau fluid models of collisionless MHD, which has been published in [SNYDER et al. 1997] and is included in Appendix C.

Chapter 2

Simple Physics of Relevant Microinstabilities

THE PHYSICS OF PLASMA INSTABILITIES has been a rich field of inquiry dating back to the very beginnings of the fusion program. The plasma literature explores the subject in enormous depth. The discussion here centers on those microinstabilities which are most likely to impact turbulent transport in tokamaks. Furthermore, because the electrostatic limit of these microinstabilities has been explored extensively, we focus on the impact of finite-β on predominantly electrostatic modes such as the ITG, as well as on electromagnetic shear Alfvén instabilities, such as the kinetic ballooning mode (KBM).

The linear physics of both toroidal finite-β ion temperature gradient (ITG) modes and kinetic Alfvén instabilities has been treated in the literature. However, due to the long history of the study of Alfvén instabilities, the literature is filled with a large number of different approximations, and a great deal of varied and sometimes inconsistently-applied terminology. The purpose of this chapter is not to break new scientific ground, but rather to clarify and give a brief review of the finite-β instability physics relevant for understanding and motivating work in the succeeding chapters.

Many useful references are available on the linear instability issues considered here. Notable for background is a review article on long wavelength microinstabilities by [Tang 1978], particularly Secs. 2.3 and 5.1, and more specific articles on finite-β effects on the slab [Dong et al. 1988; Reynders 1994] and toroidal [Dong et al. 1992; Kim et al. 1993] ITG mode, and articles on kinetic Alfvén instabilities by [Tang et al. 1980; Cheng 1982; Hahm and Chen 1985; Kotschenreuther 1986; Hong et al. 1989; Zonca et al. 1996]. Also of interest is an article on collisional effects on these modes by [Rewoldt et al. 1987]. The results of the local fluid analysis of [Kim et al. 1993] are employed extensively in Sec. 2.3.

2.1 Shear Alfvén Waves and Instabilities

The shear Alfvén wave is perhaps the simplest of all magnetized plasma oscillations to understand intuitively. To a good approximation, a hot plasma can often be considered to be "frozen-in" to a strong magnetic field. That is, the plasma basically oscillates along with the field. The Alfvén wave can then be thought of as a simple analogue of an oscillating guitar string, with the magnetic field providing the tension force, and the plasma providing the inertia. For the shear Alfvén wave, fluctuations are perpendicular to the background field, and propagate along the field. For a homogeneous plasma in a straight magnetic field, the shear Alfvén frequency can be written $\omega_A^2 = k_\parallel^2 B^2/4\pi n_0 m_i = k_\parallel^2 v_A^2$, where $k_\parallel$ is the wave number along the field, and the electron mass has been neglected because $m_e \ll m_i$.

There also exist compressional Alfvén oscillations, with $\omega^2 = (k_\perp^2 + k_\parallel^2)\, v_A^2$. However, the compressional waves tend to be both very fast[1] and very stable in tokamaks, as it takes a great deal of energy to compress the strong toroidal field. Hence compressional oscillations are not generally associated with microinstability behavior, and are ordered out in the standard gyrokinetic treatment.[2] Here we focus on the shear wave, which can contribute to microturbulence directly and through coupling to other modes.

The dispersion relation for a simple shear Alfvén wave in a straight magnetic field, with no equilibrium gradients, can be easily derived from a simple fluid

---

[1] In a tokamak, the strong anisotropy imposed by the magnetic field leads to long parallel and short perpendicular scale lengths ($k_\parallel^2 \ll k_\perp^2$).

[2] It is possible to treat the small $k_\perp$ compressional Alfvén wave in a standard gyrokinetic framework, and also to treat the general compressional wave within an extended gyrokinetics, as described by [Qin 1998; Qin et al. 1999].

description, such as ideal MHD. In the context of a local fluid description based on gyrokinetics,[3] it can be derived as follows.[4] For the simplest case, $\omega \sim k_\parallel v_A \gg k_\parallel v_{ti}, \omega_*$, there is no gyrocenter ion response ($n_i = 0$ using definitions from Ch. 3). The ion response comes entirely from the polarization term in the gyrokinetic Poisson's equation. For small $k_\perp^2 \rho_i^2 \ll 1$, Poisson's equation with $\bar{n}_i = 0$ can be written:

$$n_e = -n_0 \frac{e\phi}{T_{0i}} b, \tag{2.1}$$

where $b = k_\perp^2 \rho_i^2$. In this simple limit ($\omega \sim k_\parallel v_A \gg k_\parallel v_{ti}, \omega_*$), the electrons are described by a linearized continuity equation,

$$\frac{\partial n_e}{\partial t} + n_0 i k_\parallel u_{\parallel_e} = 0, \tag{2.2}$$

and a parallel electron momentum equation,

$$n_0 m_e \frac{\partial u_{\parallel_e}}{\partial t} + i k_\parallel p_{\parallel e} - n_0 e \left(\frac{1}{c}\frac{\partial A_\parallel}{\partial t} + i k_\parallel \phi\right) = 0. \tag{2.3}$$

In the limit $\omega \ll k_\parallel v_{te}$, the electrons thermalize quickly along the field, leaving $\nabla_\parallel T_{\parallel e} = 0$ and $i k_\parallel p_{\parallel e} = T_{0e} i k_\parallel n_e$. The system is completed with the parallel component of Ampere's Law, which for case $u_{\parallel i} \ll u_{\parallel e}$ can be written:

$$k_\perp^2 A_\parallel = -\frac{4\pi n_0 e}{c} u_{\parallel_e}. \tag{2.4}$$

Eqs. 2.1-2.4 yield the dispersion relation

$$\omega^2 = k_\parallel^2 v_A^2 \frac{1 + b_s}{1 + b_s \frac{m_e}{m_i} \frac{2}{\beta_e}}, \tag{2.5}$$

where $b_s = k_\perp^2 \rho_s^2$, $\rho_s^2 = c_s^2/\Omega_{ci}$, $c_s^2 = T_{0e}/m_i$, $\beta_e = 8\pi n_0 T_{0e}/B^2$, and the useful identity $c_s^2/v_A^2 = \beta_e/2$ has been employed. This reduces to the familiar MHD

---

[3] A detailed derivation of the kinetic Alfvén wave dispersion relation from gyrokinetics is given in [HAHM and CHEN 1985]. The equations given here can be viewed as the $b \to 0$, $\omega_* \ll \omega$, $\nu \to 0$ limit of Hahm and Chen's results.

[4] See Sec. 3.1 and following for a description of gyrokinetics, and a derivation of fluid equations which reduce in the appropriate limits to the simple equations given here.

result, $\omega^2 = k_\parallel^2 v_A^2$ in the usual limit $b_s \ll 1$.[5]

The focus of this thesis is on the regime where $\beta_e \gg m_e/m_i$, which corresponds to the electron thermal speed being much faster than the Alfvén speed v_A. This regime is appropriate for most magnetic fusion plasmas except very near the edge. In this limit, Eq. 2.5 simplifies to $\omega^2 = k_\parallel^2 v_A^2(1 + b_s)$, and the electron inertia term in Eq. 2.3 can be neglected. Eq. 2.3 can then be considered an evolution equation for $A_\parallel$, and Ampere's Law determines $u_{\parallel e}$. Even if the electron inertia term is kept, Eq. 2.3 does not involve the numerically challenging electron transit time scales ($\omega \sim k_\parallel v_{te}$), as these have been removed via the isothermal assumption $\nabla_\parallel T_e = 0$.

It is interesting to note that in ideal MHD, the third and fourth terms in Eq. 2.3, corresponding to $E_\parallel = 0$, are dominant, while for ITG/drift wave dynamics, the second and fourth terms of Eq. 2.3 are often dominant (corresponding to an adiabatic electron response, $n_e \propto \phi$). In this thesis, we keep all these terms, and can thus study the interaction between drift waves and MHD-type effects.

It is also interesting to note that, when extending the study of drift wave phenomena beyond the simple adiabatic electron assumption, it is actually numerically helpful to also include magnetic fluctuations. This is because dropping the $\partial A_\parallel/\partial t$ term in Eq. 2.3 while keeping the electron inertia term corresponds to taking the $\beta_e \to 0$ limit of the dispersion relation in Eq. 2.5, leading to waves with $\omega^2 = k_\parallel^2 v_{te}^2/k_\perp^2 \rho_s^2$. This is the "electrostatic shear Alfvén wave," [LEE 1983] and is very high frequency relative to drift waves, particularly at low $k_\perp$, making it numerically challenging to resolve in simulations. In this work, we keep magnetic fluctuations, and for $\beta \gg m_e/m_i$ this makes the frequency of the shear Alfvén root much lower, making it easier to handle in explicit numerical simulations.

The simple model discussed above (Eqs. 2.1-2.4) yields roots that are purely real, and are thus neither unstable nor damped. Instability requires additional physics, most importantly a source of free energy, such as an equilibrium density

---

[5] However, it is still necessary to keep the term proportional to b in Eq. 2.1 in order to get the lowest order shear Alfvén wave. It turns out that in the $b \to 0$ limit, it is the first two terms in Eq. 2.3 that can be neglected relative to the last two terms (the last two terms are equivalent to the ideal MHD constraint $E_\parallel = 0$), so that the $k_\perp^2$ from Eq. 2.1 ends up cancelling the $k_\perp^2$ term in Eq. 2.4 to give a dispersion relation independent of $k_\perp^2$.

or temperature gradient, and an accessibility mechanism, which may or may not involve wave-particle resonance, to tap the free energy.

A basic description of shear Alfvén instabilities is provided by the widely-used ideal MHD model, described in detail by [Freidberg 1987]. Here we consider equilibria which are current-free to lowest order, and focus on the pressure driven instabilities.[6] In the tokamak geometry considered here, the kinetic analog of the well-known ideal MHD ballooning mode is the primary Alfvén instability of interest. This instability is driven by the pressure gradient[7] in regions of bad magnetic curvature. The most unstable modes have a mode structure that balloons out in the bad curvature regions while remaining small in the good curvature regions. In tokamaks, ballooning modes typically have $k_\parallel \sim 1/qR$ and $k_\perp^{-1} \ll a$, where q is the safety factor, and a is the minor radius. A very simple local analysis in the ideal MHD limit finds that the ballooning mode is unstable for $\beta > \beta_c$, with (see Sec. 2.3.2):

$$\beta_c \simeq \frac{\epsilon_n}{q^2[1 + \eta_i + \tau(1 + \eta_e)]}, \tag{2.6}$$

where $\epsilon_n = L_n/R$ is the density scale length divided by the plasma major radius, $\eta_i = L_n/L_{Ti}$ and $\eta_e = L_n/L_{Te}$ are the usual ratios of density and temperature scale lengths, and $\tau = T_i/T_e$. A more detailed analysis finds that magnetic shear ($\hat{s}$), ion drift resonance, and other effects play a role in ballooning mode stability, as discussed in Sec. 2.3. Nonetheless, the basic behavior of the ballooning mode, providing a β (or, more precisely, $\alpha = -q^2 R\beta'$) limit above which it is difficult to operate a plasma experiment, survives. Because the fusion energy produced by a reactor scales with β^2, this and related β limits have hindered efforts to design an attractive toroidal magnetic fusion reactor. For this reason, a firm and thorough understanding of ballooning instabilities, including their nonlinear behavior and kinetic effects which may drive them unstable below the ideal β_c, is of great

---

[6] The usual derivation of the gyrokinetic equation and the Maxwellian equilibrium assumed in Ch. 3 do not include current driven instabilities, as no zeroth order equilibrium current is present to provide the energy source for such instabilities. Developing a model which includes zeroth order flows and currents is left for future work.

[7] In a more detailed kinetic model, the density and temperature gradients must be considered separately.

importance.

While a detailed stability analysis requires consideration of the mode structure, a rough description of the ballooning instability is possible with a local fluid treatment. The effects of magnetic field, density and temperature gradients enter the simple fluid model through ω_* and ω_d terms. An accurate description of Alfvén instabilities, even in the fluid limit, requires ion physics, and we revisit the fluid model in Sec. 2.3 after discussing the ITG mode in Sec. 2.2.

A Note on Terminology

As more physics is added to the model, the mode frequency may differ significantly from the simple $\omega = \pm k_\| v_A$ limit, and the growth rate can be quite different from the ballooning mode growth rate predicted by ideal MHD theory. We nonetheless continue to refer to these roots as the shear Alfvén wave, or, when unstable, the shear Alfvén instability (sometimes omitting "shear" for conciseness). The shear Alfvén roots are defined to be those which reduce in the straight magnetic field, $b \to 0$, cold ion, $m_e \to 0$, no equilibrium gradient limit to $\omega = \pm k_\| v_A$. The term "kinetic" is sometimes also used to emphasize the importance of velocity space effects such as Landau damping and drift resonance. There are multiple types of shear Alfvén instabilities. One type, known as the toroidal Alfvén eigenmode (TAE), resides in the gap in the Alfvén wave continuum created by toroidicity, and can be driven unstable by resonant interaction with non-Maxwellian fast particle distributions.[8] Here we focus on "kinetic ballooning modes" (KBM) which are driven unstable largely by bad curvature effects in the presence of density and/or temperature gradients. Note however that kinetic effects such as ion drift resonance and Landau damping can also contribute to the destabilization of the KBM.

In the literature, varying notation has been introduced to describe this instability. In the ideal MHD limit it is often called the "ideal ballooning mode" or just the "ballooning mode", and when kinetic effects are added it is referred

---

[8] The TAE is generally believed to be linearly stable in the predominantly Maxwellian plasmas considered here, and for this reason it is not a focus of this work. However, TAE dynamics can be quite complex nonlinearly and are an active subject of investigation. See for example [ZONCA and CHEN 1993; HAHM and CHEN 1995; FU and PARK 1995].

to as the “kinetic ballooning mode”. However, in the historic progression of the literature, the term “kinetic ballooning mode” has been used to describe the instability in many different limits, often including some kinetic effects and not others, and sometimes including non-Maxwellian beam or α-particle distributions. Here the terms “kinetic ballooning mode” or “kinetic Alfvén instability” refer to the instability of the shear Alfvén wave in which bad curvature plays a critical role, in a plasma whose components are approximately Maxwellian but with density and temperature gradients across the flux surfaces, and with all relevant kinetic effects considered, including Landau damping and drift resonance.

When this shear Alfvén wave is driven unstable by a particular kinetic effect, it is sometimes given a separate name in the literature. Of particular importance is the effect referred to in Secs. 1.1.3 and 2.3, and benchmarked in Fig. 4.8; whereby, in the presence of a finite ion temperature gradient, the ion drift resonance drives the kinetic Alfvén mode unstable below the ideal MHD ballooning limit. This effect has been labeled the “Alfvén ITG mode” [Zonca et al. 1998], and, in an experimental context on the JET tokamak, the “β-induced ITG mode”. Here we do not employ these terms, as we believe they could generate confusion with the much different ITG mode, an instability in a different branch of the dispersion relation with very different properties, as described in the following section. Instead, recognizing that at all ranges of parameters there is a complex mix of driving and damping effects, we refer to the mode simply as the kinetic Alfvén instability or kinetic ballooning mode (KBM), whether it occurs above or below the ideal MHD critical β.

2.2 The ITG Mode

The toroidal ion temperature gradient (ITG) instability has received a great deal of attention in recent years, as it has come to be viewed as the most likely drive for turbulent ion heat transport in the core of tokamaks. The ITG mode is an instability in the sound wave branch of the dispersion relation, with a real frequency that scales roughly with the ion diamagnetic drift frequency. Unlike the slab ITG mode (often called the η_i mode) which is driven by parallel sound wave dynamics, the toroidal ITG is driven primarily by bad curvature. The rather complex instability

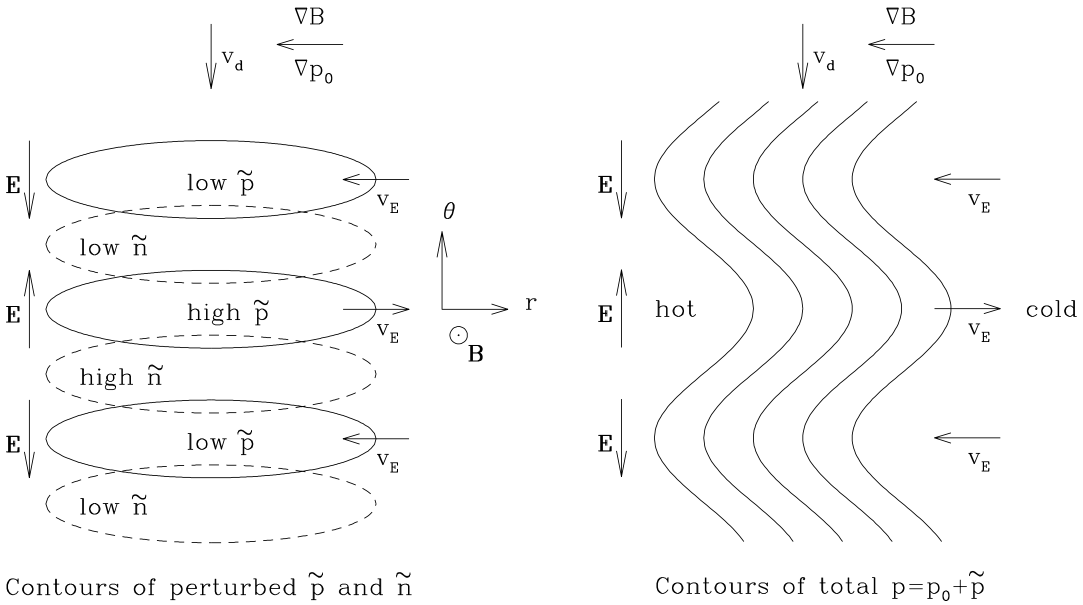

Figure 2.1: Simple diagram of the toroidal ITG instability mechanism on the outer midplane of a tokamak. The velocity dependence of the downward ∇B and curvature drifts cause ion density to build up below the hot spots and above the cold spots. This produces an electric field, which $\mathbf{E}\times\mathbf{B}$ convects hotter plasma into the hot spots, and colder plasma into the cold spots. On the inner midplane where ∇p_0 is reversed with respect to ∇B, colder plasma is convected into the hot spots, and the feedback mechanism is shut off. [Figure courtesy of M. A. Beer]

mechanism, which involves the combination of the velocity dependent curvature and ∇B drifts and the $\mathbf{E}\times\mathbf{B}$ drift, is illustrated in Fig. 2.1.

The electrostatic toroidal ITG mode can be approximately described by a simple set of two ion fluid moment equations (density and pressure), coupled to an adiabatic electron response. Such a description is given in Sec. 1.3 of [Beer 1995], and leads to a growth rate of

$$\gamma_{ITG} \equiv \sqrt{\frac{2\omega_{di}\omega_{*i}\eta_i}{\tau + b}}, \tag{2.7}$$

in the strongly unstable ($R/L_{T_i}, \eta_i \gg 1$) limit. For the low β, high aspect ratio tokamak geometry considered in this simple illustration, the combined curvature and ∇B drift frequency for ions is $\omega_{di} = -(\rho_i v_{ti}/R)(k_r \sin\theta + k_\theta \cos\theta)$, and the ion diamagnetic drift frequency is $\omega_{*i} = -k_\theta \rho_i v_{ti}/L_{ni}$. Here $\eta_i = L_{ni}/L_{Ti}$ is the ratio of the ion density scale length (L_{ni}) to the ion temperature scale length (L_{Ti}), $\tau = T_i/T_e$, $b = k_\perp^2 \rho_i^2$ has been assumed to be small, $v_{ti} = \sqrt{T_i/m_i}$ is the ion thermal speed, $\rho_i = v_{ti}/\Omega_i$ is the ion thermal gyroradius, $\Omega_i = ZeB/m_i c$ is the ion cyclotron frequency, and r and θ are the radial and poloidal coordinates.

With normal profiles (positive L_n and L_T), η_i, b and τ are all positive, and instability requires that ω_{*i} and ω_{di} have the same sign. This occurs whenever ∇P and ∇B are aligned, that is, in the "bad curvature" region. The stabilizing effect of $T_i > T_e$ is evident from the factor of τ in the denominator, and this effect persists in the presence of kinetic effects, as has been shown in various geometries by [HAHM and TANG 1989; ROMANELLI 1989; BIGLARI et al. 1989]. Furthermore, since both ω_{di} and ω_{*i} are proportional to $k_\perp$, it is clear that the growth rate is zero at $k_\perp = 0$, then increases with $k_\perp$ before leveling off. With full consideration of finite Larmor radius effects, the peak in the growth rate is found to occur around $k_\perp \rho_i \sim 1/2$.

Beyond this basic description of the electrostatic ITG instability, our main interest is in the impact of finite β. The required electromagnetic description of the ITG is fairly involved even in the fluid limit, and requires a proper treatment of both ion and electron dynamics. In the next section, we derive the dispersion relation in the local fluid limit, and describe both the finite-β ITG mode and the kinetic ballooning mode.

2.3 Local Fluid Analysis of the Finite-β ITG and KBM

A great deal of physical insight about both the finite-β ion temperature gradient mode (ITG) and the kinetic ballooning mode (KBM) can be gained by exploring dynamics in the local fluid limit.

In the local limit, $k_\parallel$, $k_\perp$, ω_* and ω_d are treated as constants. The local fluid dispersion relation can be derived directly from the gyrokinetic Vlasov-Poisson-Ampere system by taking the appropriate fluid limits, $k_\parallel^2 v_{ti}^2 \ll \omega^2 \ll k_\parallel^2 v_{te}^2$, $|\omega_d| \ll |\omega|$, and $k_\perp^2 \rho_i^2 \ll 1$, as in [KIM et al. 1993].

Here we derive the local dispersion relation starting with the moment equations derived in Ch. 3. This serves as a demonstration that, as expected, the electromagnetic gyrofluid model correctly reproduces the local dispersion relation in the fluid limit. Furthermore, the use of a set of fluid equations allows for exploration of the impact of additional approximations sometimes made in fluid models.

For simplicity, we invoke the normalizations introduced in Eqs. 3.66-3.67 and 3.101. All quantities in this section are normalized unless otherwise noted, and a single species of $Z = 1$ ions is assumed.

In the simple fluid case, neglecting collisions and Landau damping, the appropriate electron density and velocity response follow directly from Eqs. 3.114-3.116:

$$n_e = \tau\phi - \tau(1 - \frac{\omega_{*e}}{\omega})\psi \tag{2.8}$$

$$u_{\|e} = \frac{\tau\omega}{k_\|}(1 - \frac{\omega_{*e}}{\omega})(\phi - \psi) - \frac{2\omega_d}{k_\|}(1 - \frac{\omega_{*pe}}{\omega})\psi, \tag{2.9}$$

where $\psi = A_\|\omega/k_\|$, $\omega_{*pe} = \omega_{*e}(1+\eta_e)$, and the electron diamagnetic frequency $\omega_{*e} = -\omega_*/\tau$, where ω_* is the single species ion diamagnetic frequency. The combined ion ∇B and curvature drift frequency is denoted by $\omega_d = -\tau\omega_{de}$.

The appropriate single species ion response can be calculated from Eqs. 3.87-3.92 by neglecting collisions, and the Landau and drift resonance closures. We first substitute $\psi = A_\|\omega/k_\|$, and simultaneously expand in the three small parameters $k_\perp^2 \ll 1$ ($k_\perp^2\rho_i^2 \ll 1$ in unnormalized units), $|\omega_d/\omega| \ll 1$, and $k_\|^2/\omega^2 \ll 1$ ($k_\|^2 v_{ti}^2 \ll \omega^2$ in unnormalized units). By keeping terms through first order in the small parameters, we capture the important physics related to curvature, sound wave dynamics, and FLR effects in the ion density response:

$$n_i = -\frac{\omega_*}{\omega}\phi + \frac{k_\perp^2}{2}\frac{\omega_{*pi}}{\omega}\phi + \frac{k_\|^2}{\omega^2}(1 - \frac{\omega_{*pi}}{\omega})(\phi - \psi) + \frac{2\omega_d}{\omega}(1 - \frac{\omega_{*pi}}{\omega})\phi, \tag{2.10}$$

where $\omega_{*pi} = \omega_*(1+\eta_i)$. Because the largest terms in $u_{\|i}$ are smaller than the largest terms in $u_{\parallel e}$ by a factor of $k_\parallel^2/\omega^2$, only the lowest order ion velocity response,

$$u_{\parallel i} = \frac{k_\parallel}{\omega}(1 - \frac{\omega_{*pi}}{\omega})(\phi - \psi) \tag{2.11}$$

is needed in Ampere's Law.

We now wish to substitute the above electron and ion density response into the gyrokinetic Poisson's equation, which, for $k_\perp^2 \ll 1$, is $n_e = \bar{n}_i - k_\perp^2 \phi$. To first order in $k_\perp^2$, the real space ion density $\bar{n}_i$ can be written in terms of the gyrocenter density n_i and perpendicular temperature $T_{\perp i}$ as in Eq. 3.124:

$$\begin{aligned} \bar{n}_i &= \frac{1}{1 + k_\perp^2/2} n_i - \frac{2k_\perp^2}{(2 + k_\perp^2)^2} T_{\perp i} \simeq (1 - \frac{k_\perp^2}{2}) n_i - \frac{k_\perp^2}{2} T_{\perp i} \\ &= n_i - \frac{k_\perp^2}{2} p_{\perp i} \simeq n_i + \frac{k_\perp^2}{2} \frac{\omega_{*pi}}{\omega} \phi, \end{aligned} \tag{2.12}$$

where the lowest order ion perpendicular pressure response, $p_{\perp i} = -(\omega_{*pi}/\omega)\phi$, has been substituted in the final step. Substituting for $\bar{n}_i$ and n_e, we find the gyrokinetic Poisson equation in the fluid limit:

$$\left[\tau(1 - \frac{\omega_{*e}}{\omega}) - \frac{k_\parallel^2}{\omega^2}(1 - \frac{\omega_{*pi}}{\omega})\right](\phi - \psi) + (k_\perp^2 - \frac{2\omega_d}{\omega})(1 - \frac{\omega_{*pi}}{\omega})\phi = 0. \tag{2.13}$$

Similarly, substituting $u_{\parallel e}$ and $u_{\parallel i}$ into Ampere's Law, $(2k_\perp^2 k_\parallel/\tau\beta_e\omega)\psi = \bar{u}_{\parallel i} - u_{\parallel e}$, noting that $\bar{u}_{\parallel i} = u_{\parallel i}$ to the required order, yields:

$$\frac{2k_\perp^2 k_\parallel^2}{\tau\beta_e}\psi = \omega^2 \left[\tau(1 - \frac{\omega_{*e}}{\omega}) - \frac{k_\parallel^2}{\omega^2}(1 - \frac{\omega_{*pi}}{\omega})\right](\phi - \psi) + 2\omega_d(\omega - \omega_{*pi})\psi, \tag{2.14}$$

or, substituting Eq. 2.13,

$$\frac{2k_\perp^2 k_\parallel^2}{\tau\beta_e}\psi = -2\omega_d(\omega - \omega_{*pi})\phi + 2\omega_d(\omega - \omega_{*pe})\psi + \omega(\omega - \omega_{*pi})k_\perp^2\phi. \tag{2.15}$$

Combining Eqs. 2.13 and 2.15 gives the general electromagnetic dispersion relation in the local fluid. The above result, derived from our electromagnetic gyrofluid model, is identical to that found directly from the gyrokinetic Vlasov-Poisson-Ampere system by [Kim et al. 1993].

Before exploring the full dispersion relation, it is useful to take simpler limits.

2.3.1 The Electrostatic Limit

In the limit $\beta \to 0$ at finite $k_\perp$ and $k_\parallel$, one possible limit for Eq. 2.15 is $\psi \to 0$, leading to the usual electrostatic drift wave result.[9]

However, it is useful to be more specific about the requirements for the validity of the electrostatic limit, $\psi \ll \phi$. Noting that $\beta_i = \tau\beta_e$, Eq. 2.15 can be rewritten:

$$\psi = \beta_i \frac{\omega(\omega - \omega_{*pi})k_\perp^2 - 2\omega_d(\omega - \omega_{*pi})}{2k_\perp^2 k_\parallel^2 - \beta_i 2\omega_d(\omega - \omega_{*pe})}\phi. \tag{2.16}$$

In general, each term in the numerator must be small compared to the denominator to satisfy the electrostatic limit. For the first term in the numerator, this requires $\beta_i\omega^2/2k_\parallel^2 \ll 1$, or $\omega^2 \ll 2k_\parallel^2/\beta_i$. In unnormalized units this is $\omega^2 \ll k_\parallel^2 v_A^2$, where v_A is the usual Alfvén speed. Turning to the last term in the numerator, $2\omega_d\omega_{*pi}$, the requirement for the electrostatic limit is $\beta_i\omega_d\omega_*(1+\eta_i)/k_\perp^2 k_\parallel^2 \ll 1$. In the local limit, $\omega_* = k_\theta$, $\omega_d = \epsilon_n\omega_*$, $k_\perp \sim k_\theta$, and $k_\parallel \simeq \epsilon_n/q$, where $\epsilon_n = L_{ne}/R$, this requirement becomes $\beta_i q^2(1+\eta_i)/\epsilon_n \ll 1$. Or, noting that $\epsilon_n/q^2(1+\eta_i)$ is roughly the local ideal ballooning limit (β_{ic}), the requirement becomes $\beta_i \ll \beta_{ic}$.

Hence the electrostatic limit does not require simply that the value of β be small. Rather, it requires both that the frequency of interest be small compared to the shear Alfvén frequency, and that the plasma be far from the ideal ballooning limit, β_c. Because laboratory fusion plasmas are often close to this β limit, the electrostatic approximation can break down even though β may be quite small. This is especially true near the edge of fusion plasmas, where β is generally small,

---

[9] Another possibility is for ψ to remain finite while $\omega \to \infty$, in which case Eqs. 2.15 and 2.13 reduce to the simple shear Alfvén wave, $\omega^2 = 2k_\parallel^2/\tau\beta_e(1 + k_\perp^2/\tau)$, or in unnormalized units, $\omega^2 = k_\parallel^2 v_A^2(1 + b_s)$.

yet large values of q and sharp gradients (small ϵ_n) push the plasma close to the ideal ballooning limit.

In the electrostatic limit ($\psi \ll \phi$), Eq. 2.13 becomes,

$$\tau(1 - \frac{\omega_{*e}}{\omega}) - \frac{k_\parallel^2}{\omega^2}(1 - \frac{\omega_{*pi}}{\omega}) + (k_\perp^2 - \frac{2\omega_d}{\omega})(1 - \frac{\omega_{*pi}}{\omega}) = 0. \tag{2.17}$$

In the limit of a homogeneous plasma in a straight magnetic field ($\omega_* = \omega_d = 0$), the above reduces to the simple ion acoustic wave $\omega^2 = k_\parallel^2/\tau$ ($\omega^2 = k_\parallel^2 c_s^2$ in unnormalized units) for small $k_\perp$. In the slab limit, $\omega_d = 0$, the unstable root of Eq. 2.17 is the slab ITG or "η_i" mode, with the instability drive provided by the $k_\parallel^2\omega_{*pi}$ term. With finite ω_d, Eq. 2.17 is the dispersion relation for the electrostatic ITG mode in the local fluid limit. The $2\omega_d\omega_{*pi}$ term provides the toroidal drive for the ITG instability.

In a torus, the $2\omega_d\omega_{*pi}$ driving term is generally dominant, and parallel dynamics can be omitted in an approximate description ($k_\parallel^2/\omega^2 \to 0$). The simple toroidal ITG dispersion relation with small $k_\perp$ and $k_\parallel$ is then:

$$\omega = \frac{1}{2\tau}\left[-\omega_* + 2\omega_d \pm \sqrt{(-\omega_* + 2\omega_d)^2 - 8\tau\omega_d\,\omega_{*pi}}\right]. \tag{2.18}$$

In the strongly unstable ($R/L_{T_i}, \eta_i \to \infty$) limit, this reduces to Eq. 2.7 (with $b \to 0$) as expected.

2.3.2 The Kinetic Ballooning Mode

The ballooning mode in the local fluid limit can be approximately described by making the usual ideal MHD approximation $E_\parallel \simeq 0$, or $\phi \simeq \psi$.

Eq. 2.15 then reduces to:

$$\omega(\omega - \omega_{*pi}) = \frac{2k_\parallel^2}{\beta_i} - \frac{2\omega_d^2}{k_\perp^2}(\omega_{*pi} - \omega_{*pe}), \tag{2.19}$$

and the critical β_i for instability is:

$$\beta_{ic} = \frac{k_\perp^2 k_\parallel^2}{\omega_d(\omega_{*pi} - \omega_{*pe}) - \omega_{*pi}^2 k_\perp^2/4} \simeq \frac{\epsilon_n^2/q^2}{\epsilon_n \left[1 + \eta_i + (1+\eta_e)/\tau\right] - k_\perp^2 (1+\eta_i)^2/8}, \tag{2.20}$$

where the approximations $k_\theta \sim k_\perp$ and $k_\parallel \simeq \epsilon_n/q$ have been used in the final step. For long wavelength modes ($k_\perp^2 \ll 1$), this threshold β_i agrees with MHD theory in the local limit ($\beta_{ic} = \epsilon_n/q^2[1 + \eta_i + (1+\eta_e)/\tau]$), and demonstrates that the MHD α parameter, which in normalized units is

$$\alpha = \frac{q^2 \beta_i}{\epsilon_n}\left[1 + \eta_i + (1+\eta_e)/\tau\right], \tag{2.21}$$

provides a much better gauge of proximity to ideal ballooning instability ($\alpha \simeq 1$), and validity of the electrostatic approximation (which requires $\alpha \ll 1$) than does β alone. A nonlocal treatment brings in additional parameters, such as the magnetic shear $\hat{s}$. However, the above local approximation for the ballooning mode β limit, $\alpha \simeq 1$, provides a reasonable, factor of two type estimate of the nonlocal MHD β_c in $\hat{s} - \alpha$ geometry over a wide range of typical values of $1/2 \lesssim \hat{s} \lesssim 3$.

The local fluid model predicts a marginal real frequency for the KBM of $\omega \simeq \omega_{*pi}/2$, quite different from the ideal MHD prediction of $\omega = 0$.

Kinetic effects such as Landau damping and ion drift resonance, which can significantly change the behavior of the KBM from that predicted in the local fluid limit, are discussed briefly in Sec. 2.3.5.

2.3.3 The Finite-β ITG

Combining Eqs. 2.13 and 2.15, the general electromagnetic dispersion relation in the local fluid limit can be written:

$$\begin{aligned} \tau(1 - \frac{\omega_{*e}}{\omega}) \quad &- \quad \frac{k_\parallel^2}{\omega^2}(1 - \frac{\omega_{*pi}}{\omega}) \\ &= \quad \left[(\frac{2\omega_d}{\omega} - k_\perp^2)(1 - \frac{\omega_{*pi}}{\omega})\right]\left[1 - \frac{\omega(\tau\omega + \omega_*) - k_\parallel^2(1 - \frac{\omega_{*pi}}{\omega})}{(2k_\perp^2 k_\parallel^2/\beta_i) - 2\omega_d(\omega - \omega_{*pe})}\right]. \end{aligned} \tag{2.22}$$

Comparing with Eq. 2.17 we can see that the final term in brackets represents the electromagnetic, or "finite-β" effect.

For a toroidal ITG mode, with $\omega \ll \omega_{*pi}$, at very low $\beta_i \ll 1$, the effect of the electromagnetic correction is to reduce the ITG driving term $(2\omega_d\,\omega_{*pi})$ by a factor of roughly $1 - \beta_i(\tau\omega^2 + \omega\omega_* + k_\parallel^2\omega_{*pi}/\omega)/2k_\perp^2 k_\parallel^2$. The toroidal ITG drive vanishes entirely when:[10]

$$\beta_i = \frac{2k_\parallel^2 k_\perp^2}{\omega(\tau\omega + \omega_*) + 2\omega_d(\omega - \omega_{*pe}) - k_\parallel^2(1 - \omega_{*pi}/\omega)}. \tag{2.23}$$

Note that for typical ITG frequencies, $\omega \sim \omega_*$, and for small $k_\parallel$ and $k_\perp^2$, this expression is very similar to the β_i threshold for kinetic ballooning instability given in Eq. 2.20. The stabilization of the toroidal ITG mode and the onset of kinetic ballooning instability are closely linked, both in the local fluid limit and in a full kinetic treatment.

2.3.4 Growth Rates in the Local Fluid Limit

A quantitative exploration of growth rates in the local fluid limit provides physical insight about the behavior of both the ITG and KBM instabilities, and also allows for a simple evaluation of various approximations often made in fluid and gyrofluid turbulence models.

Fig. 2.2 shows the growth rate of the dominant instability as a function of β in the local fluid limit, with the normalized parameters $\tau = 1$, $k_\perp = 0.5$, $k_\parallel = 0.1$, $\omega_* = k_\theta = 0.5$, $\epsilon_n = 0.2$, $\eta_i = \eta_e = 3$. The solid line shows the correct local fluid growth rate as calculated from Eq. 2.22. The ITG mode dominates at low β and is stabilized with increasing β. The KBM becomes unstable near $\beta \simeq 1.8\%$ and its growth rate increases with β.[11]

---

[10] When the toroidal ITG is strongly stabilized by finite β, it is possible for the slab ITG mode to become important, as pointed out by [Cummings 1995]. However, in the local fluid limit, this provides only a small modification of the overall β at which complete stabilization of the ITG occurs. Furthermore, it is critical to note that in the region where the ITG is strongly stabilized, consideration of kinetic effects is very important, as discussed in the following section.

[11] The "island of stability" between the ITG and KBM is, unfortunately, but a mirage. It vanishes with the addition of kinetic effects.

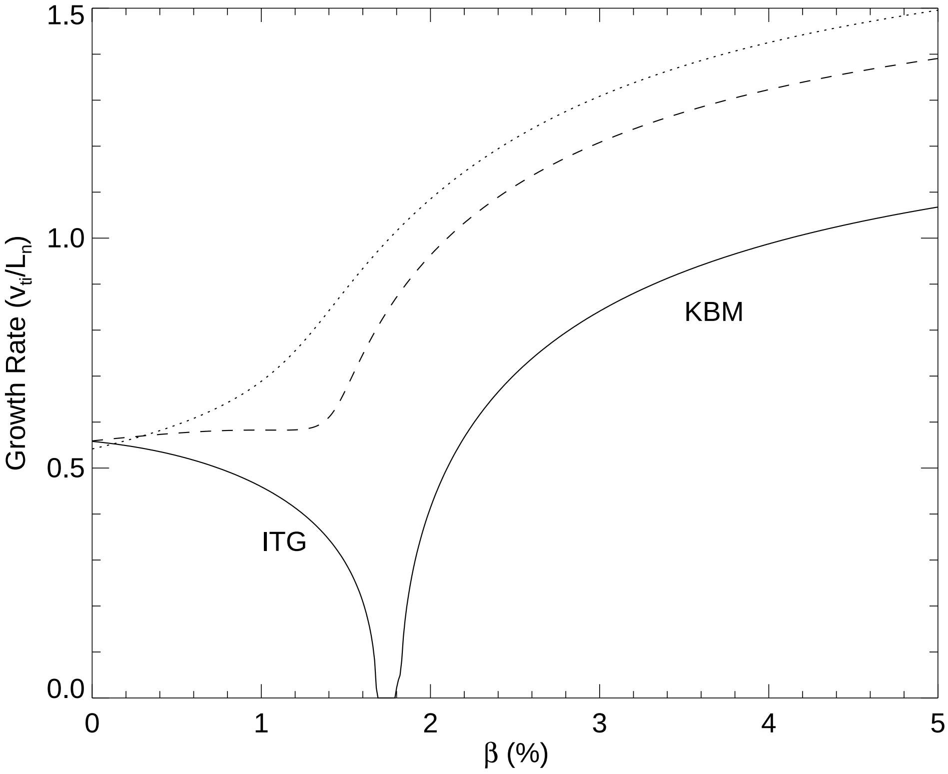

Figure 2.2: β dependence of the linear growth rate of the dominant mode in the local fluid limit. The solid line shows the correct local fluid growth rate, while the dotted and dashed lines show growth rates predicted by models which are missing certain finite-Larmor-radius terms. Parameters chosen are $\tau = 1$, $k_\perp = 0.5$, $k_\parallel = 0.1$, $\omega_* = k_\theta = 0.5$, $\epsilon_n = 0.2$, and $\eta_i = \eta_e = 3$. The ITG mode dominates for $\beta \lesssim 1.7\%$, while the KBM is dominant for $\beta > 1.8\%$.

Many past models of plasma turbulence have only partially accounted for ion finite Larmor radius (FLR) effects. To first order in $b = k_\perp^2 \rho_i^2$, finite Larmor radius effects enter both in the gyrocenter ion density response [through the $(1 + \eta_i \hat{\nabla}_\perp^2/2) i\omega_* \Gamma_0^{1/2} \phi$ term in Eq. 3.87] and in the gyrokinetic Poisson's equation. In Poisson's equation, first order FLR effects enter through the first order polarization term $(-k_\perp^2 \rho_i^2 \, \phi)$ and through the conversion from real space $\bar{n}_i$ to the gyrocenter space n_i as in Eq. 2.12. While nearly all models include the polarization term, some have omitted either the ion response FLR terms or the real space transformation term, or both. Omitting both effects leads to the predicted dominant growth rate illustrated by the dotted line in Fig. 2.2. While this predicted growth rate is quite accurate in the electrostatic limit ($\beta \to 0$), it is seriously in error at larger values of β, missing the finite-β stabilization of the ITG entirely. The dashed line in Fig. 2.2 shows the growth rate that is predicted if either the ion response FLR term or the real space transformation FLR term, but not both, is included.[12] Again this partial FLR model provides accurate growth rate predictions at very small β, but introduces large errors at finite β. Hence, a proper treatment of FLR effects is of great importance for an electromagnetic fluid turbulence model. Models which do not account for all FLR effects at least through first order in $k_\perp^2 \rho_i^2$ risk introducing serious errors for finite-β cases, even though such models may be able to treat the electrostatic ITG mode with reasonable accuracy.

Simple electron fluid models developed for the regime $\omega \ll k_\parallel v_{te}$ sometimes assume that the perturbed electron temperature vanishes ($\tilde{T}_e = 0$). This neglects the impact of fluctuating magnetic field lines moving across equilibrium electron temperature gradients. The fast motion of the electrons along the perturbed field lines allows the electrons to thermalize to a uniform temperature along the perturbed field, locally cancelling the equilibrium electron temperature gradient when the fluctuating field moves across it. This leads to the appropriate electron temperature response given by Eq. 3.116. If $\tilde{T}_e = 0$ is instead assumed, the electron temperature gradient drive of the kinetic ballooning mode is missed, and the predicted growth rate, shown by the dotted line in Fig. 2.3, is in error when η_e is finite. It has also been commonly assumed that, because $\omega_d \ll k_\parallel v_{te}$, electron ∇B and curvature drifts can be neglected. This assumption removes the electron density

---

[12] Linearly, each term contributes an identical factor of $-(\omega_{*pi}/\omega) k_\perp^2 \phi$ to Eq. 2.13.

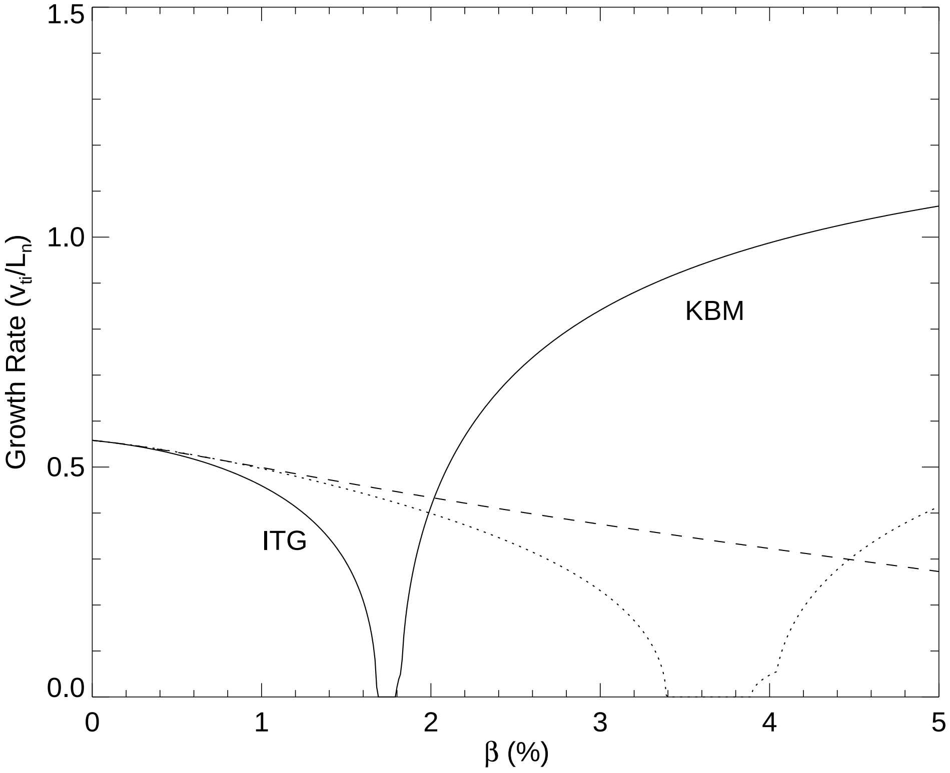

Figure 2.3: Linear growth rate of the dominant mode vs. β in the local fluid limit. The solid line again shows the correct local fluid growth rate. The dotted line shows the growth rate predicted by a model which assumes the perturbed electron temperature is zero. The dashed line shows the prediction of a fluid model which omits electron ∇B and curvature drifts entirely. Parameters are identical to those in Fig. 2.2.

and temperature gradient drive of the KBM, and leads to the growth rate prediction shown by the dashed line in Fig. 2.3. Note that both of the above approximations work well at very small β values, but lead to large errors as β approaches the MHD ballooning limit, $\beta = \beta_c$.

A final common approximation made in fluid models is the neglect of the ion current in Ampere's Law. As noted, the ion current is smaller than the dominant piece of the electron current by a factor of $k_\parallel^2/\omega^2$ in the local fluid limit. Thus, for small values of $k_\parallel$ typical of ballooning modes ($k_\parallel \sim \epsilon_n/q$), the ion current is often negligible. More specifically, when $k_\parallel^2/\omega^2 \ll 2\omega_d/\omega$ the ion current can generally be neglected. The growth rate calculated without ion current is almost indistinguishable from the growth rate with ion current for the parameters used in Figs. 2.2 and 2.3. However, at larger values of $k_\parallel$, the ion current can have a significant impact, and we believe it unwise to neglect the ion current in a numerical simulation which treats a wide range of $k_\parallel$. The neglect of the ion current is also not consistent with fluid equations which incorporate Landau damping physics.

The electromagnetic gyrofluid model developed in Ch. 3 avoids the above assumptions, and is thus able to exactly reproduce the behavior of the ITG and KBM in the local fluid limit.

2.3.5 Kinetic Effects

The local fluid analysis in the previous sections orders out important kinetic effects such as Landau damping and ion drift resonance. Including these effects significantly alters the fluid growth rates, as has been discussed extensively in the literature, for example [Hong et al. 1989; Kim et al. 1993]. Landau damping tends to reduce the predicted fluid growth rates, though it increases growth rates in the "island of stability" between the ITG and KBM instabilities, eliminating the island. Ion drift resonance causes the KBM to go unstable below the ideal ballooning limit when η_i is finite.

Models of Landau damping and drift resonance are included in the electromagnetic gyrofluid model as described in Ch. 3. The ability of these models to properly account for the relevant kinetic effects is gauged with a series of nonlocal linear benchmarks presented in Ch. 4. See in particular Fig. 4.8, which demonstrates the effect of drift resonance reducing the KBM threshold below the ideal ballooning limit.

Chapter 3

Derivation of the Electromagnetic Gyrofluid Equations

THE ELECTROMAGNETIC GYROFLUID EQUATIONS are derived from a series of velocity space moments of the nonlinear gyrokinetic equation. The moment hierarchy is truncated using a set of closures derived to model kinetic effects, including collisionless phase mixing due to parallel streaming and toroidal drifts, as well as linear and nonlinear finite-Larmor-radius (FLR) effects.

The ion equations are derived first, as a natural extension of the electrostatic toroidal gyrofluid equations of [Beer 1995] to include magnetic fluctuations.

Electron equations are derived from the electromagnetic drift kinetic equation using an analytic expansion which removes small spatial scales and fast temporal scales from the system. These equations include the effects of electron temperature and density gradients, electron $\mathbf{E} \times \mathbf{B}$ motion, Landau damping, electron-ion collisions and the parallel electron currents which, along with parallel ion currents, give rise to the parallel magnetic potential.

The system is closed with the gyrokinetic Poisson equation and parallel Ampere's Law.

3.1 The Gyrokinetic Equation

The starting point for the derivation of the fluid equations is the nonlinear electromagnetic gyrokinetic equation of [Brizard 1992], based upon earlier gyrokinetic work by many authors, notably [Hahm et al. 1988; Brizard 1988; Lee 1983; Dubin et al. 1983; Frieman and Chen 1982; Catto and Tsang 1977].

The standard gyrokinetic ordering is invoked as follows:

$$\frac{\omega}{\Omega_i} \sim \frac{k_\parallel v_{ti}}{\Omega_i} \sim \frac{e\phi}{T} \sim \frac{\delta B}{B} \sim \frac{F_1}{F_0} \sim \frac{\rho_i}{L} \sim \varepsilon \ll 1, \qquad k_\perp \rho_i \sim 1, \tag{3.1}$$

where ω is a characteristic frequency of the fluctuations, and $k_\parallel$ and $k_\perp$ are typical fluctuation wavenumbers parallel and perpendicular to the equilibrium magnetic field. Ω_i is the ion cyclotron frequency, $v_{ti} = \sqrt{T_i/m_i}$ is the ion thermal speed, and $\rho_i = v_{ti}/\Omega_i$ is the thermal ion gyroradius. L is a typical equilibrium scale length, such as the density scale length $L_n = -\nabla(\ln n_0)^{-1}$, the temperature scale length $L_T = -\nabla(\ln T_0)^{-1}$, or the plasma minor radius (a) or major radius (R). T and B are typical equilibrium temperatures and magnetic fields, and F_0 is the equilibrium distribution. F_1 is the fluctuating distribution function, ϕ is the electrostatic potential (which is assumed to have no equilibrium component), and δB is the fluctuating component of the magnetic field.

Gyrokinetics averages over the fast gyromotion of the particles around a strong magnetic field, reducing the kinetic equation from three to two velocity space dimensions, and leaving the magnetic moment μ as a rigorously conserved quantity. The gyrokinetic ordering takes advantage of the spatial anisotropy created by the strong magnetic field. Parallel to the field, particles can stream freely, and fluctuating wavelengths are long, $k_\parallel L \sim 1$. Perpendicular to the field, particle motion is strongly restricted, and wavelengths scale with the gyroradius $k_\perp \rho_i \sim 1$.

The fluctuating distribution function is ordered small compared to the equilibrium distribution, which here is taken as a Maxwellian. Nonetheless, perpendicular gradients of fluctuating quantities are the same order as perpendicular gradients of the equilibrium ($k_\perp F_1 \sim F_0/L$), and hence the perpendicular nonlinearities due to the $\mathbf{E}\times\mathbf{B}$ drift and field line bending are kept, while parallel nonlinearities are small, and are ordered out here.

Brizard's electromagnetic gyrokinetic equation can be written in the form:

$$\frac{\partial F}{\partial t} + \dot{\mathbf{X}} \cdot \nabla F + \dot{v}_\parallel \frac{\partial F}{\partial v_\parallel} = C(F), \tag{3.2}$$

where F is the gyrocenter distribution function in the gyrocenter phase space coordinates $(\mathbf{X}, v_\parallel, \mu, \zeta)$. Within the gyrokinetic ordering $(\omega \ll \Omega_i)$, the gyrophase angle ζ is effectively averaged over, and does not appear explicitly $(\partial F/\partial\zeta = 0)$.[1] The gyrocenter magnetic moment $\mu = v_\perp^2/2B + \mathcal{O}(\varepsilon)$ is exactly conserved and enters the equations only as a parameter. An as yet undefined collision operator $C(F)$ has been added to the right hand side.

Eq. 3.2 is solved through $\mathcal{O}(\varepsilon^2)$ in the gyrokinetic ordering defined above. When ordering terms in the gyrokinetic equation, all frequencies are compared to Ω_i, and all lengths to ρ_i. Hence $\frac{\partial F}{\partial t} \sim \omega F_1$ is $\mathcal{O}(\varepsilon^2)$, because $\frac{\partial F_0}{\partial t} = 0$, $F_1/F_0 \sim \varepsilon$, and $\omega/\Omega_i \sim \varepsilon$. Any gradient operator acting on F_0 or B is $\mathcal{O}(\varepsilon)$ because $\rho_i/L \sim \varepsilon$. A parallel gradient on F_1 is $\mathcal{O}(\varepsilon^2)$ because $k_\parallel \rho_i \sim \varepsilon$. However, a perpendicular gradient acting on F_1 is $\mathcal{O}(\varepsilon)$ because $k_\perp \rho_i \sim 1$. Because ∇F is $\mathcal{O}(\varepsilon)$, $\dot{\mathbf{X}}$ is needed only to $\mathcal{O}(\varepsilon)$, while $\dot{v}_\parallel$ must include terms through $\mathcal{O}(\varepsilon^2)$.

The fluctuating magnetic field $\delta\mathbf{B}$ is described to lowest order in terms of a magnetic potential along the equilibrium field, $\delta\mathbf{B} = \nabla \times A_\parallel \hat{\mathbf{b}}$, where $\hat{\mathbf{b}}$ is a unit vector along the equilibrium field.[2] The perturbation along the equilibrium field $(\delta B_\parallel)$ is small for $\beta \ll 1$, as can be seen from perpendicular force balance, and $\delta B_\parallel$ is neglected here. A local kinetic analysis by [Horton et al. 1985] has found $\delta B_\parallel$ to be unimportant for β of the order of the MHD critical β_c or smaller. However, the toroidal kinetic code of [Kotschenreuther et al. 1995] has included $\delta B_\parallel$ and found it to be somewhat important for $\beta \sim \beta_c$, particularly at low aspect ratio

---

[1] See [Qin et al. 1999] for a discussion of a formulation of gyrokinetics which relaxes the low frequency approximation, and includes gyrophase dependence. This introduces perpendicular dynamics and allows a full description of compressional Alfvén and Bernstein waves.

[2] Note that $A_\parallel$ and $A_\perp$ are fluctuating quantities. The equilibrium magnetic field is described here by $\mathbf{B}$ or $B\hat{\mathbf{b}}$, never as a magnetic potential.

[KOTSCHENREUTHER 1998]. We wish to include $\delta B_\parallel$ in future work to achieve better accuracy, particularly in high β, low aspect ratio cases.

The gyrocenter velocity is then given by

$$\dot{\mathbf{X}} = v_\parallel(\hat{\mathbf{b}} + \frac{\langle \delta \mathbf{B}_\perp \rangle}{B}) + \mathbf{v}_E + \mathbf{v}_d, \tag{3.3}$$

where the angular brackets denote gyroangle averages. The first term on the right represents free streaming along the total magnetic field. The second term is the gyroaveraged $\mathbf{E} \times \mathbf{B}$ drift velocity, $\mathbf{v}_E = \frac{c}{B} \hat{\mathbf{b}} \times \nabla \langle \phi \rangle$. $\mathbf{v}_d$ is the combined curvature and ∇B drift velocity. In general, $\mathbf{v}_d$ can be written

$$\begin{aligned} \mathbf{v}_d &= \frac{v_\parallel^2}{\Omega} \hat{\mathbf{b}} \times (\hat{\mathbf{b}} \cdot \nabla \hat{\mathbf{b}}) + \frac{\mu}{\Omega} \hat{\mathbf{b}} \times \nabla B \\ &= \frac{v_\parallel^2 + \mu B}{\Omega B^2} \mathbf{B} \times \nabla B + \frac{v_\parallel^2}{\Omega B^2} \hat{\mathbf{b}} \times (\nabla \times \mathbf{B} \times \mathbf{B}). \end{aligned} \tag{3.4}$$

Using the equilibrium relations $\nabla p = \frac{1}{c} \mathbf{J} \times \mathbf{B}$ and $\nabla \times \mathbf{B} = \frac{4\pi}{c} \mathbf{J}$, this can be written

$$\mathbf{v}_d = \frac{v_\parallel^2 + \mu B}{\Omega B^2} \mathbf{B} \times \nabla B + \frac{v_\parallel^2}{\Omega B^2} \hat{\mathbf{b}} \times \nabla p. \tag{3.5}$$

The second term on the right is small for $\beta \ll 1$,[3] and is neglected here for simplicity and to maintain consistency with neglecting $\delta B_\parallel$.[4] The definition

$$\mathbf{v}_d \doteq \frac{v_\parallel^2 + \mu B}{\Omega B^2} \mathbf{B} \times \nabla B \tag{3.6}$$

is used henceforth.

---

[3] The use of this $\beta \ll 1$ approximation may seem inconsistent with our desire to handle moderate β cases. However, it allows us to treat β values up to the MHD critical β_c for all except very low aspect ratio cases, where $\beta_c \sim 1$. The critical point is that while the electrostatic approximation requires $\beta \ll \beta_c$, the above equilibrium approximation requires only that $\beta \ll 1$. That is, our equations are valid for $m_e/m_i \ll \beta \sim \beta_c \ll 1$, and can be extended to $\beta \sim 1$ by adding $\delta B_\parallel$ and separately treating the curvature and ∇B drifts.

[4] A cancellation occurs between the ∇p term in $\mathbf{v}_d$ and a finite $\delta B_\parallel$ term [TANG et al. 1980; KOTSCHENREUTHER 1998]. Hence it does not improve accuracy to keep the ∇p term until $\delta B_\parallel$ has been fully included.

The gyrocenter parallel acceleration can be written:

$$\dot{v}_\parallel = -\frac{e}{mc}\frac{\partial \left\langle A_\parallel \right\rangle}{\partial t} - \frac{e}{m}(\hat{\mathbf{b}} + \frac{\left\langle \delta\mathbf{B}_\perp \right\rangle}{B}) \cdot \nabla \left\langle \phi \right\rangle - \mu(\hat{\mathbf{b}} + \frac{\left\langle \delta\mathbf{B}_\perp \right\rangle}{B}) \cdot \nabla B + v_\parallel(\hat{\mathbf{b}}\cdot\nabla\hat{\mathbf{b}}) \cdot \mathbf{v}_E. \tag{3.7}$$

The first two terms on the right hand side represent the total parallel electric field, which includes both a magnetic induction term $-\frac{1}{c}\frac{\partial\left\langle A_\parallel\right\rangle}{\partial t}$, and an electrostatic term evaluated along the total magnetic field. The next term is the total mirror force, and the final term is important for phase space conservation, as shown in [HAHM 1988; BEER 1995].

Using the definition $\delta\mathbf{B} = \nabla \times A_\parallel \hat{\mathbf{b}}$, the term $\delta\mathbf{B}_\perp$ can be written as follows:

$$\delta\mathbf{B}_\perp = \hat{\mathbf{b}} \times (\delta\mathbf{B} \times \hat{\mathbf{b}}) = -\hat{\mathbf{b}} \times \nabla A_\parallel + \hat{\mathbf{b}} \times \hat{\mathbf{b}}\cdot\nabla\hat{\mathbf{b}}\, A_\parallel, \tag{3.8}$$

or upon gyroaveraging,

$$\left\langle \delta\mathbf{B}_\perp \right\rangle = -\hat{\mathbf{b}} \times \nabla \left\langle A_\parallel \right\rangle + \hat{\mathbf{b}} \times \hat{\mathbf{b}}\cdot\nabla\hat{\mathbf{b}} \left\langle A_\parallel \right\rangle. \tag{3.9}$$

The second term on the right hand side is $\mathcal{O}(\varepsilon^2)$ and does not enter Eq. 3.2 to the required order.

The gyroangle averages are expressed in terms of a gyroaveraging operator J_0 as follows:

$$\left\langle \phi \right\rangle = J_0(\alpha)\phi, \qquad \left\langle A_\parallel \right\rangle = J_0(\alpha)\, A_\parallel,$$

where α is the operator defined by

$$\alpha \doteq -i\frac{\sqrt{2\mu B}}{\Omega_i}\nabla_\perp = \frac{\sqrt{2\mu B}}{v_{ti}}k_\perp \rho_i.$$

The operator J_0 is simply a Bessel function in Fourier space:

$$\begin{aligned} J_0(\alpha) &= \frac{1}{2\pi}\int_0^{2\pi} d\zeta\, \exp(i\alpha\cos\zeta) = \sum_{n=0}^{\infty}\frac{1}{(n!)^2}\left(\frac{i\alpha}{2}\right)^{2n} \\ &= \sum_{n=0}^{\infty}\frac{1}{(n!)^2}\left(\frac{\sqrt{2\mu B}}{2\Omega}\right)^{2n}\nabla_\perp^{2n}. \end{aligned} \tag{3.10}$$

In real space, J_0 is an operator which does not in general commute with other operators, and must be treated with care. It should be noted that J_0 operates only on the electrostatic potential ϕ and the parallel magnetic potential $A_\parallel$ in Eq. 3.2.

Defining the unit vector along the total magnetic field $\tilde{\mathbf{b}} = \hat{\mathbf{b}} + \frac{\langle \delta \mathbf{B}_\perp \rangle}{B}$ and the total parallel electric field $\tilde{E}_\parallel = -\frac{1}{c}\frac{\partial}{\partial t} J_0 A_\parallel - \tilde{\mathbf{b}} \cdot \nabla J_0 \phi$, the gyrokinetic equation can be written:

$$\begin{aligned} \frac{\partial F}{\partial t} &+ (v_\parallel \tilde{\mathbf{b}} + \mathbf{v}_E + \mathbf{v}_d) \cdot \nabla F \\ &+ \left[\frac{e}{m} \tilde{E}_\parallel - \mu \tilde{\mathbf{b}} \cdot \nabla B + v_\parallel (\hat{\mathbf{b}} \cdot \nabla \hat{\mathbf{b}}) \cdot \mathbf{v}_E \right] \frac{\partial F}{\partial v_\parallel} = C(F). \end{aligned} \tag{3.11}$$

3.2 The Ion Gyrofluid Equations

Gyrofluid equations are derived by taking velocity space moments of Eq. 3.11, and implementing closures to model kinetic effects. For simplicity of notation, the single ion species case is presented here. The subscript i is omitted in this section, and all quantities $(v_t, \Omega, T$ etc.$)$ are taken to refer to the ions unless otherwise noted. The full, normalized equations for the multi-species case are given in Sec. 3.2.6.

For the ions, $k_\perp \rho_i \sim 1$, and finite-Larmor-radius (FLR) effects must be accounted for, both in the moment equations and in the closures. The gyroaveraging operator $J_0(\alpha)$ appears repeatedly, and it must be treated carefully as it is a function of both configuration and velocity space (through μ).

In order to simplify the process of taking velocity space moments, it is best to move all functions of velocity space $(F, J_0, \mu, v_\parallel$ etc.$)$ to the same side of the spatial and temporal operators. We also multiply through by a factor of B in order to simplify the μ integral.

The first two terms in Eq. 3.11, $B\frac{\partial F}{\partial t} = \frac{\partial}{\partial t} FB$ and $B v_\parallel \hat{\mathbf{b}} \cdot \nabla F = \mathbf{B} \cdot \nabla (F B v_\parallel / B)$ are easily put in a form suitable for taking moments. The next three terms require modification.

Noting that spatial derivatives are taken with μ and $v_\parallel$ fixed, we can write for any field A:

$$\nabla J_0 A = J_0 \nabla A + A \nabla J_0, \tag{3.12}$$

where

$$\nabla J_0(\alpha) = \frac{\partial J_0}{\partial \alpha} \nabla \alpha = J_1(\alpha) \frac{\alpha}{2B} \nabla B. \tag{3.13}$$

The term representing free streaming along the fluctuating magnetic field, $-\frac{v_\parallel}{B} \hat{\mathbf{b}} \times \nabla J_0 A_\parallel$, can be combined with the $\mathbf{E} \times \mathbf{B}$ drift by introducing the notation:

$$\phi' = \phi - \frac{v_\parallel}{c} A_\parallel, \quad \mathbf{v}'_E = \frac{c}{B} \hat{\mathbf{b}} \times \nabla J_0 \phi', \quad \mathbf{v}'_\phi = \frac{c}{B} \hat{\mathbf{b}} \times \nabla \phi' \tag{3.14}$$

Using Eqs. 3.12 and 3.13 we can then write:

$$B \mathbf{v}'_E \cdot \nabla F = B \frac{c}{B} \hat{\mathbf{b}} \times (J_0 \nabla \phi' + J_1 \frac{\alpha}{2B} \phi' \nabla B) \cdot \nabla F. \tag{3.15}$$

The J_1 term above can be neglected as it is $\mathcal{O}(\varepsilon^3)$ due to the presence of ϕ', ∇B, and ∇F, each of which are $\mathcal{O}(\varepsilon)$. Noting that $J_0 \nabla F = \nabla J_0 F - (\alpha/2B) F J_1 \nabla B$, and introducing the notation

$$i\omega_d \doteq \frac{v_t^2}{\Omega B^2} \mathbf{B} \times \nabla B \cdot \nabla, \tag{3.16}$$

allows us to write

$$\begin{aligned} B \frac{c}{B} \hat{\mathbf{b}} \times J_0 \nabla \phi' \cdot \nabla F &= B \frac{c}{B} \hat{\mathbf{b}} \times \nabla \phi' \cdot \nabla (J_0 F) - F \frac{c\alpha}{2B} J_1 \hat{\mathbf{b}} \times \nabla \phi' \cdot \nabla B \qquad (3.17) \\ &= B \frac{c}{B} \hat{\mathbf{b}} \times \nabla \phi' \cdot \nabla (J_0 F) + \frac{e}{T} F B J_1 \frac{\alpha}{2} i\omega_d \phi' \\ &= \frac{c}{B} \hat{\mathbf{b}} \times \nabla \phi' \cdot \nabla (J_0 F B) + \frac{e}{T} F B (J_0 + J_1 \frac{\alpha}{2}) i\omega_d \phi' \\ &= \mathbf{v}'_\phi \cdot \nabla (J_0 F B) + \frac{e}{T} F B (J_0 + J_1 \frac{\alpha}{2}) i\omega_d \phi' \end{aligned}$$

Invoking the approximation outlined in Eqs. 3.4-3.6, and noting that $i\omega_d B =$

0, the ∇B and curvature drift term can be written:

$$B\mathbf{v}_d \cdot \nabla F = i\omega_d[FB(v_\parallel^2 + \mu B)]. \tag{3.18}$$

Turning now to the $\dot{v}_\parallel \frac{\partial F}{\partial v_\parallel}$ terms, we note first that all components of $\dot{v}_\parallel$ except the lowest order mirror force $-\mu\hat{\mathbf{b}} \cdot \nabla B$ are $\mathcal{O}(\varepsilon^2)$ and therefore involve only the equilibrium distribution, which is taken to be:

$$F_0 = \frac{n_0}{(2\pi v_t^2)^{3/2}} e^{-v_\parallel^2/2v_t^2 - \mu B/v_t^2}. \tag{3.19}$$

The electric field terms can be written as follows to $\mathcal{O}(\varepsilon^2)$:

$$\begin{aligned} -B\frac{e}{m}\hat{\mathbf{b}}\cdot\nabla(J_0\phi)\frac{\partial F}{\partial v_\parallel} &= -\frac{e}{m}\frac{\partial F_0}{\partial v_\parallel}B\hat{\mathbf{b}}\cdot\nabla(J_0\phi) \qquad (3.20) \\ &= -\frac{e}{m}\hat{\mathbf{b}}\cdot\nabla(\frac{\partial F_0}{\partial v_\parallel}BJ_0\phi) + \frac{e}{m}J_0\phi\frac{\partial F_0}{\partial v_\parallel}B(1 - \frac{\mu B}{v_t^2})\hat{\mathbf{b}}\cdot\nabla \ln B \end{aligned}$$

$$\begin{aligned} \frac{\partial F}{\partial v_\parallel}\frac{e}{m}(\hat{\mathbf{b}} \times \nabla J_0 A_\parallel) \cdot \nabla J_0\phi &= \frac{e}{m}\frac{\partial F_0}{\partial v_\parallel}(\hat{\mathbf{b}} \times J_0\nabla A_\parallel) \cdot J_0\nabla\phi \qquad (3.21) \\ &= \frac{e}{m}\frac{\partial F_0}{\partial v_\parallel}J_{0A_\parallel}J_{0\phi}(\hat{\mathbf{b}} \times \nabla A_\parallel) \cdot \nabla\phi, \end{aligned}$$

where the notation $J_{0A_\parallel}$ and $J_{0\phi}$ is used to indicate the field on which the Bessel function operator acts. All J_1 terms above have been dropped as they are $\mathcal{O}(\varepsilon^3)$.

The mirror force terms can be written:

$$\frac{\partial F}{\partial v_\parallel}B(-\mu\hat{\mathbf{b}}\cdot\nabla B) = -\mu B^2\frac{\partial F}{\partial v_\parallel}\hat{\mathbf{b}}\cdot\nabla \ln B \tag{3.22}$$

$$\begin{aligned} \frac{\partial F}{\partial v_\parallel}\mu(\hat{\mathbf{b}} \times \nabla J_0 A_\parallel) \cdot \nabla B &= \frac{\partial F_0}{\partial v_\parallel}\frac{\mu}{B}J_0(\nabla B \times \mathbf{B}) \cdot \nabla A_\parallel \qquad (3.23) \\ &= -\frac{\partial F_0}{\partial v_\parallel}BJ_0\frac{e\mu B}{cT}i\omega_d A_\parallel, \end{aligned}$$

where the $J_1\nabla B$ term has vanished exactly.

Finally, the phase space conservation term can be rewritten, omitting the finite β component for consistency with the treatment of the curvature drift:

$$\begin{align}
\frac{\partial F}{\partial v_\parallel} B v_\parallel (\hat{\mathbf{b}}\cdot\nabla\hat{\mathbf{b}})\cdot\mathbf{v}_E &= -\frac{\partial F_0}{\partial v_\parallel} v_\parallel \frac{c}{B^2}\mathbf{B}\times\nabla B\cdot\nabla J_0\phi \tag{3.24}\\
&= -\frac{\partial F_0}{\partial v_\parallel} v_\parallel \frac{c}{B^2}\mathbf{B}\times\nabla B\cdot\left(J_0\nabla\phi + J_1\frac{\alpha}{2B}\nabla B\right) \nonumber\\
&= -\frac{\partial F_0}{\partial v_\parallel} B J_0 v_\parallel \frac{e}{T} i\omega_d\phi. \nonumber\\
&= -\frac{e}{T}\left[\frac{\partial}{\partial v_\parallel}(F_0 B J_0 v_\parallel) - F_0 B J_0\right] i\omega_d\phi \tag{3.25}
\end{align}$$

Combining all the above terms, and defining $\nabla_\parallel = \hat{\mathbf{b}}\cdot\nabla$, the electromagnetic gyrokinetic equation can be written in the following cumbersome but useful form:

$$\begin{align}
\frac{\partial}{\partial t}FB &+ B\nabla_\parallel F v_\parallel + \mathbf{v}'_\phi\cdot\nabla(FBJ_0) + 2FBJ_0 i\omega_d\frac{e\phi'}{T} \tag{3.26}\\
&+ FBJ_1\frac{\alpha}{2}i\omega_d\frac{e\phi'}{T} + \frac{e}{cT}v_\parallel FBJ_0 i\omega_d A_\parallel \nonumber\\
&+ \frac{1}{v_t^2}i\omega_d[FB(v_\parallel^2+\mu B)] - \frac{e}{mc}\frac{\partial}{\partial v_\parallel}\left(F_0BJ_0\frac{\partial A_\parallel}{\partial t}\right) \nonumber\\
&- \frac{e}{m}\nabla_\parallel\left(\frac{\partial F_0}{\partial v_\parallel}BJ_0\phi\right) + \frac{e}{m}J_0\phi\frac{\partial F_0}{\partial v_\parallel}B\left(1-\frac{\mu B}{v_t^2}\right)\nabla_\parallel\ln B \nonumber\\
&+ \frac{e}{m}\frac{\partial F_0}{\partial v_\parallel}J_{0A_\parallel}J_{0\phi}(\hat{\mathbf{b}}\times\nabla A_\parallel)\cdot\nabla\phi - \mu B^2\frac{\partial F}{\partial v_\parallel}\nabla_\parallel\ln B \nonumber\\
&- \frac{\partial F_0}{\partial v_\parallel}BJ_0\frac{e\mu B}{cT}i\omega_d A_\parallel - \frac{\partial}{\partial v_\parallel}(FBJ_0v_\parallel)\frac{e}{T}i\omega_d\phi = 0. \nonumber
\end{align}$$

Nearly all terms with velocity space dependence are now grouped on the same side of spatial and temporal operators so that moments may easily be taken. The exception is the $v_\parallel$ term which appears in $\phi' = \phi - \frac{v_\parallel}{c}A_\parallel$ and $\mathbf{v}'_\phi = \frac{c}{B}\hat{\mathbf{b}}\times\nabla\phi'$. However, $v_\parallel$ commutes with J_0, J_1 and all spatial operators, and may be easily moved to the appropriate place inside velocity space integrals. The collision operator $C(F)$ has been omitted here. Collisions are considered in Sec. 3.2.4.

Eq. 3.26 contains terms up to $\mathcal{O}(\varepsilon^2)$ in the gyrokinetic ordering. Assuming a time independent equilibrium distribution F_0 with gradients that scale as $1/L$, only two first order terms remain. These terms represent free streaming along the equilibrium field, and the lowest order mirror force. To first order, the equation can be written:

$$B\nabla_{\|}F_0 v_{\|} - \mu B^2 \frac{\partial F_0}{\partial v_{\|}}\nabla_{\|}\ln B = 0, \tag{3.27}$$

a condition which is satisfied exactly by the equilibrium Maxwellian

$$F_0 = F_M = \frac{n_0}{(2\pi v_t^2)^{3/2}} e^{-v_{\|}^2/2v_t^2 - \mu B/v_t^2}.$$

This leaves only second order terms in the equation.

We furthermore divide the first order distribution F_1 into two parts, $F_1 \doteq \tilde{f} + F_{1nc}$. Here F_{1nc} is defined to be an equilibrium part of the distribution with no time dependence and gradients which scale as $1/L$. It is further defined to be an exact solution of the equation:

$$B\nabla_{\|}F_{1nc}v_{\|} + \frac{1}{v_t^2} i\omega_d [F_0 B(v_{\|}^2 + \mu B)] - \mu B^2 \frac{\partial F_{1nc}}{\partial v_{\|}}\nabla_{\|}\ln B = 0. \tag{3.28}$$

Note that the F_{1nc} contribution to all other terms is $\mathcal{O}(\varepsilon^3)$ or higher and can be neglected. This removes all terms with no time dependence, and leaves us with an evolution equation for the fluctuating first order distribution $\tilde{f}$, containing only second order terms which are either linear or quadratic in the fluctuating quantities

$\tilde{f}$, ϕ, and $A_\parallel$:

$$\begin{aligned}\frac{\partial}{\partial t}\tilde{f}B &+ B\nabla_\parallel \tilde{f}v_\parallel + \mathbf{v}_\phi\cdot\nabla[(F_0+\tilde{f})BJ_0] - \mathbf{v}_{A_\parallel}\cdot\nabla[(F_0+\tilde{f})B\frac{v_\parallel}{c}J_0] \\ &+ 2F_0BJ_0 i\omega_d\frac{e\phi}{T} - F_0B\frac{v_\parallel}{c}J_0 i\omega_d\frac{eA_\parallel}{T} + F_0BJ_1\frac{\alpha}{2}i\omega_d\frac{e\phi}{T} \\ &- F_0B\frac{v_\parallel}{c}J_1\frac{\alpha}{2}i\omega_d\frac{eA_\parallel}{T} + \frac{i\omega_d}{v_t^2}[\tilde{f}B(v_\parallel^2+\mu B)] - \frac{e}{mc}\frac{\partial F_0}{\partial v_\parallel}BJ_0\frac{\partial A_\parallel}{\partial t} \\ &- \frac{e}{m}\nabla_\parallel(\frac{\partial F_0}{\partial v_\parallel}BJ_0\phi) + \frac{e}{m}J_0\phi\frac{\partial F_0}{\partial v_\parallel}B(1-\frac{\mu B}{v_t^2})\nabla_\parallel \ln B \\ &+ \frac{e}{m}\frac{\partial F_0}{\partial v_\parallel}J_{0A_\parallel}J_{0\phi}(\hat{\mathbf{b}}\times\nabla A_\parallel)\cdot\nabla\phi - \mu B^2\frac{\partial \tilde{f}}{\partial v_\parallel}\nabla_\parallel \ln B \\ &- \frac{\partial F_0}{\partial v_\parallel}BJ_0\frac{\mu B}{c}i\omega_d\frac{eA_\parallel}{T} - \frac{\partial}{\partial v_\parallel}(F_0BJ_0v_\parallel)i\omega_d\frac{e\phi}{T} = 0.\end{aligned} \tag{3.29}$$

Terms containing ϕ and $A_\parallel$ have been separated by defining $\mathbf{v}_\phi = \frac{c}{B}\hat{\mathbf{b}}\times\nabla\phi$ and $\mathbf{v}_{A_\parallel} = \frac{c}{B}\hat{\mathbf{b}}\times\nabla A_\parallel$. Nonlinear terms enter through $\mathbf{v}_\phi\cdot\nabla[\tilde{f}BJ_0]$, $\mathbf{v}_{A_\parallel}\cdot\nabla[\tilde{f}B\frac{v_\parallel}{c}J_0]$, and $\frac{e}{m}\frac{\partial F_0}{\partial v_\parallel}J_{0A_\parallel}J_{0\phi}(\hat{\mathbf{b}}\times\nabla A_\parallel)\cdot\nabla\phi$.

It is also possible to derive Eq. 3.29 starting with the conservative form of the gyrokinetic equation. Making sure to include the second order part of $\langle\delta\mathbf{B}_\perp\rangle$ from Eq. 3.9, it is possible to prove Liouville's theorem,[5]

$$\frac{\partial B^*}{\partial t} + \nabla\cdot[B^*\dot{\mathbf{X}}] + \frac{\partial}{\partial v_\parallel}[B^*\dot{v}_\parallel] = 0, \tag{3.30}$$

where $B^* = B + (mc/e)v_\parallel\hat{\mathbf{b}}\cdot\nabla\times\hat{\mathbf{b}}$ contains the parallel velocity correction. The gyrokinetic equation can then be written:

$$\frac{\partial}{\partial t}FB^* + \nabla\cdot[FB^*\dot{\mathbf{X}}] + \frac{\partial}{\partial v_\parallel}[FB^*\dot{v}_\parallel] = 0. \tag{3.31}$$

Again working within the context of the low β approximation $\hat{\mathbf{b}}\times(\hat{\mathbf{b}}\cdot\nabla\hat{\mathbf{b}}) = (1/B^2)\mathbf{B}\times\nabla B$, and rearranging terms, one finds Eq. 3.29 to second order as expected.

A further check on Eq. 3.29 is to calculate the linear non-adiabatic response

---

[5] to the required order, $\mathcal{O}(\varepsilon^3)$

in the local limit. Dividing the distribution into adiabatic and non-adiabatic pieces, $\tilde{f} = g - F_0 J_0 e\phi/T_0$, linearizing, transforming, and taking the $\nabla_\parallel \ln B = 0$ limit, we find the expected non-adiabatic distribution:

$$g = F_0 \frac{\omega - \omega_*^T}{\omega - k_\parallel v_\parallel - \omega_{dv}} \frac{e}{T} J_0(\phi - \frac{v_\parallel}{c} A_\parallel), \tag{3.32}$$

where $\omega_*^T = \omega_*[1 + \eta(v_\parallel^2/2v_t^2 + \mu B/v_t^2 - 3/2)]$, $\omega_{dv} = \omega_d(v_\parallel^2 + \mu B)/v_t^2$, and we have introduced the diamagnetic frequency $i\omega_* \doteq -(cT_0/eBn_0)\nabla n_0 \cdot \hat{\mathbf{b}} \times \nabla$, and the ratio of scale lengths $\eta = L_n/L_T$.

3.2.1 The Ion Moment Equations

Ion fluid equations can now be derived by taking velocity space moments of Eq. 3.29. In this section a careful distinction is made between equilibrium and fluctuating components, and equilibrium quantities are written with a subscript 0. Both $v_t = \sqrt{T_0/m}$ and $\rho_i = v_t/\Omega$ are defined in terms of equilibrium quantities. It should also be noted that because all terms in Eq. 3.29 are $\mathcal{O}(\varepsilon^2)$, only their lowest order components need be kept, eg. $T \to T_0$.

Velocity space moments are often defined in terms of the total distribution function F. Here we again separate F into equilibrium and fluctuating components $F = F_0 + \tilde{f}$.[6] Velocity space moments of

$$F_0 = F_M = \frac{n_0}{(2\pi v_t^2)^{3/2}} e^{-v_\parallel^2/2v_t^2 - \mu B/v_t^2}$$

are all well defined. We define the following moments of the fluctuating distribution:

$$\begin{aligned}
\tilde{n} &= \int \tilde{f}\, d^3v & n_0\tilde{u}_\parallel &= \int \tilde{f} v_\parallel\, d^3v \\
\tilde{p}_\parallel &= m \int \tilde{f} v_\parallel^2\, d^3v & \tilde{p}_\perp &= m \int \tilde{f} B\mu\, d^3v \\
\tilde{q}_\parallel &= -3mv_t^2 n_0 \tilde{u}_\parallel + m\int \tilde{f} v_\parallel^3\, d^3v & \tilde{q}_\perp &= -mv_t^2 n_0\tilde{u}_\parallel + m\int \tilde{f} B\mu\, v_\parallel\, d^3v \\
\tilde{r}_{\parallel,\parallel} &= m\int \tilde{f} v_\parallel^4\, d^3v & \tilde{r}_{\parallel,\perp} &= m\int \tilde{f} B\mu\, v_\parallel^2\, d^3v \\
\tilde{r}_{\perp,\perp} &= m\int \tilde{f} B^2\mu^2\, d^3v & \tilde{s}_{\perp,\perp} &= -2mv_t^4 n_0\tilde{u}_\parallel + m\int \tilde{f} B^2\mu^2 v_\parallel\, d^3v \\
\tilde{s}_{\parallel,\parallel} &= -15mv_t^4 n_0\tilde{u}_\parallel + m\int \tilde{f} v_\parallel^5\, d^3v & \tilde{s}_{\parallel,\perp} &= -3mv_t^4 n_0\tilde{u}_\parallel + m\int \tilde{f} B\mu\, v_\parallel^3\, d^3v,
\end{aligned}$$

---

[6] F_{1nc} and its moments do not enter the equations and can be neglected.

where $d^3v = 2\pi dv_\parallel\, B\, d\mu$. The modifications to the q and s moments above have been chosen for consistency of notation with [Beer 1995], in which the first order fluctuating moments are defined to have components due both to $\tilde{f}$ and to factors of $\tilde{u}_\parallel$ multiplying F_0.

We can now proceed to take moments of Eq. 3.29. Each moment is coupled to higher moments through the terms which contain factors of $v_\parallel$ or μ, including terms due to parallel free streaming, toroidal drift, FLR effects, and the mirror force. This moment hierarchy is truncated using closures described in the following sections in order to generate a useful set of equations.

Taking integrals of Eq. 3.29 of the form $2\pi \int dv_\parallel\, d\mu\, v_\parallel^j \mu^k$, and defining the shorthand $\langle A\rangle \doteq 2\pi \int A dv_\parallel\, B d\mu$ yields the following set of moment equations:

$$\begin{aligned} \frac{\partial \tilde{n}}{\partial t} &+ B\nabla_\parallel \frac{n_0 \tilde{u}_\parallel}{B} + \mathbf{v}_\phi \cdot \nabla \langle F J_0\rangle - \frac{1}{c}\mathbf{v}_{A_\parallel}\cdot \langle F v_\parallel J_0\rangle \\ &+ \left\langle F_0(2J_0 + J_1\frac{\alpha}{2})\right\rangle i\omega_d \frac{e\phi}{T_0} + \frac{1}{T_0} i\omega_d(\tilde{p}_\parallel + \tilde{p}_\perp) = 0, \end{aligned} \tag{3.33}$$

$$\begin{aligned} n_0\frac{\partial \tilde{u}_\parallel}{\partial t} &+ B\nabla_\parallel \frac{\tilde{p}_\parallel}{mB} + \mathbf{v}_\phi \cdot \nabla \langle F v_\parallel J_0\rangle - \frac{1}{c}\mathbf{v}_{A_\parallel}\cdot \nabla \left\langle F v_\parallel^2 J_0\right\rangle \\ &- \left\langle F_0 v_\parallel^2 (J_0 + J_1\frac{\alpha}{2})\right\rangle i\omega_d \frac{eA_\parallel}{cT_0} + \frac{1}{T_0} i\omega_d(\tilde{q}_\parallel + \tilde{q}_\perp + 4p_0\tilde{u}_\parallel) \\ &+ \langle F_0 J_0\rangle \frac{e}{mc}\frac{\partial A_\parallel}{\partial t} + \frac{e}{m}\nabla_\parallel \langle F_0 J_0\rangle \phi - \frac{e}{m}\phi \left\langle F_0 J_0 (1 - \frac{\mu B}{v_t^2})\right\rangle \nabla_\parallel \ln B \\ &- \frac{e}{mB}\left\langle F_0 J_{0A_\parallel} J_{0\phi}\right\rangle \hat{\mathbf{b}}\times\nabla A_\parallel \cdot \nabla\phi + \frac{\tilde{p}_\perp}{m}\nabla_\parallel \ln B + \langle F_0 \mu B J_0\rangle i\omega_d \frac{eA_\parallel}{cT_0} = 0, \end{aligned} \tag{3.34}$$

$$\begin{aligned} \frac{\partial \tilde{p}_\parallel}{\partial t} &+ B\nabla_\parallel \frac{\tilde{q}_\parallel + 3p_0\tilde{u}_\parallel}{B} + m\mathbf{v}_\phi \cdot \nabla \left\langle F v_\parallel^2 J_0\right\rangle \\ &- \frac{m}{c}\mathbf{v}_{A_\parallel}\cdot \nabla \left\langle F v_\parallel^3 J_0\right\rangle + m\left\langle F_0 v_\parallel^2 (2J_0 + J_1\frac{\alpha}{2})\right\rangle i\omega_d \frac{e\phi}{T_0} \\ &+ \frac{1}{v_t^2} i\omega_d(\tilde{r}_{\parallel,\parallel} + \tilde{r}_{\parallel,\perp}) + 2(\tilde{q}_\perp + p_0\tilde{u}_\parallel)\nabla_\parallel \ln B + 2m\left\langle F_0 v_\parallel^2 J_0\right\rangle i\omega_d \frac{e\phi}{T_0} = 0, \end{aligned} \tag{3.35}$$

$$\begin{aligned}\frac{\partial \tilde{p}_\perp}{\partial t} &+ B^2\nabla_\parallel\left[\frac{1}{B^2}(\tilde{q}_\perp + p_0\tilde{u}_\parallel)\right] + mB\mathbf{v}_\phi\cdot\nabla\left\langle F\mu J_0\right\rangle \\ &- \frac{mB}{c}\mathbf{v}_{A_\parallel}\cdot\nabla\left\langle F\mu v_\parallel J_0\right\rangle + mB\left\langle F_0\mu(2J_0 + J_1\frac{\alpha}{2})\right\rangle i\omega_d\frac{e\phi}{T_0} \\ &+ \frac{1}{v_t^2}i\omega_d(\tilde{r}_{\parallel,\perp} + \tilde{r}_{\perp,\perp}) = 0,\end{aligned} \tag{3.36}$$

$$\begin{aligned}\frac{\partial}{\partial t}(\tilde{q}_\parallel + 3p_0\tilde{u}_\parallel) &+ B\nabla_\parallel\frac{\tilde{r}_{\parallel,\parallel}}{B} + m\mathbf{v}_\phi\cdot\nabla\left\langle F v_\parallel^3 J_0\right\rangle \\ &- \frac{m}{c}\mathbf{v}_{A_\parallel}\cdot\nabla\left\langle F v_\parallel^4 J_0\right\rangle - m\left\langle F_0 v_\parallel^4(J_0 + J_1\frac{\alpha}{2})\right\rangle i\omega_d\frac{eA_\parallel}{cT_0} \\ &+ \frac{1}{v_t^2}i\omega_d(\tilde{s}_{\parallel,\parallel} + \tilde{s}_{\parallel,\perp} + 18mv_t^4 n_0\tilde{u}_\parallel) + \frac{3e}{c}\left\langle F_0 v_\parallel^2 J_0\right\rangle\frac{\partial A_\parallel}{\partial t} \\ &+ 3e\nabla_\parallel\left\langle F_0 v_\parallel^2 J_0\right\rangle\phi - 3e\left\langle F_0 v_\parallel^2(1 - \frac{\mu B}{v_t^2})J_0\right\rangle\phi\nabla_\parallel\ln B \\ &- \frac{3e}{B}\left\langle F_0 v_\parallel^2 J_{0A_\parallel}J_{0\phi}\right\rangle\hat{\mathbf{b}}\times\nabla A_\parallel\cdot\nabla\phi + 3\tilde{r}_{\parallel,\perp}\nabla_\parallel\ln B \\ &+ 3mB\left\langle F_0\mu v_\parallel^2 J_0\right\rangle i\omega_d\frac{eA_\parallel}{cT} = 0,\end{aligned} \tag{3.37}$$

$$\begin{aligned}\frac{\partial}{\partial t}(\tilde{q}_\perp + p_0\tilde{u}_\parallel) &+ B^2\nabla_\parallel\frac{\tilde{r}_{\parallel,\perp}}{B^2} + mB\mathbf{v}_\phi\cdot\nabla\left\langle F v_\parallel\mu J_0\right\rangle \\ &- \frac{mB}{c}\mathbf{v}_{A_\parallel}\cdot\nabla\left\langle F v_\parallel^2\mu J_0\right\rangle - mB\left\langle F_0 v_\parallel^2\mu(J_0 + J_1\frac{\alpha}{2})\right\rangle i\omega_d\frac{eA_\parallel}{ct_0} \\ &+ \frac{1}{v_t^2}i\omega_d(\tilde{s}_{\parallel,\perp} + \tilde{s}_{\perp,\perp} + 5mv_t^4 n_0\tilde{u}_\parallel) + \frac{eB}{c}\left\langle F_0\mu J_0\right\rangle\frac{\partial A_\parallel}{\partial t} \\ &+ eB\nabla_\parallel\left\langle F_0\mu J_0\right\rangle\phi - eB\left\langle F_0\mu(1 - \frac{\mu B}{v_t^2})J_0\right\rangle\phi\nabla_\parallel\ln B \\ &- e\left\langle F_0\mu J_{0A_\parallel}J_{0\phi}\right\rangle\hat{\mathbf{b}}\times\nabla A_\parallel\cdot\nabla\phi + \tilde{r}_{\perp,\perp}\nabla_\parallel\ln B \\ &+ mB^2\left\langle F_0\mu^2 J_0\right\rangle i\omega_d\frac{eA_\parallel}{cT_0} = 0.\end{aligned} \tag{3.38}$$

3.2.2 Finite Larmor Radius Terms

Closures are developed for the finite Larmor radius terms appearing in Eqs. 3.33-3.38, using the techniques of [Dorland and Hammett 1993] as adapted to the toroidal case by [Beer 1995]. We note that we have chosen to evolve ion moments in guiding center space rather than real space in order to better describe both linear and nonlinear FLR effects, including the Bakshi-Linsker effect [Bakshi et al. 1977; Linsker 1981]. Nonetheless, our FLR terms, when expanded, contain higher velocity space moments and these must be carefully closed to properly model kinetic behavior.

Turning first to the Maxwellian FLR terms, we must close terms of the forms $\left\langle F_0 v_\parallel^{2i}\mu^j J_0\right\rangle$ and $\left\langle F_0 v_\parallel^{2i}\mu^j J_1\alpha\right\rangle$, where $i = 0, 1, 2$ and $j = 0, 1, 2$. Note that purely Maxwellian FLR terms with odd powers of $v_\parallel$ vanish identically, as F_M is even in $v_\parallel$, while J_0 and $J_1\alpha$ are independent of $v_\parallel$.

The FLR closures are chosen in careful consideration of the entire system of equations. It is the combination of J_0 terms from the $\mathbf{E}\times\mathbf{B}$ and $\mathbf{v}_{A_\parallel}$ terms with the J_0 terms in Poisson's equation and Ampere's Law which motivates the basic approximation $\langle J_0\rangle \approx \langle J_0^2\rangle^{1/2} \approx \Gamma_0(b)^{1/2}$, where $b = k_\perp^2\rho_i^2$. Following and extending [Dorland and Hammett 1993], we choose:

$$\langle F_0 J_0\rangle = n_0\Gamma_0^{1/2}, \tag{3.39}$$

$$\left\langle F_0 J_0 v_\parallel^2\right\rangle = n_0 v_t^2\Gamma_0^{1/2}, \tag{3.40}$$

$$\langle F_0 J_0 \mu\rangle = \frac{n_0 v_t^2}{B}\frac{\partial}{\partial b}(b\Gamma_0^{1/2}) = \frac{v_t^2}{2B}(2\Gamma_0^{1/2} + \hat{\nabla}_\perp^2) \tag{3.41}$$

$$\left\langle F_0 J_0 v_\parallel^4\right\rangle = 3n_0 v_t^4\Gamma_0^{1/2}, \tag{3.42}$$

$$\left\langle F_0 J_0 v_\parallel^2\mu\right\rangle = \frac{n_0 v_t^4}{B}\frac{\partial}{\partial b}(b\Gamma_0^{1/2}) = \frac{v_t^4}{2B}(2\Gamma_0^{1/2} + \hat{\nabla}_\perp^2), \tag{3.43}$$

$$\left\langle F_0 J_0 \mu^2\right\rangle \approx \frac{v_t^4}{B^2}\left[b\frac{\partial^2}{\partial b^2}(b\Gamma_0^{1/2}) + 2b\frac{\partial}{\partial b}(b\Gamma_0^{1/2})\right] = \frac{v_t^4}{B^2}\left(2\Gamma_0^{1/2} + \hat{\nabla}_\perp^2 + \hat{\hat{\nabla}}_\perp^2\right). \tag{3.44}$$

The modified Laplacian operators $\hat{\nabla}_\perp^2$ and $\hat{\hat{\nabla}}_\perp^2$ are defined as follows:

$$\frac{1}{2}\hat{\nabla}_\perp^2\Phi = b\frac{\partial\Gamma_0^{1/2}}{\partial b}\phi, \tag{3.45}$$

$$\hat{\hat{\nabla}}_\perp^2\Phi = b\frac{\partial^2}{\partial b^2}(b\Gamma_0^{1/2})\phi, \tag{3.46}$$

where the notation $\Phi = \Gamma_0^{1/2}\phi$ has been introduced for the gyroaveraged electrostatic potential. The analogous notation $\mathcal{A}_\parallel = \Gamma_0^{1/2}A_\parallel$ is used for the gyroaveraged magnetic potential.

The J_1 terms can be evaluated following [Beer 1995], using the following trick:

$$\langle FJ_1\alpha\rangle \approx -\left.\frac{\partial}{\partial\zeta}\right|_{\zeta=1}\langle FJ_0(\zeta\alpha)\rangle\,. \tag{3.47}$$

Again using $\langle FJ_0\rangle \approx \Gamma_0^{1/2}$ yields:

$$\langle F_0J_1\alpha\rangle \approx -\left.\frac{\partial}{\partial\zeta}\right|_{\zeta=1}\Gamma_0^{1/2}(\zeta^2 b) = -2b\frac{\partial\Gamma_0^{1/2}}{\partial b} = -\hat{\nabla}_\perp^2, \tag{3.48}$$

$$\left\langle F_0J_1v_\parallel^2\alpha\right\rangle \approx -2v_t^2 b\frac{\partial\Gamma_0^{1/2}}{\partial b} = -v_t^2\hat{\nabla}_\perp^2, \tag{3.49}$$

$$\langle F_0J_1\mu\alpha\rangle \approx -\left.\frac{\partial}{\partial\zeta}\right|_{\zeta=1}\frac{v_t^2}{B}\frac{\partial}{\partial T_\perp}\left(T_\perp\langle F_0J_0(\zeta\alpha)\rangle\right) = -2\frac{v_t^2}{B}\frac{\partial}{\partial b}\left(b^2\frac{\partial\Gamma_0^{1/2}}{\partial b}\right) = -2\frac{v_t^2}{B}\hat{\hat{\nabla}}_\perp^2, \tag{3.50}$$

$$\left\langle F_0J_1v_\parallel^4\alpha\right\rangle \approx -6v_t^4 b\frac{\partial\Gamma_0^{1/2}}{\partial b} = -3v_t^4\hat{\nabla}_\perp^2, \tag{3.51}$$

$$\left\langle F_0J_1v_\parallel^2\mu\alpha\right\rangle \approx= -2\frac{v_t^4}{B}\hat{\hat{\nabla}}_\perp^2, \tag{3.52}$$

The Maxwellian terms which contain more than one factor of J_0 are closed analogously:

$$\left\langle F_0 J_{0A_\parallel} J_{0\phi} \right\rangle = n_0 \Gamma_{0A_\parallel}^{1/2} \Gamma_{0\phi}^{1/2}, \tag{3.53}$$

$$\left\langle F_0 v_\parallel^2 J_{0A_\parallel} J_{0\phi} \right\rangle = n_0 v_t^2 \Gamma_{0A_\parallel}^{1/2} \Gamma_{0\phi}^{1/2}, \tag{3.54}$$

$$\left\langle F_0 \mu J_{0A_\parallel} J_{0\phi} \right\rangle = \frac{v_t^2}{2B} [(2\Gamma_0^{1/2} + \hat{\nabla}_\perp^2)_{A_\parallel} + (2\Gamma_0^{1/2} + \hat{\nabla}_\perp^2)_\phi], \tag{3.55}$$

where the subscript ϕ or $A_\parallel$ again designates the field on which the operator acts. These closures can be thought of in terms of separate expansions of the two Bessel function operators, through first order in b, so that no cross term enters.

Turning now to the $\mathbf{v}_\phi \cdot \nabla \langle F J_0 \ldots \rangle$ and $\mathbf{v}_{A_\parallel} \cdot \nabla \langle F J_0 \ldots \rangle$ terms, we note that there are two additional complications. These terms contain both the Maxwellian and the perturbed distribution, and the gyroaveraging terms are acted on by a perpendicular gradient operator, requiring that gradients of both fluctuating and equilibrium quantities be kept. In considering these terms, we redefine $b \doteq \frac{1}{\Omega}\sqrt{\frac{T_\perp}{m}}$, in terms of the total perpendicular temperature $T_\perp$, which contains both an equilibrium part (T_0, as the equilibrium is assumed isotropic) and a fluctuating part, $\tilde{T}_\perp = (\tilde{p}_\perp - T_0 \tilde{n})/n_0$. The gradient of b is then calculated as follows:

$$\nabla b = \frac{b}{T_0}(\nabla T_0 + \nabla \tilde{T}_\perp) - \frac{2b}{B}\nabla B. \tag{3.56}$$

Closing these FLR terms analogously to Eqs. 3.39-3.44 leads to, for example:

$$\mathbf{v}_\phi \cdot \nabla \langle J_0 F \rangle = \mathbf{v}_\phi \cdot \nabla (n \Gamma_0^{1/2}(b)), \tag{3.57}$$

where n is the total density, $n_0 + \tilde{n}$. Introducing the diamagnetic frequency $i\omega_* \doteq -(cT_0/eBn_0)\nabla n_0 \cdot \hat{\mathbf{b}} \times \nabla$, and ratio $\eta_i = L_n/L_T$, where L_T is the scale length of the equilibrium temperature, this leads to three linear terms:

$$\mathbf{v}_\phi \cdot \nabla \left\langle J_0 F \right\rangle = -n_0 i\omega_* \Gamma_0^{1/2} \frac{e\phi}{T_0} - \frac{n_0}{2}\eta_i \hat{\nabla}_\perp^2 i\omega_* \frac{e\Phi}{T_0} + n_0 \hat{\nabla}_\perp^2 i\omega_d \frac{e\phi}{T_0} + NL. \tag{3.58}$$

Nonlinear terms arise both from $\tilde{n}$ and b, and can be written:

$$NL = \mathbf{v}_\Phi \cdot \nabla\tilde{n} + \frac{n_0}{2T_0}[\hat{\nabla}_\perp^2 \mathbf{v}_\Phi] \cdot \nabla\tilde{T}_\perp. \tag{3.59}$$

To account for the $\mathbf{v}_{A_\parallel} \cdot \nabla$ and $\mathbf{v}_\phi \cdot \nabla$ terms with higher powers of $v_\parallel$ and μ, we note that the linear terms from Eq. 3.58 can be generalized as follows:

$$\mathbf{v}_\phi \cdot \nabla n_0 g(b) = -n_0 g(b) i\omega_* \frac{e\phi}{T_0} - n_0 \eta_i b \frac{\partial g}{\partial b} i\omega_* \frac{e\phi}{T_0} + 2n_0 b \frac{\partial g}{\partial b} i\omega_d \frac{e\phi}{T_0}. \tag{3.60}$$

The treatment of the nonlinear terms is somewhat more subtle, as these can involve higher moments which are not evolved. Following [Dorland and Hammett 1993], and introducing the notation $NL(x)$ for the nonlinear terms generated by $\mathbf{v}_\phi \cdot \nabla \left\langle F J_0 x \right\rangle$:

$$NL(v_\parallel) = \mathbf{v}_\Phi \cdot \nabla\tilde{n} + \frac{1}{2T_0}[\hat{\nabla}_\perp^2 \mathbf{v}_\Phi] \cdot \nabla\tilde{q}_\perp, \tag{3.61}$$

$$NL(v_\parallel^2) = \mathbf{v}_\Phi \cdot \nabla\tilde{p}_\parallel + \frac{n_0}{2}[\hat{\nabla}_\perp^2 \mathbf{v}_\Phi] \cdot \nabla\tilde{T}_\perp, \tag{3.62}$$

$$NL(\mu) = \mathbf{v}_\Phi \cdot \nabla\tilde{p}_\perp + \frac{1}{2}[\hat{\nabla}_\perp^2 \mathbf{v}_\Phi] \cdot \nabla\tilde{q}_\perp, \tag{3.63}$$

$$NL(v_\parallel^3) = \mathbf{v}_\Phi \cdot \nabla\tilde{q}_\parallel + 3p_0 \mathbf{v}_\Phi \cdot \nabla\tilde{u}_\parallel + \frac{3}{2}[\hat{\nabla}_\perp^2 \mathbf{v}_\Phi] \cdot \nabla\tilde{q}_\perp, \tag{3.64}$$

$$\begin{aligned} NL(v_\parallel \mu) &= \mathbf{v}_\Phi \cdot \nabla\tilde{q}_\perp + p_0 \mathbf{v}_\Phi \cdot \nabla\tilde{u}_\parallel + \frac{p_0}{2}[\hat{\nabla}_\perp^2 \mathbf{v}_\Phi] \cdot \nabla\tilde{u}_\parallel \\ &+ \frac{1}{2}[\hat{\nabla}_\perp^2 \mathbf{v}_\Phi] \cdot \nabla\tilde{q}_\perp + [\hat{\hat{\nabla}}{}_\perp^2 \mathbf{v}_\Phi] \cdot \nabla\tilde{q}_\perp. \end{aligned} \tag{3.65}$$

The $\mathbf{v}_{\mathcal{A}} \cdot \nabla \ldots$ nonlinear terms are closed identically to the above with the substitution $\Phi \to \mathcal{A}_\parallel$. However, the $\mathbf{v}_{\mathcal{A}} \cdot \nabla \ldots$ terms in the $\tilde{q}_\parallel$ and $\tilde{q}_\perp$ equations contain higher moments which are closed using results from the next section.

To simplify the equations, we introduce the following normalization. Time, parallel lengths, and perpendicular lengths are normalized to v_t/L_n, L_n and ρ_i respectively:

$$(\hat{t}, \hat{k}_\parallel, \hat{k}_\perp) = (\frac{t v_t}{L_n}, k_\parallel L_n, k_\perp \rho_i), \tag{3.66}$$

and the fluctuating quantities are normalized as follows:

$$(\hat{\phi}, \hat{A}_\parallel, \hat{n}, \hat{u}, \hat{p}, \hat{q}, \hat{r}, \hat{s}) = \frac{L_n}{\rho_i}(\frac{e\phi}{T_0}, \frac{A_\parallel}{\rho_i B}, \frac{\tilde{n}}{n_0}, \frac{\tilde{u}}{v_t}, \frac{\tilde{p}}{n_0 m v_t^2}, \frac{\tilde{q}}{n_0 m v_t^3}, \frac{\tilde{r}}{n_0 m v_t^4}, \frac{\tilde{s}}{n_0 m v_t^5}). \tag{3.67}$$

Normalized quantities appear on the left. The caret designating a normalized quantity is dropped for simplicity of notation. Note that these normalizations mesh with the gyrokinetic ordering such that all characteristic drift scales are $\mathcal{O}(1)$. Because β is formally taken to be $\mathcal{O}(1)$, all shear Alfvén scales are $\mathcal{O}(1)$ as well.

With the above normalization, and the FLR closures discussed above, the gyrofluid equations can be written:

$$\begin{aligned}\frac{dn}{dt} &+ B\tilde{\nabla}_\parallel \frac{u_\parallel}{B} + [\frac{1}{2}\hat{\nabla}_\perp^2 \mathbf{v}_\Phi] \cdot \nabla T_\perp - [\frac{1}{2}\hat{\nabla}_\perp^2 \mathbf{v}_{\mathcal{A}}] \cdot \nabla q_\perp \\ &- \left(1 + \frac{\eta_i}{2}\hat{\nabla}_\perp^2\right) i\omega_* \Phi + \left(2 + \frac{1}{2}\hat{\nabla}_\perp^2\right) i\omega_d \Phi + i\omega_d (p_\parallel + p_\perp) = 0,\end{aligned} \tag{3.68}$$

$$\begin{aligned}\frac{du_\parallel}{dt} &+ B\tilde{\nabla}_\parallel \frac{p_\parallel}{B} + [\frac{1}{2}\hat{\nabla}_\perp^2 \mathbf{v}_\Phi] \cdot \nabla q_\perp - [\frac{1}{2}\hat{\nabla}_\perp^2 \mathbf{v}_{\mathcal{A}}] \cdot \nabla T_\perp + \frac{\partial \mathcal{A}_\parallel}{\partial t} + \tilde{\nabla}_\parallel \Phi \\ &+ \left(1 + \eta_i + \frac{\eta_i}{2}\hat{\nabla}_\perp^2\right) i\omega_* \mathcal{A}_\parallel + \left(p_\perp + \frac{1}{2}\hat{\nabla}_\perp^2 \Phi\right) \nabla_\parallel \ln B \\ &+ i\omega_d (q_\parallel + q_\perp + 4u_\parallel) = 0,\end{aligned} \tag{3.69}$$

$$
\begin{aligned}
\frac{dp_\parallel}{dt} &+ B\tilde{\nabla}_\parallel \frac{q_\parallel + 3u_\parallel}{B} + [\frac{1}{2}\hat{\nabla}_\perp^2 \mathbf{v}_\Phi]\cdot\nabla T_\perp + 2(q_\perp + u_\parallel)\nabla_\parallel \ln B \\
&- \left(1 + \eta_i + \frac{\eta_i}{2}\hat{\nabla}_\perp^2\right) i\omega_*\Phi + \left(4 + \frac{1}{2}\hat{\nabla}_\perp^2\right) i\omega_d\Phi + i\omega_d(r_{\parallel,\parallel} + r_{\parallel,\perp}) = 0,
\end{aligned}
\tag{3.70}
$$

$$
\begin{aligned}
\frac{dp_\perp}{dt} &+ B^2\tilde{\nabla}_\parallel \frac{q_\perp + u_\parallel}{B^2} + [\frac{1}{2}\hat{\nabla}_\perp^2 \mathbf{v}_\Phi]\cdot\nabla p_\perp + [\hat{\hat{\nabla}}_\perp^2 \mathbf{v}_\Phi]\cdot\nabla T_\perp \\
&- [\frac{1}{2}\hat{\nabla}_\perp^2 \mathbf{v}_\mathcal{A}]\cdot\nabla(q_\perp + u_\parallel) - \left[1 + \frac{1}{2}\hat{\nabla}_\perp^2 + \eta_i\left(1 + \frac{1}{2}\hat{\nabla}_\perp^2 + \hat{\hat{\nabla}}_\perp^2\right)\right] i\omega_*\Phi \\
&+ \left(3 + \frac{3}{2}\hat{\nabla}_\perp^2 + \hat{\hat{\nabla}}_\perp^2\right) i\omega_d\Phi + i\omega_d(r_{\parallel,\perp} + r_{\perp,\perp}) = 0,
\end{aligned}
\tag{3.71}
$$

$$
\begin{aligned}
\frac{dq_\parallel}{dt} &+ \tilde{\nabla}_\parallel(r_{\parallel,\parallel} - 3p_\parallel) + (-r_{\parallel,\parallel} + 3r_{\parallel,\perp} + 3p_\parallel - 3p_\perp)\nabla_\parallel \ln B \\
&+ 3\eta_i i\omega_*\mathcal{A}_\parallel + i\omega_d(s_{\parallel,\parallel} + s_{\parallel,\perp} - 3q_\parallel - 3q_\perp + 6u_\parallel) = 0,
\end{aligned}
\tag{3.72}
$$

$$
\begin{aligned}
\frac{dq_\perp}{dt} &+ \tilde{\nabla}_\parallel(r_{\parallel,\perp} - p_\parallel) + [\frac{1}{2}\hat{\nabla}_\perp^2 \mathbf{v}_\Phi]\cdot\nabla u_\parallel + [\hat{\hat{\nabla}}_\perp^2 \mathbf{v}_\Phi]\cdot\nabla q_\perp \\
&- [\hat{\hat{\nabla}}_\perp^2 - \frac{1}{2}\hat{\nabla}_\perp^2]\mathbf{v}_\mathcal{A}\cdot\nabla T_\perp + \left[\eta_i(1 + \hat{\hat{\nabla}}_\perp^2) + (1 + \eta_i)\frac{1}{2}\hat{\nabla}_\perp^2\right] i\omega_*\mathcal{A}_\parallel \\
&+ \frac{1}{2}\hat{\nabla}_\perp^2\left(\frac{d\mathcal{A}_\parallel}{dt} + \tilde{\nabla}_\parallel\Phi - i\omega_d\mathcal{A}_\parallel\right) + (-2r_{\parallel,\perp} + r_{\perp,\perp} + p_\parallel - p_\perp)\nabla_\parallel \ln B \\
&+ \left(\hat{\hat{\nabla}}_\perp^2\Phi - \frac{1}{2}\hat{\nabla}_\perp^2\Phi\right)\nabla_\parallel \ln B + i\omega_d(s_{\parallel,\perp} + s_{\perp,\perp} - q_\parallel - q_\perp + u_\parallel) = 0,
\end{aligned}
\tag{3.73}
$$

where we have introduced the notation $\frac{d}{dt} = \frac{\partial}{\partial t} + \mathbf{v}_\Phi\cdot\nabla$ and $\tilde{\nabla}_\parallel = \nabla_\parallel - \mathbf{v}_{A_\parallel}\cdot\nabla = \nabla_\parallel - \hat{\mathbf{b}}\times\nabla\mathcal{A}_\parallel\cdot\nabla$.

3.2.3 Closures

We must now introduce closures for the highest moments, r and s, in order to have a complete and useful set of gyrofluid equations. The terms requiring closure divide naturally into three categories, the parallel terms $\tilde{\nabla}_\parallel r_{\parallel,\parallel}$ and $\tilde{\nabla}_\parallel r_{\parallel,\perp}$, the toroidal terms $\omega_d(r_{\parallel,\parallel} + r_{\parallel,\perp})$, $\omega_d(r_{\parallel,\perp} + r_{\perp,\perp})$, $\omega_d(s_{\parallel,\parallel} + s_{\parallel,\perp})$, and $\omega_d(s_{\parallel,\perp} + s_{\perp,\perp})$, and the mirroring terms $r_{\parallel,\parallel}\nabla_\parallel \ln B$, $r_{\parallel,\perp}\nabla_\parallel \ln B$, and $r_{\perp,\perp}\nabla_\parallel \ln B$. Closely following the work of [Beer 1995], we separately treat each group of terms, making closure approximations that accurately model the physical processes that each set of terms represents.

Parallel Landau Closures

Closures which provide an accurate model of linear Landau damping are chosen for the parallel terms, $\tilde{\nabla}_\parallel r_{\parallel,\parallel}$ and $\tilde{\nabla}_\parallel r_{\parallel,\perp}$. Landau damping along the magnetic field occurs due to the velocity dependence of the $k_\parallel v_\parallel$ term in the kinetic equation. Components with different $k_\parallel$ stream along the field at different velocities, causing moments of F to phase mix away.

As an illustration, consider the one dimensional kinetic equation

$$\frac{\partial f}{\partial t} + v_\parallel \frac{\partial f}{\partial z} = \delta(t) f_0(z, v), \tag{3.74}$$

where f_0 provides the initial condition. The solution to this simple equation $f(z, v, t) = f_0(z - vt, v)H(t)$, provides Green's function which can be used to solve more general problems with additional source terms, such as the electric field $-(e/m)E_\parallel \frac{\partial F_M}{\partial v}$. Consider an initial condition with a small single harmonic perturbation $f_0 = (n_0 + n_1 e^{ikz})F_M(v)$. The general solution is just $(n_0 + n_1 e^{ik(z-vt)})$, which simply oscillates in time at $\omega = kv$ and does not damp. However, upon taking velocity space moments, the velocity integration introduces mixing of the phases as follows:

$$n(z, t) = \int f\, dv = n_0 + n_1 \frac{e^{ikz}}{\sqrt{2\pi v_t^2}} \int dv\, e^{-ikvt} e^{-v^2/(2v_t^2)}. \tag{3.75}$$

The perturbed density $n_1 = n_{1(t=0)} e^{-k^2 v_t^2 t^2/2}$ decays with a Gaussian time dependence. This decay due to linear Landau damping is not captured by a simple fluid model with a finite number of moments, and hence it must be accounted for in the fluid closure if it is to be included in a fluid model.

A method for deriving "Landau closures" which provide an accurate linear model of this effect has been developed by [Hammett and Perkins 1990;

Hammett et al. 1992; Beer 1995], and is closely followed here.

The introduction of electromagnetic effects does not significantly alter the process of deriving Landau closures. One simply writes response functions in terms of the total $E_\parallel$ rather than ϕ. In Appendix C, Landau closures are derived for the general electromagnetic case with both parallel and perpendicular magnetic fluctuations. Here we consider only perpendicular fluctuations, hence the magnitude of the fluctuating field $\tilde{B}$ is zero to first order in the perturbation. The general response functions are given in Sec. C.5.1 and closures are derived in Sec. C.5.2. Here we simply take the $B_1 = 0$ limit of the Sec. C.5.2 results, for the case in which the equilibrium distribution is isotropic. In this limit the result is identical to the earlier result of [Dorland 1993]:

$$r_{\parallel,\parallel} = 3(2p_\parallel - n) + c_\parallel T_\parallel - \sqrt{2} D_\parallel \frac{i|k_\parallel| q_\parallel}{k_\parallel} \tag{3.76}$$

$$r_{\parallel,\perp} = p_\parallel + p_\perp - n - \sqrt{2} D_\perp \frac{i|k_\parallel| q_\perp}{k_\parallel} \tag{3.77}$$

where $c_\parallel = (32 - 9\pi)/(3\pi - 8)$, $D_\parallel = 2\sqrt{\pi}/(3\pi - 8)$, and $D_\perp = \sqrt{\pi}/2$. This closure provides a good fit to the linear response functions, as shown in [Hammett and Perkins 1990; Hammett et al. 1993], as well as by the line labeled "4+2" in Figs. C.1 and C.2.

Because the dissipative part of the closure above (the $|k_\parallel|/k_\parallel$ terms) is written in terms of moments with no equilibrium component, the fluctuating field makes no contribution to the linear Landau closures. Hence the linear Landau closure is equally accurate in the electrostatic and electromagnetic cases. However there is an additional nonlinear Landau damping term due to $A_\parallel$ which is discussed in Sec. C.8. This and other nonlinear Landau damping mechanisms are not accounted for in the fluid closures given here.

Toroidal Closures

The velocity dependence of the ∇B and curvature drifts also introduces phase mixing. This process is modeled using the toroidal closures derived by [Beer 1995], including dissipative pieces proportional to $|\omega_d|/\omega_d$.

Beer's closures include both Maxwellian parts and dissipative pieces derived by careful fitting with all parts of the kinetic toroidal response function, and can be written in the following form:

$$r_{\parallel,\parallel} + r_{\parallel,\perp} = 7p_\parallel + p_\perp - 4n - 2i\frac{|\omega_d|}{\omega_d}(\nu_1 T_\parallel + \nu_2 T_\perp) \tag{3.78}$$

$$r_{\parallel,\perp} + r_{\perp,\perp} = p_\parallel + 5p_\perp - 3n - 2i\frac{|\omega_d|}{\omega_d}(\nu_3 T_\parallel + \nu_4 T_\perp) \tag{3.79}$$

$$s_{\parallel,\parallel} + s_{\parallel,\perp} = -i\frac{|\omega_d|}{\omega_d}(\nu_5 u_\parallel + \nu_6 q_\parallel + \nu_7 q_\perp) \tag{3.80}$$

$$s_{\parallel,\perp} + s_{\perp,\perp} = -i\frac{|\omega_d|}{\omega_d}(\nu_8 u_\parallel + \nu_9 q_\parallel + \nu_{10} q_\perp) \tag{3.81}$$

where the complex coefficients take the form $\nu = \nu_r + i\nu_i|\omega_d|/\omega_d$. The coefficients chosen are, in the form (ν_r, ν_i), $\nu_1 = (2.019, -1.620)$, $\nu_2 = (0.433, 1.018)$, $\nu_3 = (-0.256, 1.487)$, $\nu_4 = (-0.070, -1.382)$, $\nu_5 = (-8.927, 12.649)$, $\nu_6 = (8.094, 12.638)$, $\nu_7 = (13.720, 5.139)$, $\nu_8 = (3.368, -8.110)$, $\nu_9 = (1.974, -1.984)$, $\nu_{10} = (8.269, 2.06)$. As shown in Figs. 2.1 and 2.2 of [Beer 1995], these closures provide a good fit to the linear toroidal response functions, including a reasonable model of the toroidal branch cut at $\omega/\omega_d = -k_\parallel^2 v_t^2/4\omega_d^2$.

The issue of toroidal flow damping introduced by this closure is discussed briefly in Appendix A.

Mirroring closures

The mirroring terms $r_{\parallel,\parallel}\nabla_\parallel \ln B$, $r_{\parallel,\perp}\nabla_\parallel \ln B$, and $r_{\perp,\perp}\nabla_\parallel \ln B$ incorporate trapped ion effects and magnetic pumping. However, they do not introduce new dissipative processes and hence they are closed with simple Maxwellian closures, again following

[Beer 1995]:

$$r_{\parallel,\parallel} = 6p_{\parallel} - 3n, \tag{3.82}$$

$$r_{\parallel,\perp} = p_{\parallel} + p_{\perp} - n, \tag{3.83}$$

$$r_{\perp,\perp} = 4p_{\perp} - 2n. \tag{3.84}$$

Taken together, the closure approximations provide models of linear and nonlinear FLR effects, as well as parallel phase mixing, drift resonance, and trapped particle effects. The accuracy of these closures is tested extensively through linear benchmarks with kinetic theory given in Ch. 4. Note especially Figs. 4.6 and 4.8 in which the performance of the gyrofluid model with the closures given above can be compared to that of the MHD model with its simple collisional closures.

3.2.4 Ion Collisions

Ion-ion collisions are modeled with a simple particle, momentum and energy conserving BGK operator [Gross and Krook 1956]:

$$C(F_j) = -\sum_k \nu_{jk}(F_j - F_{Mjk}), \tag{3.85}$$

where j and k are species indices, and ν_{jk} is the collision rate of species j with species k. Collisions cause the distribution to relax to a shifted Maxwellian with the appropriate total (equilibrium+fluctuating) momentum and energy. Upon linearizing, the single species operator can be written:

$$C(F) = -\nu_{ii}\left\{F_1 - \left[n + u_{\parallel}\frac{v_{\parallel}}{v_t} + T\left(\frac{v^2}{2v_t^2} - \frac{3}{2}\right)\right]F_0\right\}, \tag{3.86}$$

where n, $u_{\parallel}$, and $T = (T_{\parallel} + 2T_{\perp})/3$ are normalized fluctuating moments, and $v^2 = v_{\parallel}^2 + 4B^2\mu^2$.

Ion-electron collisions are negligible due to the smallness of the electron-ion mass ratio. Electron-ion collisions are considered in Sec. 3.3.3.

3.2.5 Final Ion Gyrofluid Equations

Incorporating the parallel, toroidal, and mirror term closures defined above, and including moments of the ion-ion collision operator, the final set of single species electromagnetic ion gyrofluid equations can be written as follows:

$$\begin{aligned}\frac{dn}{dt} &+ B\tilde{\nabla}_\parallel \frac{u_\parallel}{B} + [\frac{1}{2}\hat{\nabla}_\perp^2 \mathbf{v}_\Phi] \cdot \nabla T_\perp - [\frac{1}{2}\hat{\nabla}_\perp^2 \mathbf{v}_{\mathcal{A}}] \cdot \nabla q_\perp \\ &- \left(1 + \frac{\eta_i}{2}\hat{\nabla}_\perp^2\right) i\omega_* \Phi + \left(2 + \frac{1}{2}\hat{\nabla}_\perp^2\right) i\omega_d \Phi + i\omega_d(p_\parallel + p_\perp) = 0\end{aligned} \tag{3.87}$$

$$\begin{aligned}\frac{du_\parallel}{dt} &+ B\tilde{\nabla}_\parallel \frac{p_\parallel}{B} + [\frac{1}{2}\hat{\nabla}_\perp^2 \mathbf{v}_\Phi] \cdot \nabla q_\perp - [\frac{1}{2}\hat{\nabla}_\perp^2 \mathbf{v}_{\mathcal{A}}] \cdot \nabla T_\perp + \frac{\partial \mathcal{A}_\parallel}{\partial t} + \tilde{\nabla}_\parallel \Phi \\ &+ \left(1 + \eta_i + \frac{\eta_i}{2}\hat{\nabla}_\perp^2\right) i\omega_* \mathcal{A}_\parallel + \left(p_\perp + \frac{1}{2}\hat{\nabla}_\perp^2 \Phi\right) \nabla_\parallel \ln B \\ &+ i\omega_d(q_\parallel + q_\perp + 4u_\parallel) = 0\end{aligned} \tag{3.88}$$

$$\begin{aligned}\frac{dp_\parallel}{dt} &+ B\tilde{\nabla}_\parallel \frac{q_\parallel + 3u_\parallel}{B} + [\frac{1}{2}\hat{\nabla}_\perp^2 \mathbf{v}_\Phi] \cdot \nabla T_\perp + 2(q_\perp + u_\parallel)\nabla_\parallel \ln B \\ &- \left(1 + \eta_i + \frac{\eta_i}{2}\hat{\nabla}_\perp^2\right) i\omega_* \Phi + \left(4 + \frac{1}{2}\hat{\nabla}_\perp^2\right) i\omega_d \Phi + i\omega_d(7p_\parallel + p_\perp - 4n) \\ &+ 2|\omega_d|(\nu_1 T_\parallel + \nu_2 T_\perp) = -\frac{2}{3}\nu_{ii}(p_\parallel - p_\perp)\end{aligned} \tag{3.89}$$

$$\begin{aligned}\frac{dp_\perp}{dt} &+ B^2\tilde{\nabla}_\parallel \frac{q_\perp + u_\parallel}{B^2} + [\frac{1}{2}\hat{\nabla}_\perp^2 \mathbf{v}_\Phi] \cdot \nabla p_\perp + [\hat{\hat{\nabla}}{}_\perp^2 \mathbf{v}_\Phi] \cdot \nabla T_\perp \\ &- [\frac{1}{2}\hat{\nabla}_\perp^2 \mathbf{v}_{\mathcal{A}}] \cdot \nabla(q_\perp + u_\parallel) - \left[1 + \frac{1}{2}\hat{\nabla}_\perp^2 + \eta_i \left(1 + \frac{1}{2}\hat{\nabla}_\perp^2 + \hat{\hat{\nabla}}{}_\perp^2\right)\right] i\omega_* \Phi \\ &+ \left(3 + \frac{3}{2}\hat{\nabla}_\perp^2 + \hat{\hat{\nabla}}{}_\perp^2\right) i\omega_d \Phi + i\omega_d(5p_\perp + p_\parallel - 3n) \\ &+ 2|\omega_d|(\nu_3 T_\parallel + \nu_4 T_\perp) = \frac{1}{3}\nu_{ii}(p_\parallel - p_\perp)\end{aligned} \tag{3.90}$$

$$
\begin{aligned}
\frac{dq_\parallel}{dt} &+ 3\tilde{\nabla}_\parallel T_\parallel + c_\parallel \nabla_\parallel T_\parallel + \sqrt{2} D_\parallel |k_\parallel| q_\parallel + i\omega_d(-3q_\parallel - 3q_\perp + 6u_\parallel) \\
&+ 3\eta_i i\omega_* \mathcal{A}_\parallel + |\omega_d|(\nu_5 u_\parallel + \nu_6 q_\parallel + \nu_7 q_\perp) = -\nu_{ii} q_\parallel
\end{aligned}
\tag{3.91}
$$

$$
\begin{aligned}
\frac{dq_\perp}{dt} &+ \tilde{\nabla}_\parallel T_\perp + \sqrt{2} D_\perp |k_\parallel| q_\perp + [\frac{1}{2}\hat{\nabla}_\perp^2 \mathbf{v}_\Phi] \cdot \nabla u_\parallel + [\hat{\hat{\nabla}}_\perp^2 \mathbf{v}_\Phi] \cdot \nabla q_\perp \\
&- [\hat{\hat{\nabla}}_\perp^2 - \frac{1}{2}\hat{\nabla}_\perp^2] \mathbf{v}_\mathcal{A} \cdot \nabla T_\perp + \left[\eta_i (1 + \hat{\hat{\nabla}}_\perp^2) + (1+\eta_i)\frac{1}{2}\hat{\nabla}_\perp^2\right] i\omega_* \mathcal{A}_\parallel \\
&+ \frac{1}{2}\hat{\nabla}_\perp^2 \left(\frac{d\mathcal{A}_\parallel}{dt} + \tilde{\nabla}_\parallel \Phi - i\omega_d \mathcal{A}_\parallel\right) + \left(p_\perp - p_\parallel + \hat{\hat{\nabla}}_\perp^2 \Phi - \frac{1}{2}\hat{\nabla}_\perp^2 \Phi\right) \nabla_\parallel \ln B \\
&+ i\omega_d(-q_\parallel - q_\perp + u_\parallel) + |\omega_d|(\nu_8 u_\parallel + \nu_9 q_\parallel + \nu_{10} q_\perp) = -\nu_{ii} q_\perp
\end{aligned}
\tag{3.92}
$$

3.2.6 The Multi-species Ion Equations

The derivation in the previous sections has focused on the single ion species case for simplicity. In general, tokamak plasmas may contain multiple ion species. In some cases, such as the deuterium-tritium plasmas used in fusion experiments, the bulk plasma may contain more than one dominant species. In addition, impurity ions are expected to play an important role, especially near the plasma edge.

The extension to multiple ion species is fairly straightforward. A separate set of gyrofluid equations must be solved for each species j, keeping in mind that charge e, mass m, and the equilibrium moments (n_0, T_0) and scale lengths are functions of the species j.

Each species is normalized to its own n_0, v_t etc., but one ion species is chosen as a reference. The reference species is designated with the subscript i, and the following dimensionless constants are introduced, $\tau_j = T_{0j}/T_{0i}$, $v_j = v_{tj}/v_{ti}$, and $\hat{\rho}_j = \rho_j/\rho_i$. Z is the ratio of the species charge to the unit charge, $Z = e_j/|e|$, and η_j is the usual ratio of scale lengths $\eta_j = L_{nj}/L_{Tj}$. The basic macroscopic length is taken to be the electron density scale length L_{ne}, and the following normalized scale length is defined for each ion species, $\hat{L}_{nj} = L_{nj}/L_{ne}$.

The multi-species equations can then been written as follows:

$$\begin{aligned}\frac{dn}{dt} &+ v_j B\tilde{\nabla}_{\parallel}\frac{u_{\parallel}}{B} + [\frac{1}{2}\hat{\nabla}_{\perp}^2\mathbf{v}_{\Phi}]\cdot\nabla T_{\perp} - [\frac{1}{2}\hat{\nabla}_{\perp}^2\mathbf{v}_{\mathcal{A}}]\cdot\nabla q_{\perp} \\ &- \left(1+\frac{\eta_j}{2}\hat{\rho}_j^2\hat{\nabla}_{\perp}^2\right)\frac{i\omega_*}{\hat{L}_{nj}}\Phi + \left(2+\frac{1}{2}\hat{\rho}_j^2\hat{\nabla}_{\perp}^2\right)i\omega_d\frac{\hat{\rho}_j v_j Z}{\tau_j}\Phi + i\omega_d\hat{\rho}_j v_j(p_{\parallel}+p_{\perp}) = 0,\end{aligned} \tag{3.93}$$

$$\begin{aligned}\frac{du_{\parallel}}{dt} &+ v_j B\tilde{\nabla}_{\parallel}\frac{p_{\parallel}}{B} + [\frac{1}{2}\hat{\nabla}_{\perp}^2\mathbf{v}_{\Phi}]\cdot\nabla q_{\perp} - [\frac{1}{2}\hat{\nabla}_{\perp}^2\mathbf{v}_{\mathcal{A}}]\cdot\nabla T_{\perp} + \frac{v_j Z}{\tau_j}\tilde{\nabla}_{\parallel}\Phi \\ &+ \frac{v_j Z}{\tau_j}\frac{\partial\mathcal{A}_{\parallel}}{\partial t} + \left(1+\eta_j(1+\frac{\hat{\rho}_j^2\hat{\nabla}_{\perp}^2}{2})\right)\frac{i\omega_*}{\hat{L}_{nj}}v_j\mathcal{A}_{\parallel} \\ &+ \left(p_{\perp}+\frac{Z}{\tau_j}\frac{\hat{\rho}_j^2\hat{\nabla}_{\perp}^2}{2}\Phi\right)v_j\nabla_{\parallel}\ln B + i\omega_d\hat{\rho}_j v_j(q_{\parallel}+q_{\perp}+4u_{\parallel}) = 0,\end{aligned} \tag{3.94}$$

$$\begin{aligned}\frac{dp_{\parallel}}{dt} &+ v_j B\tilde{\nabla}_{\parallel}\frac{q_{\parallel}+3u_{\parallel}}{B} + [\frac{1}{2}\hat{\nabla}_{\perp}^2\mathbf{v}_{\Phi}]\cdot\nabla T_{\perp} + 2v_j(q_{\perp}+u_{\parallel})\nabla_{\parallel}\ln B \\ &- \left(1+\eta_j(1+\frac{\hat{\rho}_j^2\hat{\nabla}_{\perp}^2}{2})\right)\frac{i\omega_*}{\hat{L}_{nj}}\Phi + \left(4+\frac{\hat{\rho}_j^2\hat{\nabla}_{\perp}^2}{2}\right)i\omega_d\frac{\hat{\rho}_j v_j Z}{\tau}\Phi \\ &+ i\omega_d\hat{\rho}_j v_j(7p_{\parallel}+p_{\perp}-4n) + 2|\omega_d|\hat{\rho}_j v_j(\nu_1 T_{\parallel}+\nu_2 T_{\perp}) = -\frac{2}{3}\nu_s(p_{\parallel}-p_{\perp}),\end{aligned} \tag{3.95}$$

$$\begin{aligned}\frac{dp_{\perp}}{dt} &+ v_j B^2\tilde{\nabla}_{\parallel}\frac{q_{\perp}+u_{\parallel}}{B^2} + [\frac{1}{2}\hat{\nabla}_{\perp}^2\mathbf{v}_{\Phi}]\cdot\nabla p_{\perp} + [\hat{\rho}_j^2\hat{\hat{\nabla}}_{\perp}^{2}\mathbf{v}_{\Phi}]\cdot\nabla T_{\perp} \\ &- [\frac{1}{2}\hat{\nabla}_{\perp}^2\mathbf{v}_{\mathcal{A}}]\cdot\nabla(q_{\perp}+u_{\parallel}) - \left[1+\frac{\hat{\rho}_j^2\hat{\nabla}_{\perp}^2}{2}+\eta_j\left(1+\frac{\hat{\rho}_j^2\hat{\nabla}_{\perp}^2}{2}+\hat{\rho}_j^2\hat{\hat{\nabla}}_{\perp}^{2}\right)\right]\frac{i\omega_*}{\hat{L}_{nj}}\Phi \\ &+ \left(3+\frac{3\hat{\rho}_j^2\hat{\nabla}_{\perp}^2}{2}+\hat{\rho}_j^2\hat{\hat{\nabla}}_{\perp}^{2}\right)i\omega_d\frac{\hat{\rho}_j v_j Z}{\tau_j}\Phi + i\omega_d\hat{\rho}_j v_j(5p_{\perp}+p_{\parallel}-3n) \\ &+ 2|\omega_d|\hat{\rho}_j v_j(\nu_3 T_{\parallel}+\nu_4 T_{\perp}) = \frac{1}{3}\nu_s(p_{\parallel}-p_{\perp}),\end{aligned} \tag{3.96}$$

$$\begin{aligned}\frac{dq_{\parallel}}{dt} &+ (3+c_{\parallel})v_j\tilde{\nabla}_{\parallel}T_{\parallel} + \sqrt{2}D_{\parallel}v_j|k_{\parallel}|q_{\parallel} + i\omega_d\hat{\rho}_j v_j(-3q_{\parallel}-3q_{\perp}+6u_{\parallel}) \\ &+ 3\eta_j\frac{i\omega_*}{\hat{L}_{nj}}v_j\mathcal{A}_{\parallel} + |\omega_d|\hat{\rho}_j v_j(\nu_5 u_{\parallel}+\nu_6 q_{\parallel}+\nu_7 q_{\perp}) = -\nu_s q_{\parallel},\end{aligned} \tag{3.97}$$

$$\begin{aligned}\frac{dq_\perp}{dt} &+ v_j\tilde{\nabla}_\parallel T_\perp + \sqrt{2}D_\perp v_j|k_\parallel|q_\perp + [\frac{1}{2}\hat{\nabla}^2_\perp \mathbf{v}_\Phi]\cdot\nabla u_\parallel + [\hat{\rho}_j^2\hat{\hat{\nabla}}^2_\perp \mathbf{v}_\Phi]\cdot\nabla q_\perp \\ &- \hat{\rho}_j^2\left[\hat{\hat{\nabla}}^2_\perp - \frac{1}{2}\hat{\nabla}^2_\perp\right]\mathbf{v}_\mathcal{A}\cdot\nabla T_\perp + \left[\eta_j(1+\hat{\rho}_j^2\hat{\hat{\nabla}}^2_\perp)(1+\eta_j)\frac{\hat{\rho}_j^2\hat{\nabla}^2_\perp}{2}\right]\frac{i\omega_*}{\hat{L}_{nj}}v_j\mathcal{A}_\parallel \\ &+ \frac{Zv_j}{\tau_j}\frac{\hat{\rho}_j^2\hat{\nabla}^2_\perp}{2}\left(\frac{d\mathcal{A}_\parallel}{dt} + \tilde{\nabla}_\parallel\Phi - i\omega_d\hat{\rho}_j v_j\mathcal{A}_\parallel\right) + i\omega_d\hat{\rho}_j v_j(-q_\parallel - q_\perp + u_\parallel) \\ &+ \left(p_\perp - p_\parallel + \frac{Z}{\tau_j}(\hat{\rho}_j^2\hat{\hat{\nabla}}^2_\perp\Phi - \frac{\hat{\rho}_j^2\hat{\nabla}^2_\perp}{2}\Phi)\right)v_j\nabla_\parallel \ln B \\ &+ |\omega_d|\hat{\rho}_j v_j(\nu_8 u_\parallel + \nu_9 q_\parallel + \nu_{10}q_\perp) = -\nu_s q_\perp. \end{aligned} \tag{3.98}$$

3.3 The Electron Landau Fluid Equations

For the electrons, a careful analytic expansion is constructed to allow a Landau fluid treatment. Electron dynamics on the characteristic ion and Alfvén scales are treated explicitly, while the fast electron transit time scale and the small spatial scales associated with the electron gyroradius and the electron skin depth are removed from the set of fluid equations to be solved numerically.

The electromagnetic electron Landau fluid equations include the effects of electron temperature and density gradients, electron $\mathbf{E}\times\mathbf{B}$ motion, Landau damping, electron-ion collisions, and the parallel electron currents which, along with parallel ion currents, give rise to the parallel magnetic potential. The equations given here focus on the dynamics of the passing electrons. Developing an electromagnetic model of trapped electron dynamics analogous to the electrostatic model of [Beer 1995] is left as an important piece of future work.

3.3.1 Analytic Expansion in the Electron Mass Ratio

Having undertaken the rather arduous task of deriving a set of electromagnetic multi-species ion gyrofluid equations, it is perhaps tempting to simply substitute the electron charge, mass, and equilibrium quantities into Eqs. 3.93-3.98 and consider oneself finished with the electrons. However, such an approach is numerically challenging, and may involve spending a large amount of computational power resolving scales that are unnecessary for an accurate description of Alfvén-ITG turbulence.[7] Here we invoke an analytic expansion in the electron/ion mass ratio, similar to the technique employed by [Kadomtsev and Pogutse 1985]. This expansion removes the small electron gyroradius scale and the fast electron transit time scale from the equations, leaving an efficient model appropriate for the study of turbulence on ion and Alfvén scales.

Electron FLR

Examining the gyrokinetic ordering given by Eq. 3.1, we first note that $k_\perp \rho_i$ is $\mathcal{O}(1)$. An analogous treatment of the electrons would take $k_\perp \rho_e \sim 1$. However, because of the large separation between ρ_e and ρ_i (by a factor of $\frac{1}{Z}\sqrt{\frac{T_{i0} m_i}{T_{e0} m_e}} \sim 60$ for a typical deuterium plasma), it is numerically quite challenging to fully resolve both scales in the same simulation. Furthermore, the focus of this work is on turbulence with perpendicular scales on the order of the ion gyroradius. Both experimental observations and theoretical considerations suggest that microturbulence with $k_\perp \rho_i \leq 1$ dominates turbulent transport in many cases.[8] Because we wish to resolve only scales on the order of the ion gyroradius or larger, it is unnecessary and computationally costly to evaluate the finite Larmor radius (J_0 and J_1) terms for the electrons.

For the above reasons, we employ a subsidiary formal ordering in the smallness of the electron/ion mass ratio in order to remove electron finite Larmor radius terms. The gyroaveraging operator J_0 can be expanded $1 + k_\perp^2 \rho_e^2 + \ldots$. Noting that, in the gyrokinetic ordering employed here, $k_\perp \rho_i \sim 1$, it is apparent that the first electron FLR term is $\mathcal{O}(m_e/m_i)$. Electron FLR terms are thus higher order in an expansion in m_e/m_i. We introduce the subsidiary ordering parameter $\delta \sim \sqrt{m_e/m_i}$ and note that electron FLR effects first enter at $\mathcal{O}(\delta^2)$. Hence it is possible to retain terms through $\mathcal{O}(\delta)$ without introducing electron FLR terms.

---

[7] Nonetheless, such an approach may prove quite useful for simulating faster and/or smaller scale turbulence such as that driven by the electron temperature gradient (ETG) mode.

[8] This is not to suggest that microturbulence on ρ_e scales does not exist or could not be important in some cases. Recent experimental observations in plasmas with ion transport barriers in fact suggest such electron scale turbulence may play a role. However, such electron scale turbulence requires a different modeling approach and is not considered here.

Electron Transit

The small electron mass also implies a fast electron thermal speed ($v_{te} \gg v_{ti}$), and rapid electron streaming along the magnetic field. The speed of this streaming motion along the field puts a constraint on the size of the time step which can be used in an explicit numerical simulation. Adding electron parallel dynamics to a simulation which previously modeled only ions reduces this time step constraint by a factor of $\sqrt{T_e m_i / T_i m_e} \sim 60$ for a deuterium fusion plasma. This is a very severe numerical burden, though perhaps one that it may be possible to contemplate bearing in the near future, as computational power continues to increase.

Here we again impose the mass ratio ordering $\sqrt{m_e/m_i} \sim \delta \ll 1$, allowing the fast electron transit motion to be analytically removed.

General Ordering

The use of the electron/ion mass ratio as an ordering parameter has a long history in plasma physics. It has been invoked in nearly all forms of the magnetohydrodynamic equations as well as in the more detailed equations of [KADOMTSEV and POGUTSE 1985], and in many other fluid and simplified kinetic formulations. In the context of gyrokinetics, the mass ratio expansion has generally been used to justify the neglect of electron FLR terms, and treatment of electron dynamics with the drift kinetic equation. However, the mass ratio ordering has often been neglected in the derivation of fluid equations from the drift kinetic equation. Here we wish to consistently apply the ordering $m_e/m_i \sim \mathcal{O}(\delta^2)$ to all terms in the drift fluid equations before relaxing this ordering to include additional physical effects in Sec. 3.3.3.

The fundamental assumption is that the fluctuating scales of interest are those typical of ion thermal, drift and gyro-motion, and those of Alfvén waves. Length and time scales associated with electron thermal and gyromotion are taken to be small.

For a typical perpendicular wavenumber $k_\perp$, we impose the following ordering:

$$k_\perp^{-1} \sim \rho_i \sim c/\omega_{pi} \gg \rho_e, c/\omega_{pe}, \tag{3.99}$$

where ω_p is the plasma frequency. The lengths on the left are independent of the electron mass, while the two lengths on the right are proportional to $\sqrt{m_e}$. Note that the skin depth c/ω_{pj} can be written as $\rho_j\sqrt{2/\beta_j}$ for the single species case, where the species $\beta_j = 8\pi n_{0j}T_{0j}/B^2$. Formally we take $\beta \sim \mathcal{O}(1)$, and then the above ordering of lengths follows directly from $\sqrt{m_e/m_i} \sim \mathcal{O}(\delta)$.

For a typical fluctuation frequency ω we choose the ordering:

$$\omega \sim k_\parallel v_{ti} \sim \omega_* \sim \omega_{Di} \sim \omega_{De} \sim k_\parallel c_s \sim k_\parallel v_A \ll k_\parallel v_{te} \sim \omega_{ETG}, \tag{3.100}$$

where ω_D is the curvature and ∇B drift frequency, $c_s = \sqrt{T_{0e}/m_i}$ is the cold ion sound speed, and $v_A = B/\sqrt{4\pi n_0 m_i}$ is the Alfvén speed. We define ω_{ETG} to be a frequency characteristic of the electron temperature gradient (ETG) mode. These short wavelength modes typically have $k_\theta \sim 1/\rho_e$, and hence $\omega_{ETG} \sim \sqrt{m_i/m_e}\,\omega_*$, where ω_* is the diamagnetic frequency taken with $k_\theta\rho_i \sim 1$. The quantities on the left are independent of m_e while those on the right are proportional to $m_e^{-1/2}$.

The desired time and length scale orderings above are both formally accomplished simply by taking $m_e/m_i \sim \mathcal{O}(\delta^2)$ and $\beta_j \sim \mathcal{O}(1)$. The constraints on the validity of this expansion are found through inspection of Eqs. 3.99 and 3.100. The separation of scales between the Alfvén frequency and the electron transit frequency (and equivalently between ρ_i and the electron skin depth) requires $\beta_e \gg 2m_e/m_i$. In fusion relevant plasmas, this condition is generally satisfied everywhere except very near the plasma edge. Another constraint is provided by the condition $\omega_* \ll k_\parallel v_{te}$. Using a typical ballooning $k_\parallel \approx 1/qR$, and $w_* \approx k_\theta\rho_i v_{ti}/L_n$, this requires $k_\theta\rho_i\sqrt{m_e/m_i} \ll L_n/qR$. For large $k_\theta\rho_i \approx 1$, this condition can break down in the extreme edge region where q is often large, while L_n can become rather short.

3.3.2 Derivation of the Electron Equations

The formal expansion in mass ratio can now be used to derive a set of equations which describe electron dynamics consistent with the time and space scale orderings described above.

It is critical to observe that the fluctuations we wish to evolve, including those in the electron moments $\tilde{n}_e$, $\tilde{u}_{\parallel e}$, $\tilde{p}_e$ etc., occur on the ion/Alfvén scales. Hence the fluctuating electron moments should be normalized to ion quantities v_{ti} and m_i, so that a consistent ordering is easily maintained.[9] We normalize the fluctuating electron moments as follows:

$$(\hat{n}_e, \hat{u}_e, \hat{p}_e, \hat{q}_e, \hat{r}_e, \hat{s}_e) = \frac{L_n}{\rho_i}(\frac{\tilde{n}_e}{n_0}, \frac{\tilde{u}_e}{v_{ti}}, \frac{\tilde{p}_e}{n_0 m_i v_{ti}^2}, \frac{\tilde{q}_e}{n_0 m_i v_{ti}^3}, \frac{\tilde{r}_e}{n_0 m_i v_{ti}^4}, \frac{\tilde{s}_e}{n_0 m_i v_{ti}^5}), \tag{3.101}$$

where the normalized quantities on the left are all $\mathcal{O}(1)$. In the general multiple ion species case, the quantities m_i and v_{ti} above refer to the reference ion species, as in Sec. 3.2.6.

This normalization is different than that employed in Sec. 3.2.6, where each species' moments are normalized to its own mass and thermal velocity. Hence we must revisit the unnormalized moment equations, and carefully implement the above electron moment normalization. Lengths, times, and the fields ϕ and $A_\parallel$ are normalized as in the ion equations. The unsubscripted normalized operators are again defined in terms of the $Z = 1$ ion charge (e), the reference ion species mass (m_i) and temperature (T_{0i}), and the equilibrium electron density (n_0) and density scale length (L_n):

$$i\hat{\omega}_* = -\frac{L_n}{v_{ti}}\frac{cT_{0i}}{eBn_0}\nabla n_0 \cdot \hat{\mathbf{b}} \times \nabla, \tag{3.102}$$

$$i\hat{\omega}_d = \frac{L_n}{v_{ti}}\frac{cT_{0i}}{eB^3}\mathbf{B} \times \nabla B \cdot \nabla. \tag{3.103}$$

---

[9] A normalization to Alfvén scales v_A and m_i, or the sound wave scales c_s and m_i would also be feasible.

The normalized electron operators are defined to be $\hat{\omega}_{*e} = \hat{\omega}_*/\tau$ and $\hat{\omega}_{de} = -\hat{\omega}_d/\tau$, where $\tau \doteq T_{0i}/T_{0e}$.

The normalized electron density equation becomes:

$$\frac{\partial n_e}{\partial t} + \mathbf{v}_E \cdot \nabla n_e + B\tilde{\nabla}_\parallel \frac{u_{\parallel e}}{B} - i\omega_*\phi + i\omega_d(2\phi - 2n_e/\tau - T_{\parallel e} - T_{\perp e}) = 0, \tag{3.104}$$

where the carets on normalized quantities have been dropped for conciseness of notation. The notation $\tilde{\nabla}_\parallel = \nabla_\parallel - \hat{\mathbf{b}} \times \nabla A_\parallel \cdot \nabla$ has been employed. Note that no factors of m_e appear in the above equation, and all terms are of the same order.

The momentum equation can be written:

$$\begin{aligned} \frac{m_e}{m_i}\frac{\partial u_{\parallel_e}}{\partial t} &+ \frac{m_e}{m_i}\mathbf{v}_E \cdot \nabla u_{\parallel_e} + B\tilde{\nabla}_\parallel \frac{p_{\parallel e}}{B} + (1+\eta_e) i\omega_* \frac{A_\parallel}{\tau} \qquad (3.105) \\ &+ \frac{m_e}{m_i} i\omega_d (q_{\parallel_e} + q_{\perp e} + 4u_{\parallel_e}/\tau) - \frac{\partial A_\parallel}{\partial t} - \tilde{\nabla}_\parallel \phi + p_{\perp e}\nabla_\parallel \ln B = 0. \end{aligned}$$

The electron momentum term, which is associated with the electron skin depth, and the curvature and ∇B drift terms are both small by a factor of $m_e/m_i \sim \delta^2$. Neglecting these higher order terms, and expanding the pressure, noting that $p_{\parallel_e} = T_{\parallel e} + n_e/\tau$ because of the normalization to ion temperature, the momentum equation can be recast as a time evolution equation for the magnetic potential:

$$\frac{\partial A_\parallel}{\partial t} + \tilde{\nabla}_\parallel \phi - \frac{1}{\tau}\tilde{\nabla}_\parallel n_e - \tilde{\nabla}_\parallel T_{\parallel_e} - (1+\eta_e) i\omega_* \frac{A_\parallel}{\tau} + (T_{\parallel_e} - T_{\perp e})\nabla_\parallel \ln B = 0. \tag{3.106}$$

The equations for $T_{\parallel_e}$ and $T_{\perp e}$ needed to complete the above set come from the $q_{\parallel_e}$ and $q_{\perp e}$ moment equations. The $p_{\parallel_e}$ and $p_{\perp e}$ moment equations provide information on the next order evolution of the temperature fluctuations.

The $q_{\parallel_e}$ and $q_{\perp e}$ equations contain the higher moments r_e and s_e which are closed as in Sec. 3.2.3. However, the electron closure terms are not in general $\mathcal{O}(1)$. Consider for example the Maxwellian closure for the moment $r_{\parallel,\parallel_e}$. This closure is derived by taking the first order fluctuating part of the generalized Maxwellian result $r_{\parallel,\parallel_e} = 3p_{\parallel_e}^2/m_e n_e$. The factor of $1/m_e$ insures that this term is $\mathcal{O}(\delta^{-2})$. In the normalized units:

$$r_{\parallel,\parallel e} \rightarrow 6\frac{m_i}{\tau m_e}T_{\parallel e} + 3\frac{m_i}{\tau^2 m_e}n_e, \tag{3.107}$$

and similarly for $r_{\parallel,\perp e}$ and $r_{\perp,\perp e}$. The Landau damping portion of the closure is smaller than the Maxwellian part by $\sqrt{m_e/m_i}$, and is neglected here, though it is reconsidered in Sec. 3.3.3.

Before normalizing or substituting in the closures, the $q_{\parallel e}$ equation can be written to lowest order:

$$B\tilde{\nabla}_\parallel \frac{\tilde{r}_{\parallel\parallel_e}}{B} - 3T_{0e}B\tilde{\nabla}_\parallel \frac{\tilde{p}_{\parallel_e}}{m_e B} + 3\eta_e \frac{n_0 T_{0e}^2}{m_e} i\omega_* \frac{eA_\parallel}{cT_{0i}} + 3(\tilde{r}_{\parallel\perp e} - \frac{T_{0i}}{m_e}\tilde{p}_{\perp e})\nabla_\parallel \ln B = 0, \tag{3.108}$$

where the d/dt and ω_d terms again drop out, as they are higher order in m_e/m_i.

Substituting the Maxwellian closures, normalizing and simplifying gives:

$$\tilde{\nabla}_\parallel T_{\parallel_e} + \eta_e i\omega_* A_\parallel/\tau = 0. \tag{3.109}$$

The second term on the left is the gradient of the equilibrium temperature T_{0e} along the perturbed field, $\hat{\mathbf{b}} \times \nabla A_\parallel \cdot \nabla T_{oe}$, or equivalently the gradient along the total field $\tilde{\nabla}_\parallel T_{0e}$, as T_{0e} is constant along the equilibrium field. Eq. 3.109 can thus be written in the more physically intuitive form:

$$\tilde{\nabla}_\parallel (T_{\parallel_e} + T_{0e}) = \frac{1}{B}(\mathbf{B}_0 + \mathbf{B}_1) \cdot \nabla (T_{\parallel_e} + T_{0e}) = 0. \tag{3.110}$$

Quite simply, the total temperature is constant along the total magnetic field including fluctuations. This result is precisely what is expected from our ordering of the velocities $v_{ti}, v_A \ll v_{te}$. The speeds of the microturbulence being evolved are all slow compared to v_{te}, and furthermore the Alfvén speed at which the magnetic field fluctuates is also much less than the electron thermal speed. Hence as the field fluctuates across the equilibrium temperature gradient, the electrons are able to almost instantaneously re-thermalize, leaving no electron temperature gradient along the total field. Note that this condition is quite different from the occasionally employed closures $\nabla_\parallel \tilde{T}_e = 0$, or $\tilde{T}_e = 0$, both of which fail to properly account for the magnetic fluctuations across the equilibrium temperature gradient, and can lead to errors when η_e is finite, as shown in Fig. 2.3 in the local fluid limit.

Turning now to the $q_{\perp e}$ moment equation, and again inserting Maxwellian closures, normalizing, and keeping only the dominant terms, the equation becomes:

$$\tilde{\nabla}_{\parallel} T_{\perp_e} + \eta_e i\omega_* A_{\parallel}/\tau + (T_{\perp_e} - T_{\parallel_e})\nabla_{\parallel} \ln B = 0. \tag{3.111}$$

Again the second term is simply the derivative along the perturbed field of the equilibrium temperature (T_{0e}). A mirror force term enters as well.

Eqs. 3.109 and 3.111 can be recast by defining $T_e = (T_{\parallel_e} + T_{\perp_e})/2$ and $\delta T_e = (T_{\perp_e} - T_{\parallel_e})$. Note that once Eq. 3.109 has been substituted into the momentum equation, the temperature enters the momentum equation only as a mirroring term $\delta T_e \nabla_{\parallel} \ln B$, and enters the density equation only as $-i\omega_d T_e$. The equations for T_e and δT_e are:

$$\tilde{\nabla}_{\parallel} T_e + \eta_e i\omega_* A_{\parallel}/\tau + \frac{\delta T_e}{2}\nabla_{\parallel} \ln B = 0, \tag{3.112}$$

$$(\tilde{\nabla}_{\parallel} + \nabla_{\parallel} \ln B)\,\delta T_e = 0. \tag{3.113}$$

The simplest solution to Eq. 3.113 is $\delta T_e = 0$. This solution is always valid, and is especially satisfactory because it is the only valid solution in the limit of high electron collisionality. Also, in the limit of small mirror force, δT_e does not appear in the moment equations. Because this model describes only passing electron dynamics, the mirror force is expected to play a small role.[10]

The full set of normalized electron equations is then:

$$\frac{\partial n_e}{\partial t} + \mathbf{v}_E \cdot \nabla n_e + B\tilde{\nabla}_{\parallel}\frac{u_{\parallel e}}{B} - i\omega_*\phi + 2i\omega_d(\phi - \frac{n_e}{\tau} - T_e) = 0, \tag{3.114}$$

---

[10] However, we intend to include a finite mirror force term in the electron momentum equation in the future, to more accurately model electron dynamics, particularly in low aspect ratio tokamaks.

$$\frac{\partial A_\parallel}{\partial t} + \tilde{\nabla}_\parallel \phi - \frac{1}{\tau}\tilde{\nabla}_\parallel n_e - \frac{1}{\tau} i\omega_* A_\parallel = 0, \tag{3.115}$$

$$\tilde{\nabla}_\parallel T_e = -\frac{\eta_e}{\tau} i\omega_* A_\parallel, \tag{3.116}$$

where the T_e term in Eq. 3.114 is calculated by numerically inverting Eq. 3.116.

The above set of equations represents a fairly simple and elegant model of the electron dynamics on Alfvén and ion scales. While only two moment equations need be solved, the physics content of a full six moment model has been incorporated to lowest order in m_e/m_i.

Though the model is simple, it represents a very substantial improvement over the adiabatic electron models ($n_e/\tau = \phi - \langle\phi\rangle_{surface}$) that have been used to describe the passing electrons in most previous gyrofluid and gyrokinetic particle simulations. In addition to finite-β effects and Alfvén wave dynamics, the above model also incorporates electron $\mathbf{E}\times\mathbf{B}$, curvature, and ∇B drift motion, as well as the $\mathbf{E}\times\mathbf{B}$ nonlinearity and four additional nonlinear terms due to magnetic flutter. The accuracy of this model in describing both finite-β drift waves and shear Alfvén waves is gauged in Ch. 4 with an extensive series of linear benchmarks.

Furthermore, the numerically crippling effects of short electron space and time scales have been entirely removed. Because the electron mass appears nowhere in Eqs. 3.114-3.116 or in the normalizations, it is apparent that the electron scales, (ρ_e, c/ω_{pe}, $k_\parallel v_{te}$, ω_{ETG}), all of which contain the electron mass, have been successfully removed from the equations which are numerically evolved.

It is shown in Appendix B that the above electron model preserves magnetic flux surfaces.

3.3.3 Electron Collisions and Landau Damping

One consequence of keeping only the lowest order terms in the mass ratio expansion is the absence of any damping mechanism in the electron channel. It is well known that damping terms, even when linearly small, can have a dramatic impact on the nonlinear dynamics of an otherwise dissipationless system. While the gyrofluid system has dissipation through ion collisions and ion Landau damping, it is expected that damping in the electron channel may play an important role as well.

The dominant electron damping mechanisms are expected to be Landau damping and pitch angle scattering collisions with ions.

Both of these mechanisms can be included via a formal relaxation of the mass ratio ordering in which terms small by $\sqrt{m_e/m_i}$ are kept, while those proportional to m_e/m_i are neglected. Formally, the subsidiary expansion in $\delta \sim \sqrt{m_e/m_i}$ is now truncated at $\mathcal{O}(\delta^2)$, and terms of $\mathcal{O}(\delta)$ are retained. Note that the finite m_e terms neglected in the derivation of Eqs. 3.114-3.116, except for the Landau closure terms, were small by a full power of m_e/m_i and do not re-enter with this relaxed ordering.

The [Hammett and Perkins 1990] Landau damping operator comes in at $\mathcal{O}(\delta)$. For a two moment model, the Landau closure appears in the momentum equation and takes the form:

$$n_0\sqrt{\frac{\pi}{2}\frac{m_e}{m_i}}\,c_s|k_\parallel|\tilde{u}_{\parallel e}, \tag{3.117}$$

where the units are appropriate for insertion into Eq. 3.105. In the normalized units of Eq. 3.115, this becomes:

$$-\sqrt{\frac{\pi}{2\tau}\frac{m_e}{m_i}}\,|k_\parallel|u_{\parallel e}. \tag{3.118}$$

Note that we have introduced the Landau damping operator in an odd moment ($u_\parallel$), which has no equilibrium component, so that there is no linear magnetic flutter contribution to the Landau closure, avoiding a concern expressed by [Finn and Gerwin 1996]. However, magnetic flutter does introduce an additional nonlinear Landau damping term, as discussed in Sec. C.8. The size of this term has been calculated in simulations and found to be small. However, including it in future simulations is of interest, as discussed in Secs. C.8 and 7.2.

Electron-ion collisions are modeled with a Lorentz pitch angle scattering operator. Adding this operator to the right hand side of the drift kinetic equation and taking moments leads to the following collision term in the normalized electron momentum equation:

$$-\nu_{ei}\frac{m_e}{m_i}(u_{\parallel e} - u_{\parallel i}), \tag{3.119}$$

where ν_{ei} is the effective scattering rate, normalized to v_{ti}/L_n. Formally we may choose to order $\nu_{ei} \sim \delta^{-1}$ so that the collision term enters at $\mathcal{O}(\delta)$. Of course this is simply a caveat to maintain a formally consistent ordering in the mass ratio. It is recognized that the collision term is often smaller than other neglected terms. The collision term is kept in some cases simply to explore the importance of this damping mechanism in the electron channel.

Including the above models of Landau damping and pitch angle scattering in the electron momentum equation, the final set of electron equations can be written:

$$\frac{\partial n_e}{\partial t} + \mathbf{v}_E \cdot \nabla n_e + B\tilde{\nabla}_\parallel \frac{u_{\parallel e}}{B} - i\omega_* \phi + 2i\omega_d(\phi - \frac{n_e}{\tau} - T_e) = 0, \tag{3.120}$$

$$\frac{\partial A_\parallel}{\partial t} + \tilde{\nabla}_\parallel \phi - \frac{1}{\tau}\tilde{\nabla}_\parallel n_e - \frac{1}{\tau} i\omega_* A_\parallel - \sqrt{\frac{\pi}{2\tau}\frac{m_e}{m_i}}|k_\parallel| u_{\parallel e} = \nu_{ei}\frac{m_e}{m_i}(u_{\parallel e} - u_{\parallel i}), \tag{3.121}$$

$$\tilde{\nabla}_\parallel T_e = -\frac{\eta_e}{\tau} i\omega_* A_\parallel. \tag{3.122}$$

This electron model can be viewed as an extension of the equations of [KADOMTSEV and POGUTSE 1985] to include toroidal drifts, parallel ion flow, and an improved Landau damping model which properly phase-mixes $\mathbf{E} \times \mathbf{B}$ driven perturbations.[11]

---

[11] [HAMMETT and PERKINS 1990; HAMMETT et al. 1992] showed that a Landau damping model like that employed in Eq. 3.121 provides an n-pole approximation to the Z-function response for all frequencies, and unlike the $q_\parallel = \hat{\mu} E_\parallel$ Landau closure employed by [KADOMTSEV and POGUTSE 1985], is of the proper form to model the linear propagator and properly phase mix $\mathbf{E} \times \mathbf{B}$ driven perturbations.

The model can be reduced to the familiar adiabatic response in the appropriate limits. Taking the limits $\beta \to 0$, which implies $A_\| \to 0$ from Eq. 3.125,[12] and $m_e/m_i \to 0$, Eq. 3.121 reduces to the adiabatic electron response $\nabla_\|(\phi - n_e/\tau) = 0$; or, with the appropriate choice of constants, $n_e = \tau(\phi - \langle\phi\rangle)$. The adiabatic response can also be derived in the formal limit $k_\| \to \infty$.

Upon neglect of the "small scale" effects associated with the ∇p term in the momentum equation (here these are the $\tilde{\nabla}_\| n_e$ and $i\omega_* A_\|$ terms), and in the limit $m_e/m_i \to 0$, Eq. 3.121 reduces to the parallel ideal MHD Ohm's Law $E_\| = -\frac{\partial A_\|}{\partial t} - \tilde{\nabla}_\| \phi = 0$. Including the collisional term gives the parallel Resistive MHD Ohm's Law. Adding the $-1/\tau(\tilde{\nabla}_\| n_e - i\omega_* A_\|)$ terms gives a version of the extended MHD Ohm's Law appropriate for $\omega \ll k_\| v_{te}$. Some versions of extended MHD treat the electrons quite similarly to the above model, though, with the exception of the version described in Appendix C, they generally do not include a Landau damping term.[13]

3.4 Poisson's Equation and Ampere's Law

The system of equations is completed using the gyrokinetic Poisson's Equation and Ampere's Law.

In the limit of small Debye length, $k\lambda_D \ll 1$, the gyrokinetic Poisson's equation becomes a quasineutrality constraint [Lee 1983]:

$$n_e = \bar{n}_i - (1 - \Gamma_0)\phi, \tag{3.123}$$

where $\bar{n}_i$ is the gyrophase independent part of the real space ion density. The $(1 - \Gamma_0)\phi$ term, often called the polarization density, arises from the gyrophase dependent part of the distribution function, and accounts for the difference between guiding center density and ion particle density.

---

[12] This of course assumes $u_{\|e}$ and $u_{\|i}$ remain finite as $\beta \to 0$. See Sec. 2.3.1 for a more detailed discussion of this electrostatic/adiabatic electron limit.

[13] Other versions of extended MHD include the electron inertia term which has been neglected here, and some versions do not assume $\omega \ll k_\| v_{te}$, and hence can have electron temperature gradients along the magnetic field.

Following [Beer 1995], the transformation from gyrocenter to real space is accomplished with the simple Padé approximation:

$$\bar{n}_i = \frac{1}{1+b/2} n_i - \frac{2b}{(2+b)^2} T_{\perp_i}, \tag{3.124}$$

where $b = k_\perp^2 \rho_i^2$. This approximation is first order accurate in b for both n_i and $T_{\perp_i}$, and it behaves properly ($\bar{n}_i \to 0$) for large b.

Within our gyrokinetic ordering, the parallel Ampere's Law can be written [Brizard 1992]:

$$\nabla_\perp^2 A_\parallel = -\frac{\tau \beta_e}{2} (\bar{u}_{\parallel_i} - u_{\parallel e}), \tag{3.125}$$

where $\beta_e = 8\pi n_0 T_{0e}/B^2$.

The transformation to real space is again accomplished with a Padé approximation:

$$\bar{u}_{\parallel_i} = \frac{1}{1+b/2} u_{\parallel i} - \frac{2b}{(2+b)^2} q_{\perp_i}. \tag{3.126}$$

Poisson's Equation (Eq. 3.123) and Ampere's Law (Eq. 3.125), together with the six ion moment equations (Eqs. 3.87-3.92), the two electron moment equations (Eqs. 3.120-3.121), and the T_e condition (Eq. 3.122), provide a complete description of the ten unknowns (n_i, $u_{\parallel_i}$, $p_{\parallel_i}$, $p_{\perp i}$, $q_{\parallel_i}$, $q_{\perp i}$, n_e, $u_{\parallel_e}$, T_e, ϕ, and $A_\parallel$). The system is solved by evolving the eight partial differential equations in time, while using Eq. 3.123 to solve for ϕ, Eq. 3.125 to solve for $u_{\parallel_e}$, and Eq. 3.122 to solve for T_e.

The full set of equations is evaluated with an extensive set of linear benchmarks in Ch. 4, and solved nonlinearly in Chs. 5 and 6.

Chapter 4

Linear Benchmarks with Kinetic Theory

BENCHMARKING THE MODEL against linear kinetic theory is an important step in verifying the accuracy and reliability of both the electromagnetic gyrofluid physics model and the simulation code used to implement the model.

An extensive series of linear benchmarks in the electrostatic case has been performed by [Beer 1995], so we focus here on the impact of finite plasma β. Finite-β effects on the ion temperature gradient (ITG) instability are benchmarked both in slab and toroidal flux tube geometry. In addition, the growth rates and real frequencies of the kinetic Alfvén instability are benchmarked in toroidal geometry. Both the case with no temperature gradient and the more interesting case with finite ion temperature gradient are investigated. It is shown that the gyrofluid model is able to reproduce the finite growth rates of the kinetic Alfvén mode below the ideal MHD β-limit in this case.

It is important to note that this set of benchmarks provides a test of the electron physics model, as well as the ion physics model. While a simple adiabatic electron model can produce the correct ITG growth rate in the electrostatic limit, this is not at all the case for the finite-β ITG and KBM cases considered here, as discussed in Sec. 2.3.4. A description of electron ∇B and curvature drift motion and proper consideration of magnetic flutter across equilibrium electron temperature gradients are required to accurately calculate growth rates of both the finite-β ITG and KBM instabilities.

It is not straightforward to do benchmarks for linearly stable modes which could play some role in nonlinear saturation. An important example is the zonal flow mode, which is discussed in Appendix A.

4.1 The Finite-β ITG Instability

As discussed in the first two chapters, the ion temperature gradient (ITG) instability is believed to play a critical role in core transport. Capturing the finite-β effects on this mode has been a principal motivation for developing an electromagnetic turbulence model.

Comparisons of predicted linear growth rates and frequencies of the finite-β ITG are made with linear kinetic integral codes in both sheared slab and toroidal geometry.

4.1.1 Benchmarks in Slab Geometry

We first test the electromagnetic gyrofluid model against linear kinetic theory in a nonlocal sheared slab geometry. This comparison emphasizes the electromagnetic effects on the ITG mode while omitting for now the effects of toroidal geometry.

The comparison uses a linear integral code developed by [REYNDERS 1994]. This code calculates the growth rates and frequencies for all the radial eigenmodes of the system, and it has been successfully benchmarked against the earlier work of [DONG et al. 1988], which considered only the fundamental eigenmode.

Fig. 4.1 shows a comparison of predictions of linear growth rate as a function of $k_y\rho_i$ at $\beta = 0$ and at $\beta = 0.2\%$. The other parameters chosen are $\eta_i = \eta_e = 3$, $T_i/T_e = 1$ and $L_s/L_n = 40$. The linear kinetic theory growth rates for two separate radial eigenmodes ($l = 1$ and $l = 2$) are shown, as well as the gyrofluid predictions. Because the gyrofluid code is an initial value code, it is expected to converge to

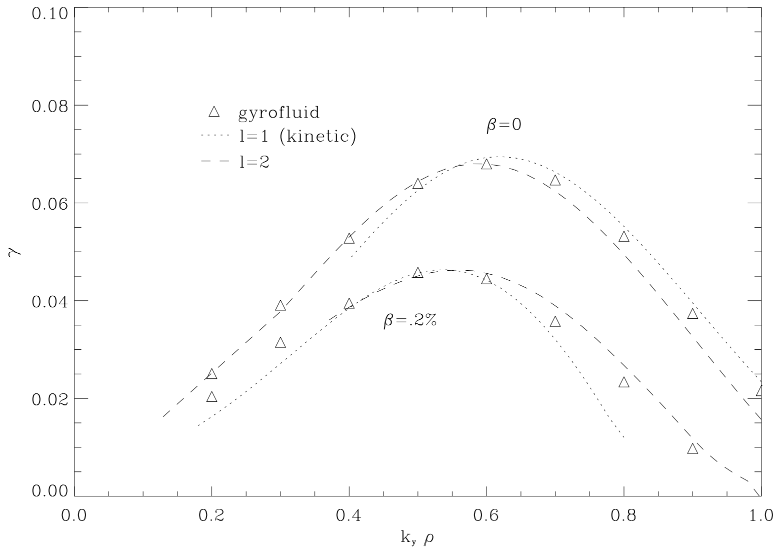

Figure 4.1: Linear growth rate spectra of the slab ITG mode, for $\beta = 0$ and $\beta = .2\%$, with $\eta_i = \eta_e = 3$, $\tau = 1$, $L_s/L_n = 40$. The growth rate, in normalized units of v_{ti}/L_n, is plotted as a function of $k_y\rho_i$. The electromagnetic gyrofluid model is compared to two radial eigenmodes calculated by Reynders' linear integral code.

the fastest growing eigenmode. Good quantitative agreement is found, with the gyrofluid model accounting for both the strong finite-β reduction in growth rate and the shift in the peak to longer wavelengths.

The sheared slab system often contains a number of eigenmodes with similar growth rates, complicating the comparisons. Fig. 4.2 shows both the linear growth rates (positive) and real frequencies (negative) for the same parameters as Fig. 4.1. The electrostatic ($\beta = 0$) case is plotted above, and the $\beta = .2\%$ case is below. Here it can be seen that different eigenmodes dominate at different values of $k_y\rho_i$, and that in some cases the growth rates of different eigenmodes are so close that the initial value gyrofluid code oscillates between two modes. For cases with a clearly dominant eigenmode, good agreement is found in both growth rate and real frequency for both electrostatic and electromagnetic cases.

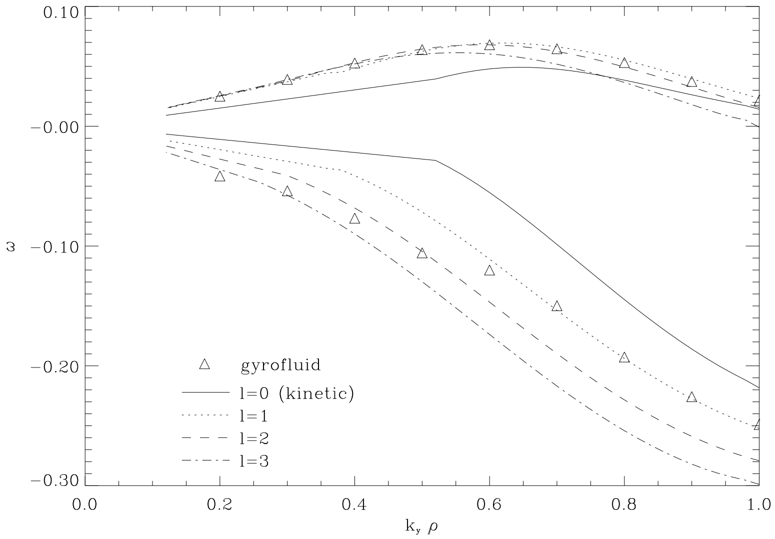

(a)

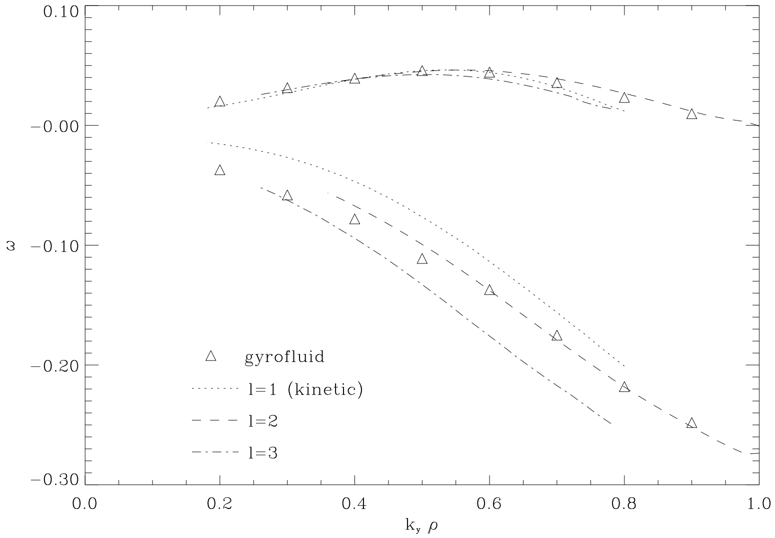

(b)

Figure 4.2: Linear growth rate (positive) and real frequency (negative) spectra of the slab ITG mode, for $\beta = 0$ (a) and $\beta = .2\%$ (b), with $\eta_i = \eta_e = 3$, $\tau = 1$, $L_s/L_n = 40$. The gyrofluid model is compared to multiple radial eigenmodes calculated with Reynders' linear integral code.

4.1.2 ITG Benchmarks in Toroidal Geometry

Ultimately, the model is to be employed in simulations in toroidal geometry, and it is here that benchmarks are most important.

Linear kinetic theory for the electromagnetic case in nonlocal toroidal geometry is quite involved, and a fairly limited set of codes is available. Two kinetic codes are considered here.

The first kinetic code, developed by [Kim, Horton, and Dong 1993], solves a simplified set of integral equations in ballooning coordinates, using an $s - \alpha$ equilibrium model. This code makes a number of approximations in order to develop a simpler set of equations. Among the most important are the neglect of $v_\parallel$ and $v_\perp$ variation along the field lines, and the ordering $\omega \sim \omega_{Di} \sim \omega_{De} \ll |k_\parallel v_{te}|$. While these approximations are similar to those used in the derivation of the electron equations in our model, they nonetheless make this code somewhat less fundamental. However, for the parameters chosen in the benchmark case (particularly $r/R = 0$), the approximations are expected to be well justified.

Fig. 4.3 shows a benchmark using parameters selected from Fig. 6a in [Kim et al. 1993]. The plot shows linear growth rate vs. the safety factor q, at two values of β. Quantitative agreement in the finite-β case is found to be as good as in the electrostatic case. The trend emphasized by [Kim et al. 1993], that finite-β effects become more important at higher q is clearly reproduced by the gyrofluid model.

The structure of the eigenfunctions of ϕ and $A_\parallel$ in ballooning space has also been analyzed. For the parameter set $\beta = 0.8\%$, $\eta_i = 2.5$, $\eta_e = 2$, $k_\theta \rho_i = 0.5$, $\epsilon_n = 0.2$, $s = 0.6$, $q = 1.5$, and $\tau = 1$, the gyrofluid eigenfunctions have been compared to Fig. 5 of [Kim et al. 1993]. Good agreement is found in both the shape and parity of the real and imaginary eigenfunctions of ϕ and $A_\parallel$ as well as in the ratio $A_\parallel/\phi \ll 1$. We note that the real part of ϕ has even parity, while the real part of $A_\parallel$ is odd, and in the normalized units, the ratio $\phi_{max}/A_{\parallel max} \simeq 15$. The eigenfunctions extend roughly 2π in ballooning angle before becoming negligible. The shape and parity of these eigenfunctions and the ratio $A_\parallel/\phi \ll 1$ are all typical of the finite-β ITG mode.

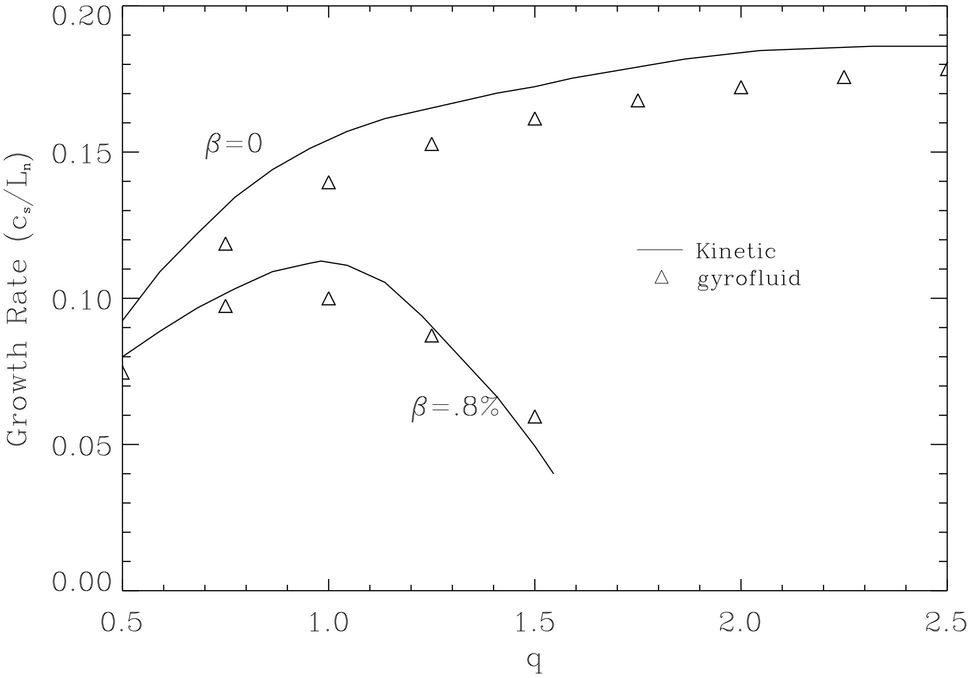

Figure 4.3: Linear growth rates of the toroidal ITG mode as a function of the safety factor q, for $\beta = 0$ and $\beta = .8\%$, with $\eta_i = 2.5$, $\eta_e = 2$, $k_\theta \rho_i = 0.5$, $\epsilon_n = 0.2$, $s = 0.6$, and $\tau = 1$. The gyrofluid model is compared to linear kinetic theory of [Kim et al. 1993] in $\hat{s} - \alpha$ geometry, with $\alpha = q^2 \beta_e / \epsilon_n [1 + \eta_e + \tau(1 + \eta_i)]$ chosen to be consistent with β and q.

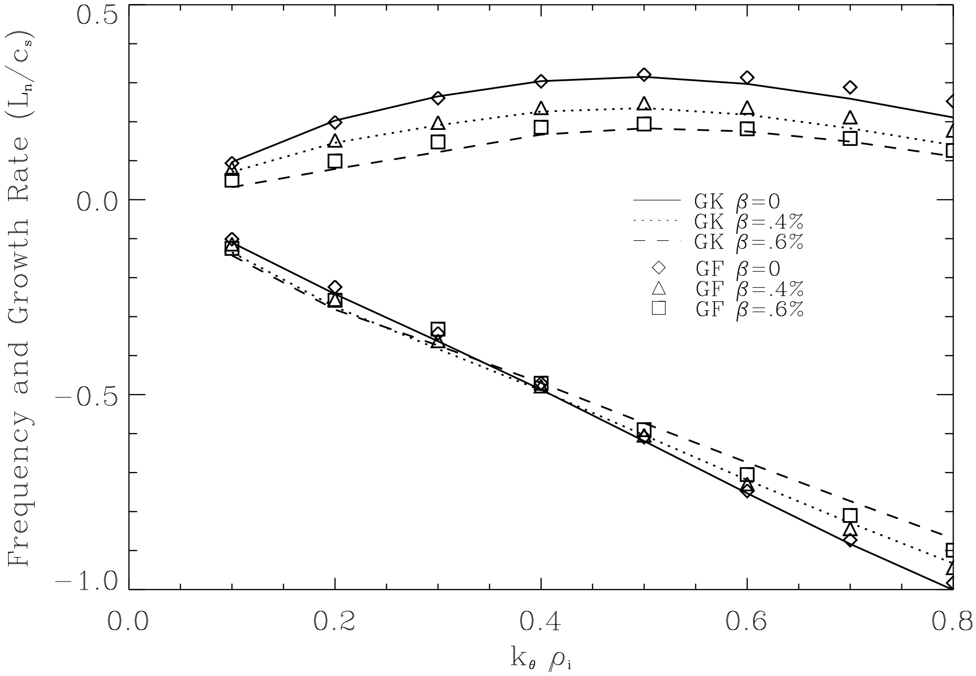

Figure 4.4: Linear growth rate (positive) and frequency (negative) spectra of the toroidal ITG mode, for $\beta = 0$, $\beta = .4\%$, and $\beta = .6\%$. The gyrofluid result is compared with results from M. Kotschenreuther's linear gyrokinetic code (runs performed by W. Dorland). Parameters are $\eta_i = \eta_e = 5$, $R/L_n = 3$, $s = 1$, $q = 2$, $\alpha = 0$, $m_e/m_i = 0$ and $\tau = 1$.

A second set of toroidal benchmarks employ the widely used `GS2` linear gyrokinetic code developed by M. Kotschenreuther [Kotschenreuther et al. 1995]. `GS2` is an initial value code which solves integral equations in ballooning coordinates. It is a very complete code which can include both finite electron mass and parallel magnetic perturbations. The code can be run in general geometry, but is operated in a simple circular equilibrium for the comparisons shown here.

Fig. 4.4 shows a comparison of linear growth rate and frequency spectra at three values of β. Good agreement is found at all three β values, and the dramatic finite-β stabilization of the ITG seen in this case is well reproduced by the gyrofluid code. Both codes have been run with zero electron mass and with $\delta B_\parallel = 0$ to simplify the comparison. It should be noted that although the absolute values of β shown are small, they represent a significant fraction of the ideal MHD β limit for this case ($\beta_c \simeq 0.8\%$).

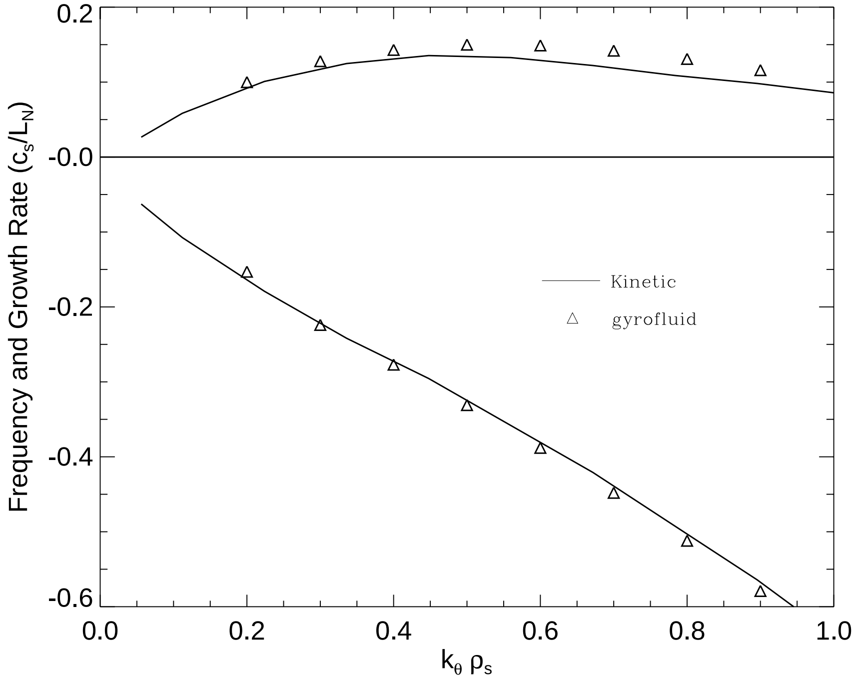

Figure 4.5: Linear growth rate (positive) and frequency (negative) spectra of the toroidal shear Alfvén mode. The gyrofluid model is compared to the kinetic code of [Hong et al. 1989], in a simple circular equilibrium at $\beta = 6.25\%$. Other parameters are $s = 1$, $q = 2$, $\tau = 1$, $\epsilon_n = 0.25$, $\eta_i = \eta_e = 0$.

4.2 The Kinetic Alfvén Instability

The electromagnetic gyrofluid model also introduces shear Alfvén wave instabilities not found in the electrostatic case, as described in Sec. 2.1. These kinetic Alfvén instabilities are expected to play an important role in transport in cases where they are driven unstable below the ideal MHD threshold by the toroidal ion drift resonance. Benchmarks are performed both in the flat temperature gradient case, where the kinetic Alfvén wave goes unstable exactly at the ideal MHD β_c, and the finite ion temperature gradient case, where the kinetic Alfvén wave is unstable below β_c.

4.2.1 Benchmarks with Zero Ion Temperature Gradient

A set of benchmarks is performed against the kinetic code developed by [Hong et al. 1989]. It should be noted that this code does not solve the complete kinetic equations, but rather focuses on the coupling between drift and shear Alfvén waves, and neglects ion transit and bounce frequency resonant effects.

Fig. 4.5 shows a comparison with Fig. 1[1] in [Hong et al. 1989]. Growth rate and frequency spectra are compared in a simple circular geometry at $\beta = 6.25\%$. Excellent agreement is found for the frequency, which is nearly dispersionless with a phase velocity of roughly $-.6 c_s \rho_s / L_n$ in the ion diamagnetic direction. Agreement for the growth rate is also good, though some variance is seen at short wavelengths. The slight disagreement at higher $k_\theta \rho_i$ may be due at least in part to differences in the numerical resolutions used in the two codes. In cases such as Figs. 4.1, 4.2, and 4.4, where the numerical resolution used in the kinetic codes is known, an attempt is made to use equivalent resolution in the gyrofluid code. However, the resolution used by [Hong et al. 1989] is unknown. High resolution gyrofluid runs[2] are shown in Fig. 4.5, although agreement is somewhat better at lower resolution.

Fig. 4.6 shows the growth rate and frequency of the Alfvén mode as a function of β, at $k_\theta \rho_i = .5$. An $s - \alpha$ equilibrium model is used, and the ideal MHD prediction is shown for comparison. Because $\eta_i = 0$, kinetic theory and ideal MHD agree about both the critical $\beta_c = 3.7\%$ for instability, and the β value at which the second stability region is entered. Agreement between the gyrofluid model and kinetic theory is very good for both frequency and growth rate.

4.2.2 Benchmarks with Finite Ion Temperature Gradient

The kinetic Alfvén wave becomes particularly interesting in the presence of finite ion temperature gradient, because as shown by [Andersson and Weiland 1988], finite η_i is a necessary and sufficient condition for instability of the shear Alfvén

---

[1] The figure captions on Figs. 1 and 2 on p.1593 of this article have been reversed. The figure in the upper right is Fig. 1, while the figure in the lower left is Fig. 2.

[2] The gyrofluid runs in Fig. 4.5 use a box length of 6π radians along the field, with 128 parallel grid points. Further increases in box size and resolution do not significantly affect the results.

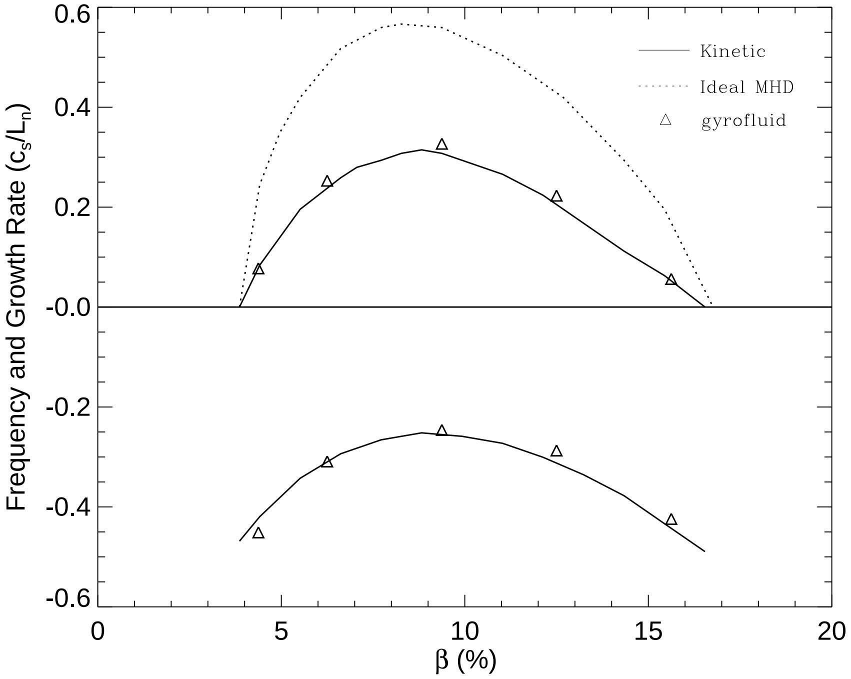

Figure 4.6: Frequency (negative) and linear growth rate (positive) of the toroidal Alfvén mode vs. β, with $\eta_i = \eta_e = 0$, $k_\theta \rho_i = 0.5$, $\epsilon_n = 0.25$, $s = 1$, $q = 2$, and $\tau = 1$. An $s - \alpha$ equilibrium model is used, and for these parameters, $\alpha = 16\,\beta$. The gyrofluid model is compared to linear kinetic theory by [Hong et al. 1989]. The ideal MHD prediction is also shown.

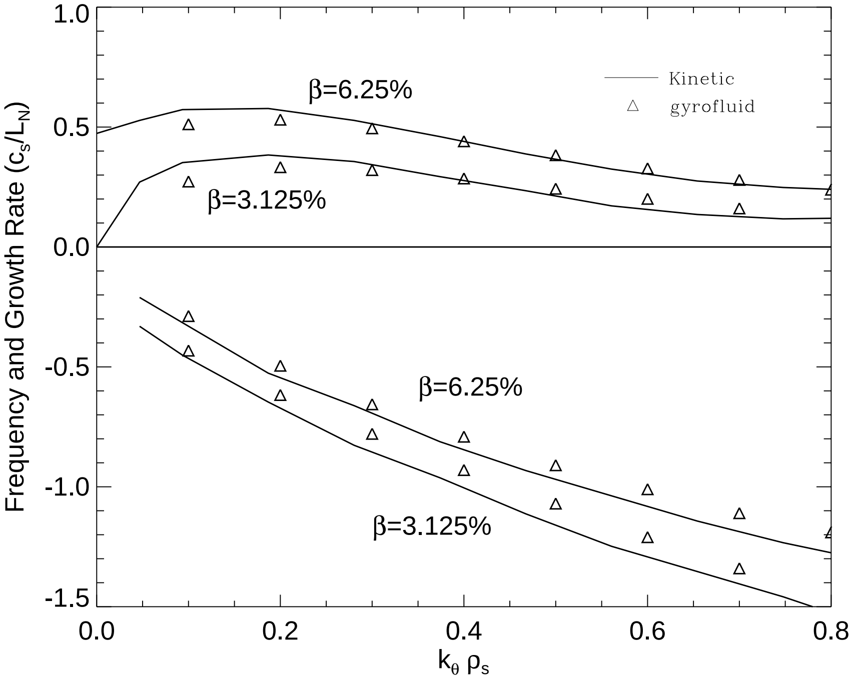

Figure 4.7: Frequency (negative) and linear growth rate (positive) spectra for the toroidal Alfvén mode in the presence of a finite ion temperature gradient. Parameters chosen are $\eta_i = 2$, $\eta_e = 0$, $\epsilon_n = 0.25$, $s = 1$, $q = 2$, and $\tau = 1$. The gyrofluid model is compared to linear kinetic theory by [Hong et al. 1989] at two values of $\beta = 3.125\%, 6.25\%$.

branch below the ideal MHD β limit. Hence this mode may play a significant and direct role in driving transport in plasmas thought to be ideal MHD stable.

A set of benchmarks is again performed, using parameters and results from [Hong et al. 1989]. Fig. 4.7 shows frequency and growth rate spectra for the toroidal shear Alfvén mode at two values of $\beta = 3.125\%, 6.25\%$. Other parameters are identical to Fig. 4.5, except that $\eta_i = 2$. Agreement between the two models is fairly good, with the gyrofluid model correctly accounting for the dramatic increase in growth rates at finite η_i. In Fig. 4.8 the growth rate of the toroidal Alfvén mode is shown as a function of β. Parameters are identical to Fig. 4.6, except that a finite ion temperature gradient has been added ($\eta_i = 2$). The Alfvén mode is now unstable both well below the ideal MHD β_c and well into the ideal MHD second stability region. The gyrofluid model is able to capture both of these effects. Note that the initial value gyrofluid code converges to the Alfvén mode only when it

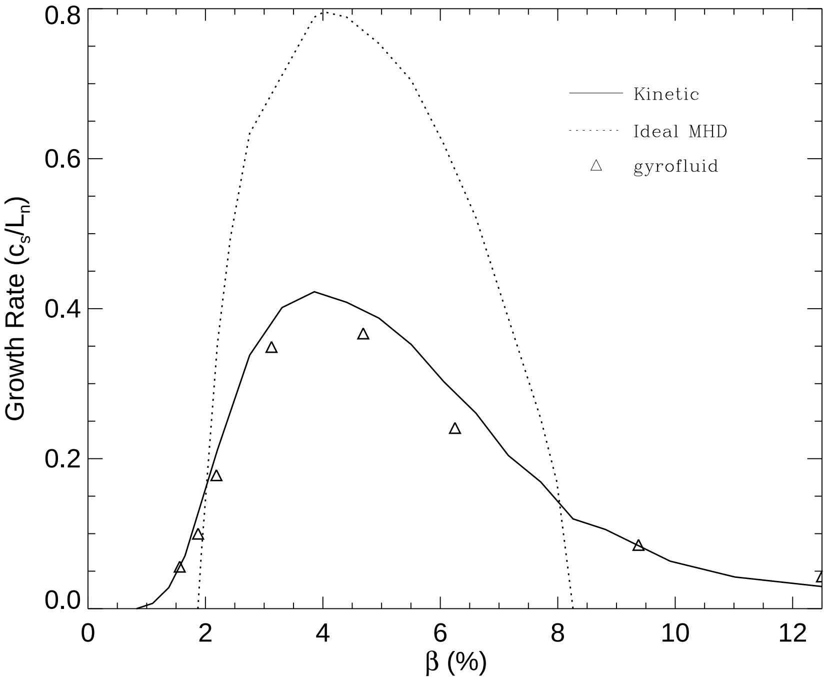

Figure 4.8: Linear growth rate of the toroidal Alfvén mode vs. β. Parameters identical to Fig. 4.6 except that $\eta_i = 2$. An $s - \alpha$ equilibrium model is used, and for these parameters, $\alpha = 32\beta$. The gyrofluid model is compared to linear kinetic theory by [Hong et al. 1989]. The ideal MHD prediction is also shown.

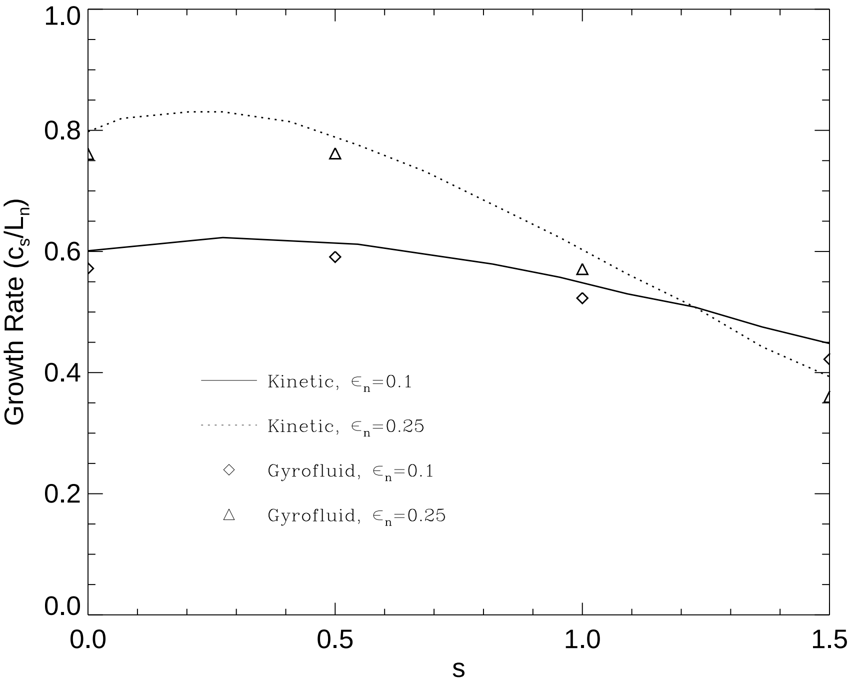

Figure 4.9: Linear growth rate of the toroidal Alfvén mode vs. magnetic shear, at two values of $\epsilon_n = 0.1, 0.25$, for $\beta = 9.375\%$, $k_\theta \rho_i = 0.3$, $q = 2$, $\tau = 1$, $\eta_i = 2$, and $\eta_e = 0$. The gyrofluid model is compared to linear kinetic theory by [Hong et al. 1989].

is dominant. Below $\beta \sim 1.5\%$, the ITG becomes the dominant mode at these parameters.

A final benchmark, Fig. 4.9, shows the growth rate dependence on the magnetic shear, for two different values of ϵ_n. Again quantitative agreement is reasonably good, with the gyrofluid model successfully reproducing the trends emphasized by [Hong et al. 1989].

4.3 Summary

A series of benchmarks has been performed against four linear kinetic codes. Generally good agreement in growth rates and real frequencies has been found between the gyrofluid model and four kinetic codes. In particular, the gyrofluid model has been found to successfully reproduce the finite-β stabilization of the ITG mode in both slab and toroidal geometry. Growth rates and frequencies of the kinetic toroidal Alfvén mode match reasonably well with kinetic theory, and the finite η_i effects on both the critical β and the second stability region are successfully reproduced. Good agreement in the linear mode structure of ϕ and $A_\parallel$ has also been found.

Chapter 5

Nonlinear Simulations

NONLINEAR SIMULATION of electromagnetic turbulence and transport can now be undertaken, using the model developed in Ch. 3 and tested linearly in Ch. 4. High resolution, three dimensional simulations are used to investigate the nonlinear behavior of microinstabilities driven linearly by both finite-β ITG and kinetic shear Alfvén instabilities.

These simulations reveal a number of interesting changes in microinstability behavior with the introduction of electromagnetic effects. At moderate β, the finite-β stabilization of the ITG mode leads to a significant reduction in heat fluxes from their $\beta = 0$ levels. However, as β approaches the ideal MHD ballooning critical β_c, a significant increase in heat flux occurs. This increase is dramatic when electron dissipation from electron Landau damping and electron-ion collisions is included in the model. The increase is accompanied by a marked reduction in dominant time-scales of the turbulence.

The electromagnetic simulations, like earlier electrostatic simulations, produce density fluctuation spectra which peak at $k_\theta \rho_i \simeq 0.1 - 0.2$, and which are strongly anisotropic in k_r and k_θ, in qualitative agreement with measurements by [Fonck et al. 1993]. Furthermore, the electromagnetic simulations produce ion temperature fluctuation spectra which are similar in shape to the density spectra, with a ratio $(\tilde{T}/T_0)/(\tilde{n_i}/n_0) = 2 \pm .5$ relatively independent of the simulation parameters, in agreement with the observations of [Evensen et al. 1998]. A narrowing in the peak of the fluctuation spectrum with increasing β is also observed.

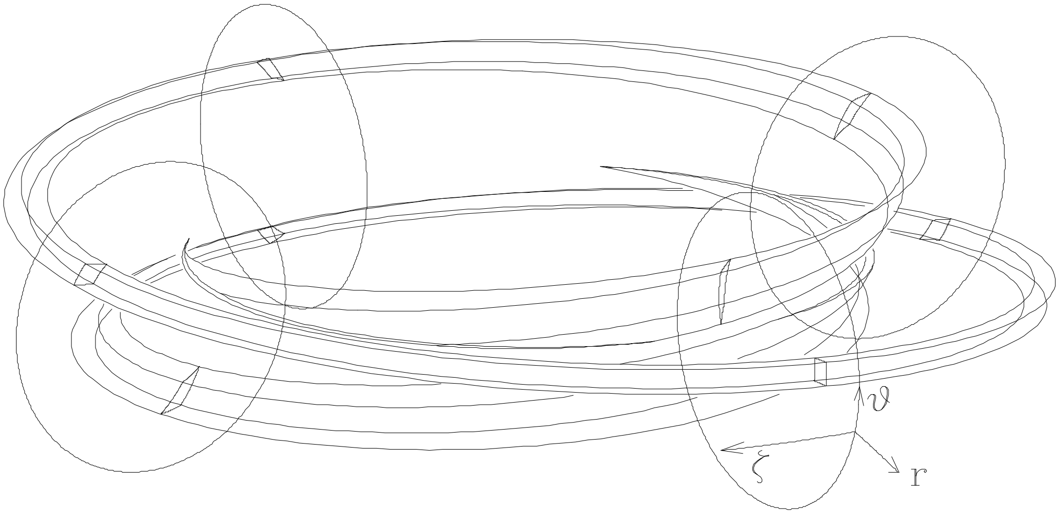

Figure 5.1: The rectangular computational domain mapped onto a flux tube in a torus, with $q_0 = 2.4$ and shear, $\hat{s} = 1.5$. The ends of the flux tube are cut off at poloidal angle $-\pi$ and π, and the sheared cross-sections of the flux tube in the poloidal plane are indicated. [Figure courtesy of M. A. Beer.]

5.1 The Flux Tube Geometry

Nonlinear simulations are carried out in a computationally efficient flux tube geometry using the field-aligned coordinates developed by [Beer et al. 1995].

This geometry takes advantage of the highly anisotropic nature of microturbulence in a strong magnetic field. Correlation lengths tend to be very long in the direction of **B** and short perpendicular to **B**. Hence a computational domain extending along the field is chosen, with a relatively short extent perpendicular to the field.

The computational domain is illustrated in Fig. 5.1. This long, thin, twisting flux tube is mapped onto a simple rectangular domain using the transformation described in detail by [Hammett et al. 1993; Beer et al. 1995], building on earlier work by [Roberts and Taylor 1965] and [Cowley et al. 1991]. The transformation can be written:

$$x = \frac{q_0}{B_0 r_0}(\psi - \psi_0), \qquad y = -\frac{r_0}{q_0}(\alpha - \alpha_0), \qquad z = \theta, \tag{5.1}$$

where $\psi = (2\pi)^{-2} \int d\tau \mathbf{B} \cdot \nabla\theta$ is the poloidal flux, $\psi_T = (2\pi)^{-2} \int d\tau \mathbf{B} \cdot \nabla\phi$ is the toroidal flux, $d\tau$ is the volume element, $q(\psi) = d\psi_T/d\psi$, $q_0 = q(\psi_0)$, $\alpha = \phi - q(\psi)\theta - \nu(\psi, \theta, \phi)$, B_0 is the field at the magnetic axis, r_0 is distance from the magnetic axis to the center of the box, and ϕ and θ are the physical toroidal and poloidal angles. All physical quantities, and $\nu(\psi, \theta, \phi)$, are periodic over 2π in ϕ and θ. The x and y coordinates are perpendicular to the field, while $z = \theta$ marks distance along the field. It is often useful to think of x as a radial coordinate and y as a poloidal coordinate, though this is only approximate. The above coordinates are linearly equivalent to the ballooning transformation [Connor et al. 1979], and similar to the coordinates employed by [Waltz and Boozer 1993] and [Dimits 1993].

Periodic boundary conditions are used in both perpendicular directions, requiring a box size large compared to perpendicular turbulent correlation lengths. The periodic parallel boundary condition must be treated with great care to avoid making all field lines into rational field lines connected with themselves. The procedure involves connecting different k_x modes with the same k_y at $\pm N\pi$, and is explained in detail in [Beer et al. 1995].

The flux tube geometry allows for computationally efficient simulations in realistic three-dimensional geometry. In addition, the flux tube domain allows for the equilibrium densities and temperatures to be described simply in terms of their equilibrium values and gradients. This limits the total number of parameters in the simulations, allowing for efficient parameter scans to accumulate physical insight and construct simplified transport models.

The primary limitation of flux tube geometry is its inability to properly treat cases where the turbulent correlation lengths become non-negligible relative to equilibrium scale lengths. Either an enhanced flux tube or annulus geometry with varying equilibrium parameters, or a full torus simulation is required to treat such cases.

5.2 Computational Details

The eight partial differential equations derived in Ch. 3 are solved pseudospectrally in flux tube geometry using an explicit two step Runge-Kutta algorithm that is second order accurate in time. A semi-implicit treatment analogous to that of [SCHNACK et al. 1987] is used in the electron moment equations, to relax the time step constraint imposed by shear Alfvén wave propagation. For toroidal simulations, the semi-implicit numerical damping coefficient is generally set to zero, but the leapfrog treatment of the $\nabla_\parallel(\phi - n_e/\tau)$ term is maintained. For the single ion species case, the numerical treatment of the electron momentum equation, Eq. 3.121, at time step $j+1$ is:

$$\begin{aligned} A_\parallel^{j+1} &= A_\parallel^j + \Delta t \left\{ \frac{1}{2} i k_\parallel \left[\frac{1}{1-\Gamma_0} + \frac{1}{\tau} \right] (n_e^j + n_e^{j+1}) \right\} \\ &- \Delta t \left\{ i k_\parallel \frac{1}{1-\Gamma_0} [n_e^j + (1-\Gamma_0)\phi^j] - \frac{1}{\tau} i k_y A_\parallel^j \ldots \right\}, \end{aligned} \tag{5.2}$$

where the ellipses refer to the nonlinear, collision, and Landau damping terms, which are all calculated at time step j. Note that this leapfrog method is employed within both the predictor and corrector steps of the Runge-Kutta algorithm.

The simulation code is based on the electrostatic `Gryffin` toroidal gyrofluid code originally developed by M. A. Beer, W. Dorland, and G. W. Hammett. The code has been enhanced to include magnetic fluctuations and non-adiabatic passing electron dynamics. The linear and nonlinear electromagnetic terms described in Ch. 3 have been implemented, including the electron $\mathbf{E} \times \mathbf{B}$ nonlinearity, and magnetic flutter nonlinearities in both the ion and electron equations. Electromagnetic nonlinear FLR terms have been implemented, but are generally found to be unimportant, and for this reason the $[\frac{1}{2}\hat{\nabla}_\perp^2 \mathbf{v}_\mathcal{A}] \cdot \nabla$ terms have been omitted from the nonlinear results presented here. The nonlinear term in the electron temperature equation (Eq. 3.122) has also been found to be unimportant, and neglected in the simulations presented here.

The simulation code employs a Fourier space representation in the two perpendicular directions, x and y, and a real space representation along the field in z. N_x evenly spaced radial modes, spanning the space $-k_{xmax}$, $-k_{xmax}+1$, ..., -1,

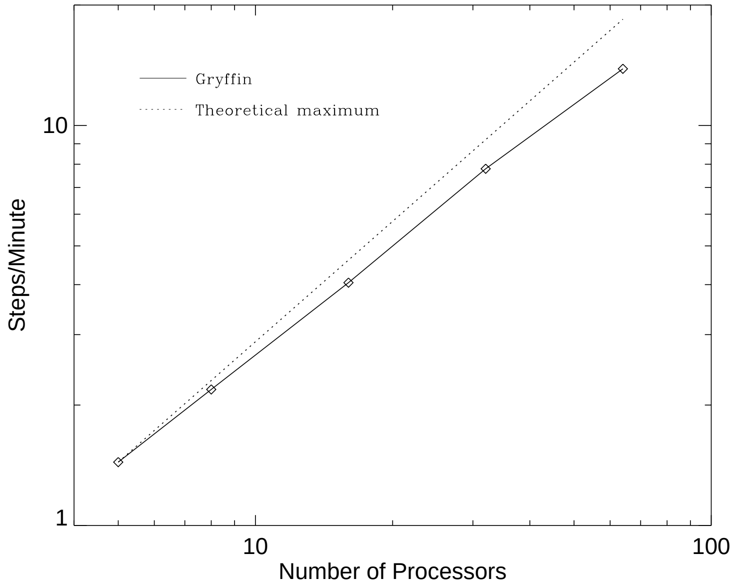

Figure 5.2: Scaling of the performance of the electromagnetic version of the `Gryffin` code with processor number. Runs are carried out on the NERSC Cray-T3E `mcurie`. A minimum of five processors is needed to meet the memory requirements of the simulation at the resolution ($N_x = 85, N_y = 127, N_z = 64$) employed. The dotted line shows the theoretical maximum performance assuming perfect parallel scaling up from 5 processors.

0, 1, ..., $k_{xmax} - 1$, k_{xmax} are employed, along with N_y poloidal modes. Only the $N_y/2+1$ positive $k_y = 0, 1, ..., k_{y_{max}} - 1, k_{y_{max}}$ need to be physically evolved in the complex wave number space, due to the reality condition. However, the numerical grid on which the fast Fourier transforms (FFT's) are performed is larger by three halves in each perpendicular direction to allow for de-aliasing ($N_{FFTx} = 3/2 \times N_x$, $N_{FFTy} = 3/2 \times\ N_y$). An evenly spaced grid of N_z points is used along the field. The total numerical grid size is thus $N_{FFTx} \times N_{FFTy} \times N_z = 9/4\, N_x\, N_y\, N_z$.

The `Gryffin` code has been parallelized using the message passage interface (`mpi`),[1] with an option to use Cray/SGI SHMEM when available, and its performance scales well to fairly large numbers of processors. The code has been parallelized along both poloidal mode number (k_y) and radial mode number (k_x), allowing it to employ a very large numbers of processors. Nonlinear results presented

---

[1] The electrostatic version of the code was made parallel by W. Dorland and Q. P. Liu. The electromagnetic enhancements were parallelized by W. Dorland and the author.

here include parallel runs on the Cray T3E and SGI Origin 2000 architectures, generally using 16, 32 or 64 processors, though performance of large runs scales well to larger numbers of processors. A typical scaling of performance with processor number is shown in Fig. 5.2. These runs use the parameters of the $\beta = 0.4\%$ case presented in the next section, with a resolution of $N_x = 85, N_y = 127, N_z = 64$. The performance of larger runs generally scales more favorably to larger numbers of processors. A scaling study by [Dorland 1999], employing a larger problem size, has found nearly linear parallel scaling up to 128 processors for a fixed sized run, and up to 512 processors for a case where the problem size scales with the number of processors employed ($N_{proc} \propto N_x N_y N_z$). Dorland's scaling study employed electrostatic `Gryffin` runs, but we expect electromagnetic runs to scale very similarly.

The data format of `Gryffin` has been converted to netCDF, and a graphical user interface has been written in Interactive Data Language (IDL) for post-processing.

5.2.1 Numerical Convergence

Numerical convergence of the electromagnetic `Gryffin` code has been tested in all three spatial dimensions as well as in the time step. The convergence tests here employ a parameter set used in the nonlinear simulations in Sec. 5.3, with $\beta = 0.4\%$ ($\beta/\beta_c = 0.36$), $\hat{s} = 1$, $q = 2$, $L_n/R = 1/3$, $\eta_i = \eta_e = 3$, and $r/R = 0$.

Fig. 5.3 illustrates numerical convergence in time step. The figure demonstrates that a factor of two reduction in the time step does not significantly change the time averaged transport. Furthermore, the fluctuation spectra and RMS values of the fluctuating quantities are also not significantly changed. The time steps used in the production simulations in the latter part of this chapter and in Ch. 6 vary somewhat with parameters, but generally fall within the range $\Delta t = 0.0025 \pm 0.0010\, L_n/v_{ti}$ typified by the larger time step in Fig. 5.3.

The convergence with perpendicular resolution is shown in Fig. 5.4a. Similar values of $k_{x max} \simeq 1.4$ and $k_{y_{max}} \simeq 1$ are used at all perpendicular grid sizes, and thus convergence with the spacing of modes in wavenumber space $(\Delta k_x, \Delta k_y)$ is

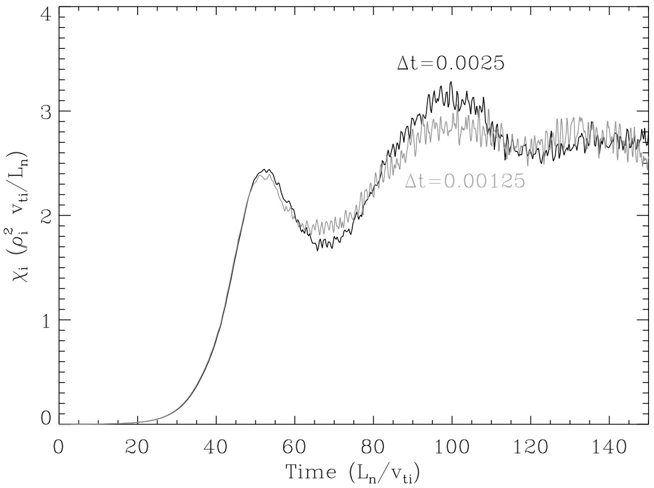

Figure 5.3: Numerical convergence in time step is illustrated with a plot of the ion heat conductivity as a function of time, employing numerical time steps which differ by a factor of two, $\Delta t = 0.0025\, L_n/v_{ti}$ and $\Delta t = 0.00125\, L_n/v_{ti}$. No significant change in the time averaged value of χ_i in the steady state, $t > 100\, L_n/v_{ti}$, is observed. The numerical resolution is $N_x = 85$, $N_y = 63$, $N_z = 16$.

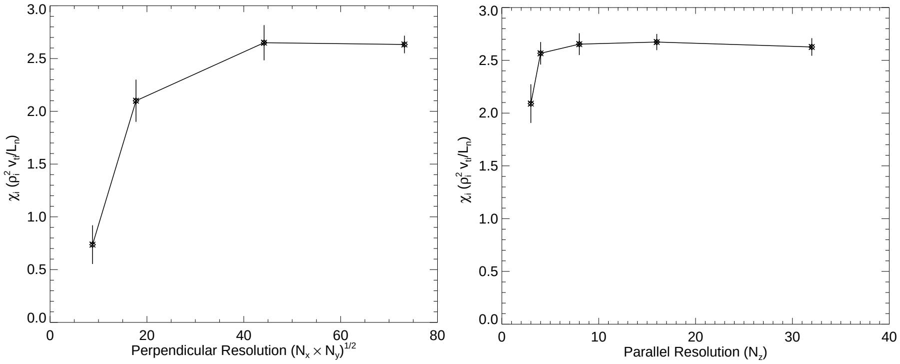

(a) (b)

Figure 5.4: The numerical convergence with perpendicular (a) and parallel (b) resolution is illustrated with a plot of ion heat conductivity (χ_i) averaged over the nonlinear steady state $[100 < t\,(L_n/v_{ti}) < 150]$ at varying resolutions, with an error bar indicating the RMS fluctuation level. Figure (a) shows four different perpendicular resolutions, $(N_x, N_y) = (11, 7), (21, 15), (63, 31), (85, 63)$, with no significant change in χ_i observed between the two highest resolutions. $N_z = 32$ and $\Delta t = 0.0025\, L_n/v_{ti}$ is used in all four cases. Figure (b) shows five parallel resolutions, $N_z = 3, 4, 8, 16, 32$, all with $N_x = 85$, $N_y = 63$ and $\Delta t = 0.0025\, L_n/v_{ti}$.

demonstrated. Extending the domain to somewhat larger $k_{x_{max}}$ and $k_{y_{max}}$ has been found to not significantly alter the results. The highest perpendicular resolution shown ($N_x = 85, N_y = 63$) is that used in the production runs in this chapter and Ch. 6. Convergence with parallel grid spacing (Δz) is illustrated by Fig. 5.4b. The simulations converge at a fairly low parallel resolution ($N_z > 8$), consistent with the expectation that the turbulence has an extended, ballooning structure along the magnetic field. Nonetheless, a somewhat higher parallel resolution ($N_z = 32$) is used in the production runs to attempt to insure adequate convergence in all regimes.

Numerical convergence in perpendicular box size is illustrated with contour plots of the turbulent ion density fluctuations in Fig. 5.5. Unlike the convergence tests discussed above, these runs include electron Landau damping and electron-ion collisions. The larger box size (a) is the resolution employed in the production simulations discussed in this chapter and in Ch. 6. The turbulent fluctuation spectra, as well as average transport levels, are virtually unchanged in the two cases.

5.3 Simulation Results

Previous gyrofluid simulations of core turbulence have generally been electrostatic, and have studied nonlinear physics exclusively in the $\beta \to 0$ limit. It is therefore of great interest to study the impact of finite β on turbulence and transport in typical tokamak parameter regimes.

A scan vs. β is performed, using β values ranging from 0 (electrostatic) up to very near the ideal MHD ballooning limit $\beta_c = 1.1\%$.[2] The remainder of the simulation parameters are chosen to be typical of the core of a large aspect ratio tokamak fusion plasma, and are held fixed as β is varied. The values chosen are

---

[2] This somewhat low value of β_c is due to the sharp gradients ($R/L_n = 3, R/L_T = 9$), and the lack of stabilizing factors such as elongation in this simple shifted circle equilibrium. It is important to keep in mind that it is the parameter $\alpha = q^2\beta_e/\epsilon_n\,[1 + \eta_e + \tau(1 + \eta_i)]$ which determines the MHD stability limit at a given $\hat{s}$, and for the given parameters, $\alpha = 48\,\beta$. In microinstability physics, the proximity to the β limit (β/β_c), which is proportional to α at a given $\hat{s}$, is the critical parameter, as explained in Sec. 2.3.

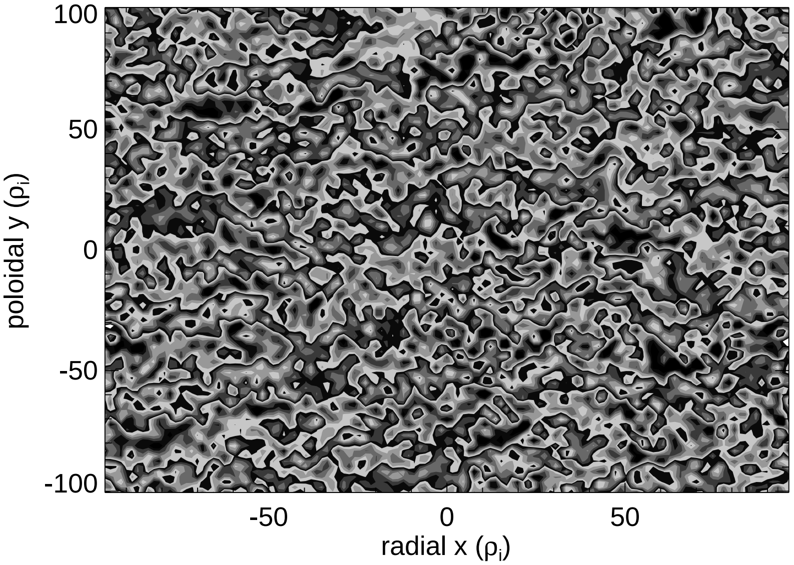

(a)

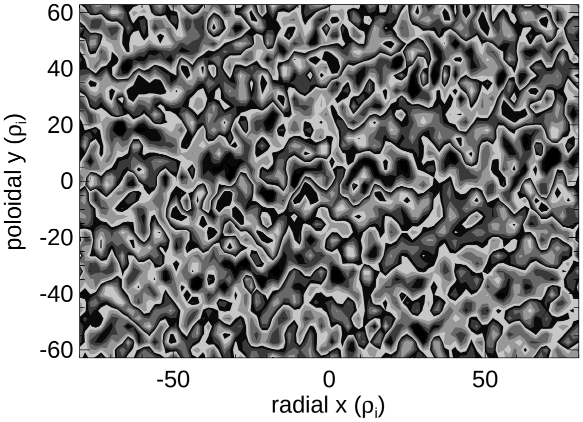

(b)

Figure 5.5: Numerical convergence in perpendicular box size is illustrated with contour plots of the turbulent ion density on the outer midplane ($\theta = 0$), at $t = 125\, L_n/v_{ti}$. Simulation parameters are from the $\beta = 0.4\%$ case discussed in Sec. 5.3, with electron Landau damping and electron-ion collisions included. The resolutions employed are (a) $N_x = 85, N_y = 63, N_z = 32$, and (b) $N_x = 63, N_y = 31, N_z = 32$. Contour levels are identical in the two plots.

$\hat{s} = 1$, $q = 2$, $L_n/R = 1/3$, $\eta_i = \eta_e = 3$, and $r/R = 0$,[3] where $\hat{s}$ is the magnetic shear, q is the safety factor, L_n is the electron density scale length, R is the plasma major radius, r is the plasma minor radius, and η_i and η_e are the ratios of L_n to the ion and electron temperature scale lengths L_{Ti} and L_{Te}. A single species of $Z = 1$ ions is assumed, with $\tau = T_{i0}/T_{e0} = 1$. The $s - \alpha$ model geometry is employed, with the Shafranov shift (α) parameter chosen to be consistent with β. For these parameters, $\alpha = q^2\beta_e/\epsilon_n\,[1 + \eta_e + \tau(1 + \eta_i)] = 48\,\beta$.

Nonlinear simulations have been performed both without (Sec. 5.3.1) and with (Sec. 5.3.2) electron dissipation, which enters through the electron Landau damping ($-\sqrt{\frac{\pi}{2\tau}\frac{m_e}{m_i}}|k_\parallel| u_{\parallel e}$) and electron-ion collision $[\nu_{ei}\frac{m_e}{m_i}(u_{\parallel e} - u_{\parallel i})]$ terms in Eq. 3.121. The deuterium/electron mass ratio is used to calculate these terms, along with a collisionality of $\nu_{ei} = 0.18$, in units of v_{ti}/L_n. This collisionality is chosen to be typical of a hot tokamak core plasma, and corresponds to $\nu_* \simeq 0.2$ at $r/R = 0.2$. Note that for these parameters, assuming a typical ballooning $k_\parallel \sim 1/qR$, the electron Landau damping term is roughly 70 times stronger than the electron-ion collision term, though it is weak compared to other terms in the electron momentum equation.

5.3.1 Simulations without Electron Dissipation

It is simplest to first investigate the case with no electron-ion collisions or electron Landau damping, formally the $m_e/m_i \to 0$ limit. The linear physics for this case is exhibited in Fig. 5.6. Linear growth rates and frequencies of the dominant mode are calculated using the initial-value electromagnetic gyrofluid code.

At $\beta = 0$, there is a strongly unstable ITG mode, which is stabilized by increasing β. This ITG instability is identified by its real frequency ($\omega \sim \omega_* \sim k_\theta\rho_i$ in the normalized units in the figure), and by noting that the instability can be stabilized by reducing η_i. The ITG mode is dominant up to $\beta \sim .8\%$ ($\beta/\beta_c \sim 0.7$). The kinetic shear Alfvén wave becomes unstable as the ideal MHD $\beta_c = 1.1\%$ is

---

[3] Setting $r/R = 0$ in the code eliminates the mirror force ($\nabla_\parallel \ln B$) terms and sets the trapped particle fraction to zero. This is an appropriate approximation near the core of most tokamaks. One reason for setting r/R exactly to zero, rather than to a small value, is to simplify comparisons with codes which do not include the mirror force or trapped particles.

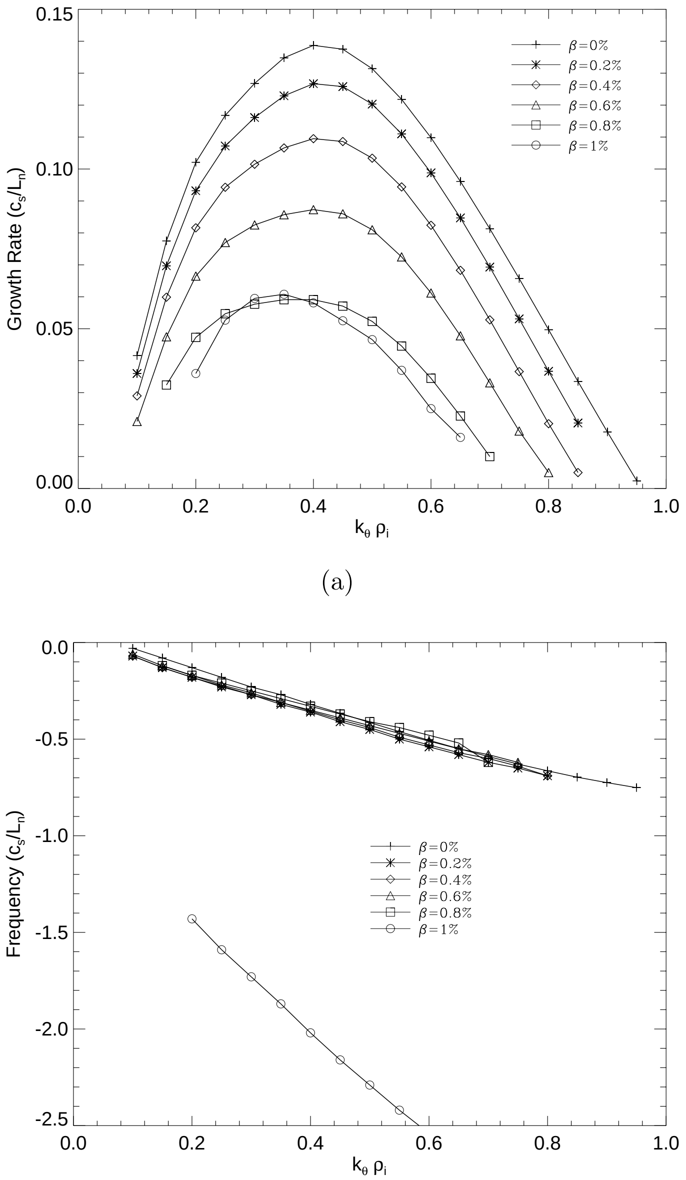

(a)

(b)

Figure 5.6: Linear growth rate (a) and frequency (b) spectra of the dominant mode at the six values of β which are used in nonlinear simulations. For $0 \leq \beta \leq 0.8\%$ ($0 \leq \beta/\beta_c \leq 0.73$) the ITG mode is dominant, while at $\beta = 1\%$ ($\beta/\beta_c = 0.91$) the kinetic shear Alfvén instability becomes dominant, as can be seen from the dramatic shift in frequency. The ideal MHD critical $\beta_c = 1.1\%$.

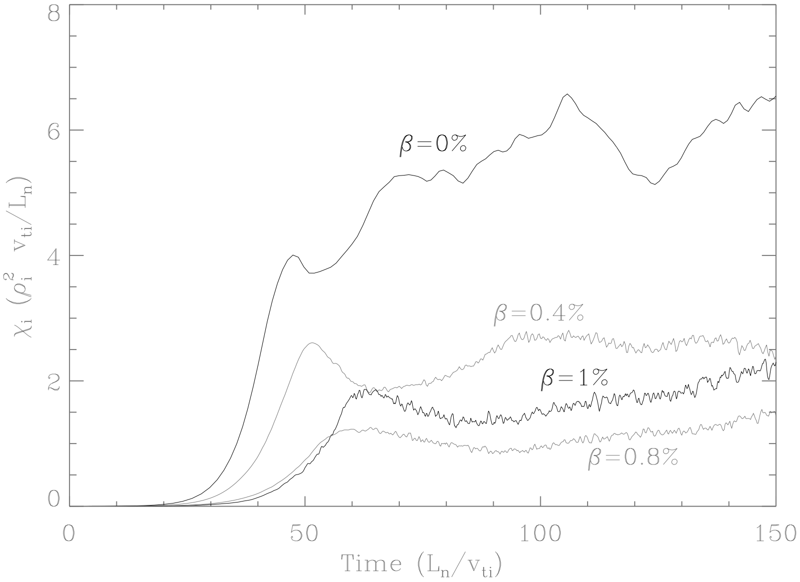

Figure 5.7: Time evolution of the ion heat conductivity (χ_i) in normalized units of ($\rho_i^2 v_{ti}/L_n$) for simulations at four values of $\beta = 0\%, 0.4\%, 0.8\%, 1\%$, with no electron dissipation. The ideal MHD $\beta_c = 1.1\%$, and at the given parameters, $\alpha = q^2\beta_e/\epsilon_n\,[1+\eta_e+\tau(1+\eta_i)] = 48\,\beta$.

approached, and its growth rate increases with β. While the Alfvén instability is destabilized near $\beta \sim .6\%$, it does not become the dominant instability until around $\beta \sim 1\%$ ($\beta/\beta_c \sim 0.9$). The dominance of the Alfvén instability at $\beta = 1\%$ is easily seen from Fig. 5.6b. A large jump in frequency occurs when the Alfvén instability becomes dominant, because for these parameters, the marginal frequency of the Alfvén instability [$\omega \sim \omega_{*pi} = (1+\eta_i)\,\omega_{*i} \sim -4\,k_\theta\rho_i$ in the normalized units of the figure] is much larger than the ITG frequency. Both modes propagate in the ion diamagnetic direction, which corresponds to a negative frequency in the convention used here.

The time evolution of the ion heat conductivity (χ_i) calculated from nonlinear gyrofluid simulations is shown in Fig. 5.7. In each case an initial exponential growth phase ends with a peak, followed by a relatively steady nonlinearly saturated state. The values of χ_i and other flux related quantities are generally averaged over the steady state phase, which here begins at $t \sim 100\,L_n/v_{ti}$.

Fig. 5.8 shows the corresponding time evolution of the ion density fluctuation

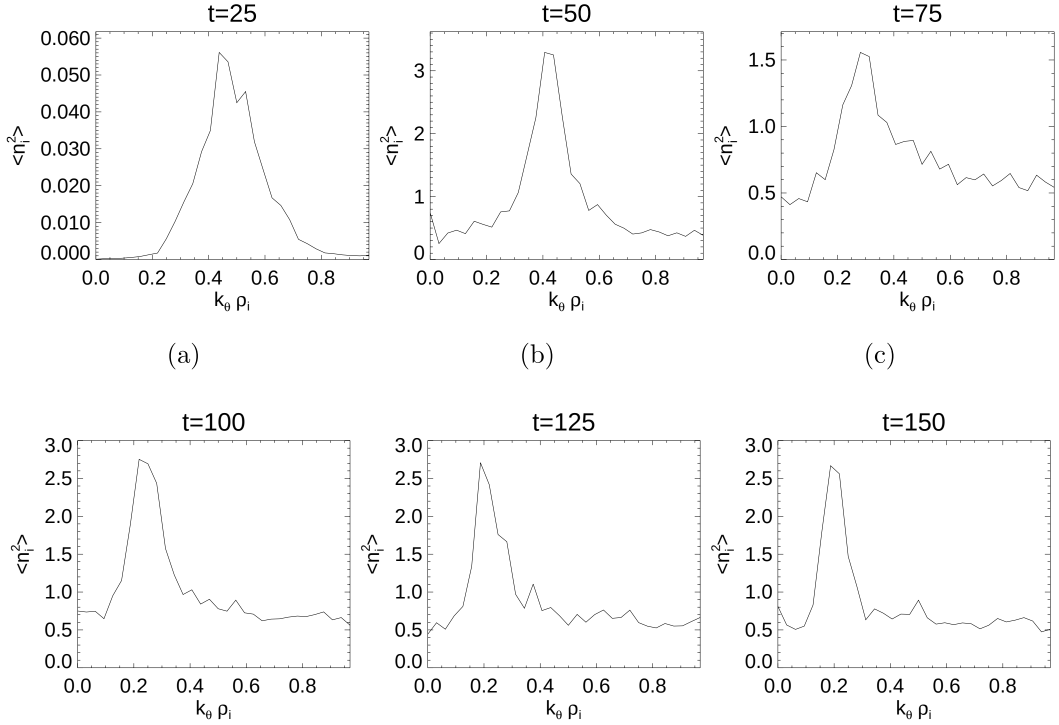

(a) (b) (c)

(d) (e) (f)

Figure 5.8: The time evolution of the ion density fluctuation spectrum $\langle n_i^2(k_\theta)\rangle$, is illustrated for $\beta = 0.4\%$ ($\beta/\beta_c = 0.36$). The six values of time are, in normalized units of L_n/v_{ti}, t=25 (a), t=50 (b), t=75 (c), t=100 (d), t=125 (e), and t=150 (f). The spectrum initially peaks near the maximum of the linear growth rate spectrum at $k_\theta\rho_i \simeq 0.4$, before a shift to longer wavelengths occurs, resulting in a peak at $k_\theta\rho_i \simeq 0.2$ in the nonlinear steady state ($t > 100$).

spectrum, $\langle n_i^2(k_\theta)\rangle$, for one of the cases, $\beta = 0.4\%$ ($\beta/\beta_c = 0.36$). At $t = 25$, the simulation is in the linear, exponential growth phase, and the peak in the spectrum coincides with the maximum linear growth rate of $k_\theta \rho_i \simeq 0.4$. At $t = 50$ the simulation has reached its initial peak in χ_i, and the nonlinear phase has begun. At $t = 75$ the shift to longer wavelengths is underway, and by $t = 100$ the simulation has settled into an approximately steady state with a peak in the spectrum near $k_\theta \rho_i \simeq 0.2$. This characteristic nonlinear downshift in the peak of the fluctuation spectrum has been seen in electrostatic simulations by several authors [Parker et al. 1993; Dimits et al. 1994; Beer 1995], and its characteristics do not change significantly for the electromagnetic case shown here. The observed downshift may be due to an inverse cascade, or it may simply be related to the fact that low k_θ modes have larger mixing length saturation amplitudes ($\sim \gamma/k_\perp^2$) but also have lower growth rates and thus take longer to reach saturation.

The time-averaged χ_i is plotted as a function of β in Fig. 5.9. Two mixing-length estimates of the expected χ_i are shown for comparison. The dotted line is a very simple estimate, $c_1 \gamma_{max}/k_\theta^2$, where γ_{max} is the maximum linear growth rate from Fig. 5.6a, k_θ is the poloidal wave number at which the maximum growth rate occurs, and the coefficient $c_1 = 7.7$ is chosen so that the mixing length estimate agrees with the simulation at $\beta = 0$.

There is rough agreement between the simulation results, and expectations based on this simple mixing length estimate. As expected, at low values of β, χ_i decreases with β, as the ITG mode driving the turbulence is stabilized by increasing β. However, the reduction in χ_i is significantly larger than would be expected from the reduction in the linear ITG growth rate.

As β approaches the ideal MHD critical $\beta_c = 1.1\%$, χ_i begins to increase with β, as expected from the onset of kinetic Alfvén instability. This turnaround appears to occur at a somewhat lower β value than would be expected from linear theory. A comparison of the $\beta = 0.6\%$ and $\beta = 0.8\%$ cases in Figs. 5.6 and 5.9 reveals that while the linear growth rate of the dominant ITG mode has decreased significantly, χ_i is virtually unchanged. We believe this behavior is related to the kinetic Alfvén instability. While the Alfvén instability is subdominant to the ITG mode at $\beta = 0.8\%$, the Alfvén wave is nonetheless unstable with a significant growth

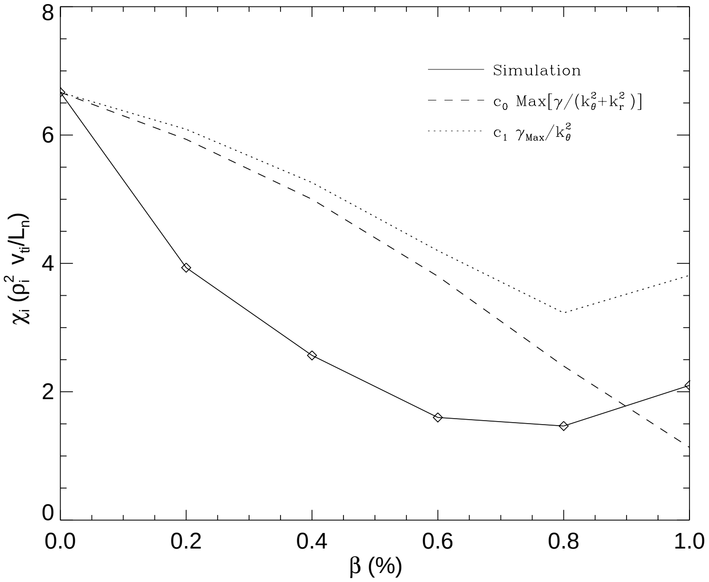

Figure 5.9: Ion heat conductivity (χ_i) from gyrofluid simulations with no electron dissipation is plotted vs. β. A simple mixing length estimate based on γ_{max}/k_θ^2, and a mixing length estimate based on $(\gamma/\langle k_\perp^2\rangle)_{max}$, both fitted to the simulation flux at $\beta = 0$, are shown for comparison. The ideal MHD $\beta_c = 1.1\%$, and at the given parameters, $\alpha = q^2\beta_e/\epsilon_n\,[1+\eta_e+\tau(1+\eta_i)] = 48\,\beta$.

rate, providing an additional drive for turbulence.[4] This Alfvén drive appears to lead to nonlinear saturation at somewhat higher amplitudes.

The dashed line shown in Fig. 5.9 is a different mixing length estimate based on the maximum over all k_θ of the function $\gamma(k_\theta)/\left\langle k_\perp^2 \right\rangle$, where $\left\langle k_\perp^2 \right\rangle = k_\theta^2(1+\hat{s}^2 \left\langle \theta^2 \right\rangle)$ is averaged over the linear eigenmode. Again a multiplicative coefficient $c_0 = 6.7$ is chosen so as to make the estimate agree with the simulation at $\beta = 0$, so that the impact of finite-β on the simulation results can be compared with that expected from mixing length theory. The maximum of $\gamma/\left\langle k_\perp^2 \right\rangle$ occurs here at rather long wavelengths, $.13 < k_\theta\rho_i < .17$, and hence exhibits somewhat different behavior from the estimate based on γ_{max}/k_θ^2. In particular, while the kinetic Alfvén ballooning mode is dominant for $k_\theta\rho_i > .2$ at $\beta = 1\%$, this mode has a very small growth rate at the lower values of k_θ where $\gamma/\left\langle k_\perp^2 \right\rangle$ has its maximum. Hence $Max(\gamma/\left\langle k_\perp^2 \right\rangle)$ continues to decrease with β due to the finite-β stabilization of the ITG mode, all the way up to $\beta = 1\%$. Therefore this estimate is unable to account for the increase in ion heat transport seen in the simulations at $\beta \sim 1\%$.

The steady state ion density fluctuation spectra $\left\langle n_i^2(k_\theta) \right\rangle$ at four values of $\beta = 0\%, 0.4\%, 0.8\%, 1\%$ are shown in Fig. 5.10. The peak in the fluctuation spectrum occurs in all cases near $k_\theta\rho_i \simeq 0.2$, well below the peaks of the linear growth rate spectra shown in Fig. 5.6. We note that the shape of these spectra qualitatively agree, in both the electrostatic and finite-β cases, with the spectra measured on TFTR by [Fonck et al. 1993]. Note also that the peaks in the steady state spectra occur not far from the value of $k_\theta\rho_i$ at which the maximum of $\gamma/\left\langle k_\perp^2 \right\rangle$ occurs, $k_\theta\rho_i = .13, .15, .16, .16$ respectively. The most notable finite-β effect is a significant narrowing of the peak, particularly for the two cases in which we believe the kinetic ballooning mode drive plays an important role in determining the steady state ($\beta = .8\%, 1\%$). This narrowing of the peaks as the ideal MHD $\beta_c = 1.1\%$ is approached appears to be qualitatively consistent with the experimental observation [Evensen et al. 1998] of narrower peaks in the edge region, where the plasma is generally closer to the ideal β_c, than in the core.

---

[4] At $\beta = 0.6\%$ the Alfvén growth rate is very small and is unlikely to significantly impact the nonlinear saturated state.

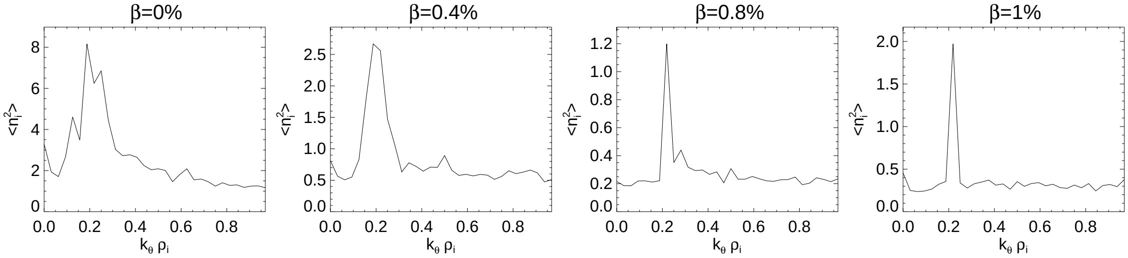

(a) (b) (c) (d)

Figure 5.10: Ion density fluctuation spectra, $\langle n_i^2(k_\theta)\rangle$, in the nonlinear saturated state, are plotted at $\beta = 0\%$ (a), $\beta = .4\%$ (b), $\beta = .8\%$ (c), and $\beta = 1.0\%$ (d). The ideal MHD $\beta_c = 1.1\%$.

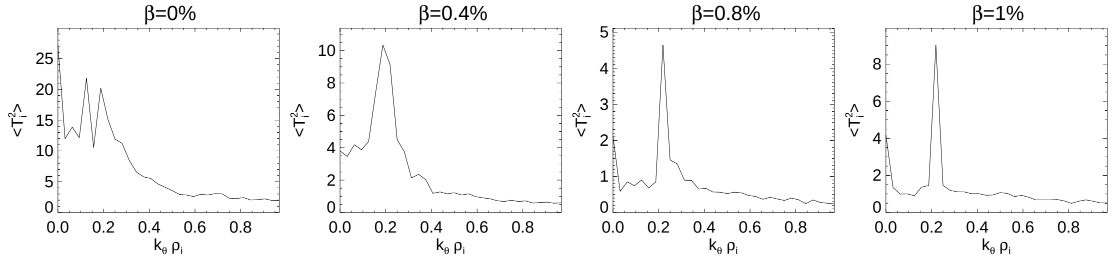

(a) (b) (c) (d)

Figure 5.11: Ion perpendicular temperature fluctuation spectra, $\langle T_{\perp i}^2(k_\theta)\rangle$, in the nonlinear saturated state, are plotted at $\beta = 0\%$ (a), $\beta = .4\%$ (b), $\beta = .8\%$ (c), and $\beta = 1.0\%$ (d). The ideal MHD $\beta_c = 1.1\%$.

Fig. 5.11 shows the steady state ion perpendicular temperature fluctuation spectra $\langle T_{\perp i}^2(k_\theta)\rangle$, at the same four values of $\beta = 0\%, 0.4\%, 0.8\%, 1\%$. The spectra are similar to the density fluctuation spectra, except for the larger magnitude of the fluctuations. Both $n_i = (L_n/\rho_i)\,\tilde{n}_i/n_{0i}$ and $T_{\perp i} = (L_n/\rho_i)\,\tilde{T}_{\perp i}/T_{0i}$ have been normalized to their equilibrium values, and their relative magnitudes can be usefully compared. Comparing Fig. 5.11 with Fig. 5.10, we find that the relative value of the RMS fluctuations at the peaks, $\sqrt{\langle T_{\perp i}^2(k_\theta)\rangle_{Max}}/\sqrt{\langle n_i^2(k_\theta)\rangle_{Max}}$ is roughly $1.6, 1.9, 2.0$, and 2.1 for the four cases.[5]

The similarity in shape between the ion density and temperature fluctuation spectra, the size of the ratio $\sqrt{\langle T_{\perp i}^2(k_\theta)\rangle}/\sqrt{\langle n_i^2(k_\theta)\rangle} \sim 2$, and the fact that the ratio changes little with β all appear to be consistent with the observations of [Evensen et al. 1998]. The BES and CHERS measurements in TFTR discussed by [Evensen et al. 1998] found that the ion temperature fluctuation spectrum is similar in shape to the ion density fluctuation spectrum across the plasma radius, and that the measured ratio, $(\tilde{T}/T_0)/(\tilde{n}_i/n_0) = 2 \pm .5$, varies little from the core (where the plasma is likely to be further from β_c) to the edge (where the plasma is likely to be close to β_c).[6] Note that only β is varied in this set of simulations, while the other parameters have been held fixed. A more thorough investigation of the agreement between simulation and experiment would use the measured equilibrium parameters at different radii and compare simulation results to measurements at the same radius. Nonetheless, the agreement with several observed trends is quite encouraging.

The transition from ITG-driven turbulence ($\beta = 0\%$) to Alfvénic turbulence

---

[5] The perpendicular temperature has been used because it is the dominant component of $T = 2/3\,T_\perp + 1/3\,T_\parallel$ and because it is easily extracted from the code data set. However, there is significant anisotropy in the fluctuating ion temperature, and using the total T rather than $T_\perp$ would moderately reduce the ratio of temperature fluctuations to density fluctuations. For the finite β cases, the ratio still falls within the observed range of $2 \pm .5$. Note also that adding electron dissipation, as in Sec. 5.3.2, tends to increase the ratio somewhat. A more detailed comparison of simulations to the results of [Evensen et al. 1998] is expected in the near future.

[6] Note that the apparent agreement between the electromagnetic gyrofluid simulations and the measurements is in contrast to disagreement between the linear-theory based predictions discussed in [Evensen et al. 1998] and the measurements. The linear and quasi-linear theory was unable to predict the observed trend of $(\tilde{T}/T_0)/(\tilde{n}_i/n_{i0}) \sim 2$ independent of radius.

($\beta = 1\%$) is illustrated in Fig. 5.12.[7] The figure shows equipotential contours at $\theta = 0$, plotted against radius and time. The most notable feature of the transition is the dramatic reduction in correlation times with increasing β. The dominant time-scale of the turbulence (measured by the typical length in the time direction of equipotential surfaces) drops from $\Delta t \simeq 5 - 15$ in the electrostatic ($\beta = 0$) case to $\Delta t \simeq 1 - 3$ at $\beta = 1\%$. This difference is roughly proportional to the difference in frequency between the ITG mode and the kinetic Alfvén instability (which is linearly dominant only at $\beta = 1\%$, but is unstable and subdominant at $\beta = 0.8\%$), shown in Fig. 5.6b. Note that the short time scales of the "Alfvénic" turbulence appear to be dominant at $\beta = 0.8\%$ as well as $\beta = 1\%$.

5.3.2 Simulations with Electron Dissipation

The impact of electron dissipation is assessed by including the electron Landau damping and electron-ion collision terms derived in Sec. 3.3.3. The deuterium to electron mass ratio is used to calculate these terms, along with a collisionality of $\nu_{ei} = 0.18$, in units of v_{ti}/L_n.

The linearly stabilizing effect of electron Landau damping and electron-ion collisions is illustrated in Fig. 5.13. At all values of β studied, the inclusion of electron dissipation significantly reduces the maximum linear instability growth rate, though it also reduces the value of k_θ at which the maximum occurs. The overall impact on a linear mixing length transport estimate is shown in Fig. 5.15.

The nonlinear time evolution of the ion heat conductivity χ_i is shown for four values of β in Fig. 5.14. Note that in the electrostatic case ($\beta = 0$), adiabatic electrons are used, and therefore the $\beta = 0$ trace is identical to that in Fig. 5.7.

The average value of the steady state χ_i is plotted as a function of β in Fig. 5.15. Also shown is a mixing length estimate of χ_i proportional to the maximum of $\gamma / \langle k_\perp^2 \rangle$, with a multiplicative coefficient, $c_0 = 6.7$, chosen so that the mixing length estimate agrees with the simulation χ_i at $\beta = 0$. The mixing length estimate

---

[7] A better illustration is provided in Fig. 5.16 for the case with electron dissipation. The qualitative features of the transition to Alfvénic turbulence are identical with or without electron dissipation.

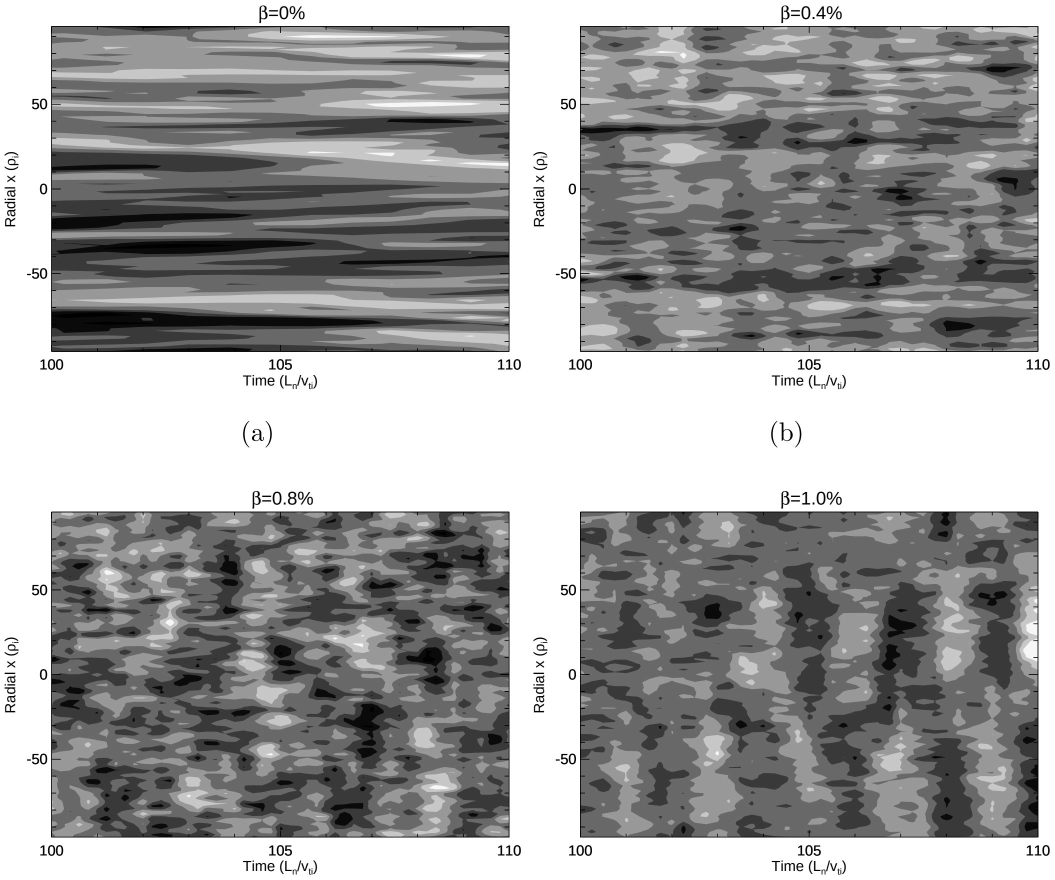

(a) (b)

(c) (d)

Figure 5.12: Equipotential contours are plotted vs. radius and time at $\theta = 0$, for the case without electron dissipation. The contours follow the evolution of turbulent eddies, and illustrate the reduction in turbulent correlation times that occurs with increasing β/β_c.

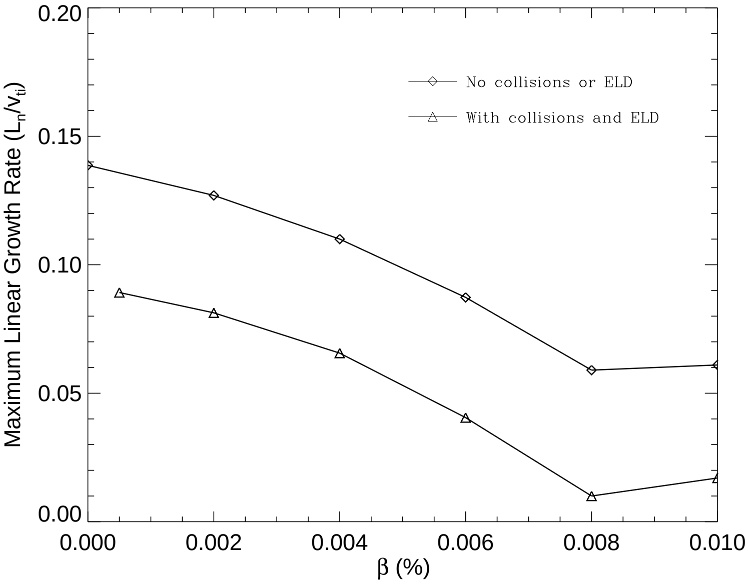

Figure 5.13: The maximum linear instability growth rate, $Max\{\gamma(k_\theta)\}$, is plotted as a function of β for cases both with and without electron dissipation, which enters through electron Landau damping and electron ion collisions. The deuterium/electron mass ratio is used calculate these terms, along with a normalized collisionality $\nu_{ei} = .18\, v_{ti}/L_n$. Electron dissipation reduces the maximum growth rate at all values of β shown. The ideal MHD $\beta_c = 1.1\%$.

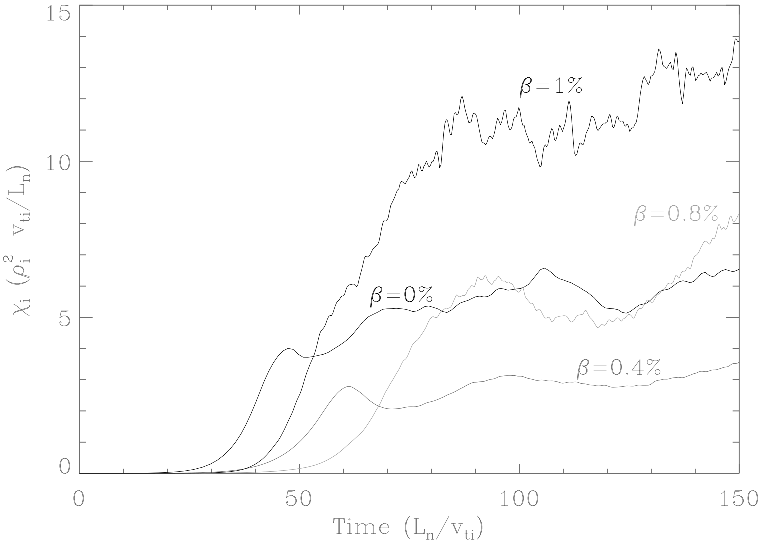

Figure 5.14: Time evolution of the ion heat conductivity (χ_i) in normalized units of $(\rho_i^2 v_{ti}/L_n)$ for simulations at four values of $\beta = 0\%, 0.4\%, 0.8\%, 1\%$, with electron dissipation. The ideal MHD $\beta_c = 1.1\%$, and at the given parameters, $\alpha = q^2\beta_e/\epsilon_n\left[1 + \eta_e + \tau(1 + \eta_i)\right] = 48\,\beta$.

accounts for the initial trend of χ_i decreasing with β at $\beta \leq 0.6\%$ quite well, but is dramatically in error for $\beta \geq 0.8\%$ $(\beta/\beta_c \geq 0.73)$.

The inclusion of electron Landau damping and electron-ion collisions reduces both the maximum linear growth rate (shown in Fig. 5.13) and the maximum of $\gamma/\left\langle k_\perp^2\right\rangle$ at all values of β shown,[8] as can seen by comparing the dashed lines in Figs. 5.15 and 5.9.

Nonlinearly, the effect of the electron Landau damping and electron-ion collision terms can be quite significant. Comparing the solid lines in Figs. 5.15 and 5.9, we see that at small values of $\beta \lesssim 0.6\%$, χ_i is not strongly affected by the inclusion of electron dissipation. However, at larger values of β, the effect is dramatic. Increases in χ_i by a factor of ~ 5 at $\beta = 0.8\%$ and a factor of ~ 8 at $\beta = 1\%$ are seen with the inclusion of electron Landau damping and electron-ion collisions.

---

[8] Except of course for $\beta = 0$ where adiabatic electrons are used.

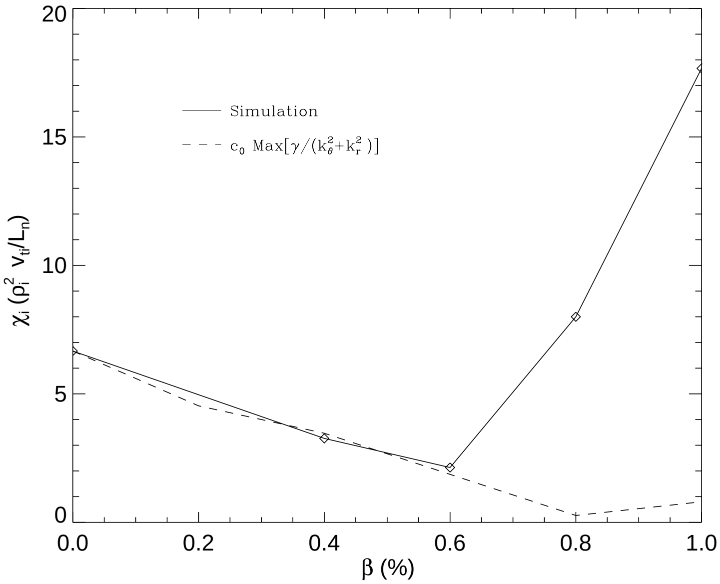

Figure 5.15: Ion heat conductivity (χ_i) from gyrofluid simulations with electron Landau damping and electron-ion collisions is plotted vs. β. A mixing length estimate based on $Max(\gamma/\langle k_\perp^2\rangle)$, fitted to the simulation flux at $\beta = 0$, is shown for comparison.

A firm explanation for this dramatic increase in χ_i at high β/β_c, in the presence of electron Landau damping and electron-ion collisions, has not yet been established, and is an important avenue for future work, as discussed in Sec. 7.2. However, possible explanations involving zonal flow dynamics have been suggested by [Waltz 1998; Diamond 1998; Das et al. 1999] and others. Collisions increase the size of the non-adiabatic electron component, and non-adiabatic electron dynamics are thought to limit the inverse cascade which drives the zonal flows. Furthermore, collisions can directly damp the otherwise weakly or un-damped components of the zonal flows, as noted by [Lin et al. 1999; Diamond et al. 1998]. This damping, in conjunction with electromagnetic effects on zonal flows discussed by [Das et al. 1999], may hinder zonal flow generation. In particular, [Das et al. 1999] note that magnetic stresses compensate electrostatic stresses and reduce the zonal flow amplification, effectively quenching zonal flow generation for purely Alfvénic turbulence. Thus in the two highest β cases, which seem to be dominated by “Alfvénic” turbulence [$\psi = (\omega/k_\parallel)A_\parallel \sim \phi$], it is possible that zonal flow generation is weak, and that the additional zonal flow damping provided by collisions is sufficient to prevent zonal flows from saturating the turbulence until it reaches very large amplitudes. Further work on both simulations and theory is needed to determine whether such a mechanism is correct, or whether another, such as the stabilization of secondary Kelvin-Helmholtz instabilities in finite-β cases with dissipation, suggested by [Rogers and Drake 1997], might be important.

The behavior of χ as a function of $\beta/\beta_c \propto \alpha_{MHD}$ shown in Fig. 5.15 offers a possible explanation for a number of trends observed in experiments. For example, it might provide an explanation for the ubiquitous trend of χ_i increasing with radius near the edge of tokamak experiments.[9] Because of sharp gradients and high q, the edge plasma is often close to ideal MHD instability. Hence, sharp increases in χ_i as the ideal β limit is approached ($\beta_c = 1.1\%$ in Fig. 5.15) would be expected to increase predicted transport in the edge region. This possibility is explored via a direct comparison of simulation results to measured transport in the outer region of a TFTR L-mode plasma in Ch. 6.

Fig. 5.16 shows equipotential contours at $\theta = 0$ plotted as a function of radius and time, at four values of $\beta = 0\%, 0.4\%, 0.8\%, 1\%$, for simulations including electron Landau damping and electron-ion collisions. Note that a much longer time period is shown here than in Fig. 5.12 for the case without electron dissipation. Again there is a marked reduction in the dominant time-scale of the turbulence (measured by the typical length in time of equipotential surfaces) from $\Delta t \simeq 5-15$ in the electrostatic ($\beta = 0$) case to $\Delta t \simeq 1-3$ at $\beta = 1\%$, which is roughly proportional to the difference in frequency between the ITG and kinetic shear Alfvén modes. The qualitative transition to "Alfvénic" time-scales appears to have largely occurred by $\beta = 0.8\%$, even though the ITG mode in linearly dominant until $\beta \simeq 1.0\%$.

Thus far we have focused on ion heat conductivity (χ_i), primarily because this has been the focus of previous ITG-based transport simulation efforts. This is in part because electrostatic simulations which use a purely adiabatic electron response ($n_e \propto \phi$) cannot predict either particle transport or electron thermal transport.

---

[9] Electrostatic simulations generally predict a small χ_i which decreases with radius near the edge.

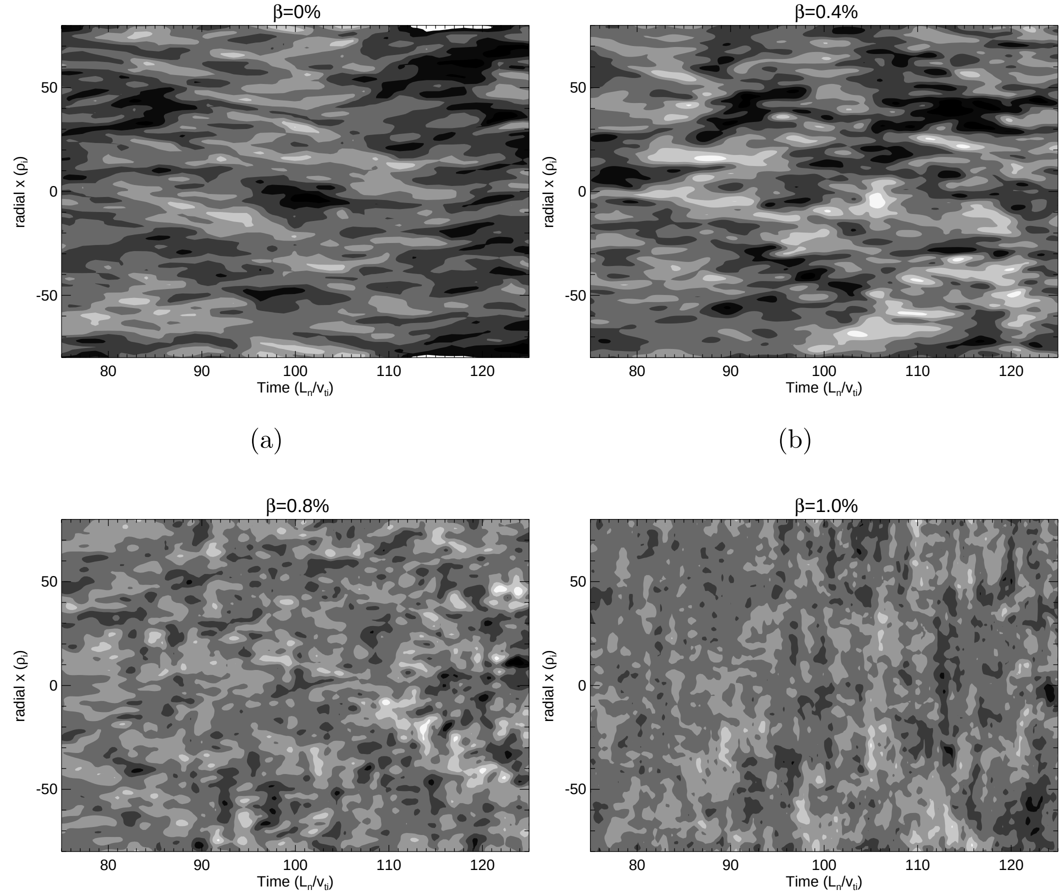

(a) (b)

(c) (d)

Figure 5.16: Equipotential contours are plotted vs. radius and time at $\theta = 0$, for the case with electron dissipation. The contours follow the evolution of turbulent eddies, and illustrate the reduction in turbulent correlation times that occurs with increasing β. The ideal MHD $\beta_c = 1.1\%$.

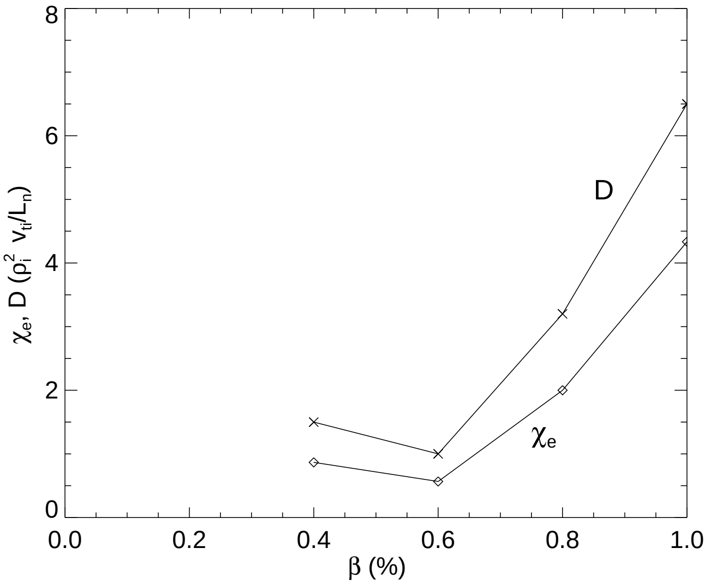

Figure 5.17: Particle diffusivity (D) and electron heat conductivity (χ_e) from gyrofluid simulations with electron Landau damping and electron-ion collisions is plotted as a function of β. The ideal MHD $\beta_c = 1.1\%$.

Because cross-field transport is driven by $\mathbf{E} \times \mathbf{B}$ convection,[10] and $v_{Er} \sim \frac{\partial}{\partial\theta}\phi$, any part of a field which is proportional to ϕ has a flux surface averaged cross field flux proportional to $\int \phi \frac{\partial\phi}{\partial\theta} d\theta$ which is exactly zero. Electron temperature fluctuations are zero in a simulation with purely adiabatic electrons, and thus electron thermal transport must also be taken to be zero ($\chi_e = 0$).

In electromagnetic simulations using the electron model derived in Ch. 3, the electron response is no longer entirely adiabatic, and electron temperature fluctuations are incorporated, so that both a finite particle diffusivity D (identical for electrons and ions for the single ion species cases considered here), and an electron heat conductivity χ_e are well defined. All of the fluxes (Q_i, Q_e, and Γ) are found to be dominated by $\mathbf{E} \times \mathbf{B}$ convection, with the magnetic flutter contribution finite but negligible.

The electron thermal conductivity χ_e and the particle diffusivity D, which

---

[10] In the electromagnetic case there is an additional "magnetic flutter" transport term proportional to $\left\langle u_\parallel \frac{\partial}{\partial\theta} A_\parallel \right\rangle$. This term has been calculated in the gyrofluid simulations, but found to be small (generally $\sim$ 2 orders of magnitude smaller than the $\mathbf{E} \times \mathbf{B}$ convected flux) for the cases considered here.

is the same for ions and electrons in this two species case, are shown in Fig. 5.17, for the case with electron Landau damping and electron-ion collisions.[11] While χ_e is significantly smaller than χ_i (shown in Fig. 5.15), it is of the same order of magnitude, as is the particle diffusivity. This behavior is fairly typical of measured transport in tokamak experiments, except in some enhanced confinement regimes.

---

[11] The code calculates a very small, but finite particle and electron heat flux for the case without electron dissipation. Preliminary quasilinear estimates do not contradict this result. However, deeper theoretical understanding would be desirable in the future because there is reason to suspect, based on arguments similar to that presented in Appendix B, that the particle flux should be zero in this case.

Chapter 6

Comparison with Experiment

COMPARISON with experimental data provides the ultimate test of the validity and relevance of simulation results. Direct comparisons between toroidal electromagnetic simulations and tokamak data are presented in this chapter, along with suggested directions for future comparisons.

As discussed in Sec. 1.1.2, there have been a number of comparisons between electrostatic gyrofluid simulations and experimentally measured transport fluxes. These have involved both direct comparisons, and indirect comparisons using parametric transport models, such as GLF23 [Waltz et al. 1997] and IFS-PPPL [Kotschenreuther et al. 1995], which use gyrokinetic calculations of linear growth rates and quasilinear transport fluxes, with mixing length characterizations of the nonlinear saturation level fit to toroidal gyrofluid simulations [Beer 1995].

Electromagnetic effects can significantly modify the gyrofluid simulation results, as demonstrated in Ch. 5. The inclusion of magnetic fluctuations and non-adiabatic passing electrons may allow the simulations to more accurately describe and predict transport in the core region of tokamaks, as well as extending the regime of validity of the simulations further toward the plasma edge. Improvements in the accuracy of direct comparisons with measured fluxes, as well as the eventual development of more accurate parametric transport models are expected.

In Ch. 5, two sets of nonlinear simulations scanning over the parameter $\beta \propto \alpha_{MHD}$ are presented, and a number of qualitative similarities between the simulation results and the fluctuation measurements of [Fonck et al. 1993; Evensen et al. 1998] are discussed. Here a simple, more direct comparison between experiment and gyrofluid simulations is undertaken. Measured temperature, density, and magnetic field profiles are used as input equilibrium parameters for electromagnetic gyrofluid simulations. The ion and electron heat fluxes predicted by the simulations are then compared to the heat fluxes inferred from power balance using experimental measurements.

While these simulations incorporate important electromagnetic and non-adiabatic passing electron physics not considered in prior investigations, they are by no means complete in all respects. Rather, they represent a demonstration of the current status and capabilities of the electromagnetic simulation code. Future avenues for further improvement are mentioned here and discussed further in Sec. 7.2.

The comparison uses TFTR L-mode shot #65018, with the input parameters coming from `SNAP` try 3. The shot is similar to #65012 discussed in [Scott et al. 1993]. Deuterium is the primary ion species, and heating is provided by 14MW of deuterium neutral beams. The plasma major radius $R = 2.45m$, the minor radius $a = 0.80m$, and the toroidal field on axis $B_0 = 4.75T$. Measured equilibrium profiles are shown in Figs. 6.1-6.3.

This shot has been chosen primarily because it was the subject of an extensive set of comparisons with electrostatic gyrofluid simulations, presented in Ch. 6 of [Beer 1995]. Beer compared the experimentally inferred χ_i and χ_e to that predicted by a set of electrostatic gyrofluid simulations with trapped electrons at several radial points throughout the plasma. Taking into account a number of factors, including uncertainty in measured equilibrium gradients, and the presence of sawtooth modes in the center ($r/a < .25$) of the plasma, Beer concluded that the results of the simulations were broadly consistent with the experiment in the core region, $r/a < .7$. However, as Beer states, “outside $r/a = .7$, the predicted χ is clearly too low.” Furthermore, while the experimental χ increases sharply with radius outside $r/a = .7$, the electrostatic simulations exhibit the opposite trend.

The electromagnetic simulations shown here focus on the outer region, $.75 < r/a < .95$. A primary goal is to determine to what extent the inclusion of electro-

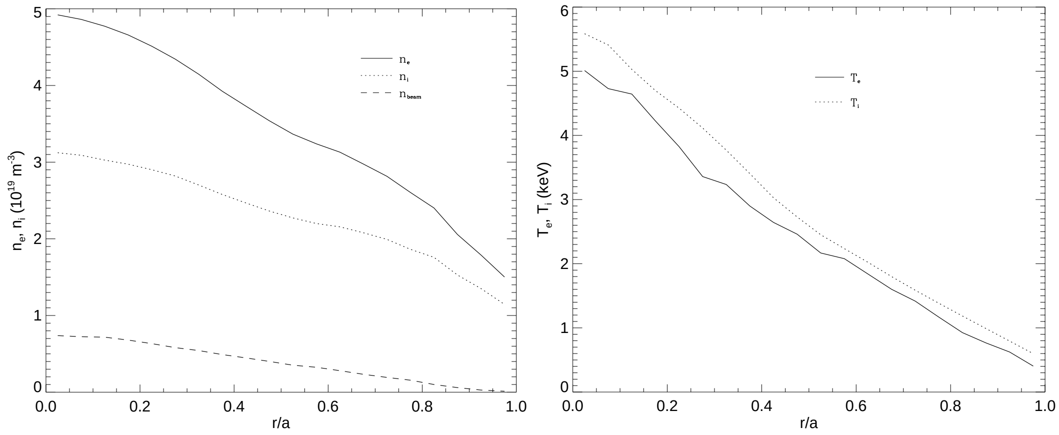

(a) (b)

Figure 6.1: Measured electron (solid), ion (dotted), and beam (dashed) density profiles (a), and electron and ion temperature profiles (b) for TFTR shot #65018.

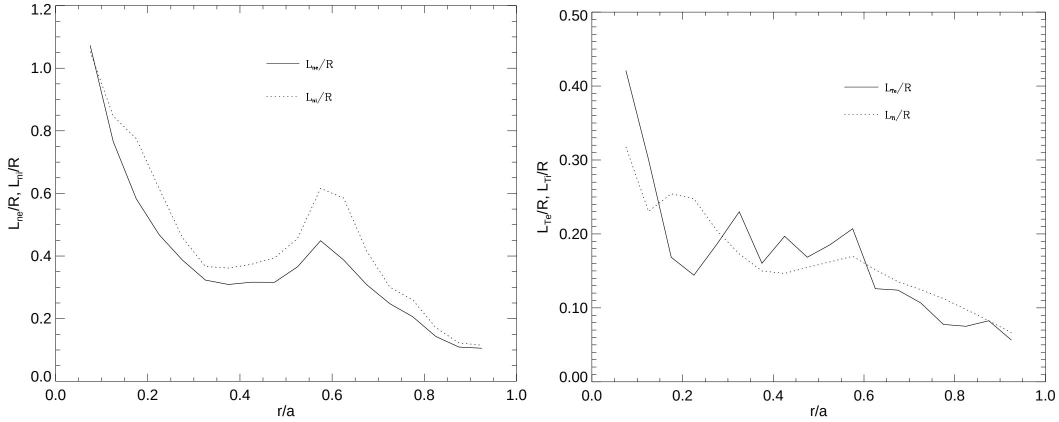

(a) (b)

Figure 6.2: Measured electron and ion density (a) and temperature (b) scale lengths for TFTR shot #65018.

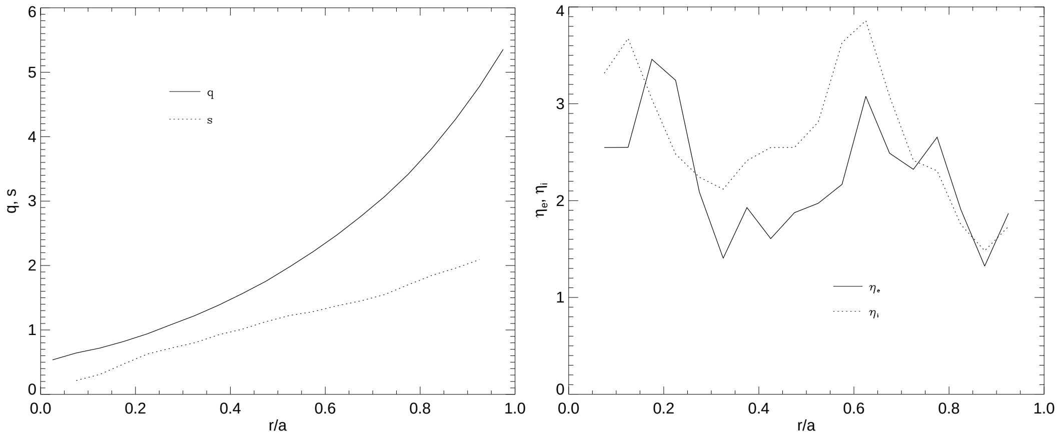

(a) (b)

Figure 6.3: Measured radial profiles of the safety factor q and magnetic shear $\hat{s}$ (a), and profiles of $\eta_i = L_{ni}/L_{Ti}$ and $\eta_e = L_{ne}/L_{Te}$ for TFTR shot #65018.

magnetic effects allows improved predictions of the value of χ in this region, and leads to an understanding of the ubiquitous trend of χ increasing with radius, seen in the edge of many tokamaks. It might at first seem surprising to suggest that electromagnetic effects would be important in the edge region, given the small values of plasma β, as shown in Fig. 6.4a. However, it is not β itself, but rather the MHD ballooning parameter $\alpha = -q^2 R\beta'$ which provides a good estimate of the drive for the Alfvén ballooning instability, and of the overall importance of electromagnetic effects.[1] Due to high q and very sharp density and temperature gradients in the edge, α increases with radius, despite the drop in β, as shown in Fig. 6.4b.

Flux tube simulations are performed, using an $s - \alpha$ equilibrium model, with the flux tubes centered at four values of $r/a = 0.775, 0.825, 0.875$, and 0.925, for which `SNAP` data is available. The electromagnetic simulations employ the full electron physics model derived in Sec. 3.3.2, including electron Landau damping and electron-ion collisions, using the measured collisionality. Ion-ion collisions have been neglected, as have trapped electrons. This shot has a fairly low impurity concentration ($Z_{eff} = 1.73$), and impurities are not considered in the analysis. The beam density is very small for $r/a > .75$, as shown in Fig. 6.1, and is neglected.

---

[1] A full kinetic analysis shows that other parameters, including η_i play an important role as well, as discussed in Secs. 2.1 and 2.3.

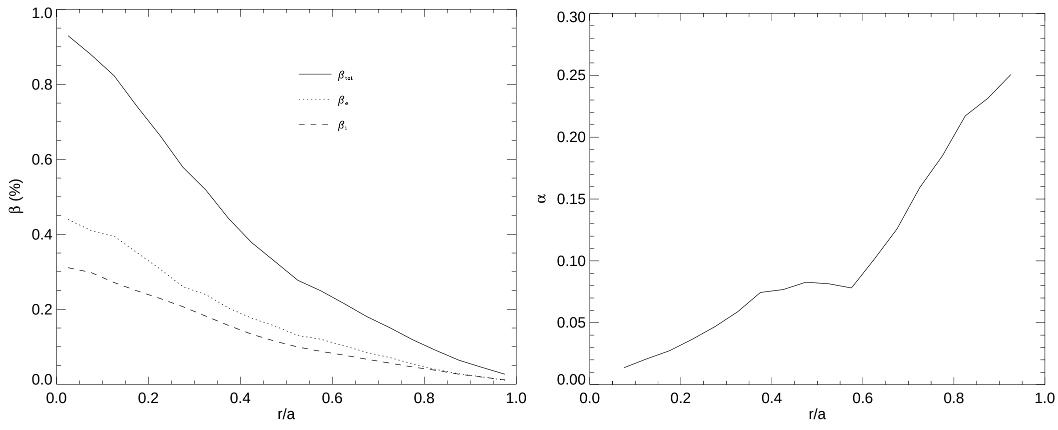

(a)

(b)

Figure 6.4: Total plasma β, electron β_e and main ion β_i profiles (a), and profile of the MHD α parameter (b) for TFTR shot #65018.

The ion thermal conductivity χ_i calculated from electromagnetic gyrofluid simulations is compared to the χ_i inferred from experimental power balance in Fig. 6.5. The prediction of a set of electrostatic gyrofluid simulations using an adiabatic electron response (no trapped electrons) is also shown, as is the prediction of the theoretical model of [Biglari, Diamond, and Rosenbluth 1989], $\chi_i = k_\theta \rho_i [q(1+\eta_i)/(\tau \hat{s})] \rho_i^2 v_{ti}/L_n$, where $k_\theta \rho_i = 0.2$ has been used, as its value is not predicted by the theory. The electromagnetic and electrostatic simulations predict similar χ_i values at $r/a = 0.775$ and 0.825, but the electromagnetic simulations predict a much larger χ_i, in better agreement with experiment, for $r/a = 0.875$ and $r/a = 0.925$.[2]

While the electrostatic simulations[3] and BDR theory both predict a small χ_i which decreases monotonically with radius (for $r/a > .7$), as the drive for the

---

[2] Note that at $r/a = 0.875$ and $r/a = 0.925$, the simulations are in a regime of strong sensitivity to input parameters, and relatively large RMS fluctuations in the steady state fluxes. The simulation at $r/a = 0.875$ in particular does not reach a very stable steady state during the time period of the simulation ($t < 440\, L_n/v_{ti}$) and the value of χ_i shown in Fig. 6.5 should be considered approximate.

[3] We emphasize that the electrostatic simulation results shown here do not include trapped electrons, to allow for a more direct comparison with the electromagnetic simulations which include only passing electrons. Beer's electrostatic simulations with trapped electrons predict a χ_i which is slightly higher, but which also decreases with r for $r/a > .7$.

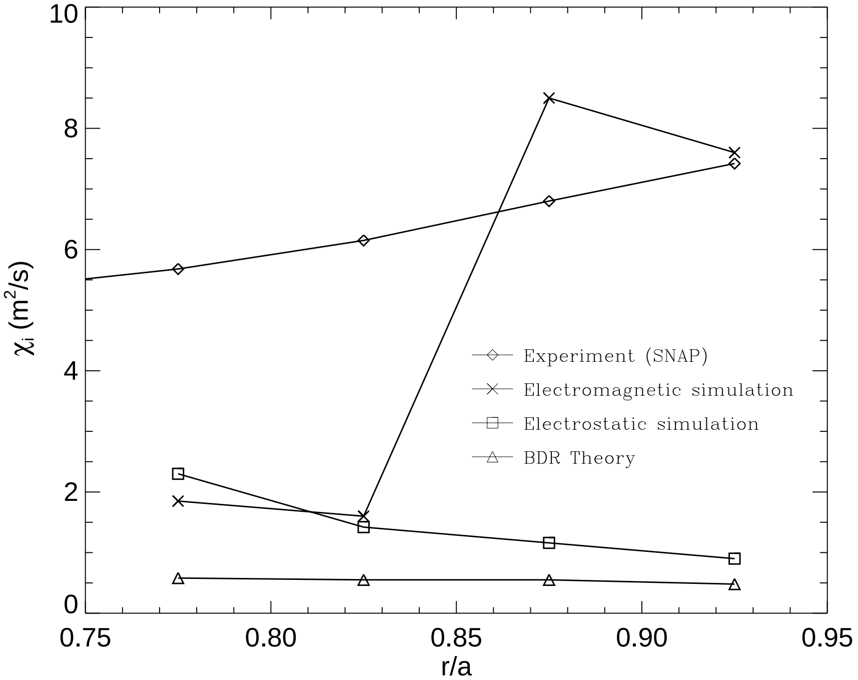

Figure 6.5: Comparison of measured and predicted χ_i in the outer region of TFTR L-mode shot #65018. The measured χ_i from `SNAP` is compared to results from electromagnetic and electrostatic gyrofluid simulations. The prediction of Biglari-Diamond-Rosenbluth theory, with $k_\theta \rho_i = 0.2$, is also shown.

ITG instability decreases, the electromagnetic simulations predict a χ_i which can dramatically increase with radius. This increase occurs in a region where the values of α_{MHD} and electron-ion collisionality are large, and increasing with radius. This behavior appears to be closely related to the dramatic increase in χ_i with α for $\alpha > 0.3$ ($\beta > 0.6\%$) seen in Fig. 5.15.[4]

There are a number of important factors that should be taken into account in assessing the level of agreement between the measured χ_i values and the electromagnetic simulation predictions shown in Fig. 6.5. There are significant uncertainties in the measured equilibrium parameters used as input in the simulations. These uncertainties are magnified because most of the simulation parameters $(\hat{s}, \epsilon_n, \eta_i, \eta_e, \alpha)$ are gradients of the local equilibrium quantities that are actually measured. Furthermore, the simulations are in a regime of extreme sensitivity to input parameters similar to that seen for $\alpha > 0.3$ ($\beta > 0.6\%$) in Fig. 5.15. In this regime, a relatively small change in the equilibrium gradients, for example ϵ_n or α, can lead to a much larger change in the predicted χ.

There are also a number of potentially important physical effects which are neglected in the simulations. Trapped electrons and impurity species can add additional instability mechanisms, as well as significantly modifying nonlinear dynamics. Ion-ion collisions can damp zonal flows, possibly increasing steady-state turbulent fluxes. The use of a simple shifted circle ($\hat{s} - \alpha$) equilibrium model, rather than a more detailed equilibrium geometry, can alter the dynamics, often significantly overstating the stabilizing effect of the Shafranov shift. Also, the use of local flux tube simulations prevents nonlocal effects such as the propagation of turbulence from one region to another. For example, it is possible that turbulence which is strongly driven in the extreme edge region propagates inward and contributes to the observed transport [Mattor and Diamond 1994; Garbet et al. 1994].[5]

Fig. 6.6 compares the electron heat conductivity χ_e inferred from measured

---

[4] Note that in the parameter scans in Ch. 5, only β is varied while all other parameters are held fixed, so that α is always proportional to β. Here α increases with r while β decreases. In both cases it is α which is of primary importance, as discussed in Sec. 2.3.

[5] Simple scaling estimates suggest a radial propagation distance of $\sim 10 - 30\rho_i$. This is quite small compared to the size of the tokamak, but may become significant relative to other scales near the edge.

power balance to that predicted by electromagnetic gyrofluid simulations. Electrostatic simulations with only adiabatic electrons do not predict a finite χ_e, and are thus not included in the figure. The electrostatic gyrofluid simulations of [Beer 1995], which include trapped electrons, predict a small χ_e which decreases from $\chi_e \simeq 0.4$ at $r/a = 0.775$ to $\chi_e \simeq 0.1$ at $r/a = 0.925$. The χ_e predicted by the electromagnetic simulations is also significantly smaller than that inferred from power balance, though it reproduces the general trend of increasing with radius. Note that, as in Ch. 5, the electromagnetic gyrofluid χ_e is dominated by $\mathbf{E} \times \mathbf{B}$ convected flux. The magnetic flutter contribution is finite, but smaller by more than an order of magnitude. The disparity between the gyrofluid prediction and the experimental χ_i inferred from power balance may be partially due to the measurement uncertainties and neglected physical effects mentioned above. It may also be due to the presence of high frequency turbulence, such as might be driven by electron drift instabilities or perhaps nonlinear instabilities. Such modes are not well described by the current electromagnetic gyrofluid model, but may be described by a future model which relaxes the assumption $k_\| v_{te} \ll 1$ and includes electron inertia. Such high frequency modes, which generally propagate in the electron diamagnetic direction, have been observed near the edge of TFTR [Evensen et al. 1998].

6.1 Summary

A direct comparison between observed transport and the predictions of electromagnetic gyrofluid simulations using measured equilibrium parameters, has been undertaken in the outer region ($.75 < r/a < .95$) of a TFTR L-mode discharge. It has been found that electromagnetic effects can significantly enhance predicted turbulent transport in the edge region, bringing predictions more in line with observations. Furthermore, the electromagnetic simulations correctly capture the trend of χ_i increasing with radius in the outer region, in contrast to electrostatic simulations and BDR theory, which predict a small χ_i decreasing with radius for $r/a > .7$. Electromagnetic gyrofluid predictions of χ_e also reproduce general trends seen in the experiment, though the χ_e values predicted by the simulations are significantly lower than those inferred from experimental power balance.

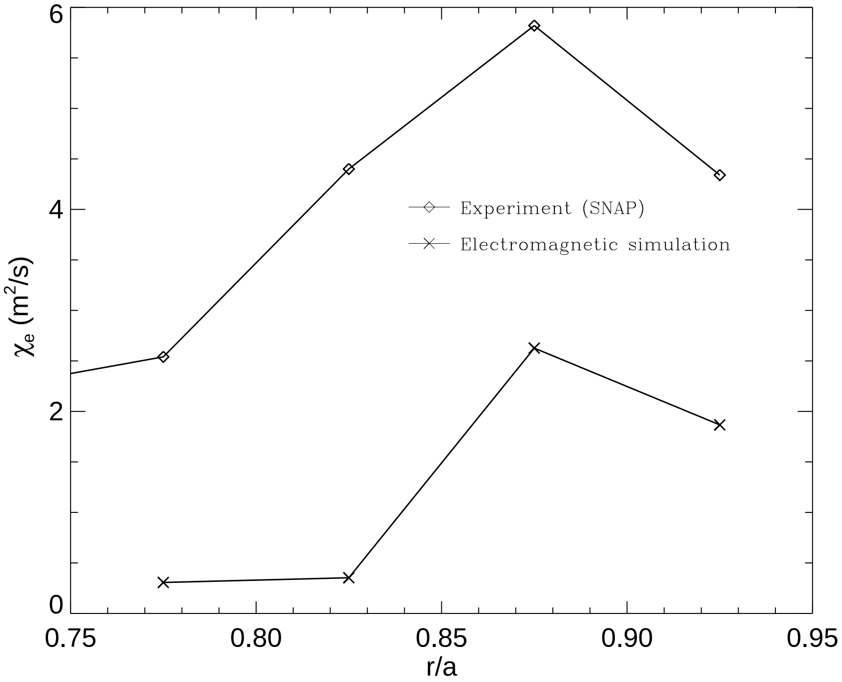

Figure 6.6: Comparison of measured and predicted electron thermal conductivity χ_e in the outer region of TFTR L-mode shot #65018. The measured χ_e from `SNAP` is compared to the predictions of electromagnetic gyrofluid simulations.

While the inclusion of additional physical effects such as trapped electrons, impurities, general geometry, and ion-ion collisions are are needed to make the simulations physically complete, these results are quite encouraging. The electromagnetic simulations clearly indicate that electromagnetic effects can dramatically increase turbulent fluxes in the outer region, where earlier electrostatic simulations have had the most difficulty accounting for observed transport.

Chapter 7

Conclusions and Future Directions

PROGRESS toward a more complete understanding of the physics of turbulent transport in tokamaks is made in this thesis, via the development of a comprehensive electromagnetic turbulence model, and its implementation in realistic nonlinear simulations. The model incorporates magnetic fluctuations and non-adiabatic passing electron dynamics, which have been neglected in previous realistic simulations. The fast temporal scales associated with electron transit motion are treated via an analytic expansion, allowing for efficient numerical solution of the equations.

The resulting model accurately reproduces the linear kinetic growth rates and frequencies of the finite-β toroidal ion temperature gradient (ITG) and kinetic ballooning (KBM) instabilities, and can be used to describe the nonlinear evolution of turbulence on both ion and Alfvén scales.

Nonlinear electromagnetic simulations have been compared to experiment, and found to reproduce a number of observed characteristics of turbulent fluctuation spectra. Electromagnetic effects are found to increase predicted ion transport in the outer region of the tokamak plasma, bringing simulation results more in line with experimental observations.

The fundamental conclusion of this work is that electromagnetic effects have a strong impact on microturbulence-driven transport, with both significant reductions and dramatic enhancements in transport possible, depending on β/β_c. Furthermore, the electromagnetic effects on transport observed in simulations are in many cases not easily explained by simple mixing length estimates, emphasizing the need for further work with numerical simulations and development of improved analytic theories.

7.1 Summary and Conclusions

A comprehensive and numerically efficient electromagnetic gyrofluid model has been developed and used to investigate turbulent transport in tokamaks. The model consists of a set of electromagnetic ion gyrofluid and electron Landau fluid equations derived by taking moments of the nonlinear toroidal electromagnetic gyrokinetic equation [Brizard 1992; Hahm et al. 1988], along with the gyrokinetic Poisson Equation and Ampere's Law.

The hierarchy of six ion moment equations is truncated with kinetic closures, based on those of [Beer 1995; Hammett and Perkins 1990; Dorland 1993], which have been carefully derived to incorporate both parallel and toroidal kinetic effects. The full set of electromagnetic ion gyrofluid equations include models of parallel Landau damping, ion drift resonance, ion-ion collisions, and linear and nonlinear finite-Larmor-radius (FLR) effects. Magnetic fluctuations enter the ion equations through the inductive electric field, as well as through several linear and nonlinear magnetic flutter terms.

A new set of electron equations is derived via a careful analytic expansion in temporal ($\omega \sim \omega_*, \omega_d, k_\| v_{ti}, k_\| v_A \ll k_\| v_{te}$) and spatial ($k_\perp^{-1} \sim \rho_i \gg \rho_e, c/\omega_{pe}$) scales. This expansion results in an elegant set of electron fluid equations which describe electromagnetic electron dynamics on the typical ion and Alfvén length and time scales, while analytically treating the numerically challenging electron transit time scale as well as the small electron gyroradius and skin depth length scales. While the resulting electron model is simple and fairly easy to implement numerically, it represents a very substantial improvement over the adiabatic electron models that have been used to describe the passing electrons in most previous gyrofluid and gyrokinetic particle simulations. In addition to finite-β effects and Alfvén wave dynamics, the model also incorporates electron $\mathbf{E} \times \mathbf{B}$, curvature, and ∇B drift motion, as well as the $\mathbf{E} \times \mathbf{B}$ nonlinearity and four additional nonlinear terms due to magnetic flutter. The use of an electron temperature closure appropriate for $\omega \sim \omega_A \ll k_\parallel v_{te}$ allows for the proper inclusion of the ∇T_e as well as the ∇n_e drive of the kinetic ballooning mode. Models of parallel electron Landau damping as well as electron-ion collisions are included.

The model has been benchmarked with linear gyrokinetic calculations, and good agreement has been found for the growth rates and real frequencies of both the finite-β toroidal ion temperature gradient (ITG) and kinetic Alfvén ballooning (KBM) instabilities. The model is able to reproduce the behavior described by [Andersson and Weiland 1988; Hong et al. 1989; Zonca et al. 1996], in which the kinetic ballooning mode is driven unstable below the ideal MHD ballooning limit (β_c) by ion drift resonance.

The electrostatic toroidal gyrofluid code (`Gryffin`) of [Beer 1995; Dorland 1993; Hammett et al. 1994] has been extended to incorporate the finite-β terms in the ion equations, the new electromagnetic electron model, and Ampere's Law. Nonlinear toroidal electromagnetic simulations have been carried out in flux tube geometry, and the results have been compared to electrostatic simulations, mixing-length estimates and experiments.

A series of nonlinear simulations has been performed which scan in $\beta \propto \alpha_{MHD}$, over the range $0 \leq \beta/\beta_c \leq 0.9$. The remainder of the simulation parameters are chosen to be typical of a tokamak core region with a strong ITG instability, and simulations are performed both with and without electron dissipation, which enters via electron Landau damping and electron-ion collisions. Electromagnetic effects are found to significantly reduce transport for $\beta/\beta_c \lesssim 0.5$, with the relative decrease similar to that expected from linear mixing length estimates due to the finite-β stabilization of the ITG instability. For larger $\beta/\beta_c > 0.5$, transport can increase with increasing β. In simulations which include electron Landau damping and electron-ion collisions, this increase in transport can be quite dramatic.

Electron Landau damping plays a critical role in our electromagnetic gyrofluid simulations at large $\beta/\beta_c > 0.5$, and low to moderate collisionality. Furthermore, electron Landau damping may be an important effect in other types of MHD or micro-turbulence simulations beyond those discussed here. Electron Landau damping acts like an enhanced resistivity in the Ohm's law, where the ratio of the Landau damping term to the usual collisional resistivity is roughly $|k_\parallel| v_{te}/\nu_{ei} \sim (|k_\parallel| qR)/[\nu_*(r/R)^{3/2}]$. Thus electron Landau damping can dominate at low to moderate collisionality, and at high $|k_\parallel|$. Note also that the electron Landau damping term is expected to be more important than the electron inertia term when $\omega < |k_\parallel| v_{te}$.

The electromagnetic simulations, like earlier electrostatic simulations, produce density fluctuation spectra which peak at $k_\theta \rho_i \simeq 0.1 - 0.2$, and which are anisotropic in k_r and k_θ, in qualitative agreement with the BES measurements on TFTR by [Fonck et al. 1993]. Furthermore, the electromagnetic simulations produce ion temperature fluctuation spectra which are similar in shape to the density spectra, with a ratio $(\tilde{T}/T_0)/(\tilde{n}_i/n_0) = 2 \pm .5$ relatively independent of the simulation parameters, similar to the observations of [Evensen et al. 1998] using BES and CHERS diagnostics on TFTR. The narrowing of the peaks in the fluctuation spectra with increasing β/β_c also appears to be consistent with the observations of [Evensen et al. 1998], though further investigation over a wider range of parameters is needed to confirm both of these results.

A direct comparison between electromagnetic toroidal gyrofluid simulations and the outer region $(.75 < r/a < .95)$ of a TFTR L-mode discharge has been undertaken, with encouraging results. In this region, electrostatic simulations and most mixing-length estimates predict small values of ion heat transport which decrease with radius, in contrast with the experimentally inferred transport which is large, and generally increasing with radius. The electromagnetic simulations predict ion heat fluxes which can increase with radius, and which are often in good quantitative agreement with the values inferred from power balance. Electromagnetic gyrofluid predictions of electron thermal conductivity (χ_e) also reproduce general trends seen in the experiment, though the χ_e values predicted by the simulations are significantly lower than those inferred from experimental power balance.

7.2 Future Directions

The incorporation of magnetic fluctuations and non-adiabatic passing electron dynamics into realistic toroidal turbulence simulations, as discussed in this thesis, represents a significant advance. Nonetheless much work is still needed to develop more complete simulations and a more thorough physical understanding of tokamak turbulence and transport.

Proposed extensions of this work can be broken down into three broad categories: extensions of the nonlinear toroidal simulation code, use of nonlinear simulation results to analyze tokamak transport experiments and to explore attractive regimes for the operation of a cost-effective fusion reactor, and thorough examination of nonlinear dynamics, including comparisons with both theoretical analyses and other nonlinear simulations.

Several extensions of the present electromagnetic gyrofluid code to enhance its flexibility and physics content should be possible in the near future. Areas of interest include multiple ion species, general geometry, trapped electrons, equilibrium $\mathbf{E} \times \mathbf{B}$ shear effects, electron inertia, and parallel magnetic perturbations, as well as investigation into higher-order models for the passing electrons. As discussed below, many of these capabilities already exist in the gyrofluid code and should be ready for immediate use, perhaps with some additional benchmarking in the electromagnetic case.

Impurity species are well known to both affect ITG growth rates [Tang et al. 1980; Rewoldt and Tang 1990; Kotschenreuther 1992] and to drive additional instabilities [Migliuolo 1992]. Our electromagnetic gyrofluid equations have been derived for arbitrary number of species (Sec. 3.2.6), and collisionless impurity dynamics are already included in the simulation code, though the multi-species electromagnetic case has not yet been thoroughly benchmarked. Collisions between ion species may also be important, particularly for electromagnetic modes [Rewoldt et al. 1987], so an interspecies collision model may need to be developed, perhaps through an extension of the work of [Chang and Callen 1992a; Chang and Callen 1992b], or by simply taking moments of the gyroaveraged Lorentz collision operator.

All electromagnetic runs discussed here have been carried out in $s-\alpha$ geometry, for simplicity and to allow for easy comparisons with linear kinetic codes. However, general equilibrium geometry has been implemented in the `Gryffin` code, and running the code in general geometry should require only additional benchmarking. The inclusion of profile variation in the simulation domain, via either enhanced flux tube, annulus, or full torus geometry is also of great interest, particularly for studying edge turbulence and enhanced confinement regimes.

Trapped electrons can dramatically alter ITG and KBM growth rates, as well as drive trapped electron modes. [BEER 1995] has developed a model for electrostatic trapped electron dynamics. In the limit of small trapped particle fraction and small β, it should be possible to combine this model with our electromagnetic passing electron model. So far, efforts to do so have proved numerically challenging, and further work is needed. The eventual development of a practical, fully electromagnetic trapped electron model is a high priority.

Work on extending the electrostatic `Gryffin` code to include equilibrium $\mathbf{E} \times \mathbf{B}$ shear flows is currently being undertaken by M. Beer. Extending this work to the electromagnetic version of the code is of great interest.

Including the electron inertia term in the electron momentum equation is straightforward, and should allow investigation of the "universal drift mode", though it may introduce numerical challenges.

At small values of β, the perpendicular component of the magnetic fluctuations ($\delta B_\perp$) tends to be much larger than the parallel component ($\delta B_\parallel$), and only $\delta B_\perp$ has been implemented in the gyrofluid code. However, linear studies show that $\delta B_\parallel$ plays an important role in Alfvén mode stability, particularly for high β equilibria [KOTSCHENREUTHER 1998; TANG et al. 1980]. It should be possible to use moments of Brizard's [BRIZARD 1992] full gyrokinetic equation, including $\delta B_\parallel$ terms, to derive the $\delta B_\parallel$ terms needed in the moment equations and Poisson's equation, and to use a perpendicular Ampere's Law to complete the system of equations. Explicitly including $\delta B_\parallel$ removes the cancellation which allowed the combination of the ∇B and curvature drift terms, and these will now need to be considered separately. The result will be a significantly more complex set of fluid equations, but the increase in computational difficulty should be minor.

The two-moment model used thus far for the electromagnetic passing electrons is elegant and simple, in addition to being quite accurate for describing the KBM and finite-β ITG, including the ∇n_e and ∇T_e drive of the KBM and the important electron contribution to the finite-β stabilization of the ITG. There are, however, cases for which a higher order electron model would be required. A prime example is the study of the electron temperature gradient (ETG) instability, which has been proposed as a possible mechanism for electron heat transport in some regimes. An accurate model of ETG requires the inclusion of finite electron mass terms, and at least four electron moments. In fact, since the electromagnetic terms have been implemented in `Gryffin` for multiple species, it is possible to simulate such cases by simply treating the electrons as an additional species with very small mass and negative charge.

It is also of interest to study the impact of nonlinear Landau damping on the simulations. Because our Landau damping closures are always implemented in odd moments ($u_\parallel$, $q_\parallel$, $q_\perp$) with no equilibrium components, magnetic flutter does not enter the linear Landau closure (avoiding a concern discussed by [FINN and GERWIN 1996]), but does contribute an additional nonlinear Landau damping term. The size of this magnetic flutter nonlinear Landau damping term has been evaluated in the simulations and found to be small for the cases considered here. Nonetheless, a number of authors [MATTOR 1992; JENKO and SCOTT 1998] have discussed the potential importance of this and other nonlinear Landau damping terms, and it is of interest to include them in future simulations. One approach is to move to coordinates which follow the perturbed field, so that the FFT's needed for the Landau closure term can be easily evaluated along the perturbed field, thus incorporating the magnetic flutter term. Other issues and approaches are discussed in Sec. C.8. Comparisons to gyrokinetic particle and Vlasov simulations which include nonlinear Landau damping is also useful for assessing the importance of these effects.

Making the above enhancements to the code should allow for more detailed quantitative comparisons with experimental turbulence and transport measurements, both in the core and the edge. Interesting regimes such as enhanced confinement modes and L-H transitions could be thoroughly investigated. If comparisons with present experiments prove successful, the code could be used as a tool to predict transport in proposed experiments, and to search for low transport regimes appropriate for a cost-effective fusion reactor.

A final avenue for future exploration is nonlinear dynamics. Preliminary results suggest complex nonlinear phenomena are involved in the saturation of electromagnetic turbulence. At high β/β_c, increases in transport are observed as linear growth rates drop, and dramatic increases in transport are observed with the addition of dissipative terms which reduce linear growth rates. The role of zonal flow dynamics in the electromagnetic case should be thoroughly investigated, including comparisons with the analytic work of [Das et al. 1999], and incorporation of neo-classical gyrofluid closures [Beer and Hammett 1998] which better account for the undamped "Rosenbluth-Hinton" component of the zonal flow. The role of secondary instabilities should also be investigated. Rogers has proposed a mechanism for the stabilization of secondary Kelvin-Helmholtz modes in the electromagnetic case with dissipation [Rogers and Drake 1997], which could be explored by studying the stability of linear eigenmodes from the Gryffin code.

In addition, comparisons to existing and future electromagnetic turbulence simulation codes should prove useful, both for debugging and to explore and compare underlying physics models. Useful comparisons could be made with electromagnetic Braginskii fluid codes such as those of [Drake et al. 1995; Rogers and Drake 1997; Zeiler et al. 1996; Xu et al. 1998] to better understand nonlinear dynamics, particularly in the edge regime. Furthermore, some of the techniques developed and tested here, such as the electron Landau damping model, may help extend the validity of these Braginskii codes to lower collisionality regimes. Comparisons to the fluid code of [Scott 1997], which now includes ion dynamics, should be useful as well. The dynamics of nonlinear instabilities [Drake et al. 1995; Scott 1997], and their relevance to edge transport could also be explored in detail. Comparisons with developing electromagnetic kinetic codes using either a particle [Lee et al. 1999] or direct "Vlasov" approach [Jenko and Scott 1999; Dorland et al. 1999] will be a high priority in the future.

Appendix A

Gyrofluid vs. δF Gyrokinetic Comparisons and the RH Mode

In addition to direct comparisons with experiments, there have been comparisons of results generated by different types of nonlinear turbulence simulations. These have primarily involved cross-checks between the results of gyrofluid (GF) simulations and δF gyrokinetic particle (GKP) simulations. Because of their computational efficiency, gyrofluid simulations have been widely used in direct comparisons with experiments and as the basis for parameterized transport models, such as GLF23 [Waltz et al. 1997] and IFS-PPPL [Kotschenreuther et al. 1995]. GKP simulations are a more direct method of solving the gyrokinetic equation, but they have been used less frequently in direct, extensive comparisons with experiments. Cross-checks between GF and GKP (preferably involving more than one simulation code of each type) provide an opportunity both to evaluate the underlying physics models and to check for errors in the particular simulation codes.

An early comparison between GF and GKP codes in a simplified geometry yielded encouraging results [Parker et al. 1994; Dorland 1993]. Excellent agreement was found in comparisons of the thermal diffusivity (χ) in both 2-D shearless slab and 3-D sheared slab geometries, though there were $\sim 40\%$ differences in the RMS ϕ.

More recent comparisons in toroidal geometry have found somewhat larger discrepancies between GKP simulations and GF simulations using the fluid closures described in [Beer 1995]. These are described in more detail in [Dimits

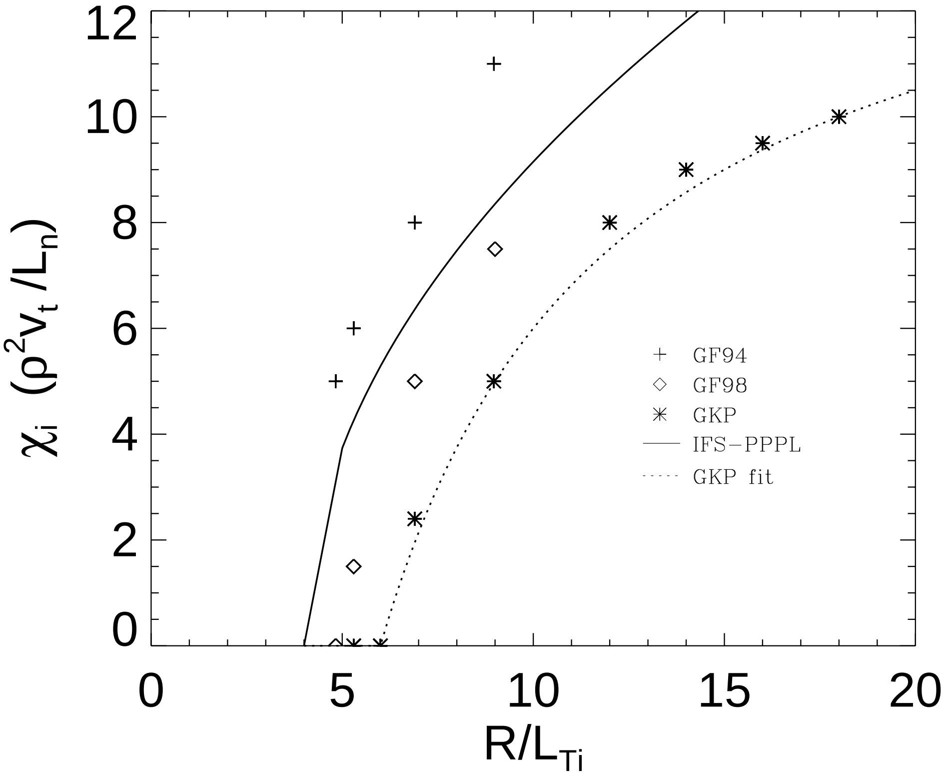

Figure A.1: Comparison of the predicted ion heat conductivity (χ_i) vs. steepness of the ion temperature gradient (R/L_{Ti}) for gyrofluid (GF) and δF gyrokinetic particle (GKP) simulations.

et al. 1999; Beer and Hammett 1998] and briefly summarized here. One such comparison is shown in Fig. A.1 for parameters similar to those from a DIII-D shot.[1] Here the χ_i predicted by several different models is plotted against the normalized temperature gradient (R/L_{Ti}). The symbols marked GF94 show simulation results from Beer's gyrofluid flux tube code with the closure described in [Beer 1995]. The solid line marked IFS-PPPL shows the predictions of the IFS-PPPL model [Kotschenreuther et al. 1995], which uses linear theory to predict the critical gradient, and a parametric fit to results from Beer's code to predict the heat flux above the critical gradient. The results of Dimits' flux tube δF simulations are marked GKP, and a simple curve fit through these points is also shown. All simulations are collisionless and electrostatic with adiabatic electrons ($n_e \sim \phi - \langle \phi \rangle$) [Dorland 1993] and a single ion species, and use a simplified circular flux surface geometry.

The qualitative behavior of all the simulation results is similar. They predict zero transport up to a critical gradient, above which the transport increases rapidly before gradually leveling off. However, the GF and GKP simulations disagree about the precise location of the critical gradient. Furthermore, the GF simulations seem to be slightly more "stiff", that is they predict a somewhat more rapid rise in transport as the gradient becomes supercritical.

Because of the different critical gradients predicted by the models, it is possible to select a value of the gradient near criticality, and find that the predictions of χ_i differ by an arbitrarily large factor. A much more practically meaningful comparison of the predictions can be made as follows. In an experiment, a heat source[2] near the center of the plasma will heat the plasma and sharpen the temperature gradient, increasing R/L_{Ti}, until the outward heat flux exactly balances the heat source and a steady state is reached. The temperature gradient at which this occurs is a relevant physical quantity for comparing the models. Fig. A.2 shows this comparison between the IFS-PPPL model and the curve fit to Dimits' δF simulations.

---

[1] This is not necessarily a typical case; it has been selected for study partly because disagreement between the two models is large.

[2] such as neutral beams or RF power in current experiments, or fusion produced alpha particles in a fusion reactor

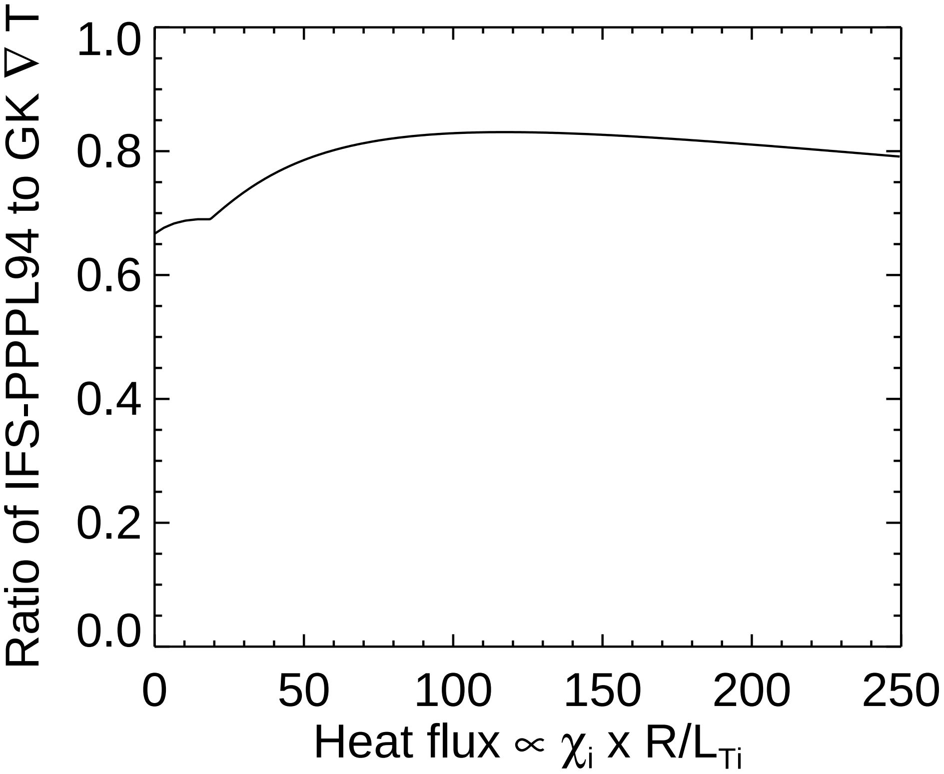

Figure A.2: Comparison of the ion temperature gradient predicted by the IFS-PPPL model to the prediction of a curve fit to Dimits' δF gyrokinetic particle simulations. The plot shows that over a wide range of heat flux, the IFS-PPPL model predicts an ion temperature gradient which is $20 - 30\%$ less steep

The conclusion is that the IFS-PPPL model predicts a temperature gradient which is $\sim 20 - 33\%$ less steep.

It has been expected that gyrofluid simulations may become inaccurate very close to the critical gradient. One reason for this is that the GF model relies on strong nonlinear couplings to wash out the effects of nonlinear Landau damping and other long time scale kinetic effects, and hence is expected to be more accurate as the turbulence becomes stronger. Another reason is that GF predictions of linear growth rates are less accurate very near marginal stability. Transport models based on GF simulations, such as GLF23 and IFS-PPPL, use linear kinetic calculations of the critical gradient to attempt to account for this.[3]

---

[3] This is in part why the IFS-PPPL curve in Fig. A.1 lies somewhat below the raw GF94 simulations.

It is perhaps surprising then that in Fig. A.1 the GKP simulation results differ significantly from the linear kinetic prediction of the critical temperature gradient (given by the point at which the IFS-PPPL line intersects the axis). The GKP simulations predict zero heat flux significantly above the point at which the ITG mode becomes unstable. There is apparently a subtle nonlinear mechanism which prevents this ITG mode from driving significant turbulent transport when turbulence is weak.

An undamped component of the zonal flow has been identified as the mechanism for this nonlinear up-shift in the critical gradient [DIMITS et al. 1999]. There is a component of the zonal flow that is linearly undamped in the absence of collisions [ROSENBLUTH and HINTON 1998]. This Rosenbluth-Hinton (RH) mode is driven up nonlinearly by the turbulence, and the RH flows then shear apart turbulent eddies and reduce transport. When the linear drive is weak enough, there is a temporary burst of turbulence which drives enough of the RH flow to completely damp any further turbulence, leading to the nonlinear up-shift observed in the GKP results. When the ion temperature gradient is large enough, a balance can be achieved between the turbulent drive and the turbulent damping of the zonal flows, leading to a non-zero χ_i.

As noted in [BEER 1995], Beer's original set of toroidal GF equations accurately model the fast linear collisionless damping of zonal flows for $t < qR/v_{ti}\sqrt{\epsilon}$. The original closure does not, however, account for the residual undamped component of the zonal flow. Recent efforts have been made to incorporate the residual flow into a new closure [BEER and HAMMETT 1998; BEER and HAMMETT 1999]. The results of a first attempt at this are labeled GF98 in Fig. A.1. While this closure only partially accounts for the residual flow, it does produce a nonlinear up-shift in the critical gradient, and it brings GF and GKP results significantly closer together. It is hoped that a more complete neoclassical closure which accurately reproduces the residual flow at all relevant wavelengths may bring the models yet closer together.

Recent full torus δF particle simulations by [LIN et al. 1999] have included a realistic model of ion-ion collisions. It has been found that collisional damping of the residual flow eliminates the nonlinear up-shift in the critical gradient. Hence, including realistic levels of collisions is expected to bring the GF and GKP results closer together. Beer's original GF closure can be viewed as an approximation of the zonal flow damping at a fixed, moderate collisionality. However, as Lin has found, the value of χ_i near marginal stability will depend on collisionality.[4]

It is noted that the closure used throughout this thesis is essentially Beer's original closure, and hence all nonlinear results include effective long-term damping of the RH flow. Nonlinear electromagnetic simulation results with a closure including the undamped RH flow are expected in the near future.

Of course electromagnetic effects have a significant impact on zonal flow dynamics, and may impact GF/GKP comparisons as well. Benchmarking the electromagnetic GF code with an equivalent GKP or 5-d gyrokinetic grid simulation will be a priority once such codes become available.

A.0.1 Conclusions

Extensive comparisons of electrostatic GF and GKP simulations have been undertaken and have provided a useful opportunity both to debug simulation codes and to test and understand underlying physics models. Reasonable overall agreement has been found, typified by the $\sim 25\%$ disagreement in predicted temperature gradient shown in Fig. A.2. A principal source of the disagreement has been identified and at least partially accounted for.

It is expected that continued refinement will lead to better agreement in the future, and that both types of simulations will be useful as complementary tools to achieve further understanding of turbulence and transport.

---

[4] The zonal flows near marginal stability are apparently driven by an inverse cascade, and it may be that the inclusion of non-adiabatic electrons (due to electromagnetic effects or trapped electrons) will limit this inverse cascade, as has been shown for simple "$i\delta$" models of electrons. This would be expected to improve comparisons between GKP and GF which included nonadiabatic electrons.

Appendix B

Flux Conservation

The conservation of magnetic flux is an important property of many dissipationless models of magnetized plasma dynamics. Here we will show that magnetic flux is conserved by the dissipation-free version of our electron equations, Eqs. 3.114-3.116. This proof closely follows that of [COWLEY 1985].

The magnetic flux Ψ is defined by the surface integral:

$$\Psi = \int_S \mathbf{B} \cdot d\mathbf{S}, \tag{B.1}$$

where $\mathbf{B}$ is here defined to be the total magnetic field, including both equilibrium and fluctuating components.

Conservation of flux requires that the total derivative $d\Psi/dt$ vanish in a frame moving at some velocity $\mathbf{v}_B$, that is:

$$\begin{aligned} \frac{d\Psi}{dt} &= \int_S \frac{\partial \mathbf{B}}{\partial t} \cdot d\mathbf{S} - \oint d\mathbf{l} \cdot (\mathbf{v}_B \times \mathbf{B}) = \int_S \left[\frac{\partial \mathbf{B}}{\partial t} - \nabla \times (\mathbf{v}_B \times \mathbf{B}) \right] \cdot d\mathbf{S} \quad \text{(B.2)} \\ &= -c \int_S \nabla \times (\mathbf{E} + \frac{\mathbf{v}_B}{c} \times \mathbf{B}) \cdot d\mathbf{S} = 0. \end{aligned}$$

This holds trivially in the electrostatic case, and for models such as ideal MHD where

$$-c\nabla \times \mathbf{E} = \frac{\partial \mathbf{B}}{\partial t} = \nabla \times (\mathbf{v} \times \mathbf{B}). \tag{B.3}$$

It is also apparent that an appropriate $\mathbf{v}_B$ for flux conservation exists (in particular the $\mathbf{E}\times\mathbf{B}$ velocity, $\mathbf{v}_E = c\mathbf{E}\times\mathbf{B}/B^2$) whenever the electric field is purely perpendicular, or when the parallel electric field can be written as a gradient, such that $\nabla\times\mathbf{E}_\parallel = 0$.

For electromagnetic drift/gyrokinetic models, the situation is somewhat more complex, as $E_\parallel$ is finite, and $\nabla\times(\hat{\mathbf{b}}E_\parallel)$ does not vanish in general. For the first case considered in Sec. 3.3.2, with zero electron inertia and no electron dissipation, the electron momentum equation is:

$$E_\parallel = \frac{\nabla_\parallel p_{\parallel e}}{en_e}, \tag{B.4}$$

where in this appendix, in contrast to Ch. 3, the moments $n_e, p_{\parallel e}, T_{\parallel e}$ etc., are all defined to be the total moments including both equilibrium and fluctuating parts, and $\nabla_\parallel$ is defined to be the gradient along the total magnetic field, including fluctuations. Invoking Eq. 3.116, which follows from the ordering $\omega \ll k_\parallel v_{te}$, and in the notation of this section is simply $\nabla_\parallel T_{\parallel e} = 0$, we can write:

$$E_\parallel = \frac{\nabla_\parallel n_e T_{\parallel e}}{en_e} = T_{\parallel e}\frac{\nabla_\parallel n_e}{en_e} = \frac{T_{\parallel e}}{e}\nabla_\parallel(\ln n_e) = \nabla_\parallel(\frac{T_{\parallel e}}{e}\ln n_e). \tag{B.5}$$

The curl of $\mathbf{E}$ is then:

$$\begin{aligned}\nabla\times\mathbf{E} &= \nabla\times\left[\mathbf{E}_\perp + \hat{\mathbf{b}}E_\parallel\right] = \nabla\times\left[\mathbf{E}_\perp + \hat{\mathbf{b}}\nabla_\parallel(\frac{T_{\parallel e}}{e}\ln n_e)\right] \\ &= \nabla\times\left[\mathbf{E}_\perp + \nabla(\frac{T_{\parallel e}}{e}\ln n_e) - \nabla_\perp(\frac{T_{\parallel e}}{e}\ln n_e)\right] \\ &= \nabla\times\left[\mathbf{E}_\perp - \nabla_\perp(\frac{T_{\parallel e}}{e}\ln n_e)\right].\end{aligned} \tag{B.6}$$

Because this is the curl of purely perpendicular quantity, it is always possible to find a $\mathbf{v}_B$ for which flux is conserved. Defining $\mathbf{v}_B = \mathbf{v}_E + \mathbf{v}'$, where $\mathbf{v}_E$ is the $\mathbf{E}\times\mathbf{B}$ velocity, the condition for flux conservation is:

$$\nabla\times(\mathbf{v}'\times\mathbf{B}) = \frac{c}{e}\nabla\times(\nabla_\perp T_{\parallel e}\ln n_e), \tag{B.7}$$

which can be satisfied by an appropriate $\mathbf{v}'$.

Appendix C

Landau Fluid Models of Collisionless Magnetohydrodynamics

The main body of this thesis has been concerned with developing and implementing a fluid model of electromagnetic microturbulence by starting with gyrokinetics, where the electrostatic approximation has traditionally been employed, and adding magnetic fluctuations and nonadiabatic passing electron dynamics.

Other approaches are possible. One such method is to start with a set of MHD-like equations which include magnetic fluctuations, but lack small scale dynamics and kinetic effects, and enhance them to include adequate physics for microturbulence studies. The work below, also published in [SNYDER et al. 1997], details an approach which adds a model of Landau damping to collisionless MHD equations. This model is most useful for large-scale MHD-type problems where kinetic effects become important. The addition of small-scale effects would be necessary for a complete electromagnetic microturbulence model.

C.1 Abstract

A closed set of fluid moment equations including models of kinetic Landau damping is developed which describes the evolution of collisionless plasmas in the magneto-

hydrodynamic parameter regime. The model is fully electromagnetic and describes the dynamics of both compressional and shear Alfvén waves, as well as ion acoustic waves. The model allows for separate parallel and perpendicular pressures $p_\parallel$ and $p_\perp$, and, unlike previous models such as Chew-Goldberger-Low theory, correctly predicts the instability threshold for the mirror instability. Both a simple 3+1 moment model and a more accurate 4+2 moment model are developed, and both could be useful for numerical simulations of astrophysical and fusion plasmas.

C.2 Introduction

The dynamics of collisionless plasmas are of great interest both in astrophysics and in laboratory fusion research. However, such plasmas are often studied using models which implicitly assume high collisionality and which ignore important kinetic effects such as parallel Landau damping. In particular, models based on ideal magnetohydrodynamics (MHD) assume collisional equilibration on a fast time scale and are not in general applicable to collisionless plasmas. Chew-Goldberger-Low (CGL) theory [Chew et al. 1956] relaxes the high collisionality assumption, but assumes an adiabaticity condition which is rarely met, and neglects parallel Landau damping, which can be important in the collisionless regime. Hence results from CGL theory are not always reliable, as evidenced by the well known factor of six error in the CGL prediction of the stability threshold for the mirror instability. [Kulsrud 1962; Kulsrud 1983] Simplified models such as ideal MHD and CGL are often employed despite their limitations because of the qualitative insights they provide and the difficulty of working directly with a kinetic formulation. There are some particle simulations of collisionless MHD phenomena, [Leboeuf et al. 1979; Sydora and Raeder 1988; Fu and Park 1995; Naitou et al. 1995] but there are also many fluid MHD simulations which could benefit from being extended into lower collisionality regimes.

In this paper we will develop a relatively simple description of collisionless plasma dynamics which includes parallel Landau damping. We wish to construct a model which is valid over a wide parameter regime and can later be narrowed and simplified for particular cases. As a starting point we will employ Kulsrud's formulation of collisionless MHD [Kulsrud 1983; Kruskal and Oberman 1958; Rosenbluth and Rostoker 1958]. Kulsrud's formulation requires solving a kinetic equation for the perturbed pressures $p_\parallel$ and $p_\perp$, or introducing further assumptions such as adiabaticity to evaluate the pressures. We shall take moments of Kulsrud's kinetic equation, and close the moment hierarchy with Landau closures analogous to those derived by Hammett, Perkins and Dorland [Hammett and Perkins 1990; Hammett et al. 1992; Dorland 1993], generalized to allow anisotropic pressures and magnetic perturbations. This yields a fairly simple set of moment equations with desirable nonlinear conservation properties, and a linear response function very similar to the kinetic response of a collisionless bi-Maxwellian plasma.

We shall refer to the model as Landau MHD, because the model incorporates the effects of parallel Landau damping, and it is valid within the collisionless MHD regime. It is useful to consider the Landau MHD model as an extension of CGL theory which incorporates Landau damping, and can incorporate collisional effects as well.

One of the limitations of the Landau MHD model we present is that it is derived only in the standard ordering of ideal MHD, $\epsilon \sim \omega/\Omega_c \sim k\rho$, where the plasma varies on frequency scales ω small compared to the gyrofrequency Ω_c, and varies on spatial scales $1/k$ long compared to the gyroradius ρ. Thus it covers phenomenon related to compressional and shear Alfvén waves and instabilities, ion acoustic waves, and ion and electron kinetic effects such as Landau damping. However, it does not include drift-waves or other micro-instabilities (which have been the focus of other Landau-fluid work) because they result from finite-Larmor/gyro radius (FLR) effects which vanish in the usual MHD ordering. Also, though collisional effects on the ion and electron heat fluxes and on the pressure tensor can be kept in our model, there is no resistive component to the ideal Ohm's law. This is because the parallel current $\sum_s n_s e_s u_{\parallel s} = 0$ to lowest order in the $1/e$ expansion of Kulsrud's collisionless MHD, and collisions would alter the Ohm's law only at higher order in the $\epsilon \sim \omega/\Omega \sim k\rho$ expansions. Thus the plasma is still an ideal electrical conductor in our model and the magnetic field lines are frozen into the plasma.

Alternative orderings are possible to bring in FLR or resistive effects. One approach would be to take fluid moments of the electromagnetic gyrokinetic equation [Hahm et al. 1988; Brizard 1992], which allows $k_\perp \rho \sim 1$, and work out the appropriate closures.[1] Another approach, taken by Chang and Callen [Chang and Callen 1992a; Chang and Callen 1992b], in effect carries Kulsrud's expansion to higher order in FLR, by using $k_\perp \rho \sim k_\parallel / k_\perp \sim \Delta$ with $\Delta^2 \sim \epsilon \sim \omega/\Omega_c$. This "extended-MHD" ordering orders the compressional Alfvén wave out of the equations, but retains the slower Shear Alfvén and ion acoustic waves, and includes resistive effects in the Ohm's law as well as drift-wave instabilities with moderate $k_\perp \rho \sim \epsilon^{1/2}$. Chang and Callen use an alternative derivation of Landau-fluid closures which is actually linearly exact (employing the full Z functions). It reduces to our formulation in the appropriate limits [Hammett et al. 1992]. Their approach advances 3 moments (density, parallel flow, and temperature) for each species with linear closures for the heat flux and stress tensor, while here we advance up to 6 moments (4 parallel and 2 perpendicular moments) for each species. These six moment equations retain additional nonlinear effects, and simplify some of the manipulations of the stress tensor by keeping separate $p_\perp$ and $p_\parallel$ (which is also essential to study the mirror instability that Kulsrud used to point out problems with the CGL theory). They can be reduced to simpler systems with fewer moments in various limits. Future work could try to extend our methods to the electromagnetic gyrokinetic equation or merge with the methods of Chang and Callen for the extended-MHD ordering.

There are previous authors who have tried some forms of Landau closures in MHD equations. [Bondeson and Ward 1994] used viscous and pressure-damped models of Landau damping in studying wall stabilization of external MHD modes in advanced tokamak designs. An important feature of this work was the use of Lagrangian variables so that the $|k_\parallel|$ operator involved in Landau-fluid closures would (at least linearly) effectively operate along perturbed magnetic field lines, which [Finn and Gerwin 1996] showed was important to do. However, Bondeson and Ward's model was a relatively low-order Landau-fluid model and was not entirely consistent, assuming high collisionality in the derivation of the initial 1-fluid equations and low collisionality elsewhere. A recent paper, [Medvedev and Dia-

---

[1] Note that this is the approach taken in the main body of this dissertation.

MOND 1996] has incorporated Hammett-Perkins type closures into a set of two fluid equations, used to describe large amplitude shear Alfvén and magnetosonic waves in interplanetary plasmas. Medvedev and Diamond's equations assume isotropic pressure, and are valid only in a limited parameter regime ($\beta \approx 1$). The Landau MHD model presented here should provide an extension of this previous work, useful for the study of resistive wall stabilization, as well as for general problems of MHD mode growth and saturation in both laboratory and astrophysical plasmas.

The organization of this paper is as follows. Section C.3 summarizes Kulsrud's collisionless MHD formulation. In Section C.4, a moment hierarchy based on Kulsrud's kinetic equation is derived and discussed. In Sections C.5 and C.6 closures for '4+2' and '3+1' models are derived, following [HAMMETT and PERKINS 1990], and [DORLAND 1993]. Section C.7 investigates collisional effects, including the reduction of the model to an appropriate limit of the Braginskii equations. Section C.8 discusses practical nonlinear implementation of the closure terms. In Section C.9, the Landau MHD formulation is applied to analyze the mirror instability, and Section C.10 offers concluding remarks.

C.3 Collisionless MHD

As a starting point, we employ the collisionless MHD model described by Kulsrud [KULSRUD 1983], based on earlier work by Kruskal and Oberman [KRUSKAL and OBERMAN 1958] and by Rosenbluth and Rostoker [ROSENBLUTH and ROSTOKER 1958]. This formulation begins with the Vlasov-Maxwell system of equations, and asymptotically expands in ρ_c/L, the smallness of the gyroradius relative to macroscopic scale lengths. This is accomplished by the formal expansion of the distribution function f, the magnetic field B, and the electric field E in the inverse charge $1/e$. This is equivalent to taking all relevant frequencies in the problem to be very small compared to the cyclotron frequency, Ω_c, and the plasma frequency, ω_p.

In this ordering, the Vlasov equation reduces to a condition on the zeroth order parallel (relative to the magnetic field) electric field $E_{\|0} = 0$, and the following kinetic equation for the zeroth order distribution function of each species

$f_{0_s}(v_\parallel, \mu, \mathbf{r}, t)$:

$$\frac{\partial f_{0_s}}{\partial t} + (v_\parallel \hat{\mathbf{b}} + \mathbf{v}_E)\cdot\nabla f_{0_s} + \left(-\hat{\mathbf{b}}\cdot\frac{D\mathbf{v}_E}{Dt} - \mu\hat{\mathbf{b}}\cdot\nabla B + \frac{e_s}{m_s}E_\parallel\right)\frac{\partial f_{0_s}}{\partial v_\parallel} = 0, \tag{C.1}$$

where e_s is the charge on species s, $\hat{\mathbf{b}}$ is a unit vector in the magnetic field direction $\hat{\mathbf{b}} = \mathbf{B}/B$, $\mathbf{v}_E \doteq c\,(\mathbf{E}\times\mathbf{B})/B^2$, $\mu \doteq v_\perp^2/2B$, and $\frac{D}{Dt} \doteq \frac{\partial}{\partial t} + (v_\parallel\hat{\mathbf{b}} + \mathbf{v}_E)\cdot\nabla$.

Combining moments of this kinetic equation with Maxwell's equations and taking the usual low Alfvén speed limit $v_A^2 \ll c^2$ yields Kulsrud's set of collisionless MHD equations:

$$\frac{\partial \rho}{\partial t} + \nabla\cdot(\rho\mathbf{U}) = 0, \tag{C.2}$$

$$\rho\left(\frac{\partial \mathbf{U}}{\partial t} + \mathbf{U}\cdot\nabla\mathbf{U}\right) = \frac{(\nabla\times\mathbf{B})\times\mathbf{B}}{4\pi} - \nabla\cdot\mathbf{P} \tag{C.3}$$

$$\frac{\partial \mathbf{B}}{\partial t} = \nabla\times(\mathbf{U}\times\mathbf{B}) \tag{C.4}$$

$$\mathbf{P} = p_\perp\mathbf{I} + (p_\perp - p_\parallel)\hat{\mathbf{b}}\hat{\mathbf{b}} \tag{C.5}$$

$$p_\perp = \sum_s \frac{m_s}{2}\int f_{0_s} v_\perp^2\, d^3v \tag{C.6}$$

$$p_\parallel = \sum_s m_s \int f_{0_s}(v_\parallel - \mathbf{U}\cdot\hat{\mathbf{b}})^2\, d^3v \tag{C.7}$$

$$\sum_s e_s \int f_{0_s}\, d^3v = 0 \tag{C.8}$$

where ρ is the total mass density, $\mathbf{U} = \mathbf{v}_E + u_\| \hat{\mathbf{b}}$ is the fluid velocity, and $\mathbf{P}$ is the pressure tensor.

The above set of equations is exact to zeroth order in the expansion parameter, but the kinetic equation itself, Eq. (C.1), must be used to evaluate $p_\|$ and $p_\perp$ to close the system. Because Eq. (C.1) is difficult to solve directly, this system is rarely employed without further simplification.

One such simplification is the introduction of the double adiabatic law (also known as CGL theory [Kulsrud 1983; Chew et al. 1956]). In the CGL model, Eq. (C.1) is replaced by two equations of state which determine $p_\perp$ and $p_\|$:

$$\frac{d}{dt}\left(\frac{p_\perp}{\rho B}\right) = 0 \tag{C.9}$$

$$\frac{d}{dt}\left(\frac{p_\| B^2}{\rho^3}\right) = 0 \tag{C.10}$$

where the total derivative is defined by $\frac{d}{dt} \doteq \frac{\partial}{\partial t} + (u_\| \hat{\mathbf{b}} + \mathbf{v}_E)\cdot\nabla$.

These equations of state are equivalent to setting the heat flow tensor $\mathbf{Q}$ to zero. This assumption that both electron and ion heat flow are negligible is strictly valid only when the mode phase velocity ($\omega/k_\|$) is much greater than the electron and ion thermal speeds, a criterion rarely satisfied for Alfvén waves and never satisfied for sound waves. Furthermore, the simple truncation of the moment hierarchy implied by this assumption eliminates Landau damping from the problem, leaving the system with no damping at all, which can lead to unphysical behavior. However, CGL theory is often employed, even when it is invalid, because of its simple, Lagrangian form. Of course this can lead to incorrect results, as in the well known case of the mirror instability.

C.4 The Moment Hierarchy

We wish to develop a formulation which maintains much of the simplicity of the CGL model, while increasing its range of applicability and including models of kinetic Landau damping. This will be accomplished by first taking moments of Eq. (C.1) and, in the next section, closing the hierarchy using Landau closures analogous to those developed for the electrostatic case by [Hammett and Perkins 1990].

Multiplying Eq. (C.1) by B and adding Eq. (C.4) multiplied by f_s, leads to a kinetic equation in phase space conserving form:

$$\begin{aligned} \frac{\partial}{\partial t} f_s B \quad &+ \quad \nabla\cdot\left[f_s B\left(v_\parallel \hat{\mathbf{b}} + \mathbf{v}_E\right)\right] \\ &+ \quad \frac{\partial}{\partial v_\parallel}\left[f_s B\left(-\hat{\mathbf{b}}\cdot\frac{D\mathbf{v}_E}{Dt} - \mu\hat{\mathbf{b}}\cdot\nabla B + \frac{e_s}{m_s}E_\parallel\right)\right] = BC(f_s), \end{aligned} \tag{C.11}$$

The subscript zero on f_s has been suppressed. All calculations involve only the zeroth order distribution function in the original expansion in $1/e$, though a subsidiary ordering will be introduced to derive the Landau closures.

Note the addition of a collision operator to the right hand side of the kinetic equation to allow for generalization to regimes where collisions play an important role. Here a simple BGK collision operator [Gross and Krook 1956] is employed:

$$C(f_j) = -\sum_k \nu_{jk}(f_j - F_{Mjk}) \tag{C.12}$$

where ν_{jk} is the effective collision rate of species j with species k. These collisions cause f_j to relax to a shifted Maxwellian with the effective temperature of species j and the mass velocity of species k,

$$F_{Mjk} = \frac{n_j}{(2\pi T_j/m_j)^{3/2}} \exp\left[-\frac{m_j(v_\parallel - u_{\parallel k})^2}{2T_j} - \frac{m_j \mu B}{T_j}\right] \tag{C.13}$$

where $T_j = (T_{\parallel j} + 2T_{\perp j})/3$. The BGK collision operator in this form conserves mass, momentum and energy.

Defining the velocity space moments as follows,

$$
\begin{aligned}
n_s &= \int f_s \, d^3v & n_s u_{\parallel s} &= \int f_s v_\parallel \, d^3v \\
p_{\parallel s} &= m \int f_s (v_\parallel - u_\parallel)^2 \, d^3v & p_{\perp s} &= m \int f_s \mu B \, d^3v \\
q_{\parallel s} &= m \int f_s (v_\parallel - u_\parallel)^3 \, d^3v & q_{\perp s} &= m \int f_s \mu B (v_\parallel - u_\parallel) \, d^3v \\
r_{\parallel,\parallel s} &= m \int f_s (v_\parallel - u_\parallel)^4 \, d^3v & r_{\parallel,\perp s} &= m \int f_s \mu B (v_\parallel - u_\parallel)^2 \, d^3v \\
r_{\perp,\perp s} &= m \int f_s \mu^2 B^2 \, d^3v,
\end{aligned}
$$

Poisson's equation and Ampere's law reduce, to lowest order in $1/e$, to the conditions $\sum_s n_s e_s = 0$ and $\sum_s n_s e_s u_{\parallel s} = 0$. Specializing to the case of one species of $Z = 1$ ions implies $n = n_e = n_i$ and $u_\parallel = u_{\parallel i} = u_{\parallel e}$. The usual definitions for total higher moments $p_\parallel = \sum_s p_{\parallel s}$, $p_\perp = \sum_s p_{\perp s}$, $q_\parallel = \sum_s q_{\parallel s}$ *etc.* are employed. Note that, because $u_{\parallel i} = u_{\parallel e}$, the collision term serves primarily to isotropize the distribution. Taking integrals of the form $\int dv_\parallel \, d\mu \, v_\parallel^j \mu^k \ldots$ of Eq. (C.11) then leads to the following set of exact moment equations:

$$\frac{\partial n}{\partial t} + \nabla \cdot (n\mathbf{U}) = 0, \tag{C.14}$$

$$
\begin{aligned}
\frac{\partial u_\parallel}{\partial t} &+ \mathbf{U} \cdot \nabla u_\parallel + \hat{\mathbf{b}} \cdot \left(\frac{\partial \mathbf{v}_E}{\partial t} + \mathbf{U} \cdot \nabla \mathbf{v}_E \right) + \frac{1}{n m_s} \nabla \cdot (\hat{\mathbf{b}} p_{\parallel s}) \\
&- \frac{p_{\perp s}}{n m_s} \nabla \cdot \hat{\mathbf{b}} - \frac{e_s}{m_s} E_\parallel = 0,
\end{aligned}
\tag{C.15}
$$

$$
\begin{aligned}
\frac{\partial p_{\parallel s}}{\partial t} &+ \nabla \cdot (\mathbf{U} p_{\parallel s}) + \nabla \cdot (\hat{\mathbf{b}} q_{\parallel s}) + 2 p_{\parallel s} \hat{\mathbf{b}} \cdot \nabla \mathbf{U} \cdot \hat{\mathbf{b}} \\
&- 2 q_{\perp s} \nabla \cdot \hat{\mathbf{b}} = -\frac{2}{3} \nu_s (p_{\parallel s} - p_{\perp s}),
\end{aligned}
\tag{C.16}
$$

$$
\begin{aligned}
\frac{\partial p_{\perp s}}{\partial t} &+ \nabla \cdot (\mathbf{U} p_{\perp s}) + \nabla \cdot (\hat{\mathbf{b}} q_{\perp s}) + p_{\perp s} \nabla \cdot \mathbf{U} - p_{\perp s} \hat{\mathbf{b}} \cdot \nabla \mathbf{U} \cdot \hat{\mathbf{b}} \\
&+ q_{\perp s} \nabla \cdot \hat{\mathbf{b}} = -\frac{1}{3} \nu_s (p_{\perp s} - p_{\parallel s}),
\end{aligned}
\tag{C.17}
$$

$$\begin{aligned}\frac{\partial q_{\parallel s}}{\partial t} &+ \nabla\cdot(\mathbf{U}q_{\parallel s}) + \nabla\cdot(\hat{\mathbf{b}}r_{\parallel,\parallel s}) + 3q_{\parallel s}\hat{\mathbf{b}}\cdot\nabla\mathbf{U}\cdot\hat{\mathbf{b}} - \frac{3p_{\parallel s}}{nm_s}\hat{\mathbf{b}}\cdot\nabla p_{\parallel s} \\ &+ 3\left(\frac{p_{\perp s}p_{\parallel s}}{nm_s} - \frac{p_{\parallel s}^{\,2}}{nm_s} - r_{\parallel,\perp s}\right)\nabla\cdot\hat{\mathbf{b}} = -\nu_s q_{\parallel s},\end{aligned} \tag{C.18}$$

$$\begin{aligned}\frac{\partial q_{\perp s}}{\partial t} &+ \nabla\cdot(\mathbf{U}q_{\perp s}) + \nabla\cdot(\hat{\mathbf{b}}r_{\parallel,\perp s}) + q_{\perp s}\nabla\cdot(u_{\parallel}\hat{\mathbf{b}}) - \frac{p_{\perp s}}{nm_s}\hat{\mathbf{b}}\cdot\nabla p_{\parallel s} \\ &+ \left(\frac{p_{\perp s}^{\,2}}{nm_s} - \frac{p_{\perp s}p_{\parallel s}}{nm_s} - r_{\perp,\perp s} + r_{\parallel,\perp s}\right)\nabla\cdot\hat{\mathbf{b}} = -\nu_s q_{\perp s},\end{aligned} \tag{C.19}$$

where $\rho = n(m_e + m_i)$, $\mathbf{U} = \mathbf{v}_E + u_{\parallel}\hat{\mathbf{b}}$, and $\nu_i = \nu_{ii} + \nu_{ie}$ and $\nu_e = \nu_{ee} + \nu_{ei}$.

Using the condition $u_{\parallel i} = u_{\parallel e}$ to solve for $E_{\parallel}$ [as given in Kulsrud's Eq. (49)], it is straightforward to show that the first two moment equations, Eqs. (C.14) and (C.15) are equivalent to Eq. (C.2), and the parallel component of Eq. (C.3), that is:

$$\frac{\partial u_{\parallel}}{\partial t} + \mathbf{U}\cdot\nabla u_{\parallel} + \hat{\mathbf{b}}\cdot\left(\frac{\partial \mathbf{v}_E}{\partial t} + \mathbf{U}\cdot\nabla\mathbf{v}_E\right) + \frac{1}{\rho}\left[\hat{\mathbf{b}}\cdot\nabla p_{\parallel} + (p_{\parallel} - p_{\perp})\nabla\cdot\hat{\mathbf{b}}\right] = 0. \tag{C.20}$$

C.4.1 Conservation Properties

Just as in the electrostatic case [Hammett and Perkins 1990], the moment hierarchy has favorable conservation properties. Each moment equation acts as a conservation relation, provided the hierarchy is closed by approximating the highest moments, without inserting additional terms such as viscosity.

Momentum is conserved by any closure which keeps Eqs. (C.2) and (C.3) and closes for pressure or higher moments. Combining Eqs. (C.2) and (C.3) yields:

$$\frac{\partial(\rho\mathbf{U})}{\partial t} = -\nabla\cdot\left[\rho\mathbf{U}\mathbf{U} + \left(\frac{B^2}{8\pi}\mathbf{I} - \frac{\mathbf{B}\mathbf{B}}{4\pi}\right) + \mathbf{P}\right]. \tag{C.21}$$

Similarly, energy is conserved by any closure which uses approximations only for the heat flow moments $q_{\parallel s}$ and $q_{\perp s}$, or higher moments. To demonstrate this, define the kinetic + thermal + magnetic energy density $\mathcal{E} = \rho U^2/2 + B^2/8\pi + p_{\perp} +$

$p_\parallel/2$. Combining Eqs. (C.2),(C.3),(C.4),(C.16), and (C.17) yields:

$$\frac{\partial \mathcal{E}}{\partial t} = -\nabla\cdot\left[\left(\frac{1}{2}\rho U^2 + p_\perp + \frac{1}{2}p_\parallel\right)\mathbf{U}\right] - \nabla\cdot\left[\frac{\mathbf{B}\times(\mathbf{U}\times\mathbf{B})}{4\pi}\right] - \nabla\cdot(\mathbf{U}\cdot\mathbf{P}) - \nabla\cdot\mathbf{q} \tag{C.22}$$

where $\mathbf{q} \equiv (q_\perp + q_\parallel/2)\hat{\mathbf{b}}$. Integrating over volume, we can take the left hand side as the rate of change of the energy inside a volume, and the right hand side as the flow of energy across the surface. We note that Kulsrud's equations (66) and (67) [KULSRUD 1983] (not employed elsewhere in the paper) appear to be in error.

C.5 The 4+2 Model

A closure for the moment hierarchy must now be derived to produce a complete model. In general, a model which evolves more moments will be more accurate, though more complex and more computationally intensive to implement. A 4+2 moment model, that is a model which evolves four parallel moments $(n, u_\parallel, p_{\parallel s}, q_{\parallel s})$ and two perpendicular moments $(p_{\perp s}, q_{\perp s})$, will be developed first. The 4+2 model will truncate the moment hierarchy with Eqs. (C.18) and (C.19), and will require closures for $r_{\parallel,\parallel s}$ and $r_{\parallel,\perp s}$. Simpler models, such as a 3+1 moment model, can be derived as the low frequency limit of the 4+2 model, following a procedure developed by [DORLAND 1993].

A closure for the 4+2 model will be derived following the procedure laid out by Hammett and Dorland [HAMMETT and PERKINS 1990; DORLAND 1993]. This procedure, derived for electrostatic perturbations, must be extended for use with general electromagnetic perturbations in two dimensions (parallel and perpendicular). The collisionless case ($\nu \ll \omega$) will be considered first, and collisional effects will be investigated in Section C.7. The closure should conserve mass, momentum, and energy, while providing a linear response which closely matches that expected from kinetic theory.

C.5.1 Linear Response from Kinetic Theory

We first use the guiding center kinetic equation, Eq. (C.1), to derive the kinetic linear response. We wish to linearize around a zeroth order distribution which allows the decoupling of electron and ion pressures as well as the decoupling of parallel and perpendicular pressures that one expects in a collisionless plasma. To accomplish this we choose a bi-Maxwellian distribution with separate equilibrium parallel and perpendicular temperatures $T_{\parallel 0s}$ and $T_{\perp 0s}$. Since the plasma is collisionless, it is not expected to be exactly Maxwellian, even for a particular species in a particular direction. However, we wish only to calculate a linear response which we can approximate with our Landau closure. The linear response thus needs to provide the correct general form of the linear Landau damping, allowing for independent variation of species pressures, and of the parallel and perpendicular pressures. Hence the bi-Maxwellian is a convenient choice.

We introduce a subsidiary ordering in which the zeroth order distribution is bi-Maxwellian with no zeroth order flows or gradients, $f_s = F_{Ms} + f_{1s}$, where:

$$F_{Ms} = \frac{n_0}{(2\pi/m_s)^{3/2} T_{\perp 0s} T_{\parallel 0s}^{1/2}} \exp\left[-\frac{m_s B_0 \mu}{T_{\perp 0s}} - \frac{m_s {v_\parallel}^2}{2T_{\parallel 0s}}\right] \tag{C.23}$$

The moments ($n = n_0 + n_1$, $\mathbf{U} = \mathbf{U}_1$ *etc.*), the magnetic field ($\mathbf{B} = \mathbf{B}_0 + \mathbf{B}_1$), and the parallel electric field ($E_\parallel = E_{\parallel 1}$) are similarly linearized, with the zeroth order part uniform. Note again that this is a subsidiary ordering. All terms are zeroth order with respect to the initial ordering in $1/e$.

Eq. (C.1) is then linearized and Fourier analyzed to find f_{1s}. Defining $\hat{\mathbf{z}}$ as the unit vector in the parallel direction $\mathbf{B}_0 = B_0\hat{\mathbf{z}}$, and defining the wave vector $\mathbf{k} = k_z\hat{\mathbf{z}} + k_x\hat{\mathbf{x}}$:

$$f_{1s} = \left(-\frac{v_\perp^2}{2}\frac{ik_z B_1}{B_0} + \frac{e_s}{m_s}E_\parallel\right)\frac{m_s v_\parallel}{T_{\parallel 0s}(-i\omega + ik_z v_\parallel)} f_{0s} \tag{C.24}$$

Taking moments, keeping in mind that $\int d^3v = 2\pi \int (B_0 + B_1) d\mu dv_\parallel$, yields:

$$n_{1s} = -\frac{in_0}{k_z T_{\parallel 0s}} e_s E_\parallel \mathcal{R}(\zeta_s) + \frac{B_1 n_0}{B_0}\left[1 - \frac{T_{\perp 0s}}{T_{\parallel 0s}}\mathcal{R}(\zeta_s)\right] \tag{C.25}$$

$$p_{\parallel 1s} = -\frac{ip_{\parallel 0s}}{k_z T_{\parallel 0s}} e_s E_\parallel \left[1 + 2\zeta_s^2 \mathcal{R}(\zeta_s)\right] + \frac{B_1 p_{\parallel 0s}}{B_0}\left[1 - \frac{T_{\perp 0s}}{T_{\parallel 0s}}\left(1 + 2\zeta_s^2 \mathcal{R}(\zeta_s)\right)\right] \tag{C.26}$$

$$p_{\perp 1s} = -\frac{ip_{\perp 0s}}{k_z T_{\parallel 0s}} e_s E_\parallel \mathcal{R}(\zeta_s) + \frac{2B_1 p_{\perp 0s}}{B_0}\left[1 - \frac{T_{\perp 0s}}{T_{\parallel 0s}}\mathcal{R}(\zeta_s)\right] \tag{C.27}$$

where $\zeta_s = \omega/\sqrt{2}|k_z|v_{t\parallel_s}$ is the normalized frequency, and $\mathcal{R}(\zeta_s) = 1 + \zeta_s Z(\zeta_s)$ is the electrostatic response function. The usual plasma dispersion function is defined [for $\mathrm{Im}(\zeta) > 0$] by $Z(\zeta) = (1/\sqrt{\pi}) \int dt \, \exp(-t^2)/(t - \zeta)$, and the thermal velocities are defined to be $v_{t\parallel_s} = \sqrt{T_{\parallel 0s}/m_s}$ and $v_{t\perp_s} = \sqrt{T_{\perp 0s}/m_s}$.

Note that it is possible to solve for $E_\parallel$ using quasineutrality, and to solve for B_1 using Eq. (C.4). However, we find it most convenient and physically enlightening to leave the response functions in the above form for matching to the moment model.

C.5.2 The 4+2 Landau Closure

We now choose a closure for our 4+2 hierarchy which will closely match the linear response calculated in the previous section. As noted we require closures for both $r_{\parallel,\parallel_s}$ and $r_{\parallel,\perp_s}$. Additional terms such as viscosity would violate energy conservation [Hammett and Perkins 1990; Hammett et al. 1992] and so will not be employed in the 4+2 equations.

The linearized moment equations in the collisionless ($\nu = 0$) limit are, omitting the subscript on perturbed quantities and defining $\nabla_\parallel \doteq \hat{\mathbf{b}}_0 \cdot \nabla$:

$$\frac{\partial n}{\partial t} + n_0 \nabla \cdot \mathbf{U} = 0, \tag{C.28}$$

$$\frac{\partial u_\parallel}{\partial t} + \frac{1}{n_0 m_s}\nabla_\parallel p_{\parallel_s} + \frac{(p_{\perp 0s} - p_{\parallel 0s})}{n_0 m_s}\frac{\nabla_\parallel B_1}{B_0} - \frac{e_s}{m_s}E_\parallel = 0, \tag{C.29}$$

$$\frac{\partial p_{\parallel_s}}{\partial t} + p_{\parallel 0s}\nabla \cdot \mathbf{v}_E + \nabla_\parallel q_{\parallel_s} + 3p_{\parallel 0s}\nabla_\parallel u_\parallel = 0, \tag{C.30}$$

$$\frac{\partial p_{\perp s}}{\partial t} + 2p_{\perp 0s}\nabla\cdot\mathbf{v}_E + \nabla_{\parallel} q_{\perp s} + p_{\perp 0s}\nabla_{\parallel} u_{\parallel} = 0, \tag{C.31}$$

$$\begin{aligned}\frac{\partial q_{\parallel s}}{\partial t} &+ \nabla_{\parallel} r_{\parallel,\parallel s} - \frac{3p_{\parallel 0s}}{n_0 m_s}\nabla_{\parallel} p_{\parallel s} \\ &+ \left(-r_{\parallel,\parallel 0s} + 3r_{\parallel,\perp 0s} + \frac{3{p_{\parallel 0s}}^2}{n_0 m_s} - \frac{3p_{\parallel 0s}p_{\perp 0s}}{n_0 m_s}\right)\frac{\nabla_{\parallel} B_1}{B_0} = 0,\end{aligned} \tag{C.32}$$

$$\begin{aligned}\frac{\partial q_{\perp s}}{\partial t} &+ \nabla_{\parallel} r_{\parallel,\perp s} - \frac{p_{\perp 0s}}{n_0 m_s}\nabla_{\parallel} p_{\parallel s} \\ &+ \left(r_{\perp,\perp 0s} - 2r_{\parallel,\perp 0s} - \frac{{p_{\perp 0s}}^2}{n_0 m_s} + \frac{p_{\perp 0s}p_{\parallel 0s}}{n_0 m_s}\right)\frac{\nabla_{\parallel} B_1}{B_0} = 0,\end{aligned} \tag{C.33}$$

The bi-Maxwellian values $r_{\parallel,\parallel 0s} = 3p_{\parallel 0s}/n_0 m_s$, $r_{\parallel,\perp 0s} = p_{\parallel 0s}p_{\perp 0s}/n_0 m_s$ and $r_{\perp,\perp 0s} = 2p_{\perp 0s}/n_0 m_s$ are easily calculated. Fourier transforming into ($\mathbf{k}$,t) space, and using the linearized Eq. (C.4), $\mathbf{k}\cdot\mathbf{v}_E = \omega B_1/B_0$, yields a simple set of equations for each moment in terms of the other moments and the perturbed magnetic field.

The system is closed by writing the highest moments ($r_{\parallel,\parallel s}$ and $r_{\parallel,\perp s}$) as a linear sum of the lower moments, with coefficients that are in general functions of $\mathbf{k}$ and the equilibrium quantities. Generalized linear response functions can then be derived. The closure coefficients are determined by comparison with linear kinetic theory in the high and low frequency limits.

Guided by previous work [Hammett and Perkins 1990; Dorland 1993], we choose closures with a bi-Maxwellian part and an additional term which models phase mixing. We first try a simple generalization of the 4+2 closure derived in [Dorland 1993] for the electrostatic case, modified for the case of a bi-Maxwellian equilibrium distribution:

$$r_{\parallel,\parallel s} = 3v_{t\parallel_s}^2(2p_{\parallel s} - T_{\parallel 0s}n) + c_{\parallel} n_0 v_{t\parallel_s}^2 T_{\parallel s} - \sqrt{2}D_{\parallel} v_{t\parallel_s}\frac{ik_{\parallel} q_{\parallel s}}{|k_{\parallel}|} \tag{C.34}$$

$$r_{\parallel,\perp s} = v_{t\perp_s}^2 p_{\parallel s} + v_{t\parallel_s}^2 p_{\perp s} - v_{t\parallel_s}^2 T_{\perp 0s} n - \sqrt{2}D_{\perp} v_{t\parallel_s}\frac{ik_{\parallel} q_{\perp s}}{|k_{\parallel}|} \tag{C.35}$$

The coefficients $c_{\parallel}$, $D_{\parallel}$, and $D_{\perp}$ are determined by matching the perturbed density and perpendicular pressure to the kinetic results in the adiabatic ($|\zeta| \ll 1$) and fluid ($|\zeta| \gg 1$) limits. It is possible to match the density response through order ζ^2 for small $|\zeta|$ and through order $1/\zeta^5$ for large $|\zeta|$. The $p_{\perp}$ response can be matched through order ζ for small $|\zeta|$ and through order $1/\zeta^2$ for large $|\zeta|$. This yields $c_{\parallel} = (32 - 9\pi)/(3\pi - 8)$, $D_{\parallel} = 2\sqrt{\pi}/(3\pi - 8)$, and $D_{\perp} = \sqrt{\pi}/2$ (the same result as in the earlier electrostatic derivation [Dorland 1993]).

The density response is then:

$$n_{1s} = -\frac{in_0}{k_z T_{\parallel 0s}} e_s E_{\parallel} \mathcal{R}_4(\zeta_s) + \frac{B_1 n_0}{B_0}\left[1 - \frac{T_{\perp 0s}}{T_{\parallel 0s}}\mathcal{R}_4(\zeta_s)\right] \tag{C.36}$$

where $\mathcal{R}_4(\zeta_s)$ is a four-pole model of the electrostatic response function $\mathcal{R}(\zeta_s)$:

$$\mathcal{R}_4(\zeta_s) = \frac{4 - 2i\sqrt{\pi}\zeta_s + (8 - 3\pi)\zeta_s^2}{4 - 6i\sqrt{\pi}\zeta_s + (16 - 9\pi)\zeta_s^2 + 4i\sqrt{\pi}\zeta_s^3 + (6\pi - 16)\zeta_s^4}. \tag{C.37}$$

The linear kinetic response functions for the 4 parallel moments $n, u_{\parallel}, p_{\parallel s}, q_{\parallel s}$ are all modeled equally well, with $\mathcal{R}_4(\zeta_s)$ replacing $\mathcal{R}(\zeta_s)$ in the expressions for each. The 4+2 density response is compared to linear kinetic response in Fig. (C.1).

Note that in the figures, the quasineutrality relation $n_{1i} = n_{1e}$ has been used to eliminate $E_{\parallel}$ from the expressions for the response functions.

In the $p_{\perp s}$ response, $\mathcal{R}(\zeta_s)$ is modeled partially by the four-pole function $\mathcal{R}_4(\zeta_s)$ and partially by the two-pole function $\mathcal{R}_2(\zeta_s) = 1/(1 - i\sqrt{\pi}\zeta_s - 2\zeta_s^2)$, yielding:

$$p_{\perp s} = -\frac{ip_{\perp 0s}}{k_z T_{\parallel 0s}} e_s E_{\parallel} \mathcal{R}_4(\zeta_s) + \frac{2B_1 p_{\perp 0s}}{B_0}\left[1 - \frac{T_{\perp 0s}}{T_{\parallel 0s}}\left(\frac{\mathcal{R}_4(\zeta_s)}{2} + \frac{\mathcal{R}_2(\zeta_s)}{2}\right)\right] \tag{C.38}$$

As shown in Fig. (C.2), the $p_{\perp s}$ response is not matched as closely as the parallel moment response for large ζ_s, but the fit is still quite good.

Note that we could have chosen a more general form for the $r_{\parallel,\parallel s}$ and $r_{\parallel,\perp s}$ closures, involving all lower moments and the perturbed magnetic field. However,

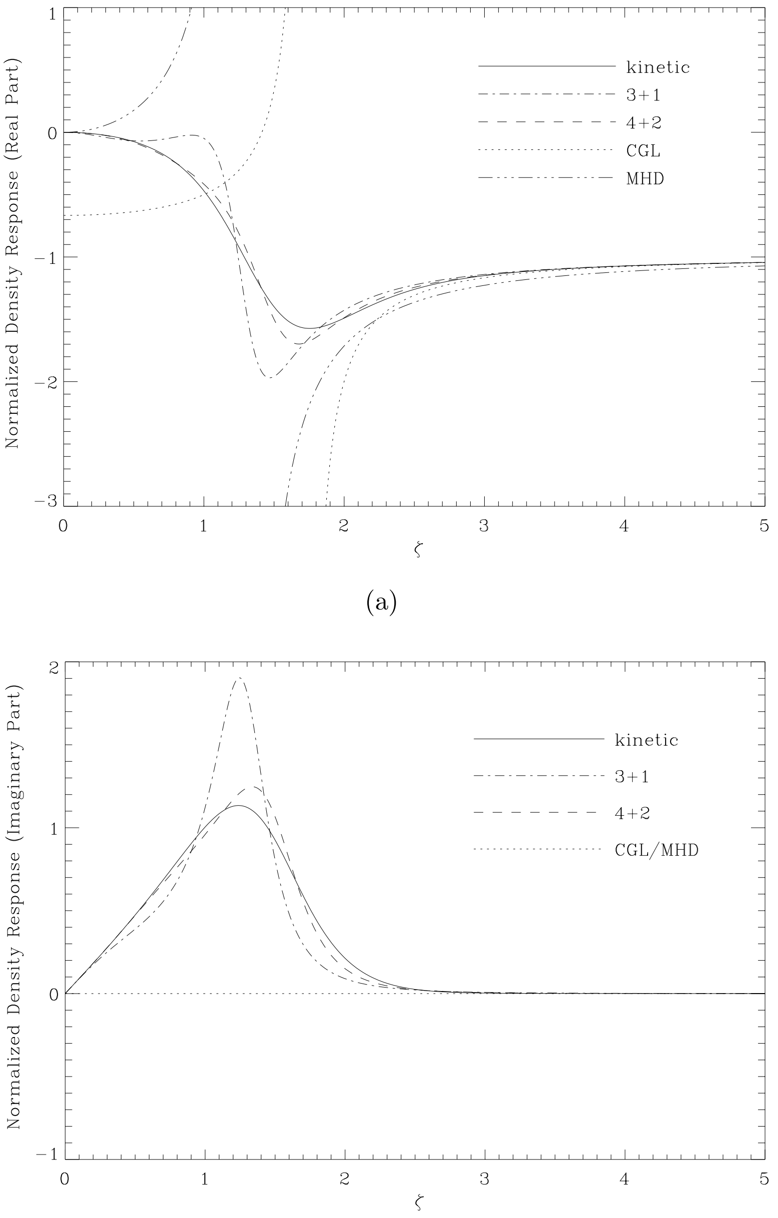

(a)

(b)

Figure C.1: The real (a) and imaginary (b) parts of the normalized linear density response ($n_1/ik_x\xi_x n_0$), versus real normalized frequency ($\zeta_i = \omega/\sqrt{2}|k_\parallel|v_{T_{\parallel i}}$). The 3+1 and 4+2 moment Landau MHD models are compared with linear kinetic theory. Predictions of CGL theory and ideal MHD theory are also shown. Parameters chosen are $Z = 1$, $T_{\perp 0}/T_{\parallel 0} = 1$, $T_{\perp 0i} = T_{\perp 0e}$, $T_{\parallel 0i} = T_{\parallel 0e}$, and $\sqrt{m_i/m_e} = 40$.

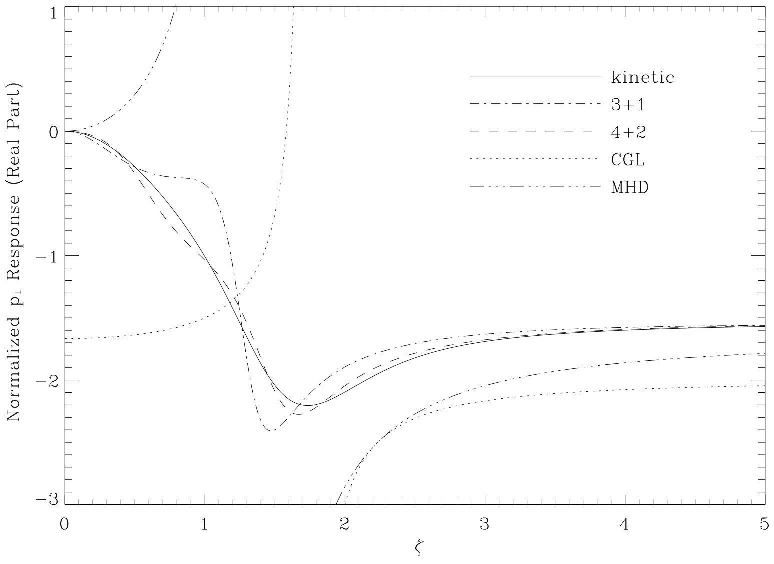

(a)

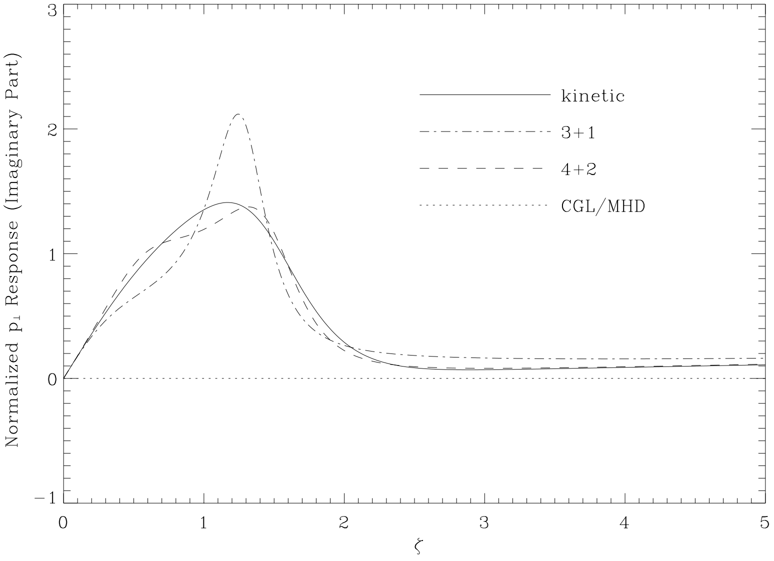

(b)

Figure C.2: The real (a) and imaginary (b) parts of the normalized linear total perpendicular pressure response ($p_{\perp 1}/ik_x\xi_x p_{\perp 0}$), versus real normalized frequency ($\zeta_i = \omega/\sqrt{2}|k_\parallel|v_{T\parallel_i}$). The 3+1 and 4+2 moment Landau MHD models are compared with kinetic theory. Predictions of CGL theory and ideal MHD theory are also shown. Note the significant variation in real $p_\perp$ response between the 3+1 model and the kinetic model, even for large ζ. Parameters are identical to those in Fig. (C.1).

upon matching the linear kinetic response in the $|\zeta| \ll 1$ and $|\zeta| \gg 1$ limits, these general closures will reduce to the closure given here.

The complete 4+2 system of equations is Eqs. (C.2) through (C.5), plus Eqs. (C.16) through (C.19) closed by the inverse Fourier transform of Eqs. (C.34) and (C.35). The system can be solved numerically in k-space where the closure functions are more easily evaluated.

C.6 The 3+1 Model

For many applications, a simpler, less computationally intensive model will prove adequate. The simplest model which evolves $p_\parallel$ and $p_\perp$ involves truncating the hierarchy with Eqs. (C.16) and (C.17), using closure approximations for $q_\parallel$ and $q_\perp$. We refer to such a model as a '3+1 model' because it evolves 3 parallel moments (n, $u_\parallel$, $p_\parallel$) and 1 perpendicular moment ($p_\perp$). Note that the CGL model is a 3+1 model which invokes the simple closure $q_\parallel = q_\perp = 0$.

The 3+1 closures can be derived following the procedure laid out in the previous section, by writing $q_\parallel$ and $q_\perp$ as a sum of the lower moments and B_1, and solving for coefficients by matching with the linear kinetic density and perpendicular pressure response. However, the 3+1 closures for both $q_{\parallel s}$ and $q_{\perp s}$ can be more simply derived as the $\zeta_s \to 0$ limit of the 4+2 model, following the moment reduction scheme outlined by [Dorland 1993]. [Parker and Carati 1995] showed how to extend this scheme to an arbitrary number of moments, and used it to show some similarities to renormalization methods.

Substituting the 4+2 closures into Eqs. (C.32) and (C.33), in $(\mathbf{k}, t)$ space, and taking the limit $|\zeta_s| \ll 1$ yields:

$$q_{\parallel s} = -n_0 \sqrt{\frac{8}{\pi}} v_{t \parallel s} \frac{i k_\parallel T_{\parallel s}}{|k_\parallel|} \tag{C.39}$$

$$q_{\perp s} = -n_0\sqrt{\frac{2}{\pi}}v_{t\|_s}\frac{ik_\| T_{\perp s}}{|k_\||} + n_0\sqrt{\frac{2}{\pi}}v_{t\|_s}T_{\perp 0s}\left(1 - \frac{T_{\perp 0s}}{T_{\|0s}}\right)\frac{ik_\| B_1}{|k_\||B_0} \tag{C.40}$$

Note the term proportional to B_1 in the $q_\perp$ closure. This term is not found in the electrostatic case, where $B_1 = 0$, and it also vanishes for isotropic equilibrium pressures. This term is needed to properly conserve μ linearly in the presence of magnetic field compression and anisotropic pressure.

Substituting the closures Eqs.(C.39-C.40) into the 3+1 equations yields the density response:

$$n_{1s} = -\frac{in_0}{k_z T_{\|0s}}e_s E_\| \mathcal{R}_3(\zeta_s) + \frac{B_1 n_0}{B_0}\left[1 - \frac{T_{\perp 0s}}{T_{\|0s}}\mathcal{R}_3(\zeta_s)\right], \tag{C.41}$$

and the perpendicular pressure response:

$$p_{\perp s} = -\frac{ip_{\perp 0s}}{k_z T_{\|0s}}e_s E_\| \mathcal{R}_3(\zeta_s) + \frac{2B_1 p_{\perp 0s}}{B_0}\left[1 - \frac{T_{\perp 0s}}{T_{\|0s}}\left(\frac{\mathcal{R}_3(\zeta_s)}{2} + \frac{\mathcal{R}_1(\zeta_s)}{2}\right)\right], \tag{C.42}$$

where $\mathcal{R}_3(\zeta_s)$ is a three-pole model of the electrostatic response function:

$$\mathcal{R}_3(\zeta_s) = \frac{2 - i\sqrt{\pi}\zeta_s}{2 - 3i\sqrt{\pi}\zeta_s - 4\zeta_s^2 + 2i\sqrt{\pi}\zeta_s^3} \tag{C.43}$$

and $\mathcal{R}_1(\zeta_s)$ is a one-pole model of $\mathcal{R}(\zeta_s)$, $\mathcal{R}_1(\zeta_s) = 1/(1 - i\sqrt{\pi}\zeta_s)$. The 3+1 density and $p_\perp$ responses are plotted in Figs. (C.1) and (C.2). Of course the response functions, particularly for $p_\perp$, do not fit the kinetic results as well as for the 4+2 model. However, the qualitative behavior is correct, and the behavior in both limits $(\zeta_s \ll 1)$ and $(\zeta_s \gg 1)$ is accurate.

The complete 3+1 system of equations is Eqs. (C.2) through (C.5), plus Eqs. (C.16) and (C.17) closed by the inverse Fourier transform of Eqs. (C.39) and (C.40). This set is significantly simpler than the 4+2 equations, while still conserving particles, momentum, and energy, and providing a reasonable model of the linear kinetic response.

Further moment reduction to 3+0, 2+1, 2+0 and even 1+0 models is possible. These simpler models can be useful in certain cases where conservation of thermal energy isn't important. However, the 3+1 and 4+2 models allow separate evolution of $p_\parallel$ and $p_\perp$, which is often important in describing collisionless modes.

C.7 Collisional Effects

The 3+1 and 4+2 Landau fluid collisionless MHD models have been derived for the completely collisionless case, where the collision rate is very small compared to a typical mode frequency ($\nu \ll \omega$). However, it is possible to introduce some collisional effects into the models using a collision operator such as the BGK operator introduced in Section C.4. It is then possible to examine regimes with a wide range of collisionality, provided that $\nu \ll \Omega_c$, as required by the initial ordering. The accuracy with which collisional effects are modeled will of course be limited by the accuracy of the initial collision operator employed. Furthermore, the modeling of certain collisional effects, such as momentum transfer and resistive tearing of magnetic field lines, is hampered by the use of only the lowest order collisionless MHD expansion in inverse charge.

The moment hierarchy previously derived [Eqs. (C.14) through (C.19)] already includes the collision terms arising from a simple BGK collision operator. However, the form of the equations is quite different from the forms normally used in MHD. We will attack this discrepancy by rewriting Eqs. (C.16) through (C.19), and showing that they reduce approximately to Braginskii's transport equations [BRAGINSKII 1965] in the limit $\omega, |k|v_{t_s} \ll \nu_s \ll \Omega_c$ (ω is a typical mode frequency, and k is a typical wave number).

First define an average pressure, $p_s = (p_{\parallel s} + 2p_{\perp s})/3$, a differential pressure $\delta p_s = p_{\parallel s} - p_{\perp s}$, and a heat flow $q_s = q_{\parallel s}/2 + q_{\perp s}$. We can then divide the pressure tensor, $\mathbf{P_s}$, into an isotropic part and an anisotropic part labeled $\Pi_\mathbf{s}$. That is $\mathbf{P}_s = p_s\mathbf{I} + \Pi_\mathbf{s} = p_s\mathbf{I} + (-\delta p_s\mathbf{I} + 2\delta p_s\hat{\mathbf{b}}\hat{\mathbf{b}})/3$. Combining Eqs. (C.16) through (C.19) then yields:

$$\frac{dp_s}{dt} + \frac{5}{3}p_s\nabla\cdot\mathbf{U} = -\frac{2}{3}\nabla\cdot(\hat{\mathbf{b}}q_s) - \frac{2}{3}\Pi_\mathbf{s} : \nabla\mathbf{U} \tag{C.44}$$

$$\begin{aligned}\frac{d\delta p_s}{dt} &+ \frac{5}{3}\delta p_s\nabla\cdot\mathbf{U} + \Pi_\mathbf{s} : \nabla\mathbf{U} + 3p_s\hat{\mathbf{b}}\cdot\nabla\mathbf{U}\cdot\hat{\mathbf{b}} - p_s\nabla\cdot\mathbf{U} \\ &- 3q_{\perp s}\nabla\cdot\mathbf{U} + \nabla\cdot\left[\hat{\mathbf{b}}(q_{\parallel s} - q_{\perp s})\right] = -\nu_s\delta p_s\end{aligned} \tag{C.45}$$

$$\begin{aligned}&\frac{\partial q_s}{\partial t} + \nabla\cdot\left[\hat{\mathbf{b}}\left(\frac{r_{\parallel,\parallel s}}{2} + r_{\parallel,\perp s}\right)\right] + \frac{3}{2}q_{\parallel s}\hat{\mathbf{b}}\cdot\nabla\mathbf{U}\cdot\hat{\mathbf{b}} - \frac{\frac{3}{2}p_{\parallel s} + p_{\perp s}}{nm_s}\hat{\mathbf{b}}\cdot\nabla p_{\perp s} \\ &+q_{\perp s}\nabla\cdot(u_\parallel\hat{\mathbf{b}}) + \left(\frac{p_{\perp s}^{\;2}}{nm_s} + \frac{p_{\perp s}p_{\parallel s}}{2nm_s} - \frac{3p_{\perp s}^{\;2}}{2nm_s} - \frac{r_{\parallel,\perp s}}{2} - r_{\perp,\perp s}\right)\nabla\cdot\hat{\mathbf{b}} = -\nu_s q_s\end{aligned} \tag{C.46}$$

C.7.1 The High Collisionality Limit

In the limit of high collisionality ($\nu \gg \omega$), the above three equations yield an approximation to the Braginskii transport equations [Braginskii 1965], with the condition $\nu \ll \Omega_c$, as required by the initial ordering.

Formally expanding all moments in the collision time ($1/\nu$), it is apparent from Eqs. (C.16-C.19) that $q_{\parallel 0s} = q_{\perp 0s} = \delta p_{0s} = 0$. Eq. (C.45) then reduces, to lowest order, to:

$$\delta p_{1s} = -\frac{p_{0s}}{\nu_s}(3\hat{\mathbf{b}}\cdot\nabla\mathbf{U}\cdot\hat{\mathbf{b}} - \nabla\cdot\mathbf{U})$$

If ν_s from the original BGK collision operator is taken to be the reciprocal of Braginskii's collision time ($\nu_s = 1/\tau_{s_{Brag}}$), the resulting expression for $\Pi_\mathbf{s} = (-\delta p_s\mathbf{I} + 2\delta p_s\hat{\mathbf{b}}\hat{\mathbf{b}})/3$ matches Braginskii's result to within an order unity constant (.96 for $Z = 1$ ions, and .73 for electrons).

Similarly, a heat flux nearly matching Braginskii's can be derived in the same limit. To lowest order, Eq. (C.46) becomes:

$$\begin{aligned}\nabla\cdot\left[\hat{\mathbf{b}}\left(\frac{r_{\parallel,\parallel 0s}}{2}+r_{\parallel,\perp 0s}\right)\right]-\frac{5}{2}\frac{p_{0s}}{n_0 m_s}\hat{\mathbf{b}}\cdot\nabla p_{0s}\\ +\left(-\frac{r_{\parallel,\perp 0s}}{2}-r_{\perp,\perp 0s}\right)\nabla\cdot\hat{\mathbf{b}}=-\nu_s q_{1s}\end{aligned} \tag{C.47}$$

In this collisional limit, the r_0 moments will take on their Maxwellian values ($r_{\parallel,\parallel 0s} = 3p_0^2/m_s n_0, r_{\parallel,\perp 0s} = p_0^2/m_s n_0, r_{\perp,\perp 0s} = 2p_0^2/m_s n_0$). Substituting yields:

$$q_{1s} = -\frac{5}{2}\frac{p_0}{\nu_s m_s}\nabla_{\parallel} T_{0s}$$

which matches the Braginskii heat fluxes to within factors of order unity.

To match Braginskii's results more precisely, one could replace the simple BGK collision operator used here with a more precise Landau or Fokker-Planck operator. This should allow reproduction of the collisional energy flow between species (Q_s) as well as the above heat flow and anisotropic pressure terms. However, modeling momentum exchange terms is problematic because the initial formal expansion in $1/e$ used to derive the collisionless MHD equations implies $u_{\parallel i} = u_{\parallel e}$. The effects of resistive momentum exchange thus require going to higher order in the ideal MHD ordering, or using an alternative ordering procedure.

C.7.2 Collisionally Modified 3+1 Closure

Collisional effects have not been considered in the derivation of the Landau closures themselves. In principle, it is possible to rederive the linear kinetic response functions with collision terms, and choose Landau closures which match this collisional linear response. However, a simpler procedure appears to be adequate.

This alternate approach [Beer 1995; Beer and Hammett 1996], is to derive a collisionless closure for a many moment model (here the 4+2 model), and then reduce the number of moments by taking the low frequency limit of the highest moment equations, with the collisional terms included. This will incorporate some collisional effects into the lower moment closure (here it will include the collisional effects described by the $q_\parallel$ and $q_\perp$ equations into the 3+1 model). The modified

3+1 closures resulting from this procedure are:

$$q_{\parallel s} = -8 n_0 v_{t\parallel_s}^2 \frac{i k_\parallel T_{\parallel s}}{(\sqrt{8\pi}|k_\parallel| v_{t\parallel_s} + (3\pi - 8)\nu_s)} \tag{C.48}$$

$$q_{\perp s} = -\frac{n_0 v_{t\parallel_s}^2 i k_\parallel T_{\perp s}}{(\sqrt{\frac{\pi}{2}}|k_\parallel| v_{t\parallel_s} + \nu_s)} + \left(1 - \frac{T_{\perp 0s}}{T_{\parallel 0s}}\right) \frac{n_0 v_{t\parallel_s}^2 T_{\perp 0s} i k_\parallel B_1}{B_0(\sqrt{\frac{\pi}{2}}|k_\parallel| v_{t\parallel_s} + \nu_s)} \tag{C.49}$$

These closures allow a smooth transition from the collisionless regime where Landau damping is important, to the collisional regime where Landau damping vanishes.

Hence some collisional effects can be included within the Landau collisionless MHD model, and the model can be extended for use in the marginally collisional regime ($\nu \sim \omega$) as well as the collisionless regime ($\nu \ll \omega$). However, the accurate modeling of some collisional effects, particularly those associated with momentum exchange, is made difficult by the use of the collisionless MHD ordering. A model based on Braginskii or resistive MHD is more appropriate for use in the highly collisional regime ($\nu \gg \omega$).

C.8 Nonlinear Implementation of the Closure

The closures for both the 4+2 and 3+1 models employ terms containing $|k_\parallel|/k_\parallel$. Numerical evaluation of these terms in k-space is straightforward for electrostatic problems (such as ITG/drift-wave turbulence), since only a simple Fourier transform along the equilibrium magnetic field direction is required. But as pointed out by [Finn and Gerwin 1996], Landau damping must be evaluated along perturbed field lines, i.e. Landau damping involves particles mixing due to their free-streaming along the total (equilibrium + fluctuating) magnetic field, and so $k_\parallel$ involves Fourier transforms along these perturbed magnetic field lines. Conceptually, a parallel heat flux is driven by a parallel temperature gradient: $q_\parallel \propto \nabla_\parallel T_\parallel = \hat{\mathbf{b}} \cdot \nabla T_\parallel$. Linearizing this yields $q_{\parallel 1} \propto \hat{\mathbf{b}}_0 \cdot \nabla T_{\parallel 1} + \hat{\mathbf{b}}_1 \cdot \nabla T_{\parallel 0}$. We see that considering only the Fourier transform of $\nabla T_{\parallel 1}$ in the $\hat{\mathbf{b}}_0$ direction would not be sufficient even linearly. In fact, in the ideal MHD limit where the magnetic field is frozen into the fluid, if the temperature is initially uniform along a magnetic field line it will always remain uniform along a field line if the plasma motion is incompressible, so that the perpendicular gradient term will exactly cancel the parallel gradient term: $q_{\parallel 1} \propto \hat{\mathbf{b}}_0 \cdot \nabla T_{\parallel 1} + \hat{\mathbf{b}}_1 \cdot \nabla T_{\parallel 0} = 0$. To account for this, Bondeson and Ward [Bondeson and Ward 1994] employed Lagrangian variables and applied a Landau damping model only to the component of the temperature fluctuations driven by compression. Alternatively, one could use the higher-order 4+2 moment equations which involve $|k_\parallel|$ operating on a higher moment like $q_\parallel$. Upon linearizing $\nabla_\parallel q_\parallel = \hat{\mathbf{b}}_0 \cdot \nabla q_{\parallel 1} + \hat{\mathbf{b}}_1 \cdot \nabla q_{\parallel 0}$, we often have only to consider the first term since $q_{\parallel 0}$ is zero for many types of equilibria.

However, the situation is more complicated for nonlinear electromagnetic calculations. Then the nonlinear term $\hat{\mathbf{b}}_1 \cdot \nabla T_{\parallel 1}$ can not formally be neglected compared to $\hat{\mathbf{b}}_0 \cdot \nabla T_{\parallel 1}$. To be rigorous, the transformation between the k-space closure and its real space equivalent must be made along the perturbed field lines. One way to do this would be with a Lagrangian coordinate system which moved with the magnetic field and had one coordinate aligned with the magnetic field. Then the standard fast Fourier transform (FFT) algorithm along this coordinate could be used to evaluate the $|k_\parallel|$ closures. Alternatively, if the simulation uses a fixed Eulerian grid, then at every time step where $|k_\parallel| T_\parallel$ is to be evaluated, one would need to map $T_\parallel$ from the simulation grid to a field-line-following coordinate system, carry out the FFT, and then map the result back to the simulation grid.

One can avoid FFT's by working directly with the real-space form of the the closures. This is somewhat more expensive computationally, since it involves convolutions in one direction [$\mathcal{O}(N^4)$ operations, where N is the number of grid points in each direction] rather than the faster FFT algorithm [$\mathcal{O}(N^3 \log N)$ operations]. But because the convolutions are done in only one direction instead of a 3-D convolution [$\mathcal{O}(N^6)$ operations], this may be acceptable.

For example, the real-space form of the collisionless 3+1 moment closure for

$q_{\|}$, Eq. (C.39), is the convolution [Hammett and Perkins 1990]

$$q_{\|s}(z) = -n_0 \left(\frac{2}{\pi}\right)^{\frac{3}{2}} v_{t\|_s} \int_0^\infty dz' \frac{T_{\|s}(z+z') - T_{\|s}(z-z')}{z'}, \tag{C.50}$$

where the integration is performed along the perturbed field line. Evaluation of this integral (or its discrete analogue) in principle requires evaluation of the parallel temperature fluctuation at an infinite number of points along the field. In practice the integral can be cut off at a reasonable parallel correlation length [Beer 1995]. Truncating the integral at $z' = L$ means that the Landau damping is applied primarily to modes with $k_{\|} > 1/L$, while modes with $k_{\|} \ll 1/L$ will experience relatively little damping due to the Landau resonances. This approximation is probably adequate in cases where the Landau-damping is only important for the high-$k_{\|}$ component of the fluctuation spectrum, and convergence can be tested by varying L.

When collisions are important, the collisional form of the $q_{\|}$ closure given by Eq. (C.48) should be used. The real space form of this closure is then,

$$q_{\|s} = -n_0 \left(\frac{2}{\pi}\right)^{\frac{3}{2}} v_{t\|_s} \int_0^\infty d\hat{z}' g(\hat{z}') \left[T_{\|s}(\hat{z}+\hat{z}') - T_{\|s}(\hat{z}-\hat{z}')\right] \tag{C.51}$$

$$g(\hat{z}) = \int_0^\infty d\hat{k} \frac{\hat{k}}{\hat{k}+1} \sin(\hat{k}\hat{z})$$

where $\hat{k} \doteq kL_{\|}$ and $\hat{z} \doteq z/L_{\|}$ have been normalized to the parallel collisional mean free path

$$L_{\|} \doteq \frac{\sqrt{8\pi}}{3\pi - 8} \frac{v_{t\|_s}}{\nu_s}.$$

For small $\hat{z}$ Eq. (C.51) behaves just as Eq. (C.50), but for large $\hat{z}$, $g(\hat{z})$ falls off rapidly, as $1/\hat{z}^3$, and the closure integral may be quite accurately truncated after a few mean free paths.

Eq. (C.50) includes nonlinear magnetic effects if the integral is evaluated along perturbed magnetic field lines, but it still assumes that density and temperature vary weakly along a field line so that constant equilibrium values of n_0 and

v_t can be used. There are various possible extensions of this closure which could be proposed to model cases with stronger parallel nonlinearities (for example, see Sec. 3.4 of Smith's thesis [SMITH 1997]). The relative advantages or accuracy of various possibilities has not yet been studied, but one reasonable nonlinear model is

$$\begin{aligned} q_{\parallel s}(z) &= -\left(\frac{2}{\pi}\right)^{\frac{3}{2}} \int_0^\infty \frac{dz'}{m_s^{1/2} z'} [n(z+z')(T_{\parallel s}^{3/2}(z+z') - T_{\parallel s0}^{3/2}) \qquad \text{(C.52)} \\ &- n(z-z')(T_{\parallel s}^{3/2}(z-z') - T_{\parallel s0}^{3/2})], \end{aligned}$$

This has the physically reasonable property of weighting the convolution integral by the density, so that particles streaming from low density regions contribute less to the heat flux. This model (or some variant thereof) might be useful to model the heat flux on field lines which intersect solid materials (where the plasma density goes to zero), such as in the edge of fusion devices. A possible choice for $T_{\parallel 0}$ is $\int dz\, n(z) T_{\parallel}(z) / \int dz\, n(z)$.

C.9 An Example: The Mirror Instability

To demonstrate the usefulness of our model, and the fundamental importance of kinetic effects in simple collisionless MHD problems, we will investigate the magnetic mirror instability. Kulsrud [KULSRUD 1983] cites this example to demonstrate the use of his guiding-center kinetic theory and to expose the limitations of simple fluid theories such as CGL [CHEW et al. 1956]. We will show here that our Landau fluid models recover the exact instability threshold for the mirror mode, and provide a good model of the mode's linear growth rate above the threshold.

Consider a strongly-magnetized, homogeneous plasma consisting of electrons and singly charged ions. Take the magnetic field to be uniform in the $\hat{\mathbf{z}}$ direction, $\mathbf{B_0} = B_0 \hat{\mathbf{z}}$. The equilibrium distribution is taken to be an anisotropic bi-Maxwellian with unequal parallel and perpendicular temperatures. For simplicity, take the electron and ion temperatures to be equal in each direction, $T_{\parallel 0i} = T_{\parallel 0e} = T_{\parallel 0}$ and

$T_{\perp 0i} = T_{\perp 0e} = T_{\perp 0}$. Define the $\hat{\mathbf{x}}$ direction by writing the wave vector $\mathbf{k} = k_x\hat{\mathbf{x}}+k_z\hat{\mathbf{z}}$, and define a 'plasma displacement' vector ξ by $\mathbf{U} = -i\omega\xi$.

Linearizing and Fourier transforming Eqs. (C.2) through (C.5) then yields the following equations of motion:

$$-\rho_0\omega^2\xi_x = -ik_x p_\perp + k_z^2(p_{\parallel 0} - p_{\perp 0})\xi_x - (k_x^2 + k_z^2)(B_0^2/4\pi)\xi_x \tag{C.53}$$

$$-\rho_0\omega^2\xi_z = -ik_z p_\parallel + k_x k_z(p_{\parallel 0} - p_{\perp 0})\xi_x \tag{C.54}$$

where the subscript on the perturbed pressures is again suppressed. Expressions for the perturbed pressures $p_\parallel$ and $p_\perp$ are needed to close this system and solve for the instability growth rate. We will close the system in four different ways: first with linear kinetic theory, then using CGL theory, then with the 3+1 Landau MHD model, and finally with the 4+2 Landau MHD model, in order to compare the instability thresholds and linear growth rates determined by each.

To calculate a kinetic result, we proceed exactly as in Eqs. (C.24) through (C.27). Using quasineutrality to solve for $E_\parallel$, and using Eq. (C.4) for $B_1 = -ik_x\xi_x B_0$, yields:

$$eE_\parallel = k_x k_z \xi_x T_{\perp 0}\frac{\mathcal{R}(\zeta_i) - \mathcal{R}(\zeta_e)}{\mathcal{R}(\zeta_i) + \mathcal{R}(\zeta_e)} \tag{C.55}$$

This leads to the following expressions for the perturbed pressures:

$$p_\perp = 2ik_x\xi_x p_{\perp 0}\left[\frac{T_{\perp 0}}{T_{\parallel 0}}\left(\frac{\mathcal{R}(\zeta_i) + \mathcal{R}(\zeta_e)}{4} + \frac{\mathcal{R}(\zeta_i)\mathcal{R}(\zeta_e)}{\mathcal{R}(\zeta_i) + \mathcal{R}(\zeta_e)}\right) - 1\right] \tag{C.56}$$

$$p_\parallel = ik_x\xi_x p_{\parallel 0}\left[\frac{T_{\perp 0}}{T_{\parallel 0}}\left(1 + \frac{2\mathcal{R}(\zeta_i)\mathcal{R}(\zeta_e)(\zeta_i^2 + \zeta_e^2)}{\mathcal{R}(\zeta_i) + \mathcal{R}(\zeta_e)}\right) - 1\right] \tag{C.57}$$

Substituting for $p_\perp$ in Eq. (C.53) leads to the dispersion relation:

$$\zeta_i^2 + \zeta_e^2 = 2\frac{k_x^2}{k_z^2}\left(-\frac{{T_{\perp 0}}^2}{{T_{\parallel 0}}^2}\mathcal{A}_k(\zeta) + \frac{T_{\perp 0}}{T_{\parallel 0}} + \frac{B_0^2}{8\pi p_{\parallel 0}}\right) + \left(\frac{T_{\perp 0}}{T_{\parallel 0}} - 1 + \frac{B_0^2}{4\pi p_{\parallel 0}}\right) \tag{C.58}$$

where the function $\mathcal{A}_k(\zeta)$ is defined by

$$\mathcal{A}_k(\zeta) = \frac{\mathcal{R}(\zeta_i)^2 + 6\mathcal{R}(\zeta_i)\mathcal{R}(\zeta_e) + \mathcal{R}(\zeta_e)^2}{4(\mathcal{R}(\zeta_i) + \mathcal{R}(\zeta_e))}. \tag{C.59}$$

For parallel propagation ($|k_z| \gg |k_x|$), the above reduces to the dispersion relation for the 'firehose' instability, and the kinetic effects drop out within our ordering (note that a different ordering can be used to analyze these much smaller kinetic effects for limited parameter regimes- see [MEDVEDEV and DIAMOND 1996]). All of the models considered will reproduce the firehose linear growth rate exactly. In the opposite limit ($|k_x| \gg |k_z|$), the dispersion relation becomes:

$$\zeta_i^2 + \zeta_e^2 = 2\frac{k_x^2}{k_z^2}\left(-\frac{{T_{\perp 0}}^2}{{T_{\parallel 0}}^2}\mathcal{A}_k(\zeta) + \frac{T_{\perp 0}}{T_{\parallel 0}} + \frac{B_0^2}{8\pi p_{\parallel 0}}\right) \tag{C.60}$$

This relation has an infinite number of roots, due to the presence of plasma Z-functions. The magnetic mirror instability is the root for which the real part of the frequency goes to zero. Taking the limit $\zeta \to 0$, leads to the instability criterion for the mirror mode, $\frac{{p_{\perp 0}}^2}{p_{\parallel 0}} > p_{\perp 0} + \frac{B_0^2}{8\pi}$. The linear mirror growth rate versus the degree of anisotropy $T_{\perp 0}/T_{\parallel 0}$ is plotted in Fig. (C.3) for a fixed mass ratio at fixed total plasma beta, $\beta = [(2/3)p_{\perp 0} + (1/3)p_{\parallel 0}]/(B_0^2/8\pi)$.

Chew-Goldberger-Low [CHEW et al. 1956] theory can also be used to investigate the mirror instability. CGL's simple truncation of the moment hierarchy with $q_\parallel = q_\perp = 0$ leads to the following linearized expressions for the two perturbed pressures:

$$p_\parallel = -ip_{\parallel 0}(k_x\xi_x + 3k_z\xi_z) \tag{C.61}$$

$$p_\perp = -ip_{\perp 0}(2k_x\xi_x + k_z\xi_z) \tag{C.62}$$

Plugging these into the equations of motion leads to the following dispersion relation:

$$\begin{aligned} \zeta_i^2 + \zeta_e^2 &= 2\frac{k_x^2}{k_z^2}\left(-\frac{{T_{\perp 0}}^2}{{T_{\parallel 0}}^2}\frac{1}{6 - 2(\zeta_i^2 + \zeta_e^2)} + \frac{T_{\perp 0}}{T_{\parallel 0}} + \frac{B_0^2}{8\pi p_{\parallel 0}}\right) \\ &+ \left(\frac{T_{\perp 0}}{T_{\parallel 0}} - 1 + \frac{B_0^2}{4\pi p_{\parallel 0}}\right) \end{aligned} \tag{C.63}$$

In the $|k_z| \gg |k_x|$ limit, CGL theory correctly predicts the instability threshold for the firehose instability. However, in the opposite limit $|k_x| \gg |k_z|$, CGL's description of the mirror mode is drastically in error. CGL predicts the mirror mode goes unstable for $\frac{{p_{\perp 0}}^2}{6p_{\parallel 0}} > p_{\perp 0} + \frac{B_0^2}{8\pi}$, a factor of 6 error from kinetic theory, as noted in [Kulsrud 1983]. The linear growth rate is plotted in Fig. (C.3).

The 3+1 Landau MHD model does markedly better in modeling the mirror mode. The 3+1 dispersion relation is derived using quasineutrality and Eq. (C.41) to solve for $E_\parallel$, and using $B_1 = -ik_x\xi_x B_0$ to find:

$$eE_\parallel = k_x k_z \xi_x T_{\perp 0}\frac{\mathcal{R}_3(\zeta_i) - \mathcal{R}_3(\zeta_e)}{\mathcal{R}_3(\zeta_i) + \mathcal{R}_3(\zeta_e)} \tag{C.64}$$

Plugging this into the 3+1 model expressions for the perturbed pressures worked out in Section C.6, and summing the 2 species pressures yields:

$$p_\perp = 2ik_x\xi_x p_{\perp 0}\left[\frac{T_{\perp 0}}{T_{\parallel 0}}\left(\frac{\mathcal{R}_1(\zeta_i) + \mathcal{R}_1(\zeta_e)}{4} + \frac{\mathcal{R}_3(\zeta_i)\mathcal{R}_3(\zeta_e)}{\mathcal{R}_3(\zeta_i) + \mathcal{R}_3(\zeta_e)}\right) - 1\right] \tag{C.65}$$

$$p_\parallel = ik_x\xi_x p_{\parallel 0}\left[\frac{T_{\perp 0}}{T_{\parallel 0}}\left(1 + \frac{2\mathcal{R}_3(\zeta_i)\mathcal{R}_3(\zeta_e)(\zeta_i^2 + \zeta_e^2)}{\mathcal{R}_3(\zeta_i) + \mathcal{R}_3(\zeta_e)}\right) - 1\right] \tag{C.66}$$

Substituting these results into the equations of motion leads to the following dispersion relation:

$$\zeta_i^2 + \zeta_e^2 = 2\frac{k_x^2}{k_z^2}\left(-\frac{{T_{\perp 0}}^2}{{T_{\parallel 0}}^2}\mathcal{A}_3(\zeta) + \frac{T_{\perp 0}}{T_{\parallel 0}} + \frac{B_0^2}{8\pi p_{\parallel 0}}\right) + \left(\frac{T_{\perp 0}}{T_{\parallel 0}} - 1 + \frac{B_0^2}{4\pi p_{\parallel 0}}\right) \tag{C.67}$$

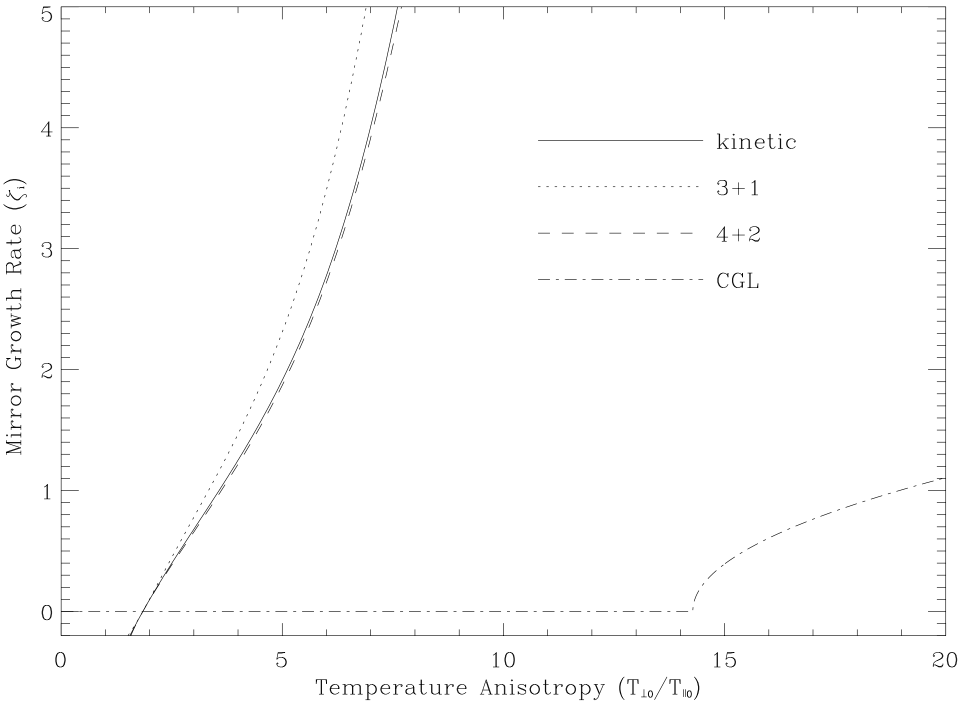

Figure C.3: Linear growth rate of the mirror instability ($k_\perp^2 \gg k_\parallel^2$) as predicted by kinetic theory, 3+1 and 4+2 Landau MHD models, and CGL theory (ideal MHD cannot predict the mirror growth rate as it posits an isotropic pressure). The normalized growth rate ($\zeta_i = Im(\omega)/\sqrt{2}|k_\parallel|v_{T\parallel_i}$) is plotted versus the temperature anisotropy ($T_{\perp 0}/T_{\parallel 0}$) at constant $\beta = \{(2/3)p_{\perp 0} + (1/3)p_{\parallel 0}\}/(B_0^2/8\pi)$. The parameters chosen are $Z = 1$, $T_{\perp 0i} = T_{\perp 0e}$, $T_{\parallel 0i} = T_{\parallel 0e}$, $\beta = 1$ and $\sqrt{m_i/m_e} = 40$.

where $\mathcal{A}_3(\zeta) \equiv [\mathcal{R}_1(\zeta_i) + \mathcal{R}_1(\zeta_e)]/4 + \mathcal{R}_3(\zeta_i)\mathcal{R}_3(\zeta_e)/[\mathcal{R}_3(\zeta_i) + \mathcal{R}_3(\zeta_e)]$. As expected, the 3+1 results are identical to the kinetic results, except that the electrostatic response function $\mathcal{R}(\zeta_s)$ is replaced everywhere by either a three-pole or a one-pole model ($\mathcal{R}_3(\zeta_s)$ or $\mathcal{R}_1(\zeta_s)$). In the limit $|k_z| \gg |k_x|$, the 3+1 model recovers the linear kinetic firehose dispersion relation. Taking the opposite limit $|k_x| \gg |k_z|$, leads to the mirror mode dispersion relation. Again the small frequency limit ($\zeta \to 0$), is taken to investigate the mirror mode. Unlike CGL, the 3+1 model recovers the correct stability threshold for the mirror instability ($\frac{p_{\perp 0}^2}{p_{\| 0}} > p_{\perp 0} + \frac{B_0^2}{8\pi}$). The mirror mode linear growth rate predicted by the 3+1 model is compared to the other models in Fig. (C.3).

The 4+2 model provides a yet more accurate model of the linear mirror mode growth rate. The calculation of the dispersion relation is completely analogous to that for the 3+1 model, and all of the results are identical to those given in the previous paragraph, with the simple substitutions $\mathcal{R}_3(\zeta_s) \to \mathcal{R}_4(\zeta_s)$ and $\mathcal{R}_1(\zeta_s) \to \mathcal{R}_2(\zeta_s)$. Again the instability threshold for the mirror mode matches the kinetic result exactly, and the linear growth rates are compared in Fig. (C.3).

C.10 Discussion

A fluid description of plasma dynamics in the collisionless MHD regime, including models of kinetic effects such as phase mixing and Landau damping, has been developed. This ‘Landau MHD’ model is based on Kulsrud’s formulation of collisionless MHD [Kulsrud 1983; Kruskal and Oberman 1958; Rosenbluth and Rostoker 1958], and it is enhanced through the use of Landau closures analogous to those developed by [Hammett and Perkins 1990]. The model is a significant improvement over previous models, such as CGL theory [Chew et al. 1956], because it includes accurate models of linear kinetic effects, while maintaining desirable nonlinear conservation properties and a fairly simple form in k-space. The model describes all waves which appear within the collisionless MHD ordering, including shear and compressional Alfvén waves, as well as ion acoustic waves. The effects of collisions have also been considered, through the use of a simple BGK collision operator. It has been shown that, in the high collisionality limit ($\omega \ll \nu \ll \Omega_c$), the model reproduces Braginskii's stress tensor and thermal conductivities approximately.

Both a 3+1 moment Landau MHD model and a more accurate but more cumbersome 4+2 moment model have been developed. Both have been derived for fairly general conditions, making no assumptions about adiabaticity or plasma beta, and including models of both ion and electron Landau damping. Collisional effects have been included in the moment equations through the use of a BGK collision operator, and a collisionally modified version of the 3+1 closure has been derived. One species of $Z = 1$ ions is assumed, but the generalization to multiple ion species is possible. The model can be easily reduced to account for further restrictions on adiabaticity, *e.g.* by replacing the full electron moment hierarchy with a simple adiabatic electron response when appropriate. Additional simplifications are easily made for isotropic pressures ($T_{\|0} = T_{\perp 0}$), or electrostatic perturbations ($\mathbf{B_1} = 0$) *etc.* For nearly incompressible modes, a different ordering which eliminates the compressional Alfvén time scale is possible, as outlined by [Medvedev and Diamond 1996].

Some of the limitations of our model are imposed by the use of a general collisionless MHD ordering together with a gyroaveraged kinetic equation. This ordering eliminates all finite Larmor radius (FLR) effects ($k_\perp \rho \to 0$), including the curvature and ∇B drifts. To bring FLR effects into the problem, it is necessary to introduce an additional ordering which removes the compressional Alfvén time scale.

Another complication is the evaluation of the $|k_\||/k_\|$ terms found in the Landau closures. As pointed out by [Finn and Gerwin 1996], the Landau damping must be evaluated along perturbed field lines. Hence, for nonlinear calculations, transforming the closure to real space requires an integral along the perturbed field line. The numerical evaluation of these nonlinear closures may be burdensome in some cases, as discussed in Section C.8.

It is anticipated that the model will be useful for nonlinear numerical simulations. Some of the caveats involved in using Landau closures in nonlinear simulations have been extensively discussed in the gyrofluid literature [Hammett et al. 1992; Dorland 1993; Beer 1995; Beer and Hammett 1996; Hedrick and

Leboeuf 1992; Hammett et al. 1993; Parker et al. 1994; Krommes and Hu 1994; Mattor 1992], but these caveats are an area of ongoing research. There are some regimes where certain nonlinear kinetic effects are not well modeled by Landau-fluid closures [Mattor 1992]. But we generally believe [Dorland 1993; Beer and Hammett 1996; Hammett et al. 1993; Parker et al. 1994] these closures will be adequate for stronger turbulence regimes where rapid decorrelation is occurring and the velocity space details of the distribution function are not critically important.

It is hoped that the model will prove useful for simulating both laboratory and astrophysical plasmas in the collisionless MHD regime. The model should be able to predict the onset and structure of instabilities, as well as the heat and particle transport caused by the instabilities.

Bibliography

Andersson, P. and J. Weiland (1988). A fully toroidal fluid analysis of the magnetohydrodynamic ballooning mode branch in tokamaks. *Phys. Fluids* **31**, 359.

Bakshi, P., W. Bellew, G. Ganguli, and P. Satyanarayana (1977). Presented at the 1977 Sherwood Theory Conference.

Beer, M. and G. Hammett (1998). The dynamics of small-scale turbulence-driven flows. In *Proc. of the Joint Varenna-Lausanne Intl. Workshop on Theory of Fusion Plasmas, (Varenna, Italy).*

Beer, M. and G. Hammett (1999). Turbulence-driven zonal flow dynamics in tokamaks. *Bull. Am. Phys. Soc.* **44**, 1265.

Beer, M. A. (1995). *Gyrofluid Models of Turbulent Transport in Tokamaks.* Ph. D. thesis, Princeton University.

Beer, M. A., S. C. Cowley, and G. W. Hammett (1995). Field-aligned coordinates for nonlinear simulations of tokamak turbulence. *Phys. Plasmas* **2**, 2687.

Beer, M. A. and G. W. Hammett (1996). Toroidal gyrofluid equations for simulations of tokamak turbulence. *Phys. Plasmas* **3**, 4046.

Beer, M. A., G. W. Hammett, W. D. Dorland, and S. C. Cowley (1992). Nonlinear ballooning gyrofluid simulations of toroidal ITG turbulence. *Bull. Am. Phys. Soc.* **37**, 1478.

Biglari, H., P. H. Diamond, and M. N. Rosenbluth (1989). Toroidal ion-pressure-gradient-driven drift instabilities and transport revisited. *Phys. Fluids B* **1**, 109.

Biglari, H., P. H. Diamond, and P. W. Terry (1990). Influence of sheared poloidal rotation on edge turbulence. *Phys. Fluids B* **2**, 1.

Birdsall, C. K. and A. B. Langdon (1991). *Plasma Physics Via Computer Simulation* (Second ed.). New York: IOP Publishing Ltd.

Bondeson, A. and D. Ward (1994). Stabilization of external modes in tokamaks by resistive walls and plasma rotation. *Phys. Rev. Lett.* **72**, 2709.

Braginskii, S. I. (1965). Transport processes in a plasma. In M. A. Leontovich (Ed.), *Reviews of Plasma Physics*, Volume 1, pp. 205–311. New York: Consultants Bureau.

Brizard, A. (1988). Nonlinear gyrokinetic Maxwell-Vlasov equations using magnetic co-ordinates. *J. Plasma Phys.* **41**, 541.

Brizard, A. (1992). Nonlinear gyrofluid description of turbulent magnetized plasmas. *Phys. Fluids B* **4**, 1213.

Carreras, B. A., V. E. Lynch, and L. Garcia (1991). Electron diamagnetic effects on the resistive pressure-gradient-driven turbulence and flow generation. *Phys. Fluids B* **3**, 1438.

Catto, P. J. and K. T. Tsang (1977). Linearized gyro-kinetic equation with collisions. *Phys. Fluids* **20**, 396.

Chang, Z. and J. D. Callen (1992a). Unified fluid/kinetic description of plasma microinstabilities. Part I: Basic equations in a sheared slab geometry. *Phys. Fluids B* **5**, 1167.

Chang, Z. and J. D. Callen (1992b). Unified fluid/kinetic description of plasma microinstabilities. Part II: Applications. *Phys. Fluids B* **4**, 1182.

Chen, Y. and S. E. Parker (1999). Turbulence simulation using a gyrokinetic ion-fluid electron hybrid model. *Bull. Am. Phys. Soc.* **44**, 357.

Cheng, C. Z. (1982). Kinetic theory of collisionless ballooning modes. *Phys. Fluids B* **25**, 1020.

Cheng, C. Z. and H. Okuda (1977). Formation of convective cells, anomalous diffusion, and strong plasma turbulence due to drift instabilities. *Phys. Rev. Lett.* **38**, 708.

Chew, G. F., M. L. Goldberger, and F. E. Low (1956). Boltzmann equation and the one-fluid hydrodynamic equations in the absence of particle collisions. *Proc. Roy. Soc.* **A236**, 112.

Cohen, B. I. and A. M. Dimits (1997). Implicit, partially linearized, electromagnetic particle simulation of plasma drift-wave turbulence.

Phys. Rev. E **56**, 2151.

Connor, J. W., R. J. Hastie, and J. B. Taylor (1979). Shear, periodicity, and plasma ballooning modes. *Proc. R. Soc. London A* **365**, 1.

Connor, J. W. and H. R. Wilson (1994). Survey of theories of anomalous transport. *Plasma Phys. Controlled Fusion* **36**, 719.

Cowley, S. C. (1985). *Some Aspects of Anomalous Transport in Tokamaks: Stochastic Magnetic Fields, Tearing Modes and Nonlinear Ballooning Instabilities.* Ph. D. thesis, Princeton University.

Cowley, S. C., R. M. Kulsrud, and R. Sudan (1991). Considerations of ion-temperature-gradient-driven turbulence. *Phys. Fluids B* **3**, 2767.

Cummings, J. (1995). *Gyrokinetic Simulation of Finite-beta and Self-Generated Sheared-Flow Effects on Pressure-Gradient-Driven Instabilities.* Ph. D. thesis, Princeton University.

Das, A., P. Diamond, M. Rosenbluth, and A. Smolyakov (1999). Zonal flows and fields in electromagnetic drift wave turbulence. *Bull. Am. Phys. Soc.* **44**, 1263.

Diamond, P. H. (1998). Private communication.

Diamond, P. H., M. N. Rosenbluth, F. L. Hinton, M. Malkov, J. Fleischer, and A. Smolyakov (1998). Dynamics of zonal flows and self-regulating drift-wave turbulence. In *1998 IAEA Conference (Yokohama, Japan), IAEA-CN-69/TH3/1.*

Dimits, A. M. (1988). *Nonlinear Mechanisms for Drift Wave Saturation and Induced Particle Transport.* Ph. D. thesis, Princeton University.

Dimits, A. M. (1993). Fluid simulations of tokamak turbulence in quasiballooning coordinates. *Phys. Rev. E* **48**, 4070.

Dimits, A. M., G. Bateman, M. A. Beer, B. Cohen, W. Dorland, G. W. Hammett, C. Kim, J. E. Kinsey, M. Kotschenreuther, A. H. Kritz, L. L. Lao, J. Mandrekas, W. M. Nevins, S. E. Parker, A. J. Redd, D. E. Shumaker, R. Sydora, and J. Weiland (1999). Comparisons and physics basis of tokamak transport models and turbulence simulations. Submitted to Phys. Plasmas.

Dimits, A. M., J. A. Byers, T. J. Williams, B. I. Cohen, X. Q. Xu, R. H. Cohen, J. A. Crotinger, and A. E. Shestakov (1994). Gyrokinetic and global fluid simulations of tokamak microturbulence and transport. In *Plasma Physics and Controlled Nuclear Fusion Research, 1994*, Volume 2, Vienna, pp. 457–462. International Atomic Energy Agency.

Dimits, A. M. and W. W. Lee (1993). Partially linearized algorithms in gyrokinetic particle simulation. *J. Comput. Phys.* **107**, 309.

Dong, J., P. Guzdar, and Y. Lee (1988). Finite beta effects on ion temperature gradient modes. *Phys. Fluids* **30**, 2694.

Dong, J. Q., W. Horton, and J. Y. Kim (1992). Toroidal kinetic η_i-mode study in high-temperature plasmas. *Phys. Fluids B* **4**, 1867.

Dorland, W. (1993). *Gyrofluid Models of Plasma Turbulence.* Ph. D. thesis, Princeton University.

Dorland, W. (1999). Fusion Strategic Simultion Initiative PAC (PPPL 6/2/99).

Dorland, W. and G. W. Hammett (1993). Gyrofluid turbulence models with kinetic effects. *Phys. Fluids B* **5**, 812.

Dorland, W., M. Kotschenreuther, and Q. P. Liu (1999). Electromagnetic, nonlinear gyrokinetic simulations. *Bull. Am. Phys. Soc.* **44**, 356.

Drake, J. F., A. Zeiler, and D. Biskamp (1995). Nonlinear self-sustained drift-wave turbulence. *Phys. Rev. Lett.* **75**, 4222.

Dubin, D. H. E., J. A. Krommes, C. Oberman, and W. W. Lee (1983). Nonlinear gyrokinetic equation. *Phys. Fluids* **26**, 3524.

Evensen, H. T., R. J. Fonck, S. F. Paul, G. Rewoldt, S. D. Scott, W. M. Tang, and M. C. Zarnstorff (1998). Measurements of ion temperature fluctuations in the Tokamak Fusion Test Reactor. *Nucl. Fusion* **38**, 237.

Finn, J. and R. Gerwin (1996). Parallel transport in ideal magnetohydrodynamics and applications to resistive wall modes. *Phys. Plasmas* **3**, 2469.

Fonck, R. J., G. Cosby, R. D. Durst, S. F. Paul, N. Bretz, S. Scott, E. Synakowski, and G. Taylor (1993). Long-wavelength density turbulence in the TFTR tokamak. *Phys. Rev. Lett.* **70**, 3736.

Freidberg, J. P. (1987). *Ideal Magnetohydrodynamics.* New York: Plenum Press.

Frieman, E. A. and L. Chen (1982). Nonlinear gyrokinetic equations for low-frequency electromagnetic waves in general plasma equilibria. *Phys. Fluids* **25**, 502.

Fu, G. Y. and W. Park (1995). Nonlinear hybrid simulation of the toroidicity induced Alfvén eigenmode. *Phys. Rev. Lett.* **74**, 1594.

Garbet, X., L. Laurent, J. P. Roubin, and A. Samain (1994). Radial propagation of turbulence in tokamaks. *Nucl. Fusion* **34**, 963.

Gross, E. and M. Krook (1956). *Phys. Rev.* **102**, 593.

Hahm, T. S. (1988). Nonlinear gyrokinetic equations for tokamak microturbulence. *Phys. Fluids* **31**, 2670.

Hahm, T. S., M. Beer, Z. Lin, G. Hammett, W. Lee, and W. Tang (1999). Shearing rate of time-dependent E×B flow. *Phys. Plasmas* **6**, 922.

Hahm, T. S. and K. H. Burrell (1995). Flow shear induced fluctuation suppression in finite aspect ratio shaped tokamak plasma. *Phys. Plasmas* **2**, 1648.

Hahm, T. S. and L. Chen (1985). Theory of semicollisional kinetic Alfvén modes in sheared magnetic fields. *Phys. Fluids* **28**, 3061.

Hahm, T. S. and L. Chen (1995). Nonlinear saturation of toroidal Alfvén eigenmodes via ion Compton scattering. *Phys. Rev. Lett.* **74**, 266.

Hahm, T. S., W. W. Lee, and A. Brizard (1988). Nonlinear gyrokinetic theory for finite-beta plasmas. *Phys. Fluids* **31**, 1940.

Hahm, T. S. and W. M. Tang (1989). Properties of ion temperature gradient drift instabilities in H-mode plasmas. *Phys. Fluids B* **1**, 1185.

Hamaguchi, S. and W. Horton (1992). Modeling of drift wave turbulence with a finite ion temperature gradient. *Plasma Physics and Controlled Fusion* **34**, 203.

Hammett, G., W. Dorland, and F. Perkins (1992). Fluid models of phase mixing, Landau damping, and nonlinear gyrokinetic dynamics. *Phys. Fluids B* **4**, 2052.

Hammett, G. and F. Perkins (1990). Fluid moment models for Landau damping with application to the ion temperature gradient instability. *Phys. Rev. Lett.* **64**, 3019.

Hammett, G. W., M. A. Beer, W. Dorland, S. C. Cowley, and S. A. Smith (1993). Developments in the gyrofluid approach to tokamak turbulence simulations. *Plasma Phys. Controlled Fusion* **35**, 973.

Hammett, G. W., W. Dorland, M. Beer, and F. W. Perkins (1994). The gyrofluid approach to simulating tokamak turbulence. In M. N. Rosenbluth (Ed.), *New Ideas in Tokamak Confinement.* New York: American Institute of Physics.

Hasegawa, A. and M. Wakatani (1987). Self-organization of electrostatic turbulence in a cylindrical plasma. *Phys. Rev. Letters* **59**, 1581.

Hedrick, C. L. and J.-N. Leboeuf (1992). Landau fluid equaitons for electromagnetic and electrostatic fluctuations. *Phys. Fluids B* **4**, 3915.

Hong, B.-G., W. Horton, and D.-I. Choi (1989). Drift-Alfvén kinetic stability theory in the ballooning mode approximation. *Phys. Fluids B* **1**, 1589.

Horton, W., R. D. Estes, and D. Biskamp (1980). Fluid simulation of ion pressure gradient driven drift modes. *Plasma Physics* **22**, 663.

Horton, W., J. Sendlak, D.-I. Choi, and B. Hong (1985). Kinetic theory of the electromagnetic drift modes driven by pressure gradients. *Phys. Fluids* **28**, 3050.

Jenko, F. and B. D. Scott (1998). Effect of nonlinear electron Landau damping in collisionless drift-wave turbulence. *Phys. Rev. Lett.* **80**, 4883.

Jenko, F. and B. D. Scott (1999). Numerical computation of collisionless drift Alfvén turbulence. *Phys. Plasmas* **6**, 2705.

Kadomtsev, B. B. and O. P. Pogutse (1985). Self-consistent transport theory in tokamak plasmas. In *Plasma Physics and Controlled Nuclear Fusion Research, 1984*, Volume 2, International Atomic Energy Agency, Vienna, pp. 69.

Kim, J. Y., W. Horton, and J. Q. Dong (1993). Electromagnetic effect on the toroidal ion temperature gradient mode. *Phys. Fluids B* **5**, 4030.

Kinsey, J. E. (1998). Private communication.

Kinsey, J. E., R. E. Waltz, and J. C. DeBoo (1999). Perturbative tests of theoretical transport models using cold pulse and modulated electron cyclotron heating experiments. *Phys. Plasmas* **6**, 1865.

Kinsey, J. E., R. E. Waltz, and D. P. Schissel (1997). Transport model testing and comparisons using the ITER and DIII-D profile database. In *Proc. of the 24th EPS Conf. on Contr. Fusion and Plasma Physics (Berchtesgaden, Germany) June 1997.*

KOTSCHENREUTHER, M. (1986). Compressibility effects on ideal and kinetic ballooning modes and elimination of finite Larmor radius stabilization. *Phys. Fluids* **29**, 2898.

KOTSCHENREUTHER, M. (1988). *Bull. Am. Phys. Soc.* **34**, 2107.

KOTSCHENREUTHER, M. (1992). Stabilization of trapped ion modes by impurities, and marginal stability of experimental profiles. *Bull. Am. Phys. Soc.* **37**, 1432.

KOTSCHENREUTHER, M. (1998). Private communication.

KOTSCHENREUTHER, M., W. DORLAND, M. BEER, and G. HAMMETT (1995). Quantitative predictions of tokamak energy confinement from first-principles simulations with kinetic effects. *Phys. Plasmas* **2**, 2381.

KOTSCHENREUTHER, M., G. REWOLDT, and W. M. TANG (1995). Comparison of initial value and eigenvalue codes for kinetic toroidal plasma instabilities. *Computer Physics Communications* **88**, 128.

KROMMES, J. (1997). Systematic statistical theories of plasma turbulence and intermittency: Current status and future prospects. *Phys. Reports* **283**, 5.

KROMMES, J. and G. HU (1994). The role of dissipation in the theory and simulations of homogeneous plasma turbulence, and resolution of the entropy paradox. *Phys. Plasmas* **1**, 3211.

KRUSKAL, M. D. and C. R. OBERMAN (1958). *Phys. Fluids* **1**, 275.

KULSRUD, R. M. (1962). General stability theory in plasma physics. In M. N. Rosenbluth (Ed.), *Proceedings of the International School of Physics Enrico Fermi, Course XXV, Advanced Plasma Theory.* Varenna, Italy: North Holland.

KULSRUD, R. M. (1983). MHD description of plasma. In M. N. Rosenbluth and R. Z. Sagdeev (Eds.), *Handbook of Plasma Physics.* New York: North Holland.

LEBOEUF, J. N., T. TAJIMA, and J. M. DAWSON (1979). *J. Comp. Phys.* **31**, 379.

LEE, G. S. and P. H. DIAMOND (1986). Theory of ion-temperature-gradient-driven turbulence in tokamaks. *Phys. Fluids* **29**, 3291.

LEE, W. W. (1983). Gyrokinetic approach in particle simulation. *Phys. Fluids* **26**, 556.

LEE, W. W. (1987). Gyrokinetic particle simulation model. *J. Comput. Phys.* **72**, 243.

LEE, W. W., Z. LIN, I. MANUILSKIY, and H. MYNICK (1999). Split-weight delta f gyrokinetic particle simulation scheme for finite-beta plasmas. *Bull. Am. Phys. Soc.* **44**, 358.

LIN, Z., T. HAHM, W. LEE, W. TANG, and R. WHITE (1998). Turbulent transport reduction by zonal flows: Massively parallel simulations. *Science* **281**, 1835.

LIN, Z., T. S. HAHM, W. W. LEE, W. M. TANG, and P. H. DIAMOND (1999). Effects of collisional flow damping on turbulent transport. Submitted to Phys. Rev. Lett.

LINSKER, R. (1981). Integral-equation formulation for drift eigenmodes cylindrically symmetric systems. *Phys. Fluids* **24**, 1485.

MATTOR, N. (1992). Can Landau-fluid models describe nonlinear Landau damping? *Phys. Fluids B* **4**, 3952.

MATTOR, N. and P. H. DIAMOND (1994). Drift wave propagation as a source of plasma edge turbulence. *Phys. Rev. Lett.* **72**, 486.

MEDVEDEV, M. and P. DIAMOND (1996). Fluid models for kinetic effects on coherent nonlinear Alfvén waves. I. Fundamental theory. *Phys. Plasmas* **3**, 863.

MIGLIUOLO, S. (1992). Ion temperature gradient driven impurity modes. *Nucl. Fusion* **32**, 1331.

MIKKELSEN, D. R. (1998). Tests of 1-D transport models, and their predictions for ITER. In *1998 IAEA Conference (Yokohama, Japan).*

NAITOU, H., K. TSUDA, W. W. LEE, and R. D. SYDORA (1995). Gyrokinetic simulation of internal kink modes. *Phys. Plasmas* **2**, 4257.

PARKER, S. E. and D. CARATI (1995). Renormalized dissipation in plasmas with finite collisionality. *Phys. Rev. Lett.* **75**, 441.

PARKER, S. E., W. DORLAND, R. A. SANTORO, M. A. BEER, Q. P. LIU, W. W. LEE, and G. W. HAMMETT (1994). Comparisons of gyrofluid and gyrokinetic simulations. *Phys. Plasmas* **1**, 1461.

PARKER, S. E. and W. W. LEE (1993). A fully nonlinear characteristic method for gyrokinetic simulation. *Phys. Fluids B* **5**, 77.

PARKER, S. E., W. W. LEE, and R. A. SANTORO (1993). Gyrokinetic simulation of ion temperature gradient driven turbulence in 3D toroidal geometry. *Phys. Rev. Lett.* **71**, 2042.

QIN, H. (1998). *Gyrokinetic Theory and Computational Methods for Electromagnetic Perturbations in Tokamaks*. Ph. D. thesis, Princeton University.

QIN, H., W. TANG, W. LEE, and G. REWOLDT (1999). Gyrokinetic perpendicular dynamics. *Phys. Plasmas* **6**, 1575.

REWOLDT, G. and W. M. TANG (1990). Toroidal microinstability studies of high-temperature tokamaks. *Phys. Fluids B* **2**, 318.

REWOLDT, G., W. M. TANG, and R. J. HASTIE (1987). Collisional effects on kinetic electromagnetic modes and associated quasilinear transport. *Phys. Fluids* **30**, 807.

REYNDERS, J. V. W. (1994). Finite-beta modification of the ion-temperature-gradient-driven instability in a sheared slab geometry. *Phys. Plasmas* **1**, 1953.

ROBERTS, K. V. and J. B. TAYLOR (1965). Gravitational resistive instability of an incompressible plasma in a sheared magnetic field. *Phys. Fluids* **8**, 315.

ROGERS, B. N. and J. F. DRAKE (1997). Enhancement of turbulence in tokamaks by magnetic fluctuations. *Phys. Rev. Lett.* **79**, 229.

ROMANELLI, F. (1989). Ion temperature-gradient-driven modes and anomalous ion transport in tokamaks. *Phys. Fluids B* **1**, 1018.

ROSENBLUTH, M. N. and F. L. HINTON (1998). Poloidal flow driven by ion-temperature-gradient turbulence in tokamaks. *Phys. Rev. Lett.* **80**, 724.

ROSENBLUTH, M. N. and N. ROSTOKER (1958). *Phys. Fluids* **2**, 23.

SCHNACK, D. D., D. C. BARNES, Z. MIKIC, D. S. HARNED, and E. J. CARAMANA (1987). Semi-implicit magnetohydrodynamic calculations. *J. Comput. Phys.* **70**, 330.

SCOTT, B. (1997). Three-dimensional computation of collisional drift wave turbulence and transport in tokamak geometry. *Plasma Phys. Controlled Fusion* **39**, 471.

SCOTT, B. (1999). Private communication.

SCOTT, S. D., C. W. BARNES, D. M. MIKKELSEN, F. W. PERKINS, M. G. BELL, R. E. BELL, C. E. BUSH, D. E. ERNST, E. D. FREDRICKSON, B. GREK, K. W. HILL, A. C. JANOS, F. C. JOBES, D. W. JOHNSON,

D. K. Mansfield, D. K. Owens, H. Park, S. F. Paul, A. T. Ramsey, J. Schivell, B. C. Stratton, E. J. Synakowski, W. M. Tang, and M. C. Zarnstorff (1993). Nondimensional transport studies in TFTR. In *Plasma Physics and Controlled Nuclear Fusion Research, 1992*, Volume 3, International Atomic Energy Agency, Vienna, pp. 427.

Smith, S. A. (1997). *Dissipative Closures for Statistical Moments, Fluid Moments, and Subgrid Scales in Plasma Turbulence.* Ph. D. thesis, Princeton University.

Snyder, P. B., G. Hammett, M. Beer, and W. Dorland (1999a). Electromagnetic turbulence and transport in tokamak plasmas. *Bull. Am. Phys. Soc.* **44**, 1013.

Snyder, P. B., G. W. Hammett, M. A. Beer, and W. Dorland (1999b). Simulations of electromagnetic turbulence and transport in tokamak plasmas. In *Proc. of the 26th EPS Conf. on Contr. Fusion and Plasma Physics (Maastrict, the Netherlands) 14-18 June 1999, ECA* **23***, 1685.*

Snyder, P. B., G. W. Hammett, and W. Dorland (1997). Landau fluid models of collisionless magnetohydrodynamics. *Phys. Plasmas* **4**, 3974.

Sydora, R. D. and J. Raeder (1988). A particle-MHD simulation approach with application to a global solar wind-cometary plasma interaction model. In B. Buti (Ed.), *Cometary and Solar Plasma Physics*, pp. 310–364. Teaneck, New Jersey: World Scientific Publishing Co.

Tang, W. M. (1978). Microinstability theory in tokamaks. *Nucl. Fusion* **18**, 1089.

Tang, W. M., J. W. Connor, and R. J. Hastie (1980). Kinetic-ballooning-mode theory in general geometry. *Nucl. Fusion* **20**, 1439.

Tang, W. M., R. B. White, and P. N. Guzdar (1980). Impurity effects on ion-drift-wave eigenmodes in a sheared magnetic field. *Phys. Fluids* **23**, 167.

Terry, P. W., J.-N. Leboeuf, P. H. Diamond, D. R. Thayer, J. E. Sedlak, and G. S. Lee (1988). Radial fluctuation scale of ion temperature gradient driven turbulence. *Phys. Fluids* **31**, 2920.

Waltz, R. E. (1988). Three-dimensional global numerical simulation of ion temperature gradient mode turbulence. *Phys. Fluids* **31**, 1962.

Waltz, R. E. (1998). Private communication.

WALTZ, R. E. and A. H. BOOZER (1993). Local shear in general magnetic stellarator geometry. *Phys. Fluids B* **5**, 2201.

WALTZ, R. E., R. R. DOMINGUEZ, and G. W. HAMMETT (1992). Gyro-Landau fluid models for toroidal geometry. *Phys. Fluids B* **4**, 3138.

WALTZ, R. E., G. D. KERBEL, J. MILOVICH, and G. HAMMETT (1995). Advances in the simulation of toroidal gyro-Landau fluid model turbulence. *Phys. Plasmas* **2**, 2408.

WALTZ, R. E., G. STAEBLER, W. DORLAND, G. HAMMETT, M. KOTSCHENREUTHER, and J. KONINGS (1997). A gyro-Landau-fluid transport model. *Phys. Plasmas* **4**, 2482.

XU, X., R. COHEN, G. PORTER, T. ROGNLIEN, D. RYUTOV, J. MYRA, D. A. D'IPPOLITO, and R. MOYER (1998). Turbulence studies in tokamak boundary plasmas with realistic divertor geometry. In *1998 IAEA Conference (Yokohama, Japan).*

ZEILER, A., D. BISKAMP, J. F. DRAKE, and P. GUZDAR (1996). Three-dimensional fluid simulations of tokamak edge turbulence. *Phys. Plasmas* **3**, 2951.

ZEILER, A., D. BISKAMP, J. F. DRAKE, and B. N. ROGERS (1998). Transition from resistive ballooning to η_i driven turbulence in tokamaks. *Phys. Plasmas* **5**, 2654.

ZONCA, F. and L. CHEN (1993). Theory of continuum damping of toroidal Alfvén eigenmodes in finite-beta tokamaks. *Phys. Fluids B* **5**, 3668.

ZONCA, F., L. CHEN, J. Q. DONG, and R. A. SANTORO (1998). Existence of ion temperature gradient driven shear Alfvén instabilities in tokamaks. In *18th International Sherwood Fusion Theory Conference.*

ZONCA, F., L. CHEN, and R. SANTORO (1996). Kinetic theory of low-frequency Alfvén modes in tokamaks. *Plasma Phys. Controlled Fusion* **38**, 2011.